Fluid Structure Interaction Modelling of Flapping Wings

Development and Validation of a General Open-source Fluid Structure Interaction Method with Analysis of Flexible Flapping Wing Aerodynamics

D. Risseeuw

Aerodynamics

Faculty of Aerospace Engineering

TU Delft

Delft University of Technology

Fluid Structure Interaction Modelling of Flapping Wings

Development and Validation of a General Open-source Fluid Structure Interaction Method with Analysis of Flexible Flapping Wing Aerodynamics

by

D. Risseeuw

to obtain the degree of Master of Science
at the Delft University of Technology,
to be defended publicly on Tuesday January 29, 2019 at 13:30 AM.

Student number:	4173058	
Project duration:	September 5, 2017 – January 29, 2019	
Thesis committee:	Dr. ir. B. W. van Oudheusden,	TU Delft, Supervisor
	Dr. ir. A. H. van Zuijlen,	TU Delft, Supervisor
	Dr. ir. A. C. Viré ,	TU Delft
	Dr. rer. nat. B W. Uekermann,	TU Eindhoven

TU Delft

Acknowledgements

This M.Sc thesis concludes my studies in Delft, and with it a remarkable period of my life. I have learned more than I could ever imagine and formed friendships for life.

Firstly I would like to thank my supervisors: Dr. ir. Bas van Oudheusden en Dr. ir. Sander van Zuijlen. They gave me large freedom to explore my own path in the research. At the same time they were always available to address my doubts and questions; My apologies for the several late hours I have caused you.

As a part of my thesis I visited Makis (Gerasimos) Chourdakis and Benjamin Uekermann from the preCICE group at the TU Munich. Thank you for the incredibly warm welcome and good support througout the thesis. I think we have achieved something great for the open-source community together!

A big thank goes out to the basement dwellers, sorry to leave you but it is time to move on. Thank you Anna for the flair you brought to the basement, Jordi and Javi for the amazing scientific attitudes. Thank you Arun, Niels, Jaime for all the good talks during the breaks, Mitro for keeping the Italian sprit up. Ventsislav: Never change, your personality brightens everybody up. Lucas, thanks for the last minute quality check of the report. The good vibe of everybody in the basement has made this thesis a treasured experience for me.

My thanks and praise go out to loved ones. Mi amor Kathy helped my many times through the night when I had to continue working, Sara and Rick always just knew how to distract me on the numerous family events. Finally I want to thank my parents: Adri Risseeuw en Brechtje de Boer. They gave me all their love and support even in times when I was so consumed with the thesis that I didn't show the proper appreciation.

D. Risseeuw
Delft, January 2019

Abstract

Flapping wings display complex flows which can be used to generate large lift forces. Flexibility in wings is widely used by natural flyers to increase the aerodynamic performance. The influence of wing flexibility on the flow can be computed using numerical analysis with Fluid Structure Interaction (FSI). However, there is a lack of open-source FSI methods. Therefore, a new implementation is developed for the well-known CFD code OpenFOAM to facilitate FSI with the multi-physics coupling library *preCICE*. The OpenFOAM adapter does not require changes to the `OpenFOAM` source code and is compatible with a variety of `OpenFOAM` versions. Structural modelling is performed using the open-source code `CalculiX`.

The method is validated using the laminar incompressible cylinder-with-a-flap benchmark for one steady and two unsteady cases. Good coherence is seen for the deflection and force generation, but the coupled method is sensitive to the eigenmodes of the structural model.

The influence of inertial, elastic and aerodynamic forces is quantified using a 2D wing. A sinusoidal flapping motion is imposed on the leading edge of the vertical wing. The inertial force on the wing dominates for high mass ratios and the wing deflection is rather independent of the flow. For a low mass ratio, the wing deformation scales with the increasing elasticity. The maximum lift and lowest drag were found for the wing with large flexibility and low mass so the passive deformation by aerodynamic forces creates a favourable shape for lift production.

Flexible translating and revolving wings at an angle of attack of 45° show that chordwise flexibility decreases both lift and drag, however the lift over drag ratio is increased. The flow around both wings forms a coherent structure with a Root Vortex (RV), Tip Vortex (TV), Leading Edge Vortex (LEV) and Trailing Edge Vortex (TEV). The LEV on the revolving wing is stable for approximately up to half the span because vorticity is transported outward in the vortex core. The flowfield and LEV breakdown are consistent with experimental data of the same wing. The translating wing builds up circulation but the LEV detaches quickly near the centre of the wing. Chordwise bending reduces the angle of attack which decreases the distance to the core of the shed LEVs.

Contents

List of Figures

List of Tables

Glossary

`MBDyn` Multibody Dynamics

`NonStaD` NONlinear STAtic and Dynamic analysis

`OpenFOAM` Open source Field Operation And Manipulation

`PIMPLE` merged PISO-SIMPLE algorithm

`PISO` Pressure Implicit with Split Operator

`SU`^{2} Stanford University Unstructured

`preCICE` Precise Code Interaction Coupling Environment

2D Two Dimensional

3D Three Dimensional

ALE Arbitrary Lagrangian Eulerian

API Application Programming Interface

CFD Computational Fluid Dynamics

CFL Courant-Friedrichs-Lewy

CHT Conjugate Heat Transfer

CPS Conventional Parallel Staggered

CSD Computational Structural Dynamics

CSS Conventional Serial Staggered

DGCL Discrete Geometric Conservation Law

DNS Direct Numerical Simulation

DOF Degrees of Freedom

ESV End of Stroke Vortex

FEM Finite Element Method

FPE Fixed Point Equation

FSI Fluid Structure Interaction

IBM Immersed Boundary Method

IQN-ILS Interface Quasi-Newton Least-Squares

IQN-LS Interface Quasi-Newton Inverse Least-Squares

IQN-MVJ Interface Quasi-Newton Multiple Vector Jacobian

LBE Lattice Boltzmann Equations

LE Leading Edge

LER Leading Edge Reinforced

LES Large Eddy Simulation

LEV Leading Edge Vortex

MAVs Micro Aerial Vehicles

ML-IQN-LS Multi-Level Quasi-Newton Least-Squares

MPI Message Passing Interface

ODE Ordinary Differential Equation

OGM Overset Grid Method

PDE Partial Differential Equation

PIV Particle Image Velocimetry

RANS Reynolds Averaged Navier Stokes

RBF Radial Basis Functions

RV Root Vortex

TE Trailing Edge

TEV Trailing Edge Vortex

TFI Transfinite Interpolation

TV Tip Vortex

URANS Unsteady Reynolds Averaged Navier Stokes

UVLM Unsteady Vortex Lattice Method

Nomenclature

Greek Symbols

Symbol	Description	Units
α	Angle of attack	rad
δ	Chord lengths travelled at reference length	–
Γ	Circulation	$\mathrm{m^2\,s^{-1}}$
Γ	Interface between fields	–
λ_2	Vortex criterion	$\mathrm{s^{-2}}$
μ	Dynamic Viscosity	$\mathrm{kg\,m^{-1}\,s^{-1}}$
ν	Kinematic Viscosity	$\mathrm{m\,s^{-1}}$
ν	Poisson's ratio	–
Ω	Angular velocity	$\mathrm{rad\,s^{-1}}$
Ω	Antisymmetric part of the velocity gradient	$\mathrm{s^{-1}}$
Ω	Solver domain	$\mathrm{rad\,s^{-1}}$
ω	Vorticity	$\mathrm{s^{-1}}$
Φ	Flapping angle amplitude	rad
ϕ	Flapping angle	rad
ϕ	Wall flux in simulation	–
Π_1	Effective Stiffness, see eq. 2.19	–
ρ	Density	$\mathrm{kg\,m^{-3}}$
τ	Dimensionless time	–
τ	Viscous stress tensor	$\mathrm{N\,m^{-2}}$
θ	Pitch angle	rad

Roman Symbols

Symbol	Description	Units
EI	Flexural stiffness	$\mathrm{N\,m^2}$
FR	Frequency Ratio	–
Re	Reynolds number	–
Ro	Rossby Number	–
St	Strouhal number	–
A^*	Dimensionless stroke amplitude	–
c	chord	m
C_d, C_D	(Sectional) Drag coefficient	m
C_l, C_L	(Sectional) Lift coefficient	m
D	Drag	N
E	Young's modulus	$\mathrm{N\,m^{-2}}$
F	Force	N
f	Frequency	Hz
g	Gravitational constant	$\mathrm{m\,s^{-2}}$
h	Helical density	$\mathrm{m\,s^{-2}}$
h	Wing thickness	m
I	Area moment of inertia	$\mathrm{m^4}$

k	Reduced frequency, see eq. 2.1	–
L	Length scale	m
m^*	Mass ratio	–
p	Pressure	$\mathrm{N\,m^{-2}}$
Q	Vortex identification criterion, see eq. 2.27	$\mathrm{s^{-2}}$
R	Wing radius	m
r	radius	m
S	Symmetric part of the velocity gradient	$\mathrm{s^{-1}}$
S	Wing area	$\mathrm{m^2}$
T	Time scale	s
t	Time	s
U	Velocity	$\mathrm{m\,s^{-1}}$
u	Flow velocity field	$\mathrm{m\,s^{-1}}$
u	Structural displacement	m
W	Work	j
x	Mesh displacement	m

Superscripts

Symbol	Description	Units
*	Dimensionless equivalent of a quantity	–

Subscripts

Symbol	Description	Units
cn	Cosine	–
D	Lift	–
f	fluid	–
L	Drag	–
LE	Leading edge	–
N	Normal	–
s	structure	–
sn	Sine	–
T	Tangential	–
TE	Trailing edge	–
dev	Deviatoric part of a tensor	–
ext	External	–
hyd	Hydrostatic part of a tensor	–
ref	Reference value	–
root	Property at the wing root	–
tip	Property at the wing	–

Other Symbols

Symbol	Description	Units
Δ	Difference	–
∇	Nabla operator	–

Chapter 1

Introduction

Over the past years an increment interest in Micro Aerial Vehicles (MAVs) has lead to an increase in research towards flapping wing aerodynamics. This research is often based on natural flyers as these display remarkable capabilities in force production, manoeuvrability and efficiency. Currently, these capabilities are unmatched by man made flyers. The aerodynamic phenomena found on flapping wing are different from the classic airfoil theory that is used at higher Reynolds numbers. Unsteady phenomena play a large role in the force production by flapping wings, as shown in figure 1.1.

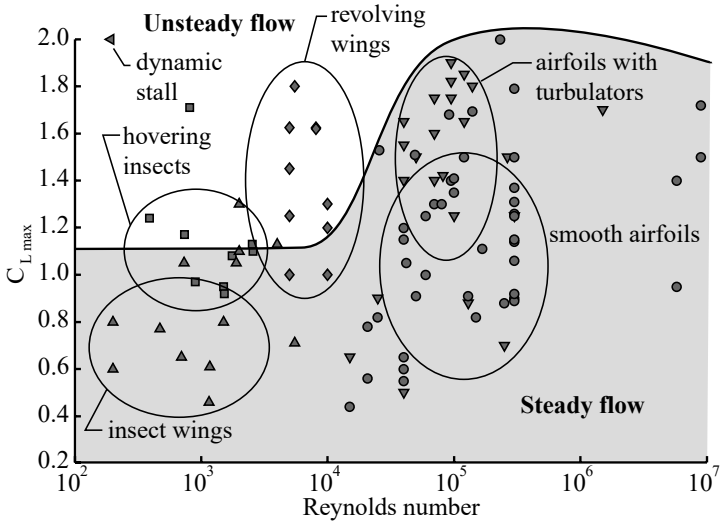

Figure 1.1: Maximum lift coefficient as a function of the Reynolds number. The shaded area indicates lift generating capabilities from steady flows. From Jones & Babinsky (2010)

As the Reynolds number decreases from 10^5 and 10^4 a sharp decline is seen for the lift generating capabilities of steady flows. This denotes the border between steady and unsteady lift generating mechanisms. Beneath this border traditional lift generation mechanisms such as translating and rotary suffer from reduced performance. In contrast flapping wings benefit from the unsteady aerodynamic phenomena at low Reynolds numbers which permit the generation of large lift forces.

Several unsteady aerodynamic effects are found on flapping wing: The Wagner effect, added mass effect, clap and fling effect, Kramer effect, wake capture effect, tip vortex contribution and a stable LEV. The latter effect was first recognised by Ellington et al. (1996) and is often the most prominent feature for lift generation in flapping wing aerodynamics. It is seen on wings moving at a high angle of attack which feature dynamic stall (Sane, 2003). A vortex is formed over the leading edge which can remain stably attacked to the wing surface. A low pressure area inherent to the vortex creates a large suction force on the wing. The suction force acts perpendicular to the wing

surface and are the dominant component of the forces. Therefore, the force contribution acts perpendicular to the wing for large angles of attack (Birch & Dickinson, 2001). The high suction force leads to a maximum in the lift coefficient for 45° angle of attack (Percin & van Oudheusden, 2015; Trizila et al., 2011; Phillips & Knowles, 2011).

The motion of flapping wings is determined by an acceleration phase and a phase of rectilinear motion. Both translating and revolving wings at high angles of attack are capable of developing a LEV at the acceleration phase, but only for revolving wings the LEV can remain stably attached to the wing surface Lentink & Dickinson (2009b). For translating wings a vortex streak is formed which resembles the von Kármán vortex street behind a cylinder. Early research by Ellington et al. (1996) postulated that the LEV stability in revolving wings was caused by outboard vorticity transport. Lentink & Dickinson (2009b); Jardin & David (2015); Jardin (2017) evaluate the influence of the various apparent rotational effects on the LEV, and reach the conclusion that mainly the Coriolis force is responsible for the stability of the LEV. The relative influence of the Coriolis force is related to the degree of translating versus rotating motion, expressed in the Rossby number. The rotational effects scale inversely with the Rossby number on the wing, and the LEV stability is deteriorates for higher Rossby numbers.

Apart from a different flapping motions, natural flyers exhibit flexible wings. Birds and bats actively deform their wings, while most insects rely on passive wing deformation (Shyy et al., 2013). Experimental research Zhao et al. (2010) showed that the application of flexibility on a simple revolving wing leads to smaller lift but decreases the drag likewise. Numerical research on 2D and 3D flapping wings showed that the wing efficiency for a given angle of attack can be increased by the application of flexible wings. The dynamic behaviour of the wing is categorised by the mass and frequency ratio, which determine the relative importance of the inertial, elastic and aerodynamic force on the wing. Vanella et al. (2008); Dai et al. (2012); Luo et al. (2010) found that relative low mass ratios flapping wing reaches the largest lift over drag (L/D) for a frequency ratio near $FR = 1/3$. Heavier wings create an advanced pitching motion and the point of best performance is reached for more flexible wings.

More recently experiments towards the influence of flexibility on flapping wings was performed using tomographic Particle Image Velocimetry (PIV) by van de Meerendonk (2016). In this work a revolving wing was tested for three wings with a varying elasticity. The lift and drag decreased for the added elasticity, but an increase in L/D ratio was noted. The flowfield showed similar structures for the flowfield with more coherency for larger elasticity. Furthermore, the LEV of the flexible cases was more compact and showed higher levels of vorticity transport through the LEV core. Breakdown of the LEV is seen for all three wings around midspan after the wing revolved for approximately 40°.

Numerical modelling of the wing using a Fluid Structure Interaction (FSI) method can be used to gain more insight in the fundamental interaction that takes place between the structure and the fluid. A FSI models The interaction between the fluid and structure by exchange of boundary data. From the fluid side, the force or equivalent quantity has to be mapped onto the structure. The structure is then evaluated which leads to a structural deformation which is which in term affects the fluid flow. FSI simulations with large interaction require implicit coupling, where multiple subiterations can be used for every coupling timestep.

Several commercial methods exist for the modelling of FSI coupled simulations. On the open-source side a smaller variety is seen. The most used open source CFD code, `OpenFOAM` does not include standard methods of creating a FSI simulation (*OpenFOAM and The OpenFOAM Foundation*, 2018).

Generic FSI coupling can be performed by simply exchanging boundary data through text files, however this poses large limits on the scalability of the simulations. More sophisticated methods also exist, such as `FOAM-FSI` developed by Blom et al. (2015). However it is not without its drawbacks, since it is not being maintained. Recent progress by Chourdakis (2017b) has opened the door

for a new approach: In this work a method is proposed to couple `OpenFOAM` with other packages for conjugate heat transfer simulations. The communication between the packages is performed using the multi-physics coupling library `preCICE` Uekermann (2017). In this thesis the OpenFOAM adapter is further developed to extend its capabilities to FSI problems with `OpenFOAM`. The research goal of this thesis can therefore be stated as:

> *This research aims at improving the understanding between the flexibility of flapping wings and the aerodynamic by constructing a numerical Fluid-Structure Interaction model using open-source software.*

To reach the goal this work is divided in three parts. First a literature review of flapping wings and fluid structure interaction is given. Chapter 2 focusses on the flow phenomena on flapping wings and the implication of flexibility in wings. Theory on FSI is treated in Chapter 3, where the different steps that are implemented in the coupling code are evaluated. The second part explains the method that is developed in this thesis. Chapter 4 treats the implementation of the OpenFOAM adapter and is followed by chapter 5 which explains the validation procedure: First the numerical model of the fluid and the structure are validated separately, which is used to quantify errors in the individual solvers. One way coupling of the coupled problem is then used to verify that the mapping of parameter is performed accordingly. Next, full coupling is performed to finalize the validation procedure. The benchmarking case by Turek & Hron (2006) is used for this purpose.

The last part of this thesis focusses on fluid structure interaction modelling of flapping wings. A strongly coupled simulation of a 2D flapping wing is evaluated in chapter 6. Here the influence of the wing mass and elasticity on the force coefficients is derived. Furthermore, the effect of the flexibility on the flow field is evaluated. The influence of flexibility on a 3D wing is treated in chapter 7. Three wings of various elasticity are tested in both a translating and revolving motion. Finally, chapter 8 summarizes the conclusions from the thesis and gives recommendations for further work.

Chapter 2

Flapping wing Aerodynamics

In this chapter the theory behind flapping wing aerodynamics is presented. This theory forms the basis for the largest part of the thesis. Numerous studies have already been performed towards flapping wing aerodynamics, and this has enlightened a lot of knowledge about the flow phenomena which are present on flapping wings. Still, much work is yet required in flapping wing aerodynamics. In the research by Gutierrez et al. (2017) it is shown that common quasi-steady methods for lift prediction are inconsistent and inaccurate. Therefore there is a need for high fidelity models to predict the aerodynamics around flapping wings.

The effect of various flapping parameters will be treated. Also the fundamental flow phenomena that are seen are discussed. First an overview of rigid wings is given, since the research in flapping wing aerodynamics has started in this field.

Next the role of flexibility in flapping wings is given in section 2.4. Here, additional parameters are treated which influence the flow around the wing. Furthermore, differences between flexible wings and rigid wings are given.

2.1. Kinematics of flapping flight

The forces on flying objects can be decomposed in four components: Lift, gravitational force, thrust and drag. For steady flight, the lift should equal gravity, and the thrust the drag, respectively. Most human made aircraft rely on a separation of the lift and thrust creation. Lift is generally created by a stationary wing and the thrust by an engine.

Natural flyers such as birds, bats and insects utilize their wings to create both lift and thrust with a single body part, eliminating the necessity for a separate thrust generating system. In the past decades, MAVs have been built which rely on flapping wings for both lift and thrust generation, such as the Delfly, described by de Croon et al. (2012). The wings of these flyers provide both lift and thrust because they create their own movement relative to the flow by flapping. With respect to stationary wings, this complicates the description of the wing kinematics, since the wing location (and shape) is now varying in time.

2.1.1. Wing movements

The movement of flapping wings is divided in two phases, respectively the upstroke and downstroke, see figure 2.1. The stroke reversal between these phases are called the supination and pronation. The former follows after the downstroke, the latter after the upstroke. Figure 2.2 denotes the parameters which are used to characterise the flapping motion.

Alternatively to the rotational flapping motion displayed in figure 2.1, a translational motion is present in many studies. The translational motion is normally referred to as a plunging, and denoted by $h(t)$ which replaces $\phi(t)$ and is a length scale.

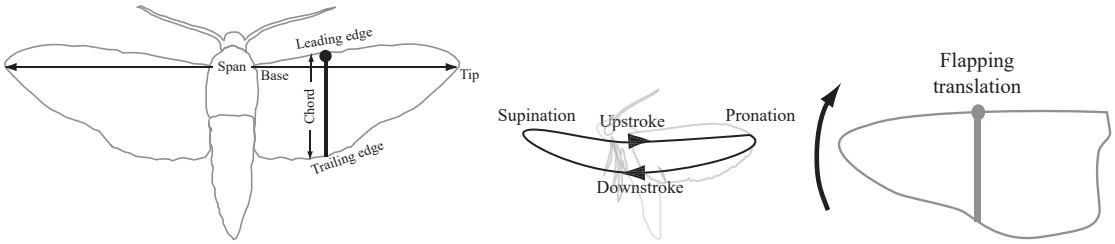

Figure 2.1: Basic kinematics of a flapping wing, modified from Sane (2003). (Left) Wing planform with the span and mean chord. (Middle) Stroke path. (Right) Flapping motion.

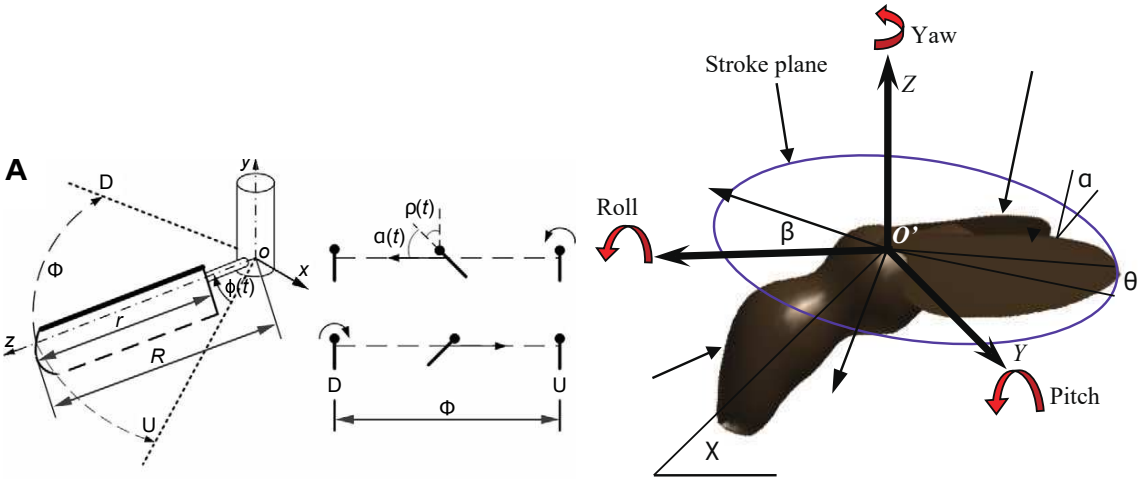

Figure 2.2: Flapping parameters, modified from Lu & Shen (2008) and Shyy et al. (2013). (Left) D and U denote the extrema which are separated by the stroke angular amplitude, Φ. $\phi(t)$ denotes the positional angle of the flapping wing, α is the geometric angle of attack with respect to the stroke plane, or the pitching angle. (Right) The stroke plane is defined by the wing base and the wing tip position at maximum and minimum sweep. The elevation angle of the wing is given by $\theta(t)$.

2.1.2. Description of the wing motion

For a given wing the positional angle, elevation angle and pitch can then be expressed as a function of the flapping frequency or its non-dimensional counterpart: the reduced frequency. Equation 2.1 gives the general expression for the reduced frequency. The second part is the form for hovering flight (no free stream velocity). In that case the reference length and velocity are respectively the span and the tip velocity: $L_{\text{ref}} = R$ and $U_{\text{ref}} = 2\pi\Phi f R$. The reference velocity in hovering flight can alternatively be defined as some other spanwise velocity. The velocity at mid-span, 75% span or at the tip are commonly used (van de Meerendonk, 2016, p. 5).

$$k = \frac{2\pi f L_{\text{ref}}}{2U_{\text{ref}}} = \frac{\pi}{\Phi AR} \tag{2.1}$$

The kinematic angles can then be expanded in Fourier series to represent a large variety of smooth motions that are found in flapping wings in nature:

$$\phi(t/T) = \sum_{n=0}^{3} \left[\phi_{cn}\cos(2\pi k t/T) + \phi_{sn}\sin(2\pi k t/T)\right], \tag{2.2}$$

$$\theta(t/T) = \sum_{n=0}^{3} \left[\theta_{cn}\cos(2\pi k t/T) + \theta_{sn}\sin(2\pi k t/T)\right], \tag{2.3}$$

$$\alpha(t/T) = \sum_{n=0}^{3} \left[\alpha_{cn}\cos(2\pi k t/T) + \alpha_{sn}\sin(2\pi k t/T)\right]. \tag{2.4}$$

2.1.3. Propagation of the wing

To quantify the flapping period, different measures exist. The Formation Number (FN) is used by Poelma et al. (2006). It is defined by the distance the wing section travelled with respect to the reference chord. Since the formation number is a function of time and spanwise location, it rises quicker at the tip than at the root:

$$FN = \frac{x(r)}{c}. \tag{2.5}$$

The formation number allows different sections of the wing to be compared for the same distance travelled. For comparing the wing at a certain time-instance the non-dimensional time or the travel length can be used. T is the flapping period, so the dimensionless time reaches one after a completed period. The measure δ is the distance travelled at some reference spanwise position, so for one chord length travelled it reaches unity:

$$t^* = \frac{t}{T}, \qquad \delta^* = \frac{\delta}{c}. \tag{2.6}$$

2.2. Flow phenomena in flapping wings

The unsteady flow that occurs on flapping wings displays a large number of aerodynamic phenomena. Depending on the type of flow, these phenomena carry varying importance in the determination of the aerodynamic forces. In flapping wing literature different effects are recognised. This may be attributed to the fact that some effects may incorporate flow features that can also be named under other effects. The different phenomena that are distinguished in this thesis are (Sane, 2003; Shyy et al., 2013):

Wagner Effect

An impulsively started wing will not create the steady state lift immediately. Rather, according to Wagner (1925) the instantaneous lift is half the steady state value, and the rest of the lift is build-up asymptotically until reaching the steady state value.

The lift builds up gradually because of two processes. First, the Kutta condition is established after a finite time because of the viscous action that causes delay. More importantly, the circulation of the trailing edge has to be shed. The so-called starting vortex influences the circulation on the airfoil which diminishes with distance. Only when the starting vortex is far away, the steady-state lift is reached.

The Wagner function shows an initial lift which is half the final lift, by non-circulatory effects. This lift is caused by the acceleration of the fluid particles and is referred to as the added mass effect. This effect is treated below more extensively.

Sane (2003) mentioned on the basis of various studies that the Wagner effect might not be very strong in Two Dimensional (2D) wings in the low Reynolds number as found in insect flight. For Three Dimensional (3D) flapping wings the Wagner effect was found to have a small influence.

Clap-and-Fling

This effect is a wing-wing interaction effect, also known as the Weis-Fogh mechanism. In nature pigeons use it for large lift creation at take-off and insects such as the dragonfly use the mechanism for high lift creation. The DelFly MAV makes use of the clap-and-fling effect as discussed by de Croon et al. (2012); Gillebaart (2011).

Figure 2.3 shows the clap and fling effect. During the clap motion the wings move towards each other (A) and touch (B). The junction of the two wing surfaces in (C) is paired with the acceleration of the fluid between the wings as a jet. The fling phase commences with the suction of fluid by the separation of the two wing surfaces (D). Next the leading edge vortices are created near the wing surfaces when the wings move apart (E). The starting vortices that are formed at the trailing edge annihilate each other since they are of opposite circulation, thereby mitigating the slowdown in lift build-up predicted by the Wagner effect.

Delayed stall and LEV

For an impulsively started inclined wing the circulation on the airfoil is build up over time. This is because a circulation is created both at the leading edge and the trailing edge, the latter in the form of the Trailing Edge Vortex (TEV). The TEV quickly convects in the free stream and thus a net circulation is the result. For low angles of attack and rounded leading edges, the flow stays attached to the airfoil and lift is created as seen on aircraft wings. For flat plates or airfoils operating at higher angles of attack, the flow separates and forms a vortex which can stay closely attached to the wing, the so-called Leading Edge Vortex (LEV).

Depending on the flow conditions and airfoil, the LEV can stay attached for some time to the airfoil, hence delaying the stall.

The LEV is an extremely important phenomenon in natural flight and is utilized by a great variety of flying insects, birds and bats. The high flow velocity induced by the vortex leads to a low pressure area on the top side of the wing which creates a lift force. The pressure contribution is creates a

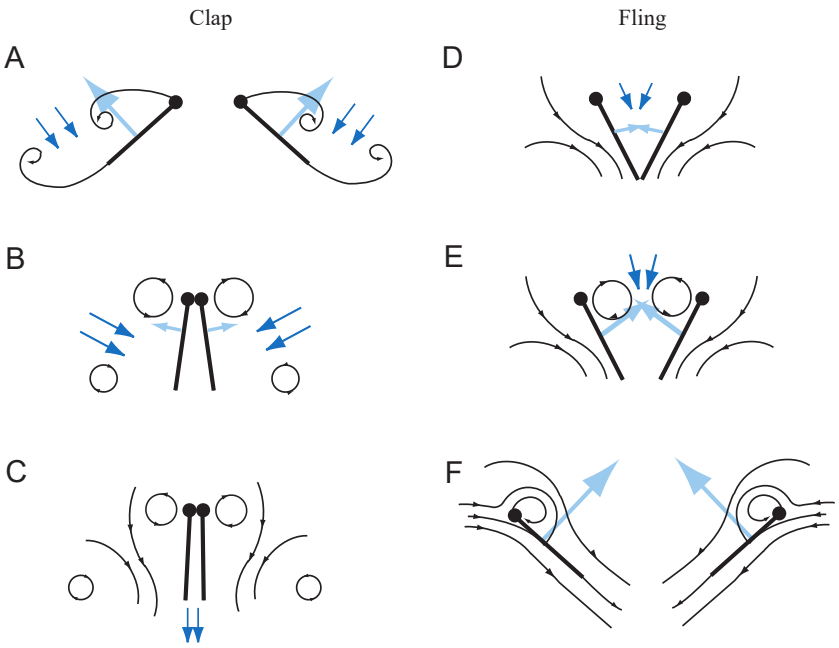

Figure 2.3: Clap and fling effect, from Sane (2003).

force normal to the wing surface, and for higher angles of attack the resulting force on the wing is virtually oriented 90° with respect to the wing surface as described by Birch et al. (2004). Hence the resulting force is dominated by the pressure forces, which are created for a large part by the LEV.

In 3D flight, the LEV can be stabilized by the presence of spanwise flow, which creates a displacement of the vorticity in the flow from the root to the tip of the flapping wing Ellington et al. (1996). An example of an insect wing with a LEV experiencing spanwise flow is given in figure 2.4.

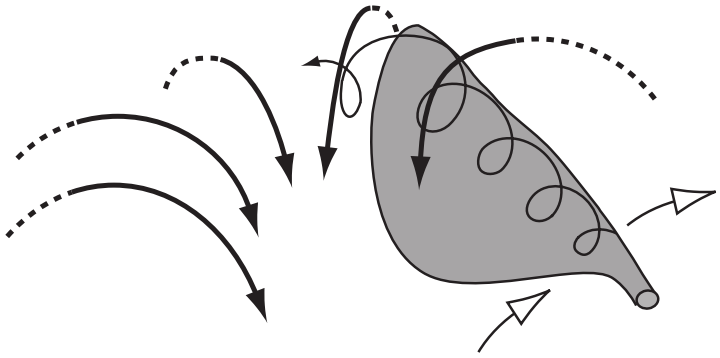

Figure 2.4: Leading edge vortex with spanwise flow, from Sane (2003).

Added mass

For any object that is accelerated in a fluid, the surrounding fluid particles will need to be accelerated too. This reaction force of the fluid with respect to the wing is felt as if the wing has more inertia, therefore this term is referred to as 'added mass' or 'added mass inertia'. The added mass effect is particularly important for high flapping frequency in a high density medium (Kang et al., 2011).

The determination of the added mass term is not trivial, because it is difficult to distinguish the different terms of the force production in the accelerating flight (Sane, 2003). The magnitude of the added mass is usually a fraction of the total fluid mass which is displaced by the body, as noted by

Kang et al. (2011). Moreover, the acceleration of the body may not be the same as the acceleration of the fluid particles (Katz & Plotkin, 2001, p. 441).

Wing-wake interactions

The flapping wings create vortices which are shed in the flow. These vortices are composed of high energy regions and therefore the creation contributes to the drag. By capturing these high energy regions, insects can regenerate part of the energy in the vortex, as hypothesised by Dickinson et al. (1999)

The mechanism is shown in figure 2.5. The set of vortices created by the previous stroke phase (A, B, C), induce a higher velocity on the wing surface, thereby augmenting the resulting force (E).

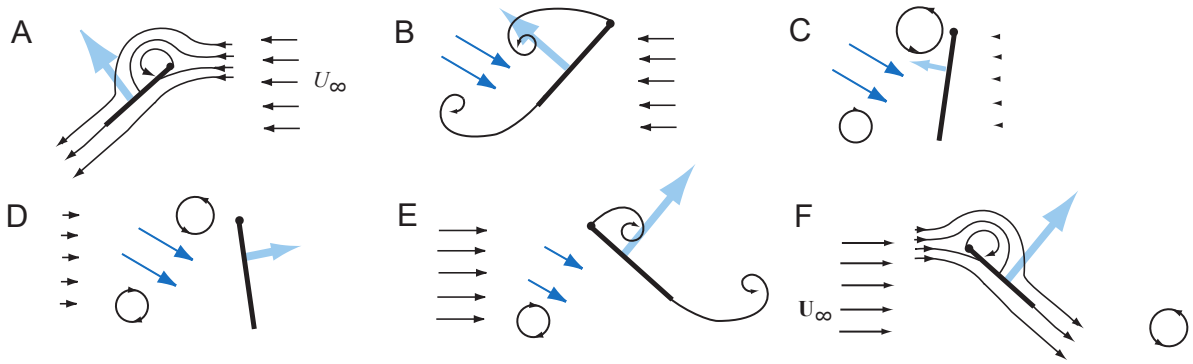

Figure 2.5: Wake capturing effect, from Sane (2003).

Kramer effect

The Kramer or rotational effect exists in the pronation and supination of the flapping phase. The effect is named after M. Kramer who first described it (Kramer, 1932).

During the pronation or the supination the wings are rotated around a spanwise axis. The trailing edge rotates and translates at the same time. The flow deviates from the Kutta condition and a separation point is created on the wing surface. As a result of this, a large shear force is created around the trailing edge to reconstruct the Kutta condition, which is paired with additional circulation to the wing. The sign of the wing rotation determines whether the restoring circulation has a positive or negative contribution to the lift (Sane, 2003). Dickinson et al. (1999) discussed the effect of advanced, symmetric and delayed rotation on a 2D model. It was found that the advanced rotation created positive effect on the lift, while a negative contribution was found for delayed rotation.

Additional to the phenomena above, Shyy et al. (2013) named the following 3D effect as an influence to the generation of aerodynamic forces on flapping wings.

Tip vortex contribution

Contrary to stationary wings where the tip vortices give rise to the induced drag, for flapping wings the tip vortices can have a beneficial effect on the lift. Whether the tip vortex actually is beneficial depends on the specific kinematics of the wing. A gain in lift can be attributed to two phenomena: Firstly, the high velocity in the tip vortex causes a low pressure area which helps to increase the lift near the tip section. Secondly, the tip vortex helps to anchor the LEV, and reduces its shedding.

The disadvantages of the tip vortex are: The induced flow by the the tip vortex reduces the effective angle of attack. Furthermore, fluid is transported from the pressure side of the airfoil to the suction side. As a result, the pressure difference over the wing is smaller and so is the resultant force.

2.3. Physics in flapping wings

The theory of flapping wings has been an object of study for the past decades. Most of this research has focussed on rigid wings to reduce the number of unknown parameters in the studies. However, the phenomena and equations described in this chapter are equally valid for wings of finite stiffness. In the next section the role of wing flexibility will be further explained.

The flow around flapping wings can be highly unsteady and displays a number of different flow phenomena which have been described in section 2.2. In the following section the important scaling parameters are treated that are of influence on the flapping wings. These are introduced with respect to the governing equations of the flow field. Non-dimensionalisation of these equations leads to an expression that shows the relative influence of the scaling parameters.

2.3.1. Scaling parameters for rigid wings

The fluid flow around the flapping wings can be modelled using the unsteady Navier-Stokes equations. The velocity regimes of interest are in the low Mach number range, and thus the incompressible Navier-Stokes equations are utilized, as given in the following equations, here in vector notation:

$$\nabla \cdot \boldsymbol{u} = 0, \tag{2.7}$$

$$\frac{\partial \boldsymbol{u}}{\partial t} + (\boldsymbol{u} \cdot \nabla)\boldsymbol{u} = -\frac{1}{\rho}\nabla p + \nu \nabla^2 \boldsymbol{u}. \tag{2.8}$$

The distinct terms of the Navier-Stokes equation treat the different effects that influence the flow. The time derivative captures the unsteadiness of the flow while the convective term relates to the inertial forces. The pressure forces are represented by the pressure gradient at the right hand side, and the last term relates to the viscous forces, that can be seen as diffusion. The relative importance of these terms can be captured in various non-dimensional numbers, which describe the relation between these parts of the equation.

For revolving or flapping wings it can be convenient to attach the frame of reference to the wing. In this case, the boundary condition on the wing simplifies to an absolute no-slip condition because the domain moves with respect to the wing. Furthermore, it can be useful for graphical purposes since the axis system is fixed on the wing, and different contributions of the fictional rotational forces can be recognised.

The wing based frame is not an inertial reference frame, such as in equation 2.7, but a rotating reference frame. In Lentink & Dickinson (2009a) the derivation of the Navier-Stokes equations on a rotating reference frame is given. The resulting form is given in equation 2.9, where the additional terms are outlined by the parenthesis. Figure 2.6 shows the inertial and rotating frame of reference for a fruit fly wing. The angular acceleration, also referred to as Euler acceleration, is only non-zero when the wing is accelerating. It is directed perpendicular to the radial distance, in the direction of the rotation. The centrifugal acceleration is directed towards the basis of rotation by definition. The Coriolis acceleration is the only rotational acceleration term which is dependent on the local velocity. Therefore the direction of this term changes with the flow vector. The figure displays the vector of the Coriolis force for isolated spanwise and chordwise flow.

$$\frac{\partial \boldsymbol{u}}{\partial t} + (\boldsymbol{u} \cdot \nabla)\boldsymbol{u} + \underbrace{\frac{\partial \boldsymbol{\Omega}}{\partial t} \times \boldsymbol{r}}_{\text{Angular}} + \underbrace{\boldsymbol{\Omega} \times (\boldsymbol{\Omega} \times \boldsymbol{r})}_{\text{Centrifugal}} + \underbrace{2\boldsymbol{\Omega} \times \boldsymbol{u}}_{\text{Coriolis}} = -\frac{1}{\rho}\nabla p + \nu \nabla^2 \boldsymbol{u} \tag{2.9}$$

Reynolds number

The Reynolds number is the ratio between the inertial and viscous forces in the flow. It is defined by:

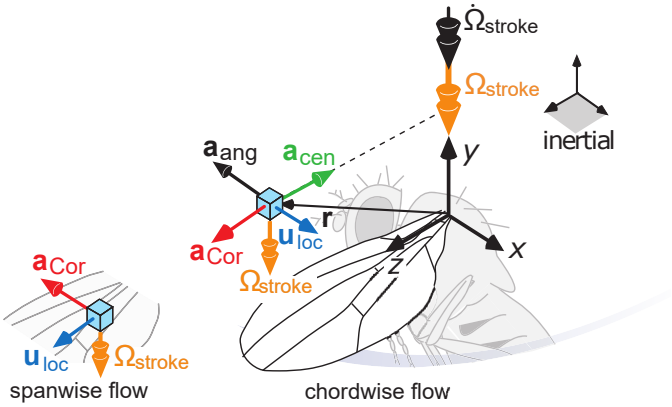

Figure 2.6: Wing rotational frame of reference, with the angular, centrifugal and Coriolis accelerations. Adapted from Lentink & Dickinson (2009b).

$$Re = \frac{U_{\text{ref}} L_{\text{ref}}}{\nu}. \tag{2.10}$$

In hovering flight, the reference velocity and length are chosen to be respectively the tip velocity and the radius at some spanwise location. The Reynolds number can then be expressed as:

$$Re = \frac{2\Phi f R^2}{\nu}. \tag{2.11}$$

The exact definition of the Reynolds number depends on the reference length and velocity scale chosen. For the length scale the mean chord (c_m) is commonly used. In 2D plunging flight, the maximum or mean plunging velocity is used and the chord length is the length scale.

Irrespective of the reference scales chosen, a Reynolds similarity criterion can be set-up. When preserving the flap angular amplitude angle, similarity between two models can be reached when the factor fR^2 is kept constant. The research of Ellington et al. (1996) and Dickinson et al. (1999) satisfied Reynolds similarity on their model by use of this factor. Similarity at very low Reynolds numbers can furthermore be achieved by testing in a high-viscous fluid. Birch & Dickinson (2001) tested a robotic model of a *Drosophila* wing in mineral oil to achieve a Reynolds number of $Re = 160$.

Reduced frequency and Strouhal number

Both the reduced frequency and the Strouhal number are used to denote the unsteadiness of the flow. The definitions of both measures are very similar, but a slight difference in definition can be distinguished. The Strouhal number relates the relative influence of the flying speed with respect to the flapping speed. Therefore, in principle the Strouhal number is meaningless for hovering flight since the free stream velocity is zero. In contrast, the reduced frequency is a non-dimensional form of the flapping frequency which represents the unsteadiness by comparing the spatial wavelength of the flow disturbance with the chord length (Triantafyllou et al., 2000).

The definition of the Strouhal number is given in equation 2.12. A famous application of the Strouhal number is the von Kármán vortex street behind a cylinder or an airfoil, where the frequency is determined by the equation with $St = 0.1 - 0.2$ (Katz & Plotkin, 2001, p. 539):

$$St = \frac{f L_{\text{ref}}}{U_{\text{ref}}}. \tag{2.12}$$

When considering a flapping or plunging airfoil, the Strouhal number is a function of the flapping or plunging frequency, the length scale (mean chord or wing span) and the free stream velocity. For a plunging airfoil, thrust is obtained at a range of Strouhal numbers. The vortices in the wake

are reversed with respect to the vortices behind a cylinder, and therefore are referred to as reverse von Kármán vortices (Lai & Platzer, 1999).

In equation 2.1 the reduced frequency was introduced. This parameter relates the flapping frequency to some reference velocity to create a non-dimensional measure for the unsteadiness of the flapping motion. For hovering flight, the tip velocity is often used:

$$k = \frac{2\pi f L_{\text{ref}}}{2U_{\text{ref}}} = \frac{\pi}{\Phi AR}. \tag{2.13}$$

Rossby number

The relative importance of the fictional rotation forces are expressed in the Rossby number, which is defined as the ratio between the inertial and Coriolis forces. A low Rossby number represents a flow with dominant rotational effects. For a rotating wing it can be expressed using the radius of gyration, which gives the distribution of the cross sectional area around the axis of rotation: $Ro = R_g/c$. Since the radius of gyration may be hard to determine, often the tip radius is used to compute the Rossby number. In that case the equation 2.14 can be used. Furthermore, at local spanwise location the relative importance of rotational forces can be derived using the local radius to compute the Rossby number:

$$Ro(r) = \frac{r}{c}. \tag{2.14}$$

For many natural flyers the wing tip based Rossby number close to $Ro = 3$, see figure 2.7. A low Rossby number means a relative high importance of the Coriolis and centrifugal force with respect to the inertial forces, and these rotational accelerations promote the LEV stability according to Lentink & Dickinson (2009b); Jardin & David (2015).

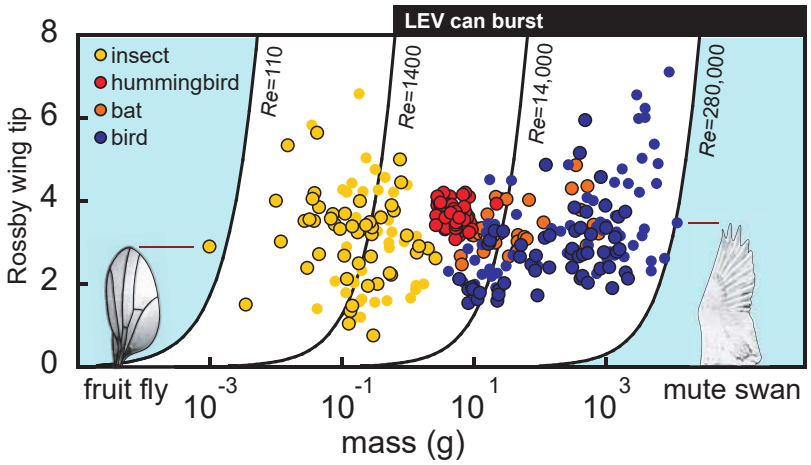

Figure 2.7: Rossby number for a range of natural flyers. Adapted from Lentink & Dickinson (2009b).

Non-dimensional form of the Navier-Stokes equations

Using the expressions for the Reynolds number and the reduced frequency, the Navier-Stokes equations as seen in 2.8 can be non-dimensionalised. The length, time and velocity scale are c_m, $1/f$ and U_{ref} respectively. The superscript (*) is used to denote a dimensionless variable:

$$\frac{k}{\pi}\frac{\partial \boldsymbol{u}^*}{\partial t^*} + (\boldsymbol{u}^* \cdot \boldsymbol{\nabla}^*)\boldsymbol{u}^* = -\boldsymbol{\nabla}^* p^* + \frac{1}{Re}\boldsymbol{\nabla}^{*2}\boldsymbol{u}^*. \tag{2.15}$$

As can be seen, the importance of the unsteady part rises with increasing reduced frequency. The viscous forces are most important for a low Reynolds number.

A similar expression can be derived taking into account the rotating frame of reference. in this case, the resulting equation 2.16 shows that the angular acceleration scales with the inverse of the dimensionless stroke amplitude, $A^* = \Phi_0 R/c$. This non-dimensional number displays the travelled tip distance in terms of chord lengths travelled. The centrifugal and Coriolis accelerations scale with the inverse of the Rossby number. A unidirectional moving wing (purely rotating or translating) leads to a an infinite stroke amplitude, hence no angular accelerations are present. For translating wings the Rossby number is infinite, hence the Coriolis and centrifugal terms go to zero:

$$\frac{k}{\pi}\frac{\partial \boldsymbol{u}^*}{\partial t^*} + (\boldsymbol{u}^* \cdot \boldsymbol{\nabla}^*)\boldsymbol{u}^* + \frac{1}{A^*}\frac{\partial \boldsymbol{\Omega}^*}{\partial t^*} \times \boldsymbol{r}^* + \frac{1}{Ro}\boldsymbol{\Omega}^* \times (\boldsymbol{\Omega}^* \times \boldsymbol{r}) + \frac{1}{Ro}2\boldsymbol{\Omega}^* \times \boldsymbol{u}^* = -\boldsymbol{\nabla}^* p^* + \frac{1}{Re}\boldsymbol{\nabla}^{*2}\boldsymbol{u}^*. \quad (2.16)$$

Before it was noted that the Rossby number found for many natural flyers is close to $Ro = 3$, where the inertial and rotational forces are in the same order of magnitude. Furthermore, wing stroke amplitude Φ_0 (half the stroke amplitude Φ) ranges from 0.6 to 1.5 for insect flight. The dimensionless stroke amplitude therefore has the same order of magnitude as the Rossby number since there exists a simple relation between these figures. This leads to the notion that all three rotational forces, angular, centrifugal and Coriolis have similar magnitudes.

2.3.2. LEV, Burst and Breakdown

Ellington et al. (1996) performed experiments on the airflow around the wing of the Hawkmoth *Manduca Sexta* and a scaled model at a Reynolds number of $\mathcal{O}(10^3)$. An intense leading edge vortex was found on the downstroke which could explain the high aerodynamic force that the insect requires to stay aloft. It was noted that the dynamic stall at the downstroke created a stable LEV. This vortex has a conical structure and grows through the sweeping motion. In figure 2.8 the conical shape of the vortex is clear and the low pressure area under the LEV is pronounced.

Ellington et al. (1996) argued that the origin of the LEV could be in the rotational phase (pronation) or in the translational phase. In the latter case, the LEV would occur due to delayed stall, while during pronation because of the rotational mechanism. It was found that a LEV was formed during the pronation which is 2-dimensional in structure. At the beginning of the translational phase, this pronation LEV is left behind and a new LEV is formed because of translational effects. This LEV grows to a conical structure. Garmann & Visbal (2013) show that the width of the vortex grows linearly from the root to the tip. For wings with an aspect ratio over 2, the LEV spans the entire chord and starts to interact with the TEV, which induces losses in the suction outboard.

Garmann & Visbal (2013) studied revolving and translating wings with an aspect ratio of 2 and at a Reynolds number of 3,000 for a flapping motion. At the beginning of the stroke the vorticity over the wing is built up. In accordance with the Kelvin's theorem the leading edge and trailing introduce circulation of the same magnitude in the flow. For a large range of angles of attack the circulation on the leading edge manifests in the form of a stable LEV. A vortex ring is formed by the LEV, Tip Vortex (TV), Root Vortex (RV) and TEV, see the upper part of figure 2.8. The lower part of the figure reflects the latter part of the downstroke, where the TEV has shed and is convected in the free-stream.

LEV Breakdown

Sane (2003) describes the difference in 2D- and 3D-LEVs. The LEV in 2D possesses inherent instability that leads to a periodic formation and shedding of the LEV and the formation of a von Kármán sheet. For 3D airfoils at similar angles of attack, a stable LEV is found that remains attached to the wing and for which the resultant force vector acts perpendicular to the wing. The stability of the 3D-LEV must therefore arise from a 3D effect, such as the transport of vorticity in the wake.

Ellington et al. (1996) recognised a spanwise flow in the experiment on *Manduca Sexta* wings. It was postulated that this axial flow is essential for the stability of the LEV because it convects vorticity to the wingtip. In 2D flows it is seen that the LEV is unstable because the vorticity cannot be

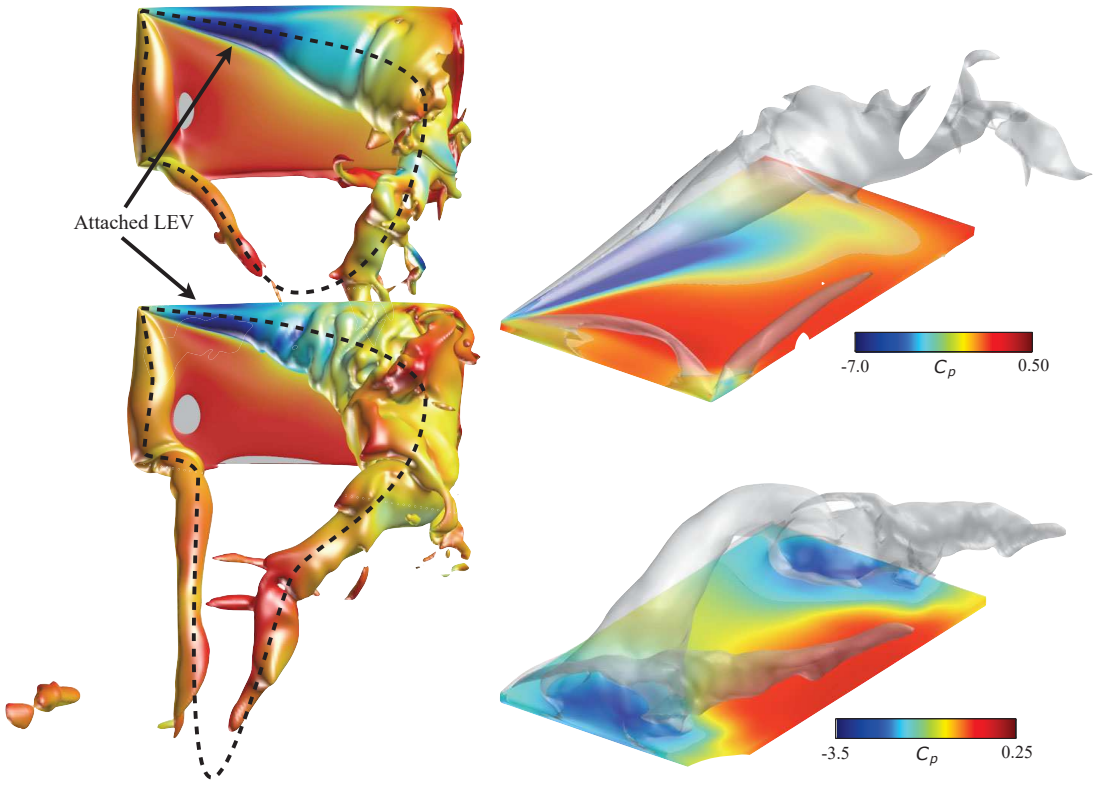

Figure 2.8: Absolute pressure contours at $Re = 3,000$ for (left) The leading edge vortex on a revolving wing for the revolving angle $\phi = 57.3°$ and $\phi = 85.9°$, at 50% and 75% of downstroke. (Top right) The conical LEV on a revolving wing. (Bottom right) The LEV lifts from the translating wing. Adapted from Garmann & Visbal (2013).

convected in spanwise direction and thus the LEV saturates. The build up of vorticity eventually causes vortex breakdown at 60-70% of the wingspan during the second half of the downstroke, and the circulation on the wing decreases. This behaviour can be seen in the bottom of figure 2.8.

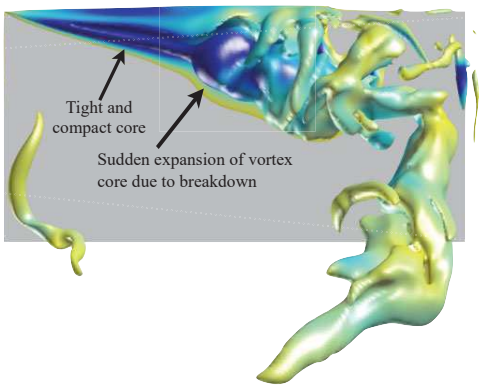

Figure 2.9: Pressure contour for 75% of the downstroke. The expansion of the vortex core denotes the onset of breakdown. Adapted from Garmann & Visbal (2013).

Garmann & Visbal (2014) investigated the breakdown of the LEV on a revolving wing and showed that breakdown characterised by sudden expansion of the vortex core. The case for a Reynolds number of 3,000 is shown in figure 2.9. At 75% of of the flapping angle vortex breakdown occurs and the LEV lifts up and orients streamwise with the TV.

Lentink & Dickinson (2009b) refer to the breakdown as bursting, and found it to occur in mid-stroke, irrespective of the angle of attack. It is thought that the breakdown is initiated by deceleration of the core flow, under influence of the TV. The vortex bursting happens at larger Reynolds numbers, where the flow is more unstable. Although the LEV is burst, the turbulent rotating fluid still remains close to the wing surface. Therefore the force production may not be significantly affected.

Ellington et al. (1996) reported breakdown of the vortex at 60%-70% spanwise position. Garmann & Visbal (2014) showed that the vortex breakdown occurred at approximately 50% of the span, irrespective of the aspect ratio. Liu & Aono (2009) investigated the size effects of hovering insects and tested wings for a Reynolds range from $\mathcal{O}(10^1)$ to $\mathcal{O}(10^4)$. Breakdown at 70%-80% span was reported for the higher Reynolds numbers.

2.3.3. Reynolds number effect

Birch & Dickinson (2001) tested the importance of the spanwise flow for the stability of the LEV. The flow was tested on the model wing of the fruit fly (*Drosophila Melanogaster*) at a Reynolds number of 160. A low spanwise flow of 2-5% of the average tip velocity was seen in the vortex core. However, a large region of strong spanwise flow was found at two-thirds of the chord from base to tip.

Measures to inhibit the spanwise flow at the wing did not lead to instability in the LEV. Fences at the Leading Edge (LE) inhibited the remaining spanwise flow in the vortex core, but had no effect on the LEV. Fences at the Trailing Edge (TE) inhibited the large portion of spanwise velocity near the TE, and decreased the overall force on the wing, but did not change the structure of the LEV. Therefore, the difference between an unstable 2D-LEV and stable 3D-LEV cannot be attributed to the spanwise flow for low Reynolds numbers. It seems that the force production at these low Reynolds numbers is dependent on the strength of the LEV, and in lesser extent to the LEV stability, since the LEV is more robust compared to LEVs at higher Reynolds numbers. Liu & Aono (2009) showed that the flow at very low Reynolds numbers showed a very weak LEV and TEV and TV, but with very stable behaviour. The flow becomes relatively 2D, with little spanwise interaction.

Insect wings display LEVs from $Re = 160$ for *Drosophila* to $Re = 5,000$ for *Manduca* wings. Lentink & Dickinson (2009b) even report on stable LEVs on high Reynolds numbers flyers such as birds.

Birch et al. (2004) tested the LEV stability for Reynolds numbers of 120 and 1,400. It is found that a stable LEV exists for both Reynolds numbers. Figure 2.10 shows the velocity field at spanwise position $0.45R$, and the LEV is clearly visible. The contour plot shows the spanwise velocity at this spanwise position. For both images, a strong outward axial flow is seen behind the LEV.

The spanwise velocity in the core is nearly zero for the low Reynolds number flow. The stability of the LEV at $Re = 120$ is therefore not dependent on the transport of vorticity in the vortex core. In contrast, at $Re = 1,400$ a peak velocity is found near the vortex core with a magnitude of 150% the wing tip velocity. This flow may transport vorticity the wingtip and thus increase the stability of the vortex. This difference in flowfield indicates that the stability mechanisms are different for high and low Reynolds numbers.

Lentink & Dickinson (2009b) show the effect of the Reynolds number in figure 2.12 for $Re = [110; 1,400]$. The main effect of the higher Reynolds number is that spiral bursting is seen for both unidirectional and reciprocating motion. The bursting of a vortex means the coherent vortex structure deteriorates to a turbulent volume of rotating fluid, which is still stably attached to the wing. It was found that the LEV stability is independent of the Reynolds number, although the stability mechanism is different. Furthermore, the importance of the Rossby number rather than the Reynolds number is stressed on the stability of the LEV.

Dai et al. (2012) presented similar results, when a flexible flapping plate was numerically tested at $Re = [176; 500; 1,000]$. The flow field showed increasingly complex vortical structures with the higher Reynolds numbers. The vortices break down and form a wake with randomly oriented vortices. The effect on the wing deformation is minimal though, with very little difference between the lowest and highest Reynolds number.

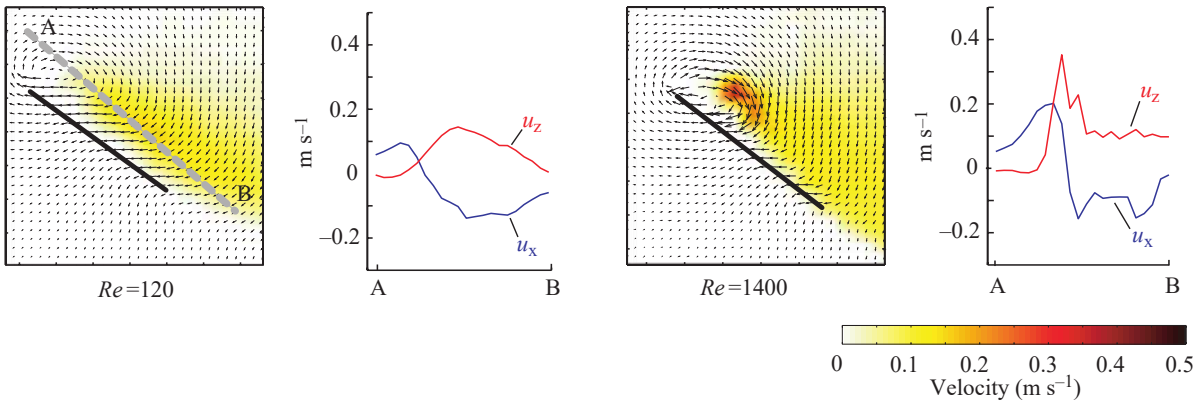

Figure 2.10: Flow field direction and magnitude at $0.45R$ in the chordwise direction is plotted using the arrows. The spanwise velocity on the wing is superimposed using a contour plot. At Reynolds numbers of 120 and 1,400, adapted from Birch et al. (2004). The spanwise velocity is plotted along the line connecting the LEV core and the highest spanwise velocity.

Figure 2.11 shows that the net force increases with the Reynolds number, an effect which is found in multiple researches (Birch et al., 2004; Lentink & Dickinson, 2009b; Percin & Oudheusden, 2015; Dai et al., 2012). Only for low angles of attack, the viscous contribution to the drag assures that the net force is larger for lower Reynolds numbers. Figure 2.17 further underlines this. The wing at $Re = 110$ shows a higher profile drag and is less able to create forces by pressure differences over the wing. Because these effects, lift over drag (L/D) ratio and wing efficiency increase significantly with the Reynolds number.

The force angle between resultant force and the wing chord approaches 90° for $\alpha > 30°$. At lower Reynolds numbers, the viscous drag contribution tilts the force vector further to the rear of the wing and the approximation of 90° is delayed. The contribution of the pressure forces acts perpendicular to the wing, indicating that the net force at the wing for high angles of attack is dominated by

pressure forces especially at higher Reynolds numbers.

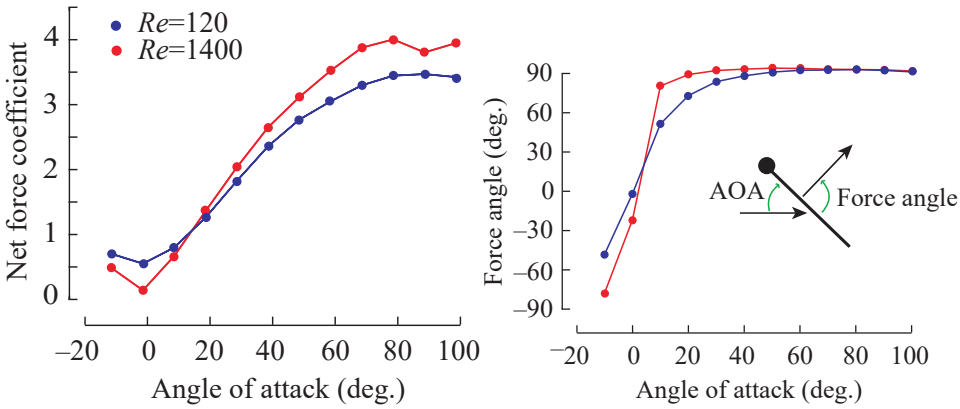

Figure 2.11: Force on the dynamically scaled wing model for different Reynolds numbers, adapted from Birch et al. (2004). (Left) Resultant force coefficient. (Right) Force angle approaches 90° for larger angles of attack, which indicates that the net force is dominated by pressure forces.

2.3.4. Wing kinematics influence

The strength, position and stability of the LEV are highly dependent on the movement of the wing. When comparing a translational motion with a revolving one, the (fictional) rotational forces have to be taken into account. Lentink & Dickinson (2009b); David et al. (2012); Jardin et al. (2012); Jardin & David (2014, 2015); Jardin (2017); Garmann & Visbal (2013) have shown the importance of the rotational forces with respect to the LEV stability. Especially the Coriolis force has an anchoring effect on the LEV.

Rotational versus Translational motion

Lentink & Dickinson (2009b) discussed the effect of the angular, centrifugal and Coriolis accelerations on the LEV. The difference of the flow characteristics were tested for differences between translation versus rotation (measured by Rossby number), unidirectional versus reciprocating (by dimensionless stroke amplitude) and the influence of viscosity (by Reynolds number). By means of flow visualisation and force measurements the effect of these dimensionless numbers were deduced. A model fruit fly wing was tested at Reynolds numbers of 110 and 1,400 in two types mineral oil. Some set-ups were also tested in water, rendering $Re = 14,000$.

The difference between rotation and translation is clear when looking at the difference between $Ro = 2.9$ and $Ro = \infty$ in figure 2.12. For a low Rossby number, a compact and stably attached LEV is seen irrespective of the Reynolds number or the dimensionless stroke amplitude. Therefore, the rotational movement with the (fictional) Coriolis and centrifugal forces are key to a stable attachment of the LEV.

The nature of the stable vortex for a rotational movement is disputed among different researches. On one side there is the research of Lentink & Dickinson (2009b), which states that the Coriolis and centrifugal force are paramount for LEV stability. This conclusion is supported by the work of Jardin & David (2014, 2015); Jardin (2017), where numerical simulation is used to individually test the effect of the rotational forces. From this research the Coriolis force is extracted as the most important factor for the LEV stability and anchoring to the wing surface.

The work by Garmann & Visbal (2013, 2014) contradicts this statement. Here the stability of the LEV is attributed to the spanwise pressure gradient and the centrifugal force. By the spanwise convection of the flow behind the LEV, the separation from the tip is prevented to propagate inboard. Because this disturbance does not reach the LEV, separation is avoided.

Both theories agree that the centrifugal force, together with the pressure gradient, creates centrifugal pumping. According to Lentink & Dickinson (2009b) the Coriolis force is pointed outboard (for positive chordwise flow), and in direction of travel (for spanwise outward flow). The latter term creates a stabilizing effect for the spanwise flow created by the centrifugal pumping. Garmann & Visbal (2014) indicate that the Coriolis force is directed away from the surface, which does not promote stable attachment of the LEV.

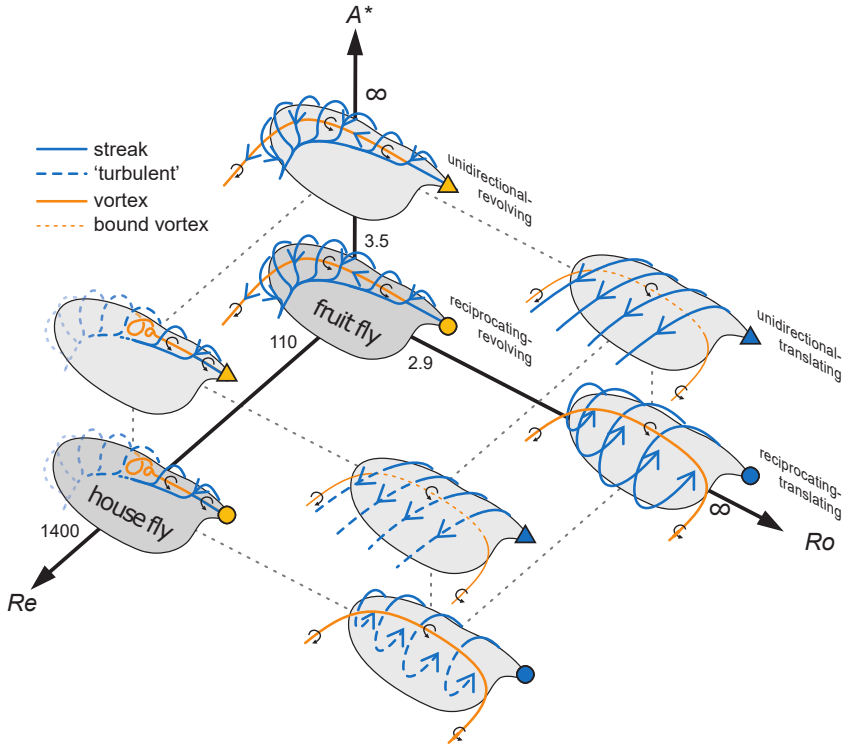

Figure 2.12: Graphic representation of the effect of the Rossby number, dimensionless stroke amplitude and the Reynolds number on the flow around a model fruit fly wing. From Lentink & Dickinson (2009b).

Jardin & David (2014) performed artificial tuning of the rotational forces, as shown in figure 2.14. Three cases, displayed in figure 2.13, are computed for a finite wing: uniform spanwise inflow (translation), spanwise varying inflow to simulate the varying inflow velocity experienced by a revolving wing without rotational terms and a rotating wing. The LEV sheds quickly for the translating case which displays 2D flow at the midplane. The spanwise velocity gradient creates a spanwise flow in the core driven by the pressure gradient. The LEV is more stable with respect to the translating case, but sheds eventually. The addition of the rotational terms can be seen for case (c), where spanwise flow is extended behind the LEV. The LEV is more stably attached to the wing and does not shed.

Recent work of Jardin & David (2015) and Jardin (2017) aims at determining the function of the centrifugal and the Coriolis term in the flow field and force production. This is done by numerical simulation of the incompressible Navier-Stokes equations in a rotational frame of reference, as in equation 2.9. In the first research the terms were taken into the calculations according to table 2.1. Figure 2.15 shows the lift coefficients of the revolving wing. Three cases follow the same trend, namely case A, B and 0 (rectilinear spanwise flow as depicted in figure 2.13b). After $\delta = 1$, the lift drops which indicated that a spanwise flow, nor the addition of centrifugal force is sufficient to anchor the LEV to the wing. From this figure it is evident that the flow field and lift force are hardly affected by the addition of the centrifugal forces.

When only the Coriolis term is considered, the highest lift is reached. It is suggested that the

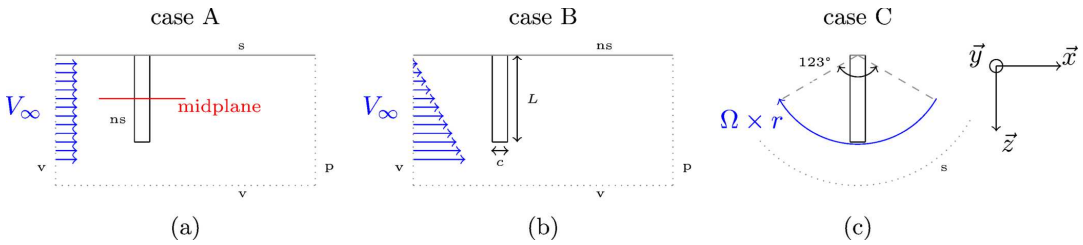

Figure 2.13: Spanwise velocity contours and vorticity $\lambda_2 < 0$ criterion iso-lines. at midplane with $Re = 500$. (a) low spanwise velocity for a translating wing and the LEV sheds. (b) spanwise gradient without rotational terms. Spanwise velocity is largest in vortex core. (c) Revolving wing. Spanwise flow is seen in the core of the LEV and behind the LEV. From Jardin & David (2014).

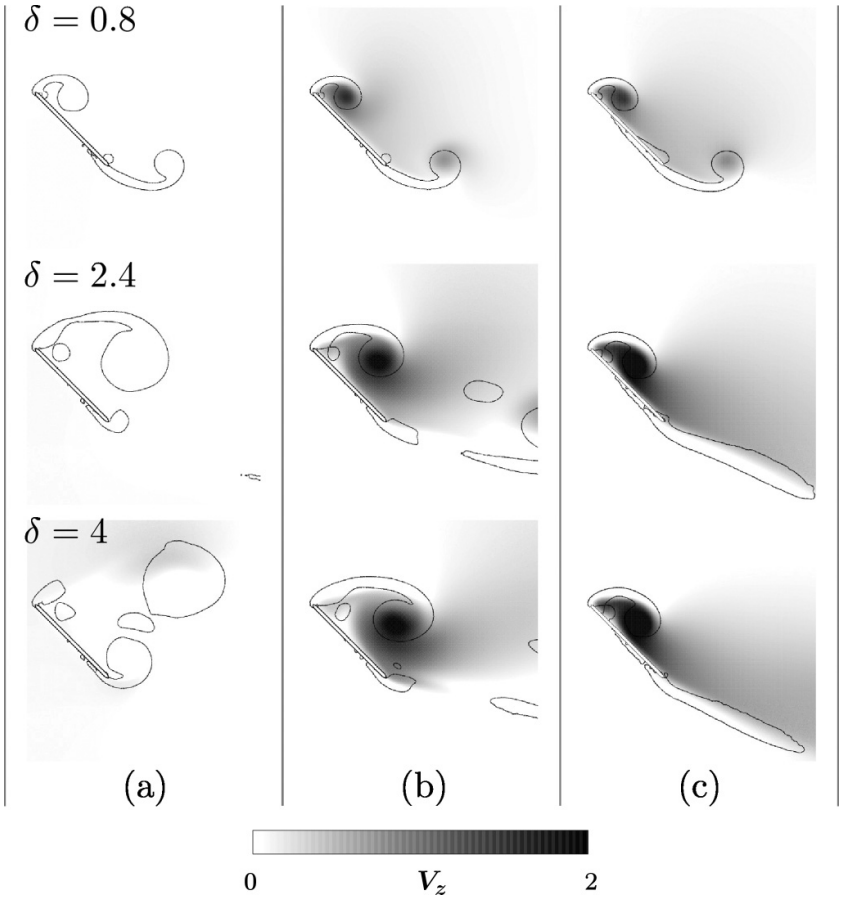

Figure 2.14: Spanwise velocity contours and vorticity $\lambda_2 < 0$ criterion iso-lines. at midplane with $Re = 500$. (a) low spanwise velocity for a translating wing and the LEV sheds. (b) spanwise gradient without rotational terms. Spanwise velocity is largest in vortex core. (c) Revolving wing. Spanwise flow is seen in the core of the LEV and behind the LEV. From Jardin & David (2014).

Table 2.1: Different testcases for Jardin & David (2015)

Case	Centrifugal term	Coriolis term
A	No	No
B	Yes	No
C	No	Yes
D	Yes	Yes

velocity changes which are produced by the centrifugal term are amplified by the Coriolis term, which alters the flow field slightly. It is however evident the Coriolis term is responsible for obtaining a high lift coefficient.

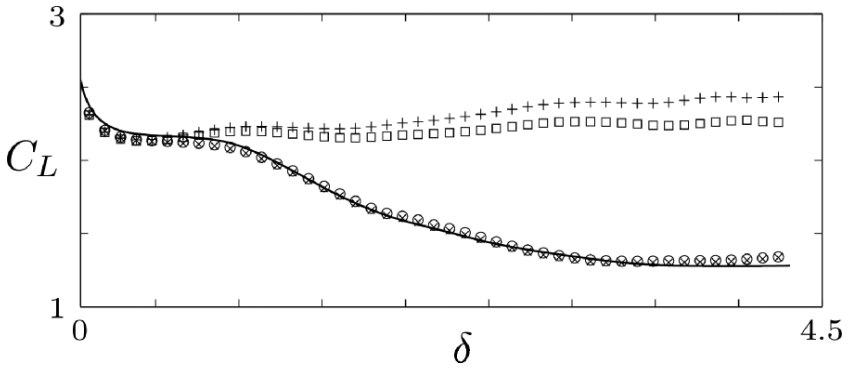

Figure 2.15: Effect of the centrifugal and Coriolis forces on the lift force on the wing, according to table 2.1. A (×), B (○), C (+), D (□). Rectilinear spanwise flow as seen in figure 2.13b is depicted by 0 (−−). Adapted from Jardin & David (2015)

Further research by Jardin (2017) evaluated the influence of the Coriolis and centrifugal terms by assigning the coefficients F_{co} and F_{ce}. A value unity for the coefficients reflects the actual physical revolving situation. A wing with an relative high aspect ratio of 9.5 is used to assure an unstable section where 2D effects dominate and a section near the root where rotational effects stabilize the flow. Figure 2.16 shows the flow field for increasing values of the Coriolis term coefficient, $F_{co} = [0.5, 1, 1.5, 2]$. In all figures, an attached LEV can be seen in the inboard part of the wing, and it is connected with the RV. more to the outboard section the initially formed LEV sheds and forms a streamwise structure. The location where the LEV sheds can approximately be seen as the region where transition occurs from the quasi-steady region with attached LEV, to the unsteady region. The unsteady region is characterised by small-scale structures. For higher Coriolis effect, these small scale structures are pushed further outboard, so more stable flow is present on the wing. It is clear therefore that the Coriolis force has a stabilising effect on the LEV.

Breakdown Jardin et al. (2012) investigated the flow on a reciprocating NACA0012 airfoil using DNS at a Reynolds number of 1,000. Both translating and revolving flapping wings were investigated. For the translating wing, strong inward velocities are seen 0.6 chord length away from the tip under the influence of the TV. In the revolving case it is known that there are strong outward velocities on the suction side. The breakdown of the LEV near the tip can thus be explained by the inward tip velocity which counteracts the outward flow, hence creating instability. At this location, the LEV lifts from the surface and tilts in the direction of the flow, after which it connects to the tip vortex. It was seen that the LEV detached from the wing at 85% of the span, after which it tilted in streamwise direction. Stabilizing effects are noted from the outboard flow that is present close to the trailing edge of the wing, created by the rotational accelerations. This inhibits the formation of TEVs and destabilizing cross-wake effects.

Forces The stable LEV creates higher forces for the revolving case compared the translating case. Garmann & Visbal (2013) reported a difference of 32%. Lentink & Dickinson (2009b) showed the effect of the Rossby number on the force coefficients in figure 2.17 (left). The LEV was shed only for $Ro = \infty$. At the other Rossby numbers ($Ro = [2.9, 3.6, 4.4]$) the LEV was attached under the influence of the rotational forces which are most dominant at the lowest Rossby number. For a wing with a large aspect ratio, this leads to a root region where rotational effects permit a stable LEV, and a outboard section which displays more 2D flow.

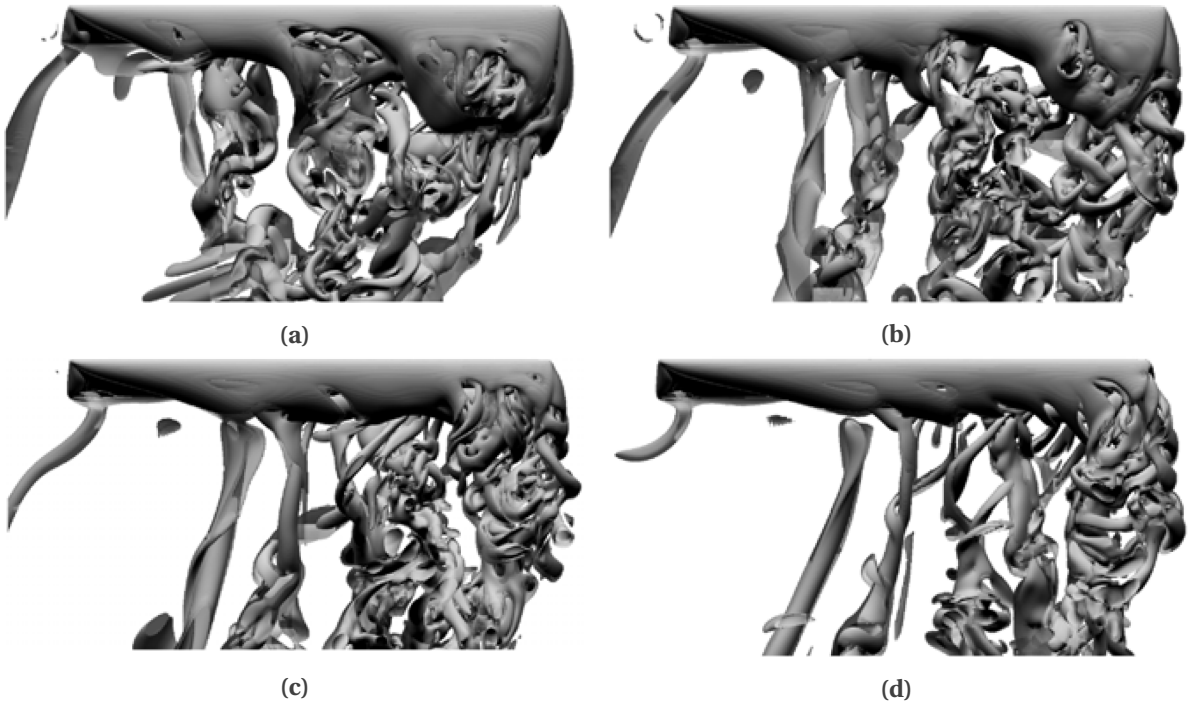

Figure 2.16: Top view with Iso-surfaces of Q-criterion to display the vortical structures at a rotation angle of $\phi = 120°$ after an impulsive start, with $Re = 500$. F_{co} is 0.5 (Top left), 1, (Top right), 1.5 (Bottom left) and 2 (Bottom right) and $F_{ce} = 1$ for all cases. Adapted from Jardin (2017).

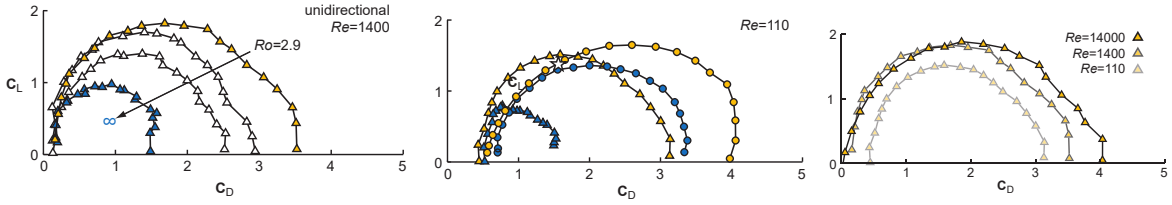

Figure 2.17: Effect of the Rossby number, dimensionless stroke parameter and Reynolds number on the force coefficients for a range of angle of attack: $\alpha = [0°;90°]$. Changes in Rossby number are denoted by Colour: Yellow $Ro = 2.9$, white $Ro = 3.6, 4.4$, blue, $Ro = \infty$. Dimensionless stroke amplitude is denoted by shape: Triangles is unidirectional, circles is reciprocating. Reynolds numbers is represented by opaqueness. (Left) A low Rossby number promotes a stable LEV and enhances the force on the wing. (Middle) The forces on the reciprocating wing are higher compared to those on the unidirectional moving wing. (Right) The vortex breakdown does not deteriorate the force on the wing, the coefficients rise with Reynolds number. Adapted from Lentink & Dickinson (2009b).

Angle of attack

Birch & Dickinson (2001) reported the strong correlation between the force production and the angle of attack. The force production is linked directly to the strength of the LEV, so the vortex strength is dependent on the angle of attack.

A LEV can be found over a large range of angle of attack. For $Re = 5,000 - 25,000$ Percin & van Oudheusden (2015) found that a LEV exists for $\alpha = 15° - 75°$. While the general behaviour of the vortices is comparable over this range, the morphology changes because spanwise gradients increase for higher angles of attack. Trizila et al. (2011) investigated the effect of the angle of attack, plunging amplitude ratio and phase lag at $Re = 100$. The numerical model investigated both a 2D and a 3D wing with an aspect ratio of 4. It was found that in general, a higher angle of attack gave a higher lift. A maximum in the lift coefficient is found for an angle of attack of 45° (Percin & van Oudheusden, 2015; Trizila et al., 2011; Phillips & Knowles, 2011).

2.3.5. Shape of the wing

Usherwood & Ellington (2002) investigated the influence of the shape of the leading edge of the wing. A hawkmoth wing at a Reynold number of Re= 5,560 was tested. The force coefficients were found to be insensitive to the radical changes in the wing geometry.

2.3.6. Spanwise characteristics and Aspect ratio

To understand how the LEV develops over the wing, and how the behaviour differs between the inboard and outboard section, the spanwise characteristics of the wing have to be evaluated. The flow on translating and revolving wings is very different as was seen in the previous section.

Jardin et al. (2012) showed that three different regions could be distinguished on the translating wing, as seen in figure 2.20. There is 2D behaviour near the root up to 1.4 chord length from the tip, with vortex shedding at both the LE and the TE. Near the tip (up to 0.6 chord lengths from the tip), the LEV connects with the tip vortex and the region is characterised by strong 3D flow. The circulation of the LEV reaches a plateau because surplus in circulation is transported in streamwise direction by the tip vortex.

Between the tip and the midplane region, there is a transition region in which both 2D and 3D effects are seen. The transition region extends 1.4 chords from the tip. In this region, a high vorticity is built up, above the margin the LEV would shed in a 2D flow. The 3D influence of the tip inhibits this shedding by of the LEV. Jardin et al. (2012) argue that the 2D instability of the LEV is partly due to the cross-wake interaction between TEVs and LEVs. The tip vortex inhibits further formation of TEVs and hence takes away a destabilizing term for the LEV for a small portion of the span.

The effect of the aspect ratio on the translating case was investigated. It was found that the influence of the tip vortex created a stabilizing effect on the LEV, until a length of 1.4 chord lengths from the tip, irrespective of the aspect ratio. Increasing the aspect ratio only leads to a larger section of 2D flow on the inboard part of the wing, which is clearly visible in figure 2.19. Similar results were found for a wing with $AR = 4$ by Garmann & Visbal (2014). For very low aspect ratio wings, the two tip vortices start counter-acting and the influence region of each tip vortex shrinks.

Poelma et al. (2006) showed that the circulation on the leading edge grows linearly with the formation number until it reaches a plateau. Since the tip moves fast, here the plateau is reached first when the LEV is saturated. In quasi steady state, the vorticity builds up nearly linearly from the root until a maximum is reached at 0.7-0.8 of the span. After this point the circulation drops to zero at the tip.

2.3.7. Temporal development of the LEV

Poelma et al. (2006) created for the first time a quantitatively measured, three-dimensional velocity field around a revolving wing. The wing model is based on a *Drosophila* wing and is tested at $Re =$

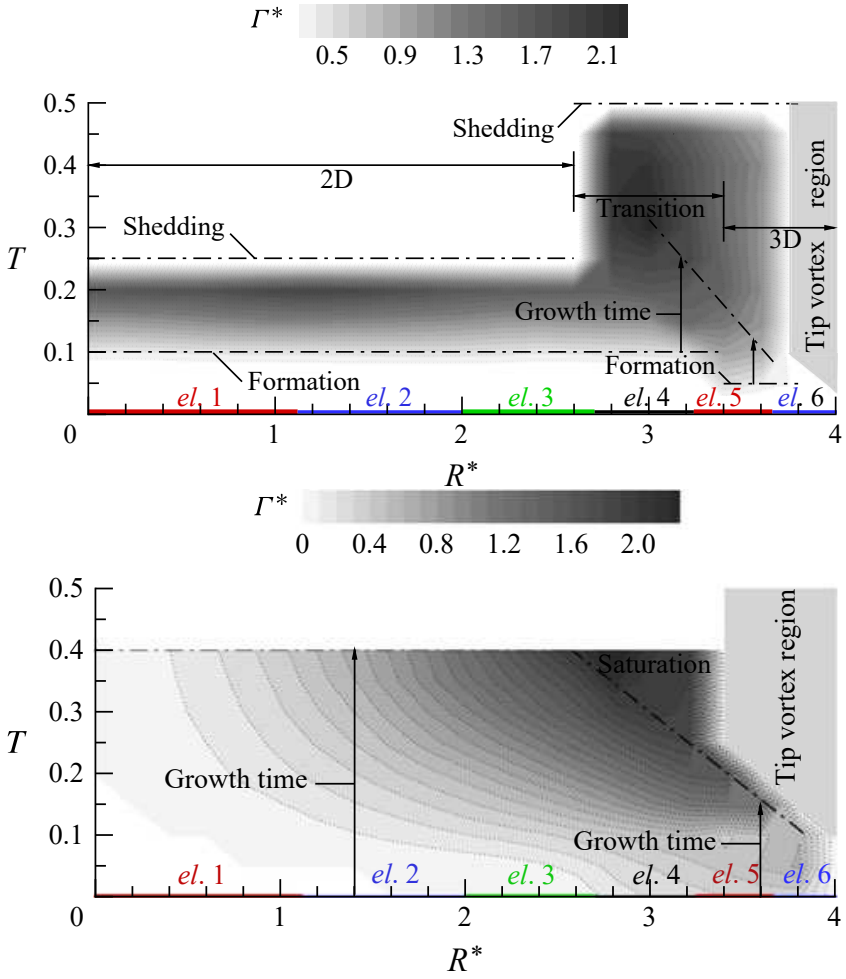

Figure 2.18: The production of circulation on a (top) translating and (bottom) revolving wing. From Jardin et al. (2012).

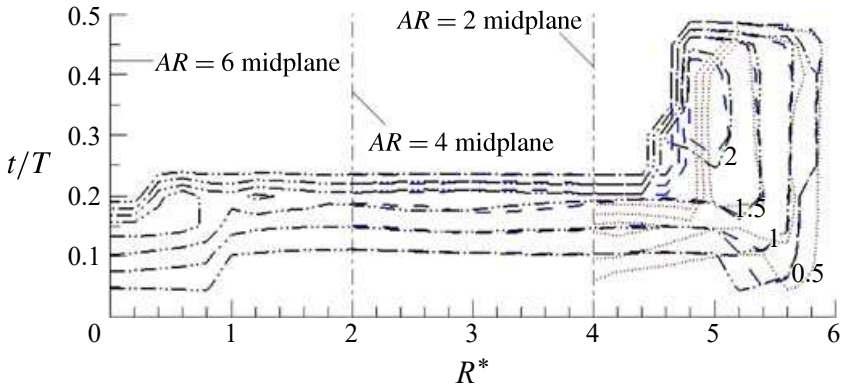

Figure 2.19: The effect of increasing the aspect ratio on the wing. Values of the dimensionless circulation are shown in the figure. From Jardin et al. (2012).

256 and $\alpha = 50°$. During the impulsively started phase it was found that the LEV grows linearly with the formation number, and that no significant spanwise flow is present. The quasi-steady state showed large spanwise flow behind the wing which could help to convect vorticity produced at the leading edge.

The build up of forces and circulation over translating and revolving wing is treated by Jardin & David (2014). Figure 2.20 shows the circulation which is built up in the LEV at midplane versus the nondimensional travel distance. Three cases are considered, which are shown in figure 2.13. All three cases show a rapid build-up of circulation in the first chord length travelled, when there is still low spanwise transport. The circulation build-up of the translating wing is higher compared to the other wings, and continues until $\delta = 2.4$ as the circulation of the LEV drops since the vortex is shed. Case (b) and (c) are similar in behaviour. The gradient of circulation build up is lowest for case (c), which indicates that this motion is most efficient in the transportation of vorticity from the LEV to the wake.

For this flapping distance range the LEV stays attached for both case B and C. However, as can be seen in figure 2.14, the distance from the LEV to the wing in case B is large, while the vortex core of the LEV in case C is very close to the wing. Figure 2.20 shows that the lift deteriorates for case B, since the LEV and associated low pressure area is too far away from the wing. Therefore, although spanwise gradients help attaching the LEV to the wing, the force generation is mainly enhanced by the rotational effects.

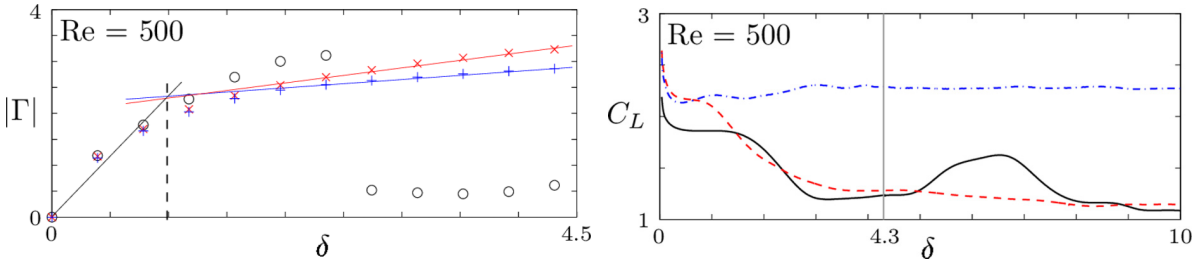

Figure 2.20: Comparison of the translating-, spanwise velocity gradient- and revolving wing. (Left) The circulation captured in the LEV defined by the $\lambda_2 = 0$ iso-line. For cases A (∘), B (×) and C (+). (Right) The lift coefficient from cases A (normal), B (dashed), C (dash-dotted). Adapted from Jardin & David (2014)

Lentink & Dickinson (2009b) tested the effect of the unsteady reciprocating wing versus the quasi-steady unidirectional wing, measured in the dimensionless stroke amplitude (A^*). The difference in LEV development is only clear for the unstable, translating wings. For these wings, the reciprocating motion does not enhance the LEV stability, but for small stroke amplitudes the wing changes direction before the LEV sheds. In this manner lift is created by means of the dynamic stall process. This is reflected in figure 2.17, where the forces on the reciprocating wings are higher than those on the unidirectional wings. This can partly be attributed to the unsteady phenomena such as the Kramer effect and added mass.

2.4. Flexible Flapping wing

Although less extensive than rigid wings, there has been a number of researches into flexible wings in the past years. Flexible wings are very common in natural flyers since wing deformation can help in achieving better performance of the wing at a lower wing mass. Birds and bats can actively deform their wings while insect wings generally deform passively (Shyy et al., 2013).

The addition of flexibility in the wings leads to an increase in difficulty in numerical modelling and increases the parameter space. The flexible structure is first introduced with its implications for the terminology and equations. The important scaling parameters with the added flexibility are treated. Next the relations between the flexibility and flow parameters are given.

The wing deformation can be assigned to three aspect: Elastic, inertial and aerodynamic forces. The former is part of the wing structure and has a restoring component to the wing initial shape. The inertial force is due to the wing kinematics, and the aerodynamic force follows from the flow field the wing develops.

2.4.1. Scaling parameters for flexible wings

Additional to the scaling parameters which are used for the fluid dynamics and kinematic motion (Reynolds number, reduced frequency, Strouhal number, Rossby number), the flexible wing requires structural modelling. The structural modelling introduces scaling parameters which relate the structure to the fluid, such that relations between the fluid-structure interaction can be quickly deduced from these parameters.

Considering the time dependent von Kármán plate equation:

$$\rho_s h_s \frac{\partial^2 W}{\partial t^2} + \frac{E h_s^3}{12(1-\nu^2)} \Delta^2 W = f_{\text{ext}}, \tag{2.17}$$

where ρ_s denotes the wing density, W the vertical displacement and h_s the wing thickness. The material properties are the Young's modulus and Poisson's ratio with respectively E and ν. Δ is the Poisson operator. The external forces per unit length acting in vertical direction are denoted by f_{ext} and will be composed of the fluid forces.

Non-dimensionalisation of equation 2.17 can be done by introducing the effective structural parameters. The ratio between the inertial forces of the wing and the inertia of the displaced fluid is referred to as the effective inertia. The effective stiffness of the wing is the ratio between wing bending forces and the fluid dynamical force. The effective rotational inertia relates the wing rotational moment of inertia with the rotational inertia of the fluid. The effective inertia, stiffness and rotational inertia are defined as:

$$\Pi_0 = \rho^* h_s^* \frac{k}{\pi}, \tag{2.18}$$

$$\Pi_1 = \frac{E h_s^{*3}}{12(1-\nu^2)\rho_f U_{\text{ref}}^2}, \tag{2.19}$$

$$\Pi_2 = \frac{I_B}{\rho U_{\text{ref}}^5}. \tag{2.20}$$

where $\rho^* = \rho_s/\rho_f$, $h_s^* = h/c$. The product of these two ratios is the mass ratio:

$$m^* = \frac{\rho_s h}{\rho_f c}, \tag{2.21}$$

which relates the inertial forces of the wing to the aerodynamic forces. For a derivation of this expression, consult appendix D.

By non-dimensionalisation of equation 2.17, the effective inertia and stiffness can be easily incorporated in the formula:

$$\Pi_0 \frac{\partial w^*}{\partial t^{*2}} + \Pi_1 \Delta^{*2} w^* = f^*_{\text{ext}}. \tag{2.22}$$

The effective stiffness of the wing can also be expressed in terms of the frequency ratio, which relates the flapping frequency f and the first natural frequency of the wing f_1. The frequency ratio is suitable for wings with a periodic motion since it depends on the flapping frequency.

$$FR = \frac{f}{f_1}. \tag{2.23}$$

2.4.2. Properties of flexible wings in nature

Daniel & Combes (2002) derived a scaling argument to investigate the importance of respectively the inertial and the aerodynamic force, and concluded that in many cases the inertial forces are significantly larger with respect to the aerodynamic ones. In the case of a Hawkmoth wing with a mass ratio of $m^* = 5$, the deformation pattern was investigated for flapping in air and helium (15% the density of air). No significant difference was seen in the deformation. Dai et al. (2012) performed more research to wing deformation, and the way this is influenced by the wing stiffness and mass ratio. They found out that the pitching behaviour is very dependent on the mass ratio, which represents the relative importance of the wing inertia and aerodynamic forces. In insects, mass ratios occur from $m^* = 0.5$.

The flexural stiffness is an important parameter to measure the resistance of the wing against bending. It is the product of the area moment of inertia (I) and the Young's modulus (E), and usually denoted by EI. For natural flyers, Combes & Daniel (2003) found that the spanwise direction has a flexural stiffness of 1-2 times that of the chordwise direction. This property is more pronounced for larger wings.

Torsion affects Camber

Ennos (1988) commented on the importance of the torsion on the design of insect wings. He posed a model of an insect wing made of a corrugated membrane and a rigid member at the leading edge which allowed for torsion, see figure 2.21. Comparing the motion of the proposed wing model with real insect wings showed that the torsional bending mechanism aligned well. The forces and moments developed during insect flight can produce the degree of camber and torsion as seen in the model. Therefore, the inertial forces during pronation and suspination and aerodynamic force during the flapping motion produce aerodynamic forces, which combined with the stiffness provided by the spars caused a positive camber. In turn, this has a positive effect on the aerodynamics.

The same structure is postulated to function in birds wings. Species like hummingbird display large wing deformation, in which camber could be formed by the orientation of the wing feathers.

Du & Sun (2008) created a numerical model to investigate the effect of a varying twist and camber deformation during a flapping motion. The twist and camber were imposed on the structure, such that there was no actual interaction in the solver. The wing kinematics and Reynolds number were specified at the radius of the second moment of area of the wing: $r_2 = 0.6R$. A linear twist was used to mimic the twist deformation as commonly seen in insects (Ellington, 1984).

With respect to the flat plate, an increase in lift and decrease in drag could be attained by varying the wing shape. It was found that the deformation of the camber is dominant for the gain in performance. Only applying a camber of 10% for an angle of attack of 40° at $Re = 200$ yielded in a C_L and C_L/C_D increase of respectively 15% and 12%. This effect was even more pronounced at the higher Reynolds number of $Re = 4,000$, since the LEV was more concentrated and located closer due to the thin shear layer. The twist did not affect the resulting force much. For sustained flight thus, the camber helps to attain a certain amount of lift at a lower angle of attack and a higher lift over

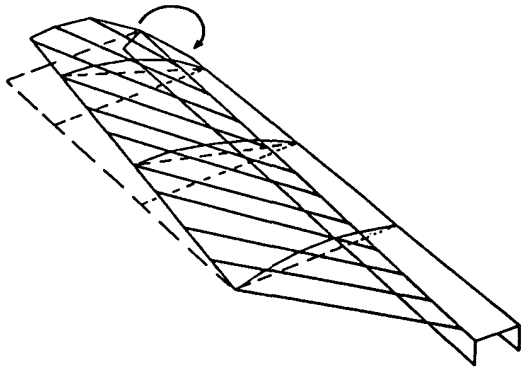

Figure 2.21: The production of camber by wing twist caused by leading edge torsion. From Ennos (1988).

drag ratio, decreasing the power demand.

The results were extrapolated to the typical flight characteristics of a bumblebee. It was found that a typical bumblebee motion with a flat plate would require a constant value angle of attack of 25° and a power consumption of 50W/kg. The application of 6% camber and a twist of 20° yielded a decrease in the angle of attack and power of respectively 20° and 42W/kg (-16%).

2.4.3. Effect of flexural stiffness

Vanella et al. (2008) performed a numerical study towards 2D flexible wings in hovering. The structural modelling was performed using a simplified wing model made up of two pseudo elements with a torsional spring. The wing body was then created using an interpolation between two elements, leading to a wing deformation with only one degree of freedom. Wing were tested for three different Reynolds number: 75, 250 and 1,000.

The frequency ratio was defined as the ratio of the flapping frequency to the natural frequency of the structure: $FR = f_f / f_n$. In this research values until $FR = 1/2$ were tested because the simplified model failed for more flexible wings. The flapping wing is modelled on a 2D grid using the immersed boundary method, and the fluid and structure integrated simultaneously and interactively.

Three different vortices were recognised: the LEV, TEV and the End of Stroke Vortex (ESV). It was found that the LEV was quite insensitive to the wing deformation, while the ESV is very dependent on the flexibility of the link. For the rigid wing and other stiffnesses, two peaks are seen: one at wing acceleration by the LEV, which quickly translates away from the wing, and second contribution from the TEV. The latter can be enhanced by a strong ESV. For the frequency ratio of $FR = 1/3$ the lift peaks were connected, because a stronger ESV was present, which created earlier in the stroke a strong TEV which enhanced the lift. The larger continuous lift on the wing creates a local optimum in terms of coefficients. at this frequency ratio the lift over drag ratio, and performance ratio (lift over power) were optimal.

The effect of the flexibility is most pronounced for the lowest number Reynolds number of 75. At $FR = 1/3$ the lift over drag ratio and performance ratio are enhanced with respectively and 28% and 39%. At the other Reynolds number the ratios are enhanced too, but not as significant. For all Reynolds numbers, the stiffness of the wing creates a sweep of the trailing edge near the end of stroke which causes a stronger ESV with respect to the rigid model or other stiffnesses. This ESV is key to producing a strong TEV which is responsible for the large lift in this 2D model.

Dai et al. (2012) found that the optimal flexibility for lift production is a function of the mass ratio. For a high mass ratio, inertial forces are dominant, and a more flexible wing gives higher lift. This can be explained by the passive rotation of the wing that is enhanced by the wing flexibility. For the right frequency ratio, the wing is deformed during the initial wing accelerations, after which

elastic forces reduce the angle of attack during the translational phase. The vibration of the first eigenmode of the wing causes an angle of attack increment before stroke reversal. At lower mass ratios, the FSI is more important and a favourable wing angle of attack can be prolonged by the contribution of the aerodynamic forces.

For a frequency ratio $FR = \leq 0.3$, the wing deformation enhances the lift produced by the wing, even thought the structure develops a disadvantageous negative camber. Under this value, especially the efficiency of the wing increases, mainly due tot he lower drag production. This is especially true for the low mass ratio wings, where the inertial and aerodynamic torque pair to form a favourable angle of attack during the entire stroke motion (for example in figure 2.25. Higher frequency ratios cause even lower drag, but also suffer a large loss of lift, and therefore lose efficiency.

The pitching angle has a profound effect on the aerodynamic forces. In general, a advanced pitching motion leads to higher lift, drag and power coefficients compared to the symmetric motion. The delayed pitch has lower coefficients. In terms of efficiency, the symmetric wing is best in providing lift per unit power. A interesting point is found for $m^* = 5$ and $FR = 0.51$. Here the delayed pitching caused by the phase delay is compensated by the high influence of the inertial forces, and a nearly symmetric motion is the result, with higher efficiency.

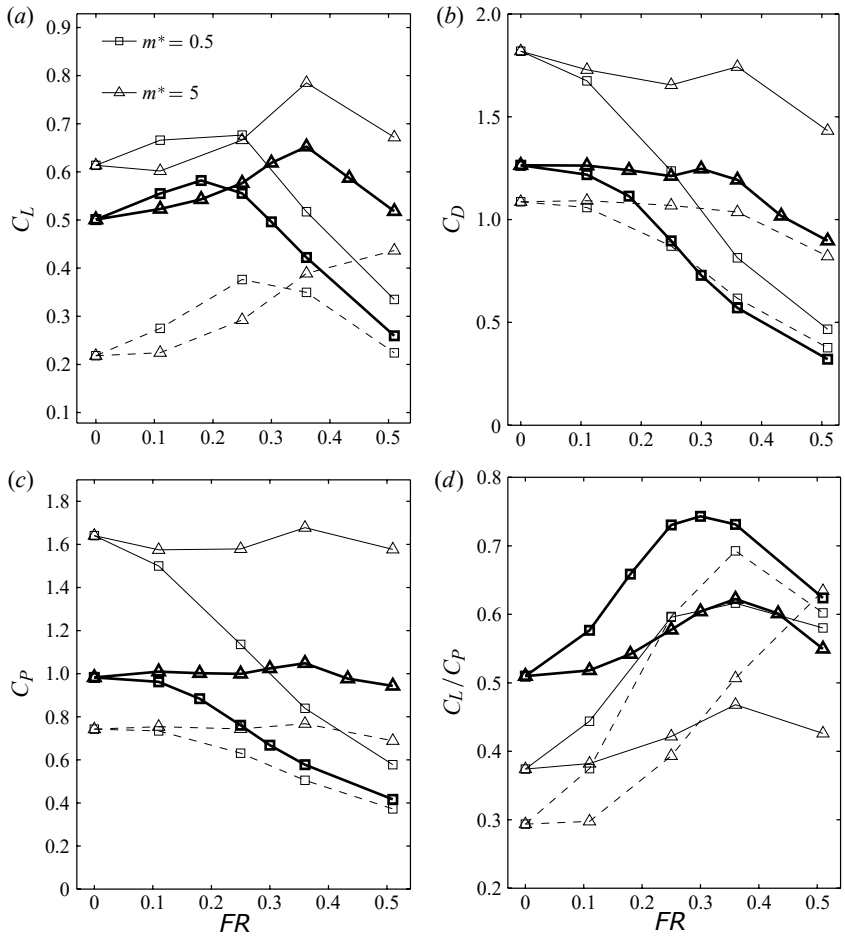

Figure 2.22: The effect of frequency ratio (FR), mass ratio (m^*) and pitching phase angle (ϕ). The thick line depicts the symmetric motion, the dotted line the delayed phase ($\phi = \pi/4$) and the normal line the advanced phase ($\phi = -\pi/4$). (Top left) The lift coefficient, (Top right) the drag coefficient, (Bottom left) the power coefficient and (B) the L/D ratio. Adapted from Dai et al. (2012)

Zhao et al. (2010) tested 16 wings of varying flexibility in chordwise direction at a Reynolds number of $Re \sim 2{,}000$. The wing planform was based on a *Drosophila* wing with a stiff leading edge, and

a range of flexural stifnesses close to those found in nature was tested. The flexibility was expressed in Flexural stiffness (EI), which can be calculated by the applied force at the trailing edge F, the local chord length w and the measured deflection δ:

$$EI = \frac{F w^3}{3\delta}. \tag{2.24}$$

The force data was gained for the wings in steady revolving motion at a range of angles of attack: $\alpha = [-9;90]$. It was found that the resultant force on the wing is highly dependent on the flexural stiffness of the wing. With increasing rigidity, the net force which is produced by the wing rises. The same figure is seen for the drag coefficient, where a monotonic increase in drag is seen for increasing angle of attack. The lift coefficient shows another trend. The highest absolute lift is produced by the rigid wing at 45° angle of attack. More flexible wings have a lower maximum lift, which also occurs at higher angles of attack. For increasing flexible wings, a plateau can be seen, at which the lift is quite constant over a large range of angle of attack.

The lift-drag polar shows that the different curves are nested into each other. The most flexible wing is encapsulated in the slightly more rigid wing, and all wings are nested in the most rigid wing. This indicates that the more rigid the wing is, the more capable it is in producing force.

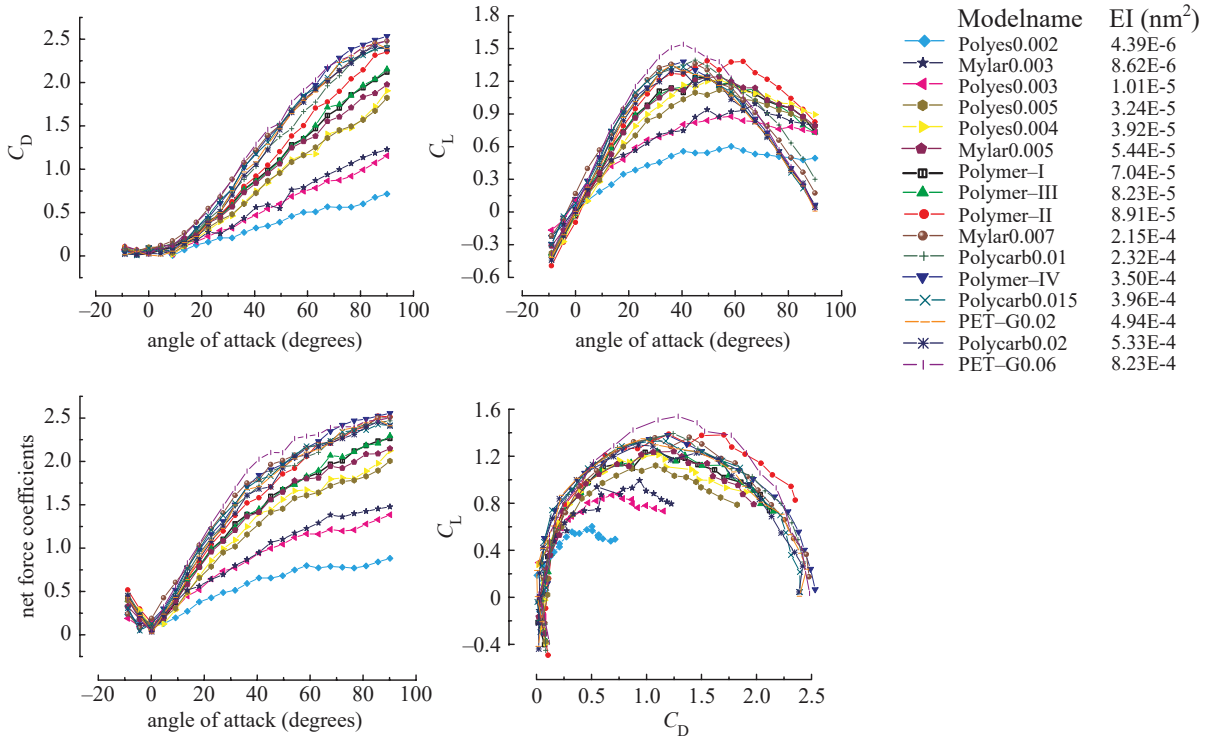

Figure 2.23: Drag, lift and resultant force coefficient for a range of flexural stiffnesses (EI). The lift-drag polar shows that the polars for decreasing flexural stiffness are nested in the stiffer wings. Figures adapted from Zhao et al. (2010).

The lift over drag ratio is shown in the left contour plot in figure 2.24. The rigid wing shows a decreasing lift over drag ratio for increasing angle of attack. The ratio is 1 at $\alpha = 45°$, which indicates that the resulting force vector has an angle 45° with respect to the incoming flow and is perpendicular to the wing surface. The flexible wings shows a slightly slower decrease of the lift over drag ratio until ~60° angle of attack. After this angle the flexible wing still retains some lift by the plateau seen in figure 2.23, so the lift over drag ratio does not go to zero, as it does for the rigid wing.

The force angle is shown in figure 2.24 and is defined as the angle the resultant force has with respect to the vector perpendicular to the angle of attack at the LE. The rigid wing has a force which

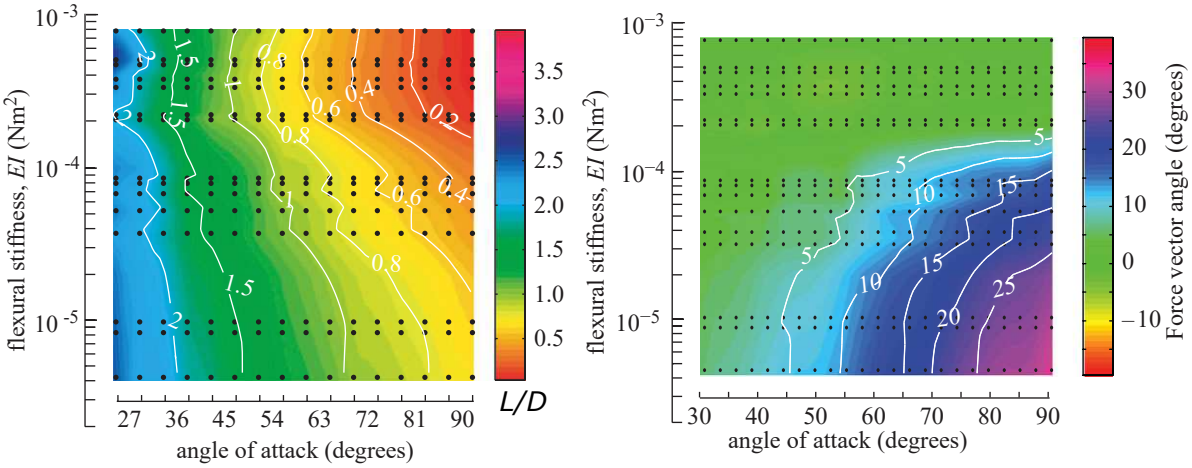

Figure 2.24: Contour plots for the effect or chordwise flexibility over a range of angles of attach on (left) the lift over drag ratio and (right) the force angle with respect to the wing angle of attack. Adapted from Zhao et al. (2010).

is always perpendicular to the wing, which indicates the resultant force is dominated by pressure differences. The same is true for the flexible wings, but here the flexible wing alters the force angle. The resultant force for very flexible wings is directed more upwards and therefore has a larger lift producing part. The most flexible wing tested showed up to 30° force vector angle.

Furthermore, the centre of pressure showed a dependency on the flexibility of the wing. For the rigid wing, the centre of pressure shifted from 0.2 to 0.35 chordlength for increasing angle of attack. The flexible wing did not display a large shift, and the centre of pressure stayed closer to the leading edge.

2.4.4. Effect of the mass ratio

Luo et al. (2010) created a high fidelity system to solve the interaction between viscous, incompressible flow and a highly deformable thin structure. The fluid was solved using the incompressible Navier-Stokes equations which were solved on a nonuniform grid using the Immersed Boundary Method (IBM). Special care was taken to decrease artificial oscillation as is often seen in IBM. the structure is solved using a Finite Element Method (FEM) tool especially designed for thin-walled structures: NONlinear STAtic and Dynamic analysis (`NonStaD`). Both frame and plate elements were used in the formations of the flexible wings that were tested. the Message Passing Interface (MPI) library was used to connect the codes.

The FSI solver was used to solve the flow around a plunging, low aspect ratio flat plate, and a simplified dragonfly wing. In both cases the mass ratio was assumed high, so inertial effects were dominant in the determination of the structure deformation. Also convergence is faster since the simulation is practically one-directional from the structure to the fluid.

Dai et al. (2012) continued the line of research using the same numerical platform to investigate the roles of the aerodynamic, elastic and inertial force on a chordwise flexible wing with $AR = 2$. In the present research, a reciprocating wing in hovering motion was investigated, using simple sinusoidal flapping and active pitching motion at the root. The role of the mass ratio was addressed to find the relative importance of the wing inertia and the aerodynamic force. Also the effect of the Reynolds number, phase angle of pitching and wing stiffness were investigated.

The effect of the mass ratio of the wing is modelled by taking different mass ratios: $m^* = 0.5, 1, 5$. The latter figure represents the situation in which inertial forces completely dominate the wing deformation. In this flow it is noticed that the inertia causes an advanced wing rotation: hence the torque about the leading edge switches signs before the pronation and suspination. Figure 2.25

shows the torque about the leading edge for a low mass ratio. Contrary to the scaling argument of Daniel & Combes (2002), the aerodynamic torque has a similar order of magnitude as the inertial torque, and therefore the wing deformation is governed by equally by the inertial and aerodynamic forces. The inertial forces are most prominent in wing reversal, where the largest kinematic accelerations take place. The aerodynamic forces are highest when the wing velocity is greatest, so in midstroke. Therefore there is a phase-lag between these two processes. As a result, during the stroke the angle of attack of the wing is reduced significantly due to the aerodynamic force.

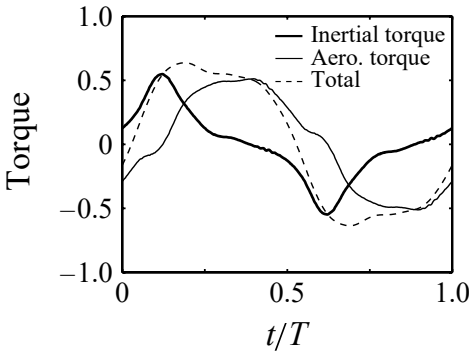

Figure 2.25: Instantaneous torque about the leading edge produced by the inertia and the aerodynamic forces, for $m^* = 0.5$ and $FR = 0.36$ in symmetric flapping. Adapted from Dai et al. (2012)

The mass ratio influences the wing deformation and forces. The thick line in figure 2.22 shows that the lift can always be increased by adding some flexibility, but there is a optimum value for this. The absolute maximum lift that can be attained is higher for the high mass ratio wing. The drag reduces with flexibility, mainly because the angle of attack is reduced and thus the force angle is more directed in the lift direction. In this figure it is clear that the low mass ratio wing deforms more and therefore has a lower drag. The power is strongly coupled to the drag curve and shows similar behaviour. At last the lift-over-power ratio is more favourable for the low mass ratio wing, mainly due to the enhanced deflection that causes less drag

Nature-inspired FSI model

Nakata & Liu (2012) presented a FSI model of an Hawkmoth wing with a realistic wing model. The structure was modelled using a FEM based model with an anisotropic stiffness, to simulate the veins in the wing. Similar to the comments of wing torsion by Ennos (1988), the anisotropy of the Hawkmoth wing incorporates more stiffness because of the diagonal veins. The structure deflection was then computed using flexible thin-shell structures to capture the nonlinear dynamic responses.

The investigation gives a comparison of rigid and flexible wings. The wing kinematics were prescribed at the root equally for both the rigid and flexible wing. No elevation was used and the positional and feathering angle were approximated with a sinusoidal wave.

The effect of the flexible wing can be seen in the deformation graphs in figure 2.26 (left). The peak in the spanwise and twist bending pattern is attributed to the inertial forces during the pronation and suspination phases. Furthermore, it is interesting to note that the anisotropic wing generates a positive camber, which helps is beneficial to the aerodynamic force, as noted by Du & Sun (2008).

The force generation is shown in figure 2.26 (right), where the most striking difference between the rigid and flexible wing is seen in the first part of the down- and upstroke. Here, both wings reach a plateau, but for the flexible wing this plateau is much more efficient in lift generation. The LEV/TV combination is more stable with respect to the rigid wing, and breaks down later in the stroke cycle. Moreover, the downstroke vortex ring is stronger and creates a stronger downwash.

The flexibility furthermore causes a slight delay in the flapping phase, which can be seen at the

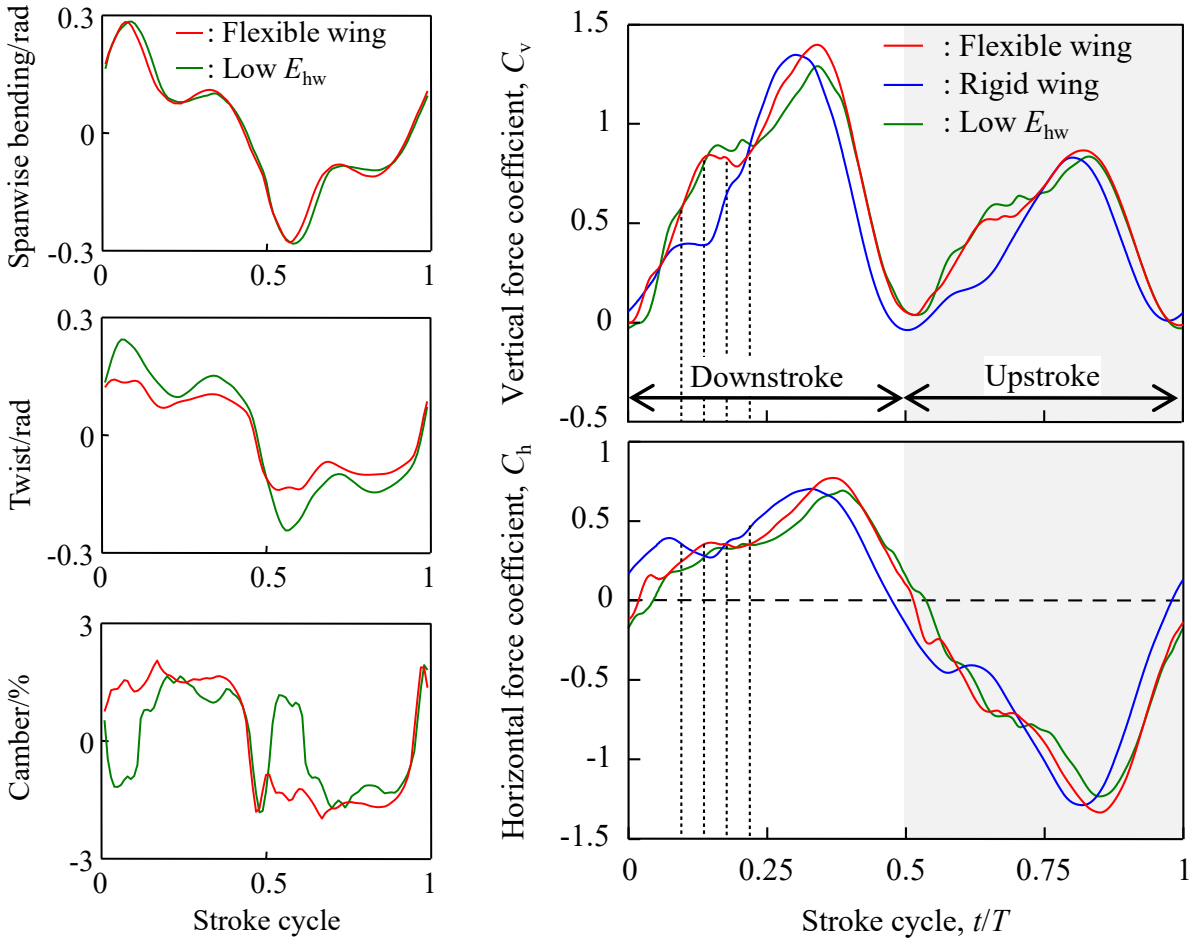

Figure 2.26: Influence of flexibility on a Hawkmoth wing. (Left) shows the bending, twist and (positive) camber at 0.8 spanwidth. (Right) The vertical (top) and horizontal (bottom) force generated by the flexible and rigid wings. Adapted from Nakata & Liu (2012)

maximum force peak. After this, the stroke reversal is more rapid due to the stored elastic energy, and as a result the flexible wing produces more lift during stroke reversal compared to the rigid wing. Overall, the flexible wing can create up to 20% more lift, given these kinematics. The smaller angle of attack by the flexible structure causes a lower average angle of attack, which increases the lift over drag ratio. Still the absolute drag increased slightly, therefore the flexible wing requires more power.

2.5. Identification of coherent structures on the wing

Understanding the nature of the flow around a wing is often performed by the identification of vortices and their coherent structure. Setting up a criterion is important to recognise the strength, location, and attachment of the vortex and associated low pressure field.

2.5.1. Vorticity and helical density

The vorticity is defined as the curl of the velocity field and this captures both the influence of shear velocity gradients by rotational effect:

$$\boldsymbol{\omega} = \nabla \times \boldsymbol{U}. \tag{2.25}$$

The transport of the vorticity is a measure which is prominently named in many researches, where it is postulated that the LEV remains stable because the excess vorticity is drained by vorticity transport through the vortex core. Moffatt (1969) defined the helicity per unit volume of the flow, or helical density as the inner product of the velocity and the vorticity:

$$h = \boldsymbol{u} \cdot \boldsymbol{\omega}. \tag{2.26}$$

Therefore the helical density can be used as a measure for the vorticity transport along a vortex axis (Carr et al., 2013). Furthermore, it also represents the three dimensionality of the vortex system. Completely 2D vortex structures feature zero helical density.

2.5.2. Q-criterion and λ_2-criterion

Carr et al. (2013) mention several criteria which are used in vortex identification. A first candidate is the usage of vorticity, where iso-surfaces of the vorticity magnitude ($|\omega|$)represent vortical structures. However, the vorticity entails both shear and swirling flows which is not desired in the identification of a vortex.

The Q-criterion by Hunt et al. (1988) is used to define a vortex as a region with the positive invariant Q of the velocity gradient. The latter property can be split in a symmetric and antisymmetric part: $S_{ij} = \frac{1}{2}\left(u_{i,j} + u_{j,i}\right)$ and $\Omega_{ij} = \frac{1}{2}\left(u_{i,j} - u_{j,i}\right)$. The Q-criterion can then be formulated as follows:

$$Q = \frac{1}{2}\left(\|\boldsymbol{\Omega}\|^2 - \|\boldsymbol{S}\|^2\right) \tag{2.27}$$

Q represent local balance between the shear rate and vorticity magnitude (Jeong & Hussain, 1995). At the wall Q is zero because of the local equilibrium between the shear strain rate and the vorticity magnitude, which is a major advantage over the usage of the vorticity magnitude in vortex identification.

The λ_2 method if proposed by Jeong & Hussain (1995). This method uses the symmetric and antisymmetric of the velocity gradient to find the locations of the vortex, in which the local pressure minimum is contained. The latter is not guaranteed by the Q-criterion. The term $(\boldsymbol{S}^2 + \boldsymbol{\Omega}^2)$ is used to identify the region of a local pressure minimum due to vortical motion. This term is symmetric and therefore has three real eigenvalues $(\lambda_i; i = 1,2,3)$. Regions where $\lambda_2 < 0$ indicates a vortex core, and the local pressure minimum due to vortical motion is enraptured within this region.

2.6. Synthesis

The above chapter presents the most relevant aspects of flapping wing aerodynamics. The scaling parameters and equations for rigid or flexible, and translational and rotational frames are given. The most important aerodynamic effects are named and the theory on flapping wings is explained. In this synthesis the most relevant parts are listed for the current thesis.

2.6.1. On the flowfield of flapping wings

The Reynolds number has a large influence on the flow field. For all Reynolds numbers the LEV can be stable, but different mechanisms assure the stability. The LEV is more stable at low Reynolds numbers, because the viscosity inhibits large vorticity growth. Very low Reynolds numbers further inhibit spanwise interaction, so the flow is largely two dimensional. Furthermore, spanwise flow in the core of the vortex creates a stabilizing effect for higher Reynolds numbers while it is hardly present for lower numbers. Because more vorticity can be built up, the force of the LEV increases for higher Reynolds numbers.

For the rotational frame of reference, the (fictional) Coriolis, centrifugal and Euler force are added to the Navier-Stokes equations. These scale respectively with the Rossby number and the dimensionless stroke amplitude. For a rotational motion, the LEV is stabilized, while on translating wings the LEV sheds more easy. Only near the tip the LEV is anchored by the TVs. Spanwise gradients help attaching the LEV to the wing and the force generation is enhanced mainly by the rotational effects. This is because the rotational forces aid in anchoring the LEV closely to the surface. According to Lentink & Dickinson (2009b,a); Jardin & David (2015), the flow field and lift force are hardly affected by the addition of the centrifugal forces. The Coriolis force is dominant in anchoring the LEV and maintaining the stability. Garmann & Visbal (2013, 2014) do not agree with this conclusion, and prescribe the stability to the role of the centrifugal force and pressure gradient.

Enlarging the aspect ratio for translating wings creates a large section of 2D flow on the inboard section. The flow at 3 chord-lengths from the tip experiences influence from the TV. Further inboard, the flow is close to 2D and shows vortex shedding. The same on a revolving wing creates a region of 2D flow on the wing section which has a high local Rossby number and is outside the influence of the TV. For a revolving wing the tip vortex creates a similar inboard flow velocity. Inboard the LEV is stabilized by the fictional forces and an outboard flow is present. When the outboard flow from the fictional forces and the inboard flow from the TV collide, the LEV lifts from the surface and merges to the TV.

For a large range of angle of attack a LEV can be recognised, and the LEV strength increases with the angle of attack. The lift force reaches a maximum at 45°. Since the force on the wing is mainly determined by pressure forces the resultant force is oriented with 90° to the wing.

For an impulsively started wing the vorticity grows linearly with the local distance travelled, until it reaches a plateau. For revolving wings this implies that the LEV is saturated first at the tip. For translating wings, a reciprocating motion can increase the lift production by changing direction before the LEV is shed.

2.6.2. Flexibility

Wing flexibility causes the wing to deform during stroke. The wing deformation can be assigned to three aspect: Elastic, inertial and aerodynamic forces. The Elastic forces can be expressed in various ways. A definition of the absolute stiffness of the wing is the flexural stiffness EI. In nature the flexural stiffness is 1-2 times higher in spanwise direction than in chordwise direction. The relative stiffness of the wing is expressed by the effective stiffness respectively Π_1. The frequency ratio (FR) relates the flapping frequency to the first eigenvalue of the motion.

The effect of the inertial forces of the wing are dominant in some insect species. The effect of the inertia over the aerodynamic forces is measured in the effective inertia or the mass ratio, respectively

Π_0 or m^*. The inertial force of the wing is important in wing reversal, when large accelerations take place. In the middle part of the flapping motion aerodynamic forces can be dominant, depending on the mass ratio.

Uniformly flexible wings under loading develop a negative camber which does not match the typical airfoil camber. For diagonal spars, the wing loading creates a positive camber. It was found that a positive camber could increase the lift and lift over drag ratio for an angle of attack of 40°.

The research on uniform simple plates, both 2D and 3D showed that the optimal stiffness for the wing was found at a frequency ratio of $FR = 1/3$. At this ratio the lift over drag is optimal. Experimental research showed that the absolute force over the wing decreased with increasing flexibility. Because of the bending of the wing, larger angles of attack could be reached without loss of lift. This causes the angle of attack for maximum lift peak to increase far above 45°. This effect is paired with a shift of of the force vector angle, which is changed when the wing deflects.

Chapter 3

Fluid-Structure Interaction

The coupling between the fluid and structure is performed by the interchange of boundary conditions. If the information is shared in both directions, interaction takes place. For strongly coupled systems, multiple iterations are required till convergence of the boundary data is reached, these are referred to a sub-iterations.

This chapter treats the various aspect that play a role in FSI. The consequences for the computational framework are treated in section 3.5.

3.1. Coupled system approaches

Since the fluid and the structure are two physical systems which interact dynamically with each other dynamically, this results in a coupled system. Two main approaches exist to solve for coupled systems. To couple these schemes the time-accuracy is critical.

The Monolithic approach captures both domains in one set of equations. Both systems are captured in one set of equations which is solved simultaneously. As an advantage, the energy is always conserved over the interface (Farhat, 2004). Furthermore, the time-accuracy of the solution is only dependent on the chosen time-integrator, whereas in the partitioned approach other components influence the accuracy.

However, there are certain drawbacks to the monolithic approach. First of all, no distinction is made in mathematical properties between the solvers. This means that optimization techniques for a certain field are not used. Difference in time-scales in the fields furthermore implies that the time-step is dependent on the field with the smallest time-scales.

In contrast, the partitioned approach handles both physical systems in different, dedicated solvers. Since these solvers are optimized for their particular field, good performance is expected here. The coupling is performed using the solvers as 'black-boxes', which only provide the boundary field of interest. In FSI, the interface between the solvers is called the wet surface. The action of both solvers can then be formulated as:

$$\begin{aligned} F^{(n)} &: \mathbb{R}^{d \cdot M_d} \rightarrow \mathbb{R}^{d \cdot M_f}, \qquad \vec{d} \rightarrow \vec{f}, \\ S^{(n)} &: \mathbb{R}^{d \cdot M_f} \rightarrow \mathbb{R}^{d \cdot M_d}, \qquad \vec{f} \rightarrow \vec{d}. \end{aligned} \tag{3.1}$$

The first part denotes the operation of the fluid mesh, which transforms the boundary displacement ($\vec{d}$) to forces ($\vec{f}$). This mapping $F^{(n)}$ is performed in timestep n, so from $t_n \rightarrow t_{n+1}$. The size of this mapping problem is given by the dimension of the problem times the number of fluid and structure mesh grid nodes, respectively d, M_f and M_d. The mapping of the structure is analogous and transfers the force input to displacement output.

The partitioned approach adds a large amount of flexibility because any solver can be incorporated given the right coupling interface. Because the coupled solvers are solved independently,

some staggered scheme must be utilized. In section 3.3 several schemes are presented and how these influence the efficiency and accuracy of the partitioned coupling.

3.2. Coupling of the Fluid and Structure

In the partitioned coupling approach there are multiple physical models, in the case of FSI a fluid dynamical and a structural model. The former makes use of the incompressible Navier-Stokes in the Arbitrary Lagrangian Eulerian formation. To assure that the equations are stable in the time-stepping method, the Discrete Geometric Conservation Law (DGCL) must be adhered to on the fluid mesh. The structure is solved using a equations in Lagrangian form. Apart from the two physical models, a computational model comes into play for the deformation of the mesh according the structural deformation. The mesh can be seen as a third field that needs to be solved, therefore, this system is in fact a Three-field formulation (Farhat, 2004).

The exchange between these fields takes place by the exchange of boundary conditions. The fluid and structure domain are respectively denoted by Ω_F and Ω_S. Their shared boundary is denoted by Γ, such that: $\Gamma(t) = \partial\Omega_F(t) \cap \partial\Omega_S(t)$.

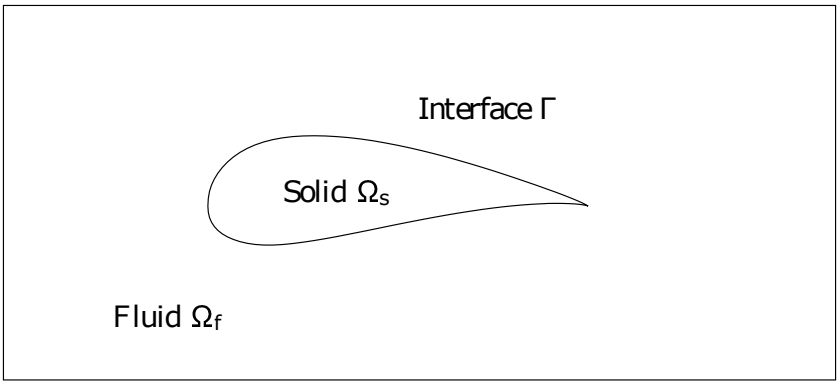

Figure 3.1: Division of the fluid and structure domain. Adapted from Blom (2017).

Furthermore, the following quantities are on the different domains. Note the structure position q is the same as the structure mesh position, since this is defined in the Lagrangian frame.

Table 3.1: Position and velocity definitions

Field	Position	Velocity
Fluid		v
Structure	u	$\dot{u}$
Dynamic mesh	x	$\dot{x}$

3.2.1. Flow domain in Arbitrary Lagrangian Eulerian form

The low velocity flow that is seen in flapping wing aerodynamics is solved using the incompressible Navier-Stokes equations as seen in equation 2.7 and 2.8, here in Eulerian form. These non-linear equations are typically solved using a finite volume approach: each cell is a control element over which the Navier-Stokes equations are integrated. For a stationary mesh the fluid is therefore solved using an Eulerian or stationary reference frame.

For the displacement of the structure, the surrounding mesh must deform. This dynamic mesh deformations means the cell faces move and cell volume changes every timestep. An extra term must be included to the convective part of the Navier-Stokes equations, which accounts for the

mesh movement. Equation 3.2 shows the semi-discrete Navier-Stokes equations in Arbitrary Lagrangian Eulerian (ALE) frame, in notation for mesh cell i:

$$\frac{d}{dt}(V_i(t)\boldsymbol{W}_i) + \boldsymbol{\Phi}_i^c(\boldsymbol{W}_j\boldsymbol{x},\dot{\boldsymbol{x}}) = \boldsymbol{R}_i(\boldsymbol{W}_j,\boldsymbol{x}) \qquad \text{in } \Omega_F, \tag{3.2}$$

where

- V_i is the the volume of the cell i. For a dynamic mesh this value is time-dependent.
- $\boldsymbol{W}_i$ is state vector including the velocity components and is defined in the centre of each cell.
- $\boldsymbol{\Phi}_i^c$ is the flux on the face of cell i, and is dependent on the states of the surrounding cells j. The flux is furthermore dependent on the mesh displacement and motion; $\boldsymbol{x},\dot{\boldsymbol{x}}$. The superscript c denotes that the dynamic mesh movement is included in this factor.
- $\boldsymbol{R}_i$ captures the contribution of the viscosity and source terms.

For the equations in ALE form, the DGCL sets requirements on the numerical method (Thomas & Lombard, 1979). This law poses a consistency criterion that the change in volume of a moving control volume must equal the sum of the total volume swept by the faces of that control volume. To reach this, the law states that the computation preserves the state of a uniform flow, independent of the mesh motion.

Adherence to the DGCL is a necessary and sufficient condition to assure that the moving grid has the same non-linear stability properties of its fixed grid counterpart. More specifically, if the DGCL is satisfied, for a time-stepping scheme with fixed grid of order p, the moving grid counterpart will have at least order $p-1$ (Guillard & Farhat, 1999). When the DGCL is violated, spurious and potentially unstable oscillations can occur.

3.2.2. Structural domain

The second field is determined by the structure. Traditionally, structural dynamics equations are posed in Lagrangian form, where the mesh follows the deformation of the structure. Furthermore, the differential equation is normally solved using the Finite Element Method:

$$\boldsymbol{M}\ddot{\boldsymbol{u}} + \boldsymbol{C}\dot{\boldsymbol{u}} + \boldsymbol{K}\boldsymbol{u} = \boldsymbol{F}^{\text{ae}} + \boldsymbol{F}^{\text{ext}} \qquad \text{in } \Omega_S. \tag{3.3}$$

where

- $\boldsymbol{u}$ is the structural displacement. The structure velocity and acceleration are the first and second time-derivative of the displacement.
- $\boldsymbol{M}$ is the mass matrix of the structure, $\boldsymbol{C}$ and $\boldsymbol{K}$ are respectively the damping and stiffness matrix of the structure.
- $\boldsymbol{F}^{\text{ae}}$ and $\boldsymbol{F}^{\text{ext}}$ are respectively the internal, aerodynamic and external force. The aerodynamic force acts on the boundary and replaces $\boldsymbol{F}^{\text{ext}}$ in this equation.

Damping

Damping of the structure can be implemented using the Rayleigh approach. The matrix $\boldsymbol{C}$ can be constructed by assuming a linear combination of the mass and stiffness matrix (Chopra, 2012):

$$\boldsymbol{C} = \alpha\boldsymbol{M} + \beta\boldsymbol{K}. \tag{3.4}$$

The damping for a specific eigenmode with a frequency can then be derived to be:

$$\zeta_n = \frac{\alpha}{2\omega_n} + \frac{\beta\omega_n}{2}. \tag{3.5}$$

Various methods exist to extract the coefficients α and β. An expression for these coefficients can be obtained by assuming a damping values for two frequencies. Then the following matrix system can be solved to obtain the coefficients:

$$\frac{1}{2}\begin{bmatrix} 1/\omega_i & \omega_i \\ 1/\omega_j & \omega_j \end{bmatrix}\begin{Bmatrix} \alpha \\ \beta \end{Bmatrix} = \begin{Bmatrix} \zeta_i \\ \zeta_j \end{Bmatrix}. \tag{3.6}$$

3.2.3. Dynamic mesh field

Depending on the type of structural deformation the mesh needs to be adjusted or not. Small structural deformations can be covered by only implementing a velocity boundary condition on the interface, which is called the transpiration technique. For larger deformations the dynamic mesh is a necessity.

The mesh deformations can be modelled as a pseudo-structural system, where the mesh therefore adds a third field to the coupled simulation. Equation 3.7 is written in the velocity form of the pseudo-structure, which can used for an incremental adaptation of the mesh. $\tilde{\boldsymbol{K}}$ denotes the stiffness of the pseudo-structure. The time-dependency here means that the deformation can be computed relatively every timestep rather than absolutely with respect to the starting mesh.

$$\tilde{\boldsymbol{K}}_{\Omega\Omega}(t)\dot{\boldsymbol{x}}_{\Omega}(t) + \tilde{\boldsymbol{K}}_{\Omega\Gamma}(t)\dot{\boldsymbol{x}}_{\Gamma}(t) = \boldsymbol{0} \qquad \text{in } \Omega_F \tag{3.7}$$

3.2.4. Conservative and Consistent coupling.

The exchange of boundary conditions takes place by transferring the boundary values from one surface mesh to the other. Since, in general the boundary cells are non-matching in multi-physics problems, an interpolation method must be used.

According to de Boer et al. (2008), the exchange of boundary values can be defined by a transformation matrix H, where respectively H_{fs} and H_{sf} bring the boundary values from the structural to the fluid mesh, and visa versa. A conservative coupling is based on the conservation of virtual work on the surface. This exists when the same one transformation matrix is the transpose of the other. To create the first transformation matrix, the integral sum of the parameter is conserved, which leads to a transformation matrix with a row-sum of one. However is often not true for the transpose.

In the consistent approach two transformation matrices are employed, both with a row-sum of one. In general these matrices are not each others transpose, therefore the method is not both conservative and consistent and the energy is not conserved over the surface.

Bungartz et al. (2016) reflects on the properties of the conservative and consistent coupling. Depending on the type of variable, either method is preferred. For integral parameters such as forces, conservative method must be used. For non-matching meshes this holds that the integral of the property is conserved. Moving from a coarse to a fine mesh, this means the point value is divided over multiple points such that the sum on both meshes is the same. Consistent mapping is applicable to fields such as pressure, fluxes or densities. For non-matching meshes this holds that the value of a constant function is maintained on the other mesh.

Various interpolation methods exist. The Nearest-Neighbour method is the simplest method available, which assigns the point data to the nearest point from the other mesh available. In general this method lacks accuracy, but for fine to coarse meshes it can be used. The Nearest-Projection Method is an improvement of the Nearest-Neighbour, where the topology of the target mesh is first mapped onto the source mesh. Using this method, the accuracy of interpolation is second order.

The Weighted Residual method is based on the weak formulation of the conservation of the parameter in question. Various choices exist for the test function, such as the mortar approach. Another coupling method used Radial Basis Functions (RBF) interpolation. For this method radially defined interpolation functions are used which transfer the parameter from one mesh to the other. In contrast to the other methods, no orthogonal or search algorithm is required, since these

functions are valid in the entire domain space.

3.2.5. Boundary conditions

The coupling between the structure, fluid and fluid mesh takes place on the interface Γ. Various strategies exist for the exchange of boundary conditions. From the fluid participant either the force of the stress can be mapped. The force is a conservative variable because the integral sum must be preserved over the boundary. The stress however requires consistent mapping since it is independent of the area on which is is present. The boundary conditions from the structure side are related to the displacement of the boundary. A straightforward approach is direct mapping of the surface deformation. Alternatively the velocity can be applied to the fluid model. Both these mappings are consistent.

In a general method the forces are transferred from the fluid to the structure and imposed as boundary condition. See equation 3.8, where the normal contribution from the pressure and stress tensor are taken equal to the structure normal surface stress. In term, for the viscous, incompressible fluid the interface velocity is the coupling boundary conditions. These boundary conditions are featured in the transmission part.

$$\begin{aligned} \text{Forces equilibrium:} \quad & -p\boldsymbol{n}_b + \boldsymbol{\tau}\cdot\boldsymbol{n}_b = \boldsymbol{\sigma}\cdot\boldsymbol{n}_b \\ \text{No slip:} \quad & \boldsymbol{v} = \dot{\boldsymbol{u}} \end{aligned} \tag{3.8}$$

Additionally, the structural displacement is used to deform the fluid mesh to the updated geometry. The equations below formulate the compatibility conditions for the boundary of the fluid mesh.

$$\begin{aligned} \text{Mesh displacement:} \quad & \boldsymbol{x} = \boldsymbol{x}(0) + \boldsymbol{u}, \\ \text{Mesh velocity:} \quad & \dot{\boldsymbol{x}} = \dot{\boldsymbol{u}}. \end{aligned} \tag{3.9}$$

3.3. Time stepping method

Time stepping methods using the partitioned approach can be divided into two groups: loosely or strongly coupled systems. For both methods the fluid and structure are updated separately, and boundary data is exchanged. The loosely coupled simulation updates both fields once per timestep, therefore it is referred to as explicit in FSI literature. This leads to discrepancies in the coupling conditions in equation 3.8. However for low amounts of interaction this method can suffice.

In strongly coupled simulation, the fluid and structural solver are iterated until the coupling conditions are satisfied at the interface to a certain convergence criterion. Since this method uses the field values from the newly computed time-instance, it is referred to as an implicit method in FSI literature. Multiple iterations are performed each time-instance, therefore this method is intrinsically computationally more expensive that the loosely coupled method.

3.3.1. staggered procedures

The way in which the solvers are computed is defined by the staggered procedure. A simple version is the Conventional Serial Staggered (CSS) procedure (Farhat & Lesoinne, 2000). This procedure depends on 4 steps. For timestep $t_n \rightarrow t_{n+1}$.

1. Update the mesh according to the structural displacement at t_n. So $x_{n+1} = u_n$.
2. Calculate the fluid field using the fluid mesh at t_n and t_{n+1}. The fluid flow state W_{N+1} is found.
3. Transfer the pressure boundary to the structure
4. Calculate the updated state for the structure u_{n+1}.

The parallel variant updates the fluid mesh x_{n+1} for the newly computed structural displacement u_{n+1}. The fluid field is computed over and the forces are coupled to the structure, which is updated again. This procedure is followed until convergence is reached.

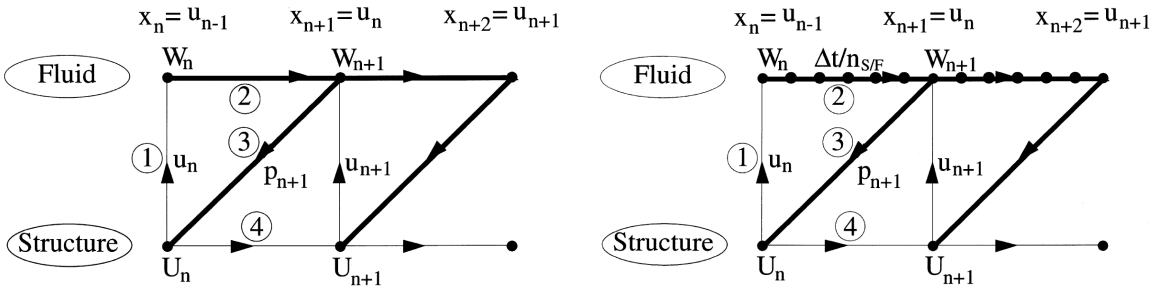

Figure 3.2: Conventional Serial Staggered procedure. (left) Basic operation. (right) with sub-cycling for the fluid solver. From Farhat & Lesoinne (2000).

Figure 3.2 (right) shows the CSS procedure with sub-cycling for the fluid solver. In general, the fluid has a much smaller time-scale than the structure and therefore requires a smaller time-step. By sub-cycling the fluid solver, the models structural model is only computed when necessary. This reduces the computational cost of the structure and the communication between both solvers.

The CSS algorithm is serial, hence the solvers are run in sequence. Parallel computation of the Computational Fluid Dynamics (CFD) and Computational Structural Dynamics (CSD) solver can be attained by a small adaptation of the procedure. The Conventional Parallel Staggered (CPS) facilitates parallel computation of the fields by limiting the exchange of data to the current time-instance. See figure 3.3 for the CPS procedure.

The procedures above can be improved using a different approach. Taking into account that the structure is usually time-discretised using the second-order midpoint rule. In this computation,

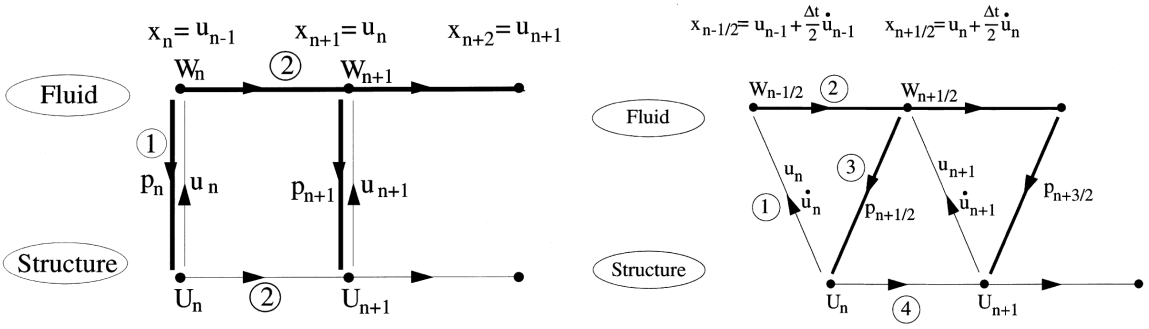

Figure 3.3: (left) Conventional Parallel Staggered procedure. (right) Alternative with mid-time force evaluation. From Farhat & Lesoinne (2000).

the force is calculated in mid-time between two timesteps. Figure 3.3 shows this procedure, which can deliver an overall second order precision, provided the fluid is solved using a second order time integration.

To speed up the current simulation with the CSS procedure, Nakata & Liu (2012) applied predicting steps to the structural solver as in figure 3.4. A prediction of the structural displacement is added for time $t+\Delta t$, using the current displacement and velocity. This predictor is only efficient if Δt is small compared to the structure dynamic deformation. Then the fluid mesh can be updated in a more precise manner compared to the CSS or CPS procedure.

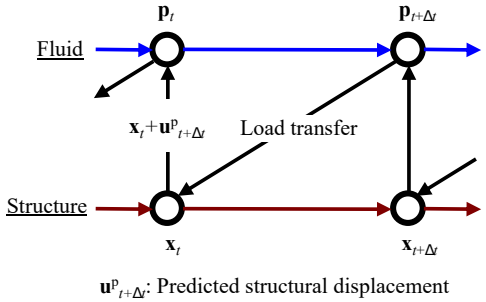

Figure 3.4: Conventional serial staggered procedure. Adapted from Nakata & Liu (2012).

3.3.2. Convergence Techniques

Mehl et al. (2016) treat several techniques for the convergence in strongly coupled systems. In this case the Fixed Point Equation (FPE) for the structure and fluid can be summarised as:

$$(S \circ F)(\vec{d}) = \vec{d} \qquad \text{or in general form} \qquad H(\vec{x}) = \vec{x}, \tag{3.10}$$

where the formulations are analogous to the previously defined operations in equation 3.1. The iteration for one timestep is complete if the above equation is satisfied. The particular form of the FPE notes here is applicable to a serial staggered computation, but alternatives exist for parallel field solving, such as the parallel Fixed Point Equation and vectorial Fixed Point Equation. It is desirable to run the CFD and CSD solver in parallel, so no computational time is lost with cores running idle.

Regardless of the type of FPE, each of these equations can be transformed to the general form.

Fixed point iteration

In this approach, the equation

$$H(\vec{i_n}) = x_{i+1}, \tag{3.11}$$

is solved until convergence, where i denotes the iteration undertaken per time-instance. This is stable for a mapping of $||H|| < 1$, which is in general not the case for FSI.

Constant under-relaxation

This approach stabilises the simulation by using a fixed scalar ω, such that:

$$\vec{x_{i+1}} = \vec{x_i} + \omega\,(H(\vec{x_i}) - \vec{x_i}) \tag{3.12}$$

is solved. In this approach multiple iterations must be performed before every timestep is converged. The subrelaxation factor ω is assigned a fixed value.

Aitken under-relaxation

The Aitken under-relaxation solves the same system defined by as the constant under-relaxation in equation 3.12. However, an adaptive algorithm is used such that the scalar ω is calculated every time-step, leading to a better convergence.

Quasi-Newton methods

For the Quasi-Newton methods equation:

$$R(\vec{x}) := H(\vec{x}) - \vec{x} \stackrel{!}{=} 0 \tag{3.13}$$

is minimized. In this method data from previous iterations is used to approximate a newton solver step for the FPE. To iteratively reach the solution, the Jacobian of the residual matrix R is estimated. Various varieties of this method exist. The Interface Quasi-Newton Inverse Least-Squares (IQN-LS) uses the least-squares method to minimize the norm of the inverse Jacobian. Lindner et al. (2015) describes a the Interface Quasi-Newton Multiple Vector Jacobian (IQN-MVJ). This method minimizes the difference in the Jacobian over timesteps.

Apart from these methods, Blom (2017) comments on methods to increase the performance of the scheme. Multi-level method take advantage of the computationally less expensive coarse grids. The Multi-Level Quasi-Newton Least-Squares (ML-IQN-LS) utilizes a coarse grid to construct an approximation of the Jacobian, which is then refined iteratively to the fine grid. Other alternatives are Aggressive Space Mapping (ASM), Output Space Mapping (OSM) or Manifold Mapping (MM).

3.4. Meshes

In this section the different properties of the fluid mesh are treated. The fluid mesh is usually denoted as 'mesh' without the adjective 'fluid' mentioned specifically. Three different strategies are often used in flapping wing aerodynamics, see also appendix A. The mesh is created in the entire domain of the solver satisfy the conservation laws. On moving meshes this is done by means of the Arbitrary Lagrangian Eulerian approach, which takes into account the mesh deformation for the flux across the mesh boundary.

A distinction can be made between structured and unstructured meshes, as seen in figure 3.5. Multi-block grids exists of blocks of structured meshes. Structured meshes are more favourable in terms of accuracy and efficiency of the solver. Unstructured meshes are easy to create around complex geometries, which makes them suitable for many engineering applications.

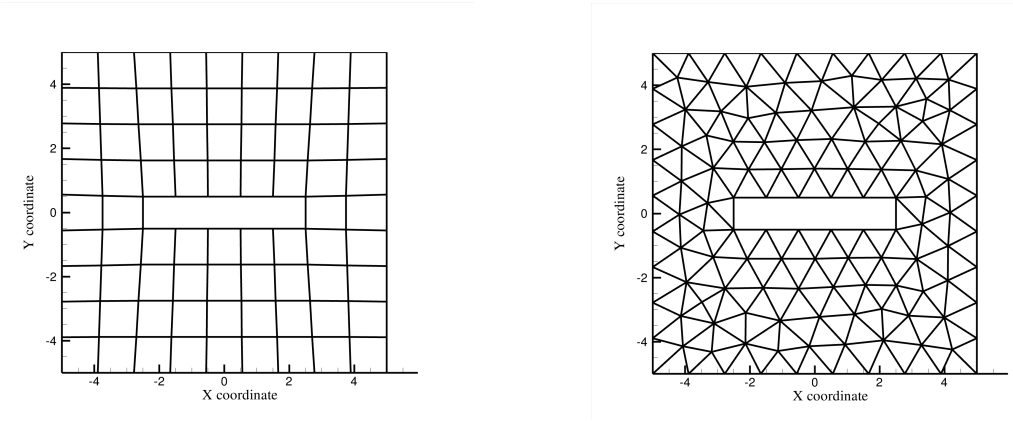

Figure 3.5: Structured (left) and unstructured (right) mesh around a simple geometry. From Bos (2010).

The numerical solution is very dependent on the interpolation of cell values over the cell faces. Therefore the quality of the mesh is important to guarantee the interpolation can be accurate. The cell non-orthogonality is defined by the angle between two mesh centres and the vector perpendicular to the cell face dividing the cells. When these vectors alight, the flux between the cells is directly pointed towards (from) the cell centre. High non-orthogonality leads to a large error in the truncation of the diffusive term.

The skewness is defined by the offset between the connecting line of cell centres, and the midpoint of the cell face. See figure 3.6, where m denotes the offset for the skewness. The skewness is important for the interpolation from the cell centre to the cell face.

H. B. Deng et al. (2013) gives an overview of several mesh methods that can be used in the numerical modelling of animals. The Immersed Boundary Method, Overset Grid Method and Body-conformal meshes are most popular in numerical flapping wing research.

3.4.1. Immersed Boundary Method

The IBM uses a Eulerian approach or the fluid, which means that a stationary grid is used to solve the Navier-Stokes equations. The force on the boundary is interpolated onto the Cartesian grid to account for the structure.

Figure 3.7 shows the basic principle of the IBM for a solid body and a membrane. The fluid mesh is composed of four different type of nodes: 'Fluid', 'Solid', 'Hybrid' and 'Ghost' nodes. The 'Solid nodes' are disregarded for the solution and on the 'Fluid nodes' the fluid is solved. The 'Hybrid nodes' are computed by averaging the solution from the Navier-Stokes equations and extrapolated flow variables from the 'Ghost nodes'.

Other researches where the IBM has been used are Yang et al. (2008), Vanella et al. (2008), Dai

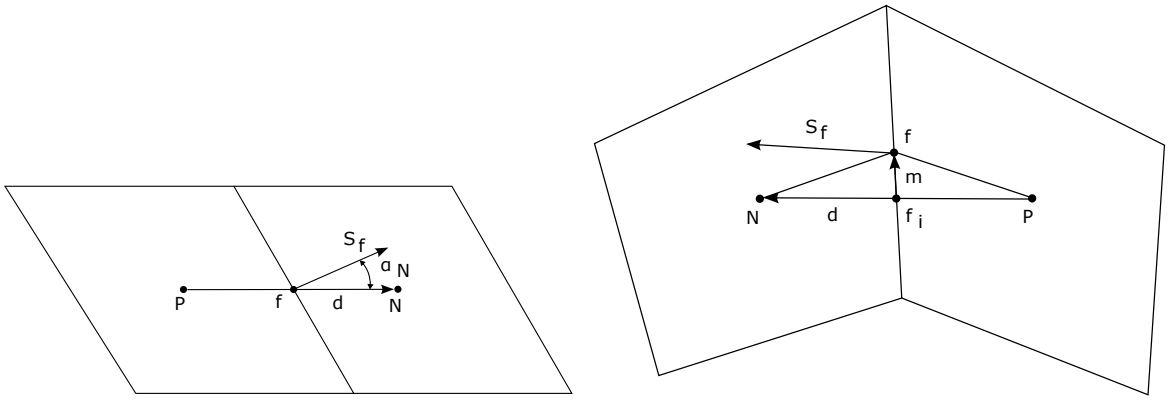

Figure 3.6: (Left) non-orthogonality between cells. (Right) Skewness between cells. From Jasak (1996).

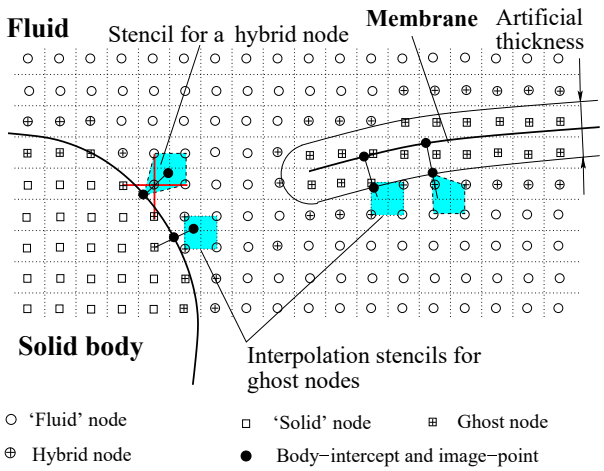

Figure 3.7: Representation of the Immersed Boundary Method on a 2D mesh. From Luo et al. (2010).

et al. (2012) and Shahzad et al. (2017). The Masters thesis by Noyon (2014) investigates the DelFLY wing using the IBM. The stationary grid gives the wing virtually unlimited space to move in the domain. Furthermore, the mesh does not deform, reducing one computational field with respect to the ALE approach. However, the wing does not have a layered mesh on the surface. In effect the boundary layer is not modelled in great detail, which is a disadvantage for this method compared to body-conformal grids.

3.4.2. Body-conformal Meshes

As the structure deforms and moves, the boundary for the fluid problem moves too. Therefore, the mesh must be adapted every timestep for the FSI problem. One option is to completely regenerate the mesh, but this is computationally very expensive. Furthermore, it requires interpolation of the data between every timestep, which causes loss of the physical conservation laws. Re-meshing of the entire domain can be used when boundary deformations are too big to create a deformed mesh. Y. H. Chen et al. (2017) used dynamic remeshing for the modelling of a flexible insect wing in counter-stroke, where very high deformations occurred

There exists a number of different mesh deformation techniques. A number of methods which can be applied to both structured and unstructured grids is listed in table 3.2. For structured meshes, the Transfinite Interpolation (TFI) is often used, for example in Du & Sun (2008). A similar approach with the Master-slave coupling was used by Aono et al. (2010). In the TFI method, the displacement of the edges and vertices of the blocks is used to deform the cells within. The movement of the edges and vertices are obtained either by the prescribed deformation on the boundary, or by interpolation by another method (for free block vertices). After the displacement of the block vertices and edges is known, the displacement is interpolated to the rest of the grid. The method is easy to implement and efficient.

Table 3.2: Deformation methods for structured and unstructured meshes

	Method	Computational effort
1	Master-Slave coupling	
2	Lineal springs	Heavy ($\mathcal{O}(N_{\text{grid}})$
3	Torsional springs	Heavy ($\mathcal{O}(2 \cdot N_{\text{grid}})$)
4	Semi-torsional springs	Heavy ($\mathcal{O}(N_{\text{grid}})$)
5	Least Squares	Very Heavy
6	Solid Body Elasticity	Very Heavy
7	Laplacian Smoothing	Heavy ($\mathcal{O}(N_{\text{grid}})$)
8	Biharmonic operator	Heavy ($\mathcal{O}(2 \cdot N_{\text{grid}})$)
9	Radial basis function interpolation	Medium ($\mathcal{O}(N_{\text{boundary}})$)

Methods 2 to 4 are the spring analogy methods, where a metric of the cell is given a spring which tries to the initial value. The lineal spring works as a normal spring between nodes, whereas the torsional spring acts to preserve the angle of a cell. For all these methods 'hanging nodes' have to be removed from the mesh. The spring analogy can be used to model rather small deformations, and the methods are computationally heavy, because a set of equations has to be solved for every mesh cell. Research in spring methods is found for example in the work from Felippa et al. (2001), where it is applied to solve the small deformations in flutter of a fighter aircraft.

Methods 5 and 6 are analogous in the type of formulation: both strive at minimizing a function for the entire mesh. The Least Squares function tries to preserve the angles of the mesh, while the Solid body elasticity method aims at minimizing the strain energy of the mesh. The grids of these two meshes are similar and of better quality compared to the spring analogy methods.

The Laplacian Smoothing and Biharmonic operator solve a set of partial differential equations applied to the nodes of the mesh. The drawback of the Laplacian smoothing is that it offers little flexibility in the boundary conditions, which leads to a system which can only cope with small deformations. The Biharmonic operator outperformes the Laplacian smoothing because it can cope with both Dirichlet and Neumann boundary conditions, but is similar to the spring analogy methods. Furthermore, it is even more heavy computationally compared to the Laplacian smoothing.

Radial basis function interpolation are generally used to transfer a function from one mesh to another, such as on the fluid-structure interface in the FSI problem. The pressure is transferred from the fluid to the structure, and the displacement is placed on the boundary of the aerodynamic mesh. When applied as a mesh deformation technique, the RBFs used to displace the fluid boundary mesh cells are also used to displace the other nodes in the fluid domain. In comparison with other dynamic mesh models, mesh deformation based on RBFs is capable of large deformations at a reasonable cost (Bos, 2010). Moreover, by utilizing a coarsening technique, only a subset of the boundary nodes is evaluated and the system of equations can be reduced (Gillebaart, 2011).

3.4.3. Overset Grid Method

The Overset Grid Method (OGM) makes use of multi-block grid on which the fluid solution is solved. The individual grids are chosen to facilitate each an own role. Common combinations in flapping wing aerodynamics are the combination of a refined grid which follows the wing movement and a Cartesian grid at the background large enough fill the entire domain.

In the case of a deforming wing, this method can be seen as a combination of the IBM and body-conformal mesh technique: the mesh around the wing deforms according to the wing, but is not bounded by the the outer boundary. On the boundary of the grid, the values are interpolated to the background Cartesian grid.

Figure 3.8 shows an example of the overset-grid method around a Hawkmoth body. For this grid, Nakata & Liu (2012) uses the overset-grid method, where one detailed mesh is formed around the insect wings, and the other is grown from the body. The latter mesh is stationary and contains the far field boundaries. The wing mesh provides the required refinement around the wings and deforms according to the wings motions.

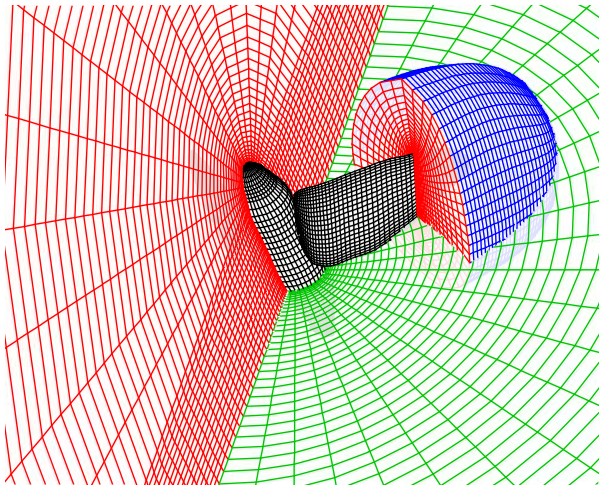

Figure 3.8: Wing-based grid and Cartesian grid around the Hawkmoth model. Adapted from Nakata & Liu (2012).

R. P. Malhan et al. (2013) use an overset-grid method with a body-fitted curvilinear wing meshed, which was combined with a Cartesian background mesh. Mayo (2014) took a similar approach, and Gordnier & Attar (2014) used a set of 7 overset meshes to create a computational grid around a

membrane wing. S. Deng et al. (2017) combined the overset grid with grid deformation based on RBFs for the body-conformal grid.

Taking this approach, the overset grid method offers a well resolved boundary layer on the wing, for a good quality background grid. Furthermore, grid deformation only has to be applied on the deforming and moving part of the grid.

3.5. Numerical Modelling

Chapter 2 has focussed on the aerodynamic and structural behaviour found in flexible flapping wings. This section focusses on a numerical implementation of a general FSI method which can be used to investigate flapping wing aerodynamics.

For strongly coupled systems, multiple iterations must be taken per timestep to reach an equilibrium in the boundary conditions, hence computationally FSI can be very heavy (Liu et al., 2017). It is therefore extremely important to design an efficient coupling approach, which does not increase the computational constraints orders of magnitude when compared to the single physics problem.

First a comparison of aerodynamic models given. Next, section 3.5.2 provides background on the available types of modelling of the structure. Finally, the coupling between both solvers is explained in section 3.5.3, in which the solvers are selected which are compatible with the demands. The solvers should be open-source and should be possible to exchange the boundary data in order to perform coupled simulations.

The fluid solver `OpenFOAM` is chosen as the most suitable candidate for the fluid dynamical side of the coupled simulation. However, in order to create the coupling, a general procedure has to be developed which provides communication with `OpenFOAM`. In section 4, the procedures of the OpenFOAM adapter are explained.

3.5.1. Computational Fluid dynamics

This section describes the basis for resolving the fluid field of the coupled FSI. The accuracy of the method is dependent on the amount of assumptions and models that are being used. In general, a higher accuracy is reached by resolving more features of the flow field, which in term increases the computational cost. There are various options to solve the flowfield.

- Panel methods
- Unsteady Vortex Lattice Method (UVLM).
- Navier-Stokes equations
- Lattice Boltzmann Equations (LBE)

In the current thesis, a high fidelity flow solver is required which can provide quantitative data about the flowfield. Furthermore, it has to be compatible with the computational method of choice. Simple solvers such as panel methods cannot provide the accuracy for the complicated aerodynamic phenomena that occur on flapping wings. The LBEs solves the flow field by modelling the interaction between particles. In terms of numerical modelling however, the Navier-Stokes equations are the logical choice since there is a broad background in these equations in terms of available methods. Looking at appendix A, it is found that the Navier-Stokes equations are by far the most used method to solve the flow field.

Fluid dynamical model parameters

Several modelling parameters can be distinguished which have a large influence on the solution. Some parameters which are of influence are explained here.

Compressibility Flapping wings in nature and on MAVs operate in the low Mach number regime. Therefore, any model which attempts to create a similar motion operates practically in incompressible flow. Therefore the incompressible Navier-Stokes equations can be adopted.

Some researches (R. P. Malhan et al., 2013; Mayo, 2014) make use of a compressible solver with low Mach preconditioning to solve the flow field. A possible effect of adding some compressibility to the flow is that it gives more stable solution for small timesteps. For incompressible flow, a small displacement error of the structure solver can cause a large velocity or acceleration error when the time-derivative is computed over a small timestep. An incompressible solver does not allow for density changes in the flow and as a result, very high pressures can occur due to the small displacement error. This type of instability especially occurs when the time step is taken low, and small displacements are perceived as a high boundary velocity.

Turbulence modelling Direct Numerical Simulation (DNS) is the most straightforward and accurate manner of applying the Navier-Stokes equations in case of turbulent flow. This method is however extremely expensive because it requires the grid to be fine enough to resolve all scales. The main application for DNS is for relative simple flow geometries which can be used as validation cases for lower fidelity models. The solver method is not feasible for the current work.

Large Eddy Simulation (LES) is less common in the field of flapping wing aerodynamics, but can equally be used. In this method the large turbulent scales are resolved while the smaller turbulent scales are captured in a sub-grid model, such as the Smagorinsky sub-grid model. Gordnier & Attar (2014) uses a 6^{th} order LES solver in combination with a high fidelity structural solver to solve the flow field around a flapping wing.

The well known unsteady RANS requires much less computational power compared to the methods above. In flapping wing aerodynamics it is by far the most popular method, as can be seen in appendix A. The Unsteady Reynolds Averaged Navier Stokes (URANS) method splits the Navier-Stokes equations in a mean and fluctuating part of the flowfield. The incompressible momentum equation (in Einstein notation) then becomes:

$$\frac{\partial \bar{u}_i}{\partial t} + \bar{u}_j \frac{\partial \bar{u}_i}{\partial x_j} = \bar{f}_i + \frac{\partial}{\partial x_j}\left[\frac{1}{\rho}\bar{p}\delta_{ij} + \nu\left(\frac{\partial \bar{u}_i}{\partial x_j} + \frac{\partial \bar{u}_j}{\partial x_i}\right) - \overline{u_i' u_j'}\right]. \tag{3.14}$$

The term $R_{ij} = \overline{u_i' u_j'}$ is the Reynolds stress tensor, which requires an additional model to be solved. Often used turbulent models are the k-ϵ or the k-ω model, which add two transport equations to the problem. For transitional Reynolds number, an additional transition modelling can be required, such as is done in the $\gamma - Re_\theta$ model. Much of the research to flapping wings aims at small insect wings at very low Reynolds numbers. At these low Reynolds numbers, the flow is completely laminar and no additional turbulence modelling is required, simplifying the set of equations.

ALE-equations The coupled problem will impose a finite displacement on the boundary surface. Several strategies were explained in chapter 3.4. Of these, the immersed boundary method features a Eulerian mesh, but both the overset and the body-conformal meshes feature a mesh movement. The Lagrangian component of the equations allows the mesh to follow the deforming structure. This additional Lagrangian term must be incorporated in the flow equations as an additional flux term, shown in 3.2.

3.5.2. Structural modelling of the wing

Similar to the computational modelling of the fluid structure, the structure of the wing can be modelled with various different models. In general, the numerical modelling of the structural part in the FSI simulation is a fraction of the time required for the fluid part. Therefore, the choice for a computationally cheap method is of lesser importance for this part.

Some of the methods that are used for FSI:

- Linear beam model
- Linear membrane model
- Hyper-elastic membrane model
- Finite element models.

Shyy et al. (2013) comments on the use of some of these models. The linear beam model is used extensively in the aeroelasticity community to study the dynamic structural response of the wing. The model is very simple, modelling the wing as a 1D entity. Linear membrane models are used to model the chordwise deflection using a membrane fixed on two sides, for example to model sails. For large deformations, non-linear effects arise which cannot be predicted by the linear membrane model. Other simplified models make use of different assumptions and feature other equations. Two models are explained in the next section.

The most used method in flapping wing research model some type of finite element. The structure is then solved using the Finite Element Method. Elements which are often used are membrane, shell or brick elements. Membrane and shell elements feature computational efficiency over brick elements, since they have less degrees of freedom. For the membrane the nodes do not rotate, since the element cannot transmit moments and out-of-plane loads.

Shell elements assume a thin structure and feature five Degrees of Freedom (DOF) rather than six. In the most general form, a shell element is a curved 2D structure, where the in-plane and out-of-plane displacements are coupled via the curvature of the shell. Both bending and membrane forces can be modelled with the shell element.

An example of the application of a simple FEM wing model is found in Masarati et al. (2011), where a the sheet is modelled by shell elements. Non-linear beam elements are used to model the stiff part of the wing. A more complicated wing of shell elements is used by Nakata & Liu (2012), see figure 3.9. Here, the non-uniform thickness of the real wing is modelled in the FEM model. The effect of the veins is captured in the non-uniform properties of the effective stiffness (*EI*) of the wing.

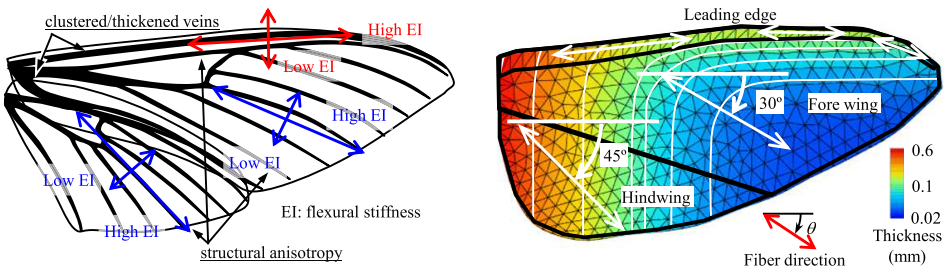

Fig. 4.

Figure 3.9: Realistic shell element representation of the Hawkmoth wing. Adapted from Nakata & Liu (2012).

3.5.3. Coupling methods

The basic theory behind the interaction of a fluid and a structure is rather straightforward, and is explained in section 3.2. Many researchers have developed their own routine, such as Wang et al. (2017) with `MATLAB`, or R. Malhan et al. (2012); R. P. Malhan et al. (2013); Mayo (2014) with a `Python` interface. Using code specifically written for the execution of processes is done by Luo et al. (2010); Dai et al. (2012), who use the MPI to communicate between the solvers. This technique is applied with minimal modifications to the existing solver software.

Some dedicated coupling methods are described in Bungartz et al. (2016). One of the standard tools is the MpCCI Coupling Environment. Another method is the ADVENTURE_Coupler (ADVanced ENgineering analysis Tool for Ultra large REal world), or EMPIRE (Enhanced Multi Physics Interface Research Engine). However, all these methods are based on the Client-server approach, which increases the required amount of data communication.

To utilize the computational power in an efficient way, point-to-point communication between solvers which permits communication between processes of the solvers is desired. OpenPALM (Open Projet d'Assimilation par Logiciel Multimethodes) and `preCICE` are dedicated coupling software packages which posses this property. These packages are built on the functionalities of the MPI. However, only the latter software has iterative methods implemented to solve the interface fixed-point equation. The advantages of `preCICE` come in the functionalities it brings within the code. In figure 3.10 some of the functionalities of `preCICE` are shown.

- The solver contains iterative methods to solve the interface fixed-point equation.
- Various data mapping methods are built in to work with non-matching grids on the interface.
- Communication between the processes of different solvers are permitted.

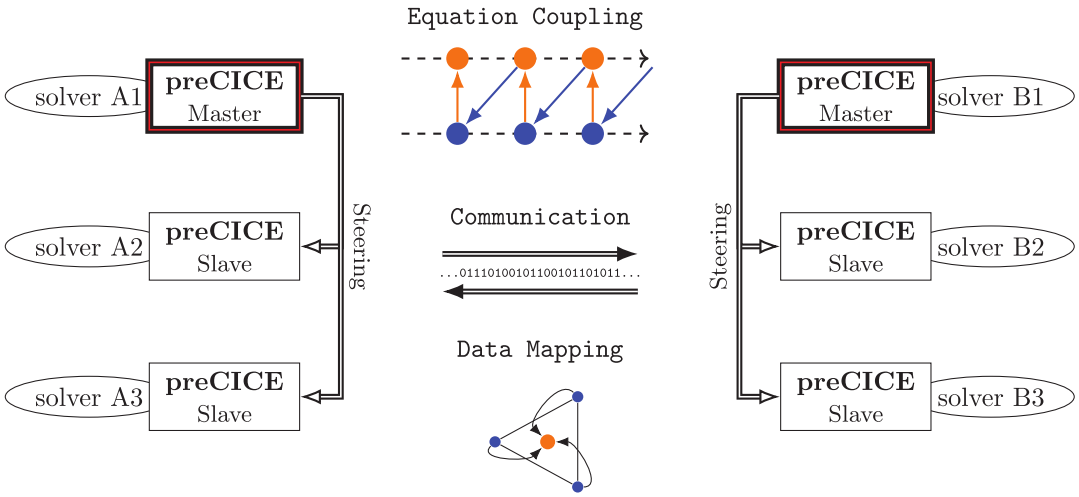

Figure 3.10: The features of the `preCICE` API. From Bungartz et al. (2016).

Adapters for `preCICE`

As mentioned, `preCICE` provides the coupling for multi-physics problems, and can assure efficient communication, data mapping and has solving iterating algorithms built in. Another advantage of the code is that several adapters for various structural and fluid dynamical codes are available. This facilitates easy coupling with limited work on the solvers which require coupling.

A version of `preCICE` is used in the framework for FSI applications called `FOAM-FSI`, developed by Blom (2017). This framework is based on the fluid capacities of the `foam-extend-3.2` and uses the coupling tools of `preCICE`. Unfortunately, this package is only compatible with the particular version of `OpenFOAM`, and is not in development any more.

In Chourdakis (2017a) the official adapter is described for Conjugate Heat Transfer (CHT), which is compatible with `OpenFOAM-4.0` and higher, and `openFOAM-1606` and higher. The CHT module has been developed and has been validated. The FSI part is further developed in the current work.

On the structural side, Rusch (2016) worked on the implementation FSI simulation with the fluid solver SU^2 and the structure solver `Calculix`. This FEM package is selected as the structural solver for the coupled simulation. The `Calculix-adapter` features an interface for both CHT and FSI.

3.6. Synthesis

This chapter gives an introduction to FSI and its numerical implementation. To solve the coupled system, either a monolithic or a partitioned approach can be taken. The latter is better applicable for this thesis, since it provides a more flexible architecture. In the partitioned approach the solvers are seen as a 'black box' to the coupling approach, where only the boundary conditions are exchanged. The partitioned approach can be split into the strongly and loosely coupled approach, also called implicit and explicit method in FSI literature. The implicit method is applicable to systems with a high level of interaction, where the convergence is reached every time-instance by iterating the solvers.

Different procedures exist to couple the fluid and structural solver. Simple methods, such as the CSS and CPS are only first order accurate in time. This means that the general system will be overall first order, no matter the order of the field solvers or the strong coupling. Improved schemes make use of different algorithms and can reach higher overall time-accuracy. Important for such schemes is that the fluid solver can perform sub-cycles, since the time-scale of the fluid solver is in general smaller than the structural time-scale.

Solving the strongly coupled system can be done iteratively using several approaches. Of these, choosing a sophisticated sub-relaxation with the Aitken method, or a Quasi-Newton method are the best options for a coupled FSI simulation. Using Multi-level meshes can help to accelerate the solution by enhancing the computational advantages of a coarse grid.

Three different mesh techniques are often encountered in FSI: the Immersed Boundary Method, body-conformal Meshes and Overset Grid Method. It is interesting to investigate the advantages and disadvantages of the latter method in the thesis.

Various numerical methods are available to solve the flow and structural domain. The methodology chosen in this thesis is to solve the flow field using the URANS, which is coupled to a FEM structural solver. In numerical flapping wing research this is the most popular approach as can be seen in A.

In terms of code, different programs are adopted with respect to the reference papers. The flow solver `OpenFOAM-1712` is chosen because it gives the user access to a large amount of solvers and utilities for incompressible flows. The program allows for overset grids, and has functions for grid deformation. Furthermore, various solvers are already defined in which the ALE Navier-Stokes equations are solved. Also rotational grid deformation is quite common, which will be required in this work.

For the structural solver, `Calculix` is chosen. This open-source structural solver can simulate non-linear structures with various type of elements, which allows it to represent the type of simple wing that is proposed in this thesis. Moreover, an adapter is available to couple the software to a flow model for FSI analysis.

It is the goal of this thesis to implement `OpenFOAM` and `Calculix` in a coupled FSI system. For that purpose, `preCICE` will be used. The adapter for `Calculix` already exists. The OpenFOAM adapter already supports coupled problems with conjugate heat transfer, and is extended in this work to solve FSI problems.

Chapter 4

Extension of the OpenFOAM Adapter

In the previous sections the necessary elements are explained that are required in a fluid-structure interaction problem. These elements are implemented in a generic method to create coupled simulations with OpenFOAM. Several objectives are defined to create a modular adapter which is easy in use. Following Chourdakis (2017a), the adapter should:

1. make no changes to the OpenFOAM source-code;
2. be solver-agnostic;
3. be loaded and configured at runtime;
4. support the full spectrum of preCICE features;
5. be compatible with multiple versions of OpenFOAM;

4.1. Adapter architecture

The OpenFOAM adapter is the result of multiple projects. First the CHT part was developed by Yau (2016) and Chourdakis (2017a) continued work to create a flexible architecture which is relatively easy to extend. In the latter work an overview is given of the adapter architecture. Note that this description is written for the adapter with only CHT capabilities.

The OpenFOAM adapter is implemented as an OpenFOAM function object. In this way, the adapter can be called at runtime, regardless of the used solver. The user only needs to include the preciceAdapterFunctionObject configuration in the controlDict file, as shown in listing 4.1. The included function must point to the OpenFOAM Adapter dynamic library.

```
functions
{
  #includeFunc <...>
  // The following lines include the OpenFOAM Adapter function object.
  preCICE_Adapter
  {
    type preciceAdapterFunctionObject;
    libs ("libpreciceAdapterFunctionObject.so");
  }
}
```

Listing 4.1: Inclusion of the OpenFOAM Adapter in the controlDict

The adapter is easy to integrate in the OpenFOAM environment. To build the adapter, a valid OpenFOAM distribution must be present on the machine, and shared library of the adapter is built in the user library folder of the distribution. This makes the adapter very portable for different platforms. Integration of the adapter in the controlDict makes coupling OpenFOAM with preCICE very straightforward.

4.1.1. Function objects

In OpenFOAM, a function object is primarily used as a post processing tool. During the initialization of the case, a list of all the function objects is created by the class `functionObjectList`. This list is then used to call the function objects by OpenFOAM routines at a set number of points which are defined in either the OpenFOAM time class or the mesh class:

1. At the beginning of the first iteration: `functionObjects().start()`
2. At every iteration of the time loop: `functionObjects().execute()`
3. After the last iteration of the time loop: `functionObjects().execute()` and `functionObjects().end()`
4. When the OpenFOAM time is adjusted `functionObjects().adjusttime step()`
5. When the OpenFOAM mesh is updated or moved: `functionObjects().updateMesh()` or `functionObjects().movePoints()`

Figure 4.1 shows the call flow of the main functions that are implemented in the function object class. The `start()` function is only ran at the first iteration of a new simulation, and here the information is read to create the function object. Similarly, the `end()` function is only called when the time loop has finished. The other functions can be adopted to inject information to the simulation from within the function object. `Write()` can be used to adapt the normal write behaviour by OpenFOAM, while `adjusttime step()` can overwrite the normal time step. Mesh changes trigger either `updateMesh()` or `movePoints()`. The latter function is used for mesh operations where the size of the mesh is not changed. The function `execute()` holds the main body of the function object, where in general the object of interest is computed.

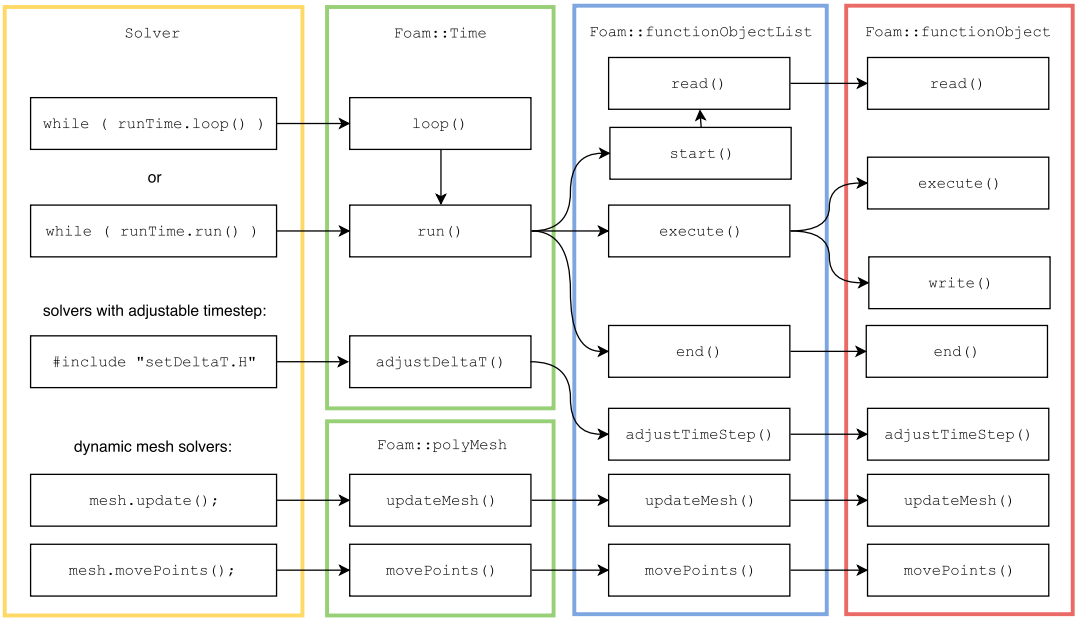

Figure 4.1: Call flow of the function object class in OpenFOAM. Adapted from Chourdakis (2017a).

4.1.2. preCICE interface

In the same way the OpenFOAM Adapter uses functions from the OpenFOAM namespace, some functions from preCICE are used as well. In particular, the functions which are used to couple the simulation are:

- `advance()`
- `isCouplingOngoing()`
- `isCouplingTimeStepComplete()`
- `isReadCheckpointRequired()`
- `isWriteCheckpointRequired()`
- `fulfilledReadCheckpoint()`
- `fulfilledWriteCheckpoint()`

The functions starting with 'is' return a boolean to check whether a certain action is required. The booleans `isCouplingTimeStepComplete()`, `isReadCheckpointRequired()` and `isWriteCheckpointRequired()` are only used for implicit coupling. These determine when a checkpoint needs to be written or read, and when the timestep has converged. The functions `fulfilledReadCheckpoint()` and `fulfilledWriteCheckpoint()` are implemented directly after a checkpoint is read or written, in order to assure that action is fulfilled prior to continuing the run.

The coupling between the solvers is performed by the `preCICE` function `advance()`. From the perspective of the fluid solver, here is where the coupling with the other participant(s) is performed. First the boundary data is mapped from the `OpenFOAM` side to the other participant(s), after which the respective solver(s) is/are ran. Next, the boundary data is mapped back to the OpenFOAM Adapter. For simulations with a serial coupling scheme this entails that the `OpenFOAM` solver is idle when the `advance()` function is called. Note that the `preCICE` `advance()` function performs many more actions required for the coupled simulation, however for the perspective of the fluid solver the mapping is the most relevant.

4.1.3. Flow of the adapter

The basis of the function object defined above is used to create a function object for the OpenFOAM Adapter. This function object is defined by the files `preciceAdapterFunctionObject.C` and `preciceAdapterFunctionObject.H` which merely provide wrappers for the rest of the adapter code. The functions `read()`, `adjustTimeStep()`, and `execute()` are actually used, as can be seen in figure 4.2. The `end()` is an empty function but can throw a warning if the `OpenFOAM` simulation finishes before the coupling is complete.

When coupling is going on, moving the points and updating the mesh does not require intervention of the adapter. Therefore the adapter does not possess functions called `updateMesh()` or `movePoints()`. The mesh deformation is performed exactly as it would be performed without calling the function object. In implicitly coupled simulations however, sub-iterations are required in which the mesh position has to be reverted to the previous time step. Therefore the adapter does call the `OpenFOAM` native function `fvMesh::movePoints()`.

The `execute()` function is called during the coupling and in this function the majority of the calls to other functions is implemented. In appendix B, the flow chart of this function is given.

4.1.4. Configuration of the coupled interface

To initialize the OpenFOAM Adapter, the function `configure()` is called. Here the OpenFOAM Adapter reads the configuration files which must be provided for the simulation. The configuration files are written in `YAML` format and the file is called `precice-adapter-config.yml`. This file specifies the interface and the data that is exchanged. Furthermore, adapter specific settings are defined in this file.

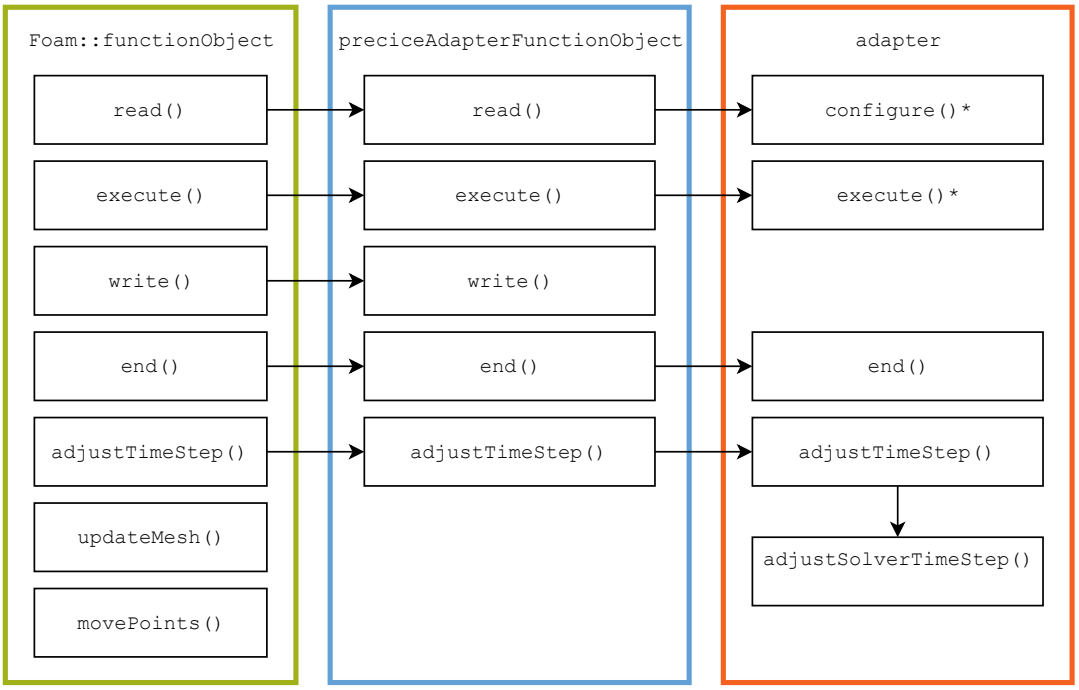

Figure 4.2: Call flow of the OpenFOAM Adapter function object object. The `execute()` and `configure()` functions are not complete here.

Based on the initialization, the `configure()` creates the coupling interfaces and initializes `preCICE`. If implicit coupling is selected, the checkpointing is set up in for objects that need to be checkpointed.

4.2. Exchange of boundary data

The `preCICE` library allows the exchange of both conservative and consistent quantities on the coupling boundary. Coupling of the quantities required for FSI was added in the scope of this work.

4.2.1. Fluid to structure

The stress on the boundary can be derived using the Cauchy stress tensor. (Holzmann, 2017). This formulation splits the stress tensor of the fluid in the deviatoric (dev) and hydrostatic (hyd) part. By definition, any two-rank tensor can be split in a hydrostatic and deviatoric part. For an incompressible flow the hydrostatic part of the Cauchy stress tensor is only determined by the pressure, as the viscous stress tensor does not include any hydrostatic parts:

$$\boldsymbol{\sigma}_{\text{hyd}} = \frac{1}{3}\text{tr}(\boldsymbol{\sigma})\boldsymbol{I} = -p\boldsymbol{I}, \tag{4.1}$$

$$\begin{aligned} \boldsymbol{\sigma} &= \boldsymbol{\sigma}_{\text{hyd}} + \boldsymbol{\sigma}_{\text{dev}} \\ &= -p\boldsymbol{I} + \boldsymbol{\tau}. \end{aligned} \tag{4.2}$$

where $\boldsymbol{\tau}$ represents the deviatoric parts of the viscous stress tensor. For a Newtonian fluid, the viscous stress tensor is linearly dependent on the strain rate tensor $\boldsymbol{E}$. The hydrostatic part is determined by the bulk viscosity times the divergence of the velocity field, which equates to zero for an incompressible flow. This underlines that the hydrostatic quantity in equation 4.1 is determined only by the pressure.

The strain rate tensor itself is the symmetric part of the velocity gradient, which governs the deformation of the fluid elements. The strain rate tensor can then be split into a hydrostatic and deviatoric part. The deviatoric part of the strain rate tensor is then used to compute the viscous stress tensor:

$$\boldsymbol{E} = \frac{1}{2}\left(\boldsymbol{\nabla u} + (\boldsymbol{\nabla u})^T\right), \tag{4.3}$$

$$\begin{aligned} \boldsymbol{\tau}_{\text{dev}} &= \boldsymbol{\tau} - \frac{1}{3}tr(\boldsymbol{\tau})\boldsymbol{I} \\ &= 2\mu\left(\boldsymbol{E} - \frac{1}{3}\text{tr}(\boldsymbol{E})\boldsymbol{I}\right) \\ &= \rho\nu\left(\boldsymbol{\nabla u} + (\boldsymbol{\nabla u})^T\right)_{\text{dev}} \end{aligned} \tag{4.4}$$

In the OpenFOAM Adapter, the Cauchy stress tensor is used to extract the load at the boundary. The load at the boundary is a vector which is defined at all the boundary faces at the interface Γ. The surface stress is then defined by the negative of the inner product of the Cauchy stress tensor and face normal vectors. The sign change is necessary because the reaction of the fluid on the boundary is considered, and not the fluid internal stress:

$$\boldsymbol{\sigma}_\Gamma = p\boldsymbol{n} - \rho\nu\left(\boldsymbol{E} - \frac{1}{3}\text{tr}(\boldsymbol{E})\boldsymbol{I}\right)\cdot\boldsymbol{n}. \tag{4.5}$$

Note that $\boldsymbol{\sigma}_\Gamma$ denotes the stress at the boundary, and therefore is a rank 1 tensor. The surface stress is a consistent quantity with units [Nm^{-2}].

A similar expression can be derived for the force on the boundary. For this quantity, the Cauchy stress tensor must be multiplied by the face normal vector and face area. The force is a conservative property and has units [N]:

$$\boldsymbol{F}_\Gamma = p\boldsymbol{S} - \rho\nu\left(\boldsymbol{E} - \frac{1}{3}\text{tr}(\boldsymbol{E})\boldsymbol{I}\right)\cdot\boldsymbol{S}. \tag{4.6}$$

4.2.2. Structure to Fluid

Various options exist to map the boundary data from the structure to the fluid which all aim at deforming the shape of the fluid boundary to follow the structural deformation. The methods which are currently implemented in the OpenFOAM adapter are based on the displacement of the structure.

The solvers in OpenFOAM which work with a dynamic mesh create fields for both the cell- and the point displacement. Since the point displacement field is specified on all points of the mesh including the coupling boundary Γ, this field is suitable to apply the boundary deformation. The Displacement class collects the displacement from the boundary and assigns this to the pointDisplacement boundary field.

A similar approach can be taken if the structural solver maps the relative displacement for every coupling step. In this case, the class DisplacementDelta maps the relative displacement incremental to the pointDisplacement boundary.

4.3. Implicit coupling and checkpointing

Implicitly coupled simulations make use of multiple sub-iterations per time step. The `preCICE` library performs a check whether a time step is completed by applying a convergence criterion on one or both the exchanged boundary data. When convergence is not reached, the simulation time should be reverted and the time step is started over.

4.3.1. Time checkpointing

Prior to every new time step, the data from the current time step is saved in a checkpoint. The time at which this takes place is stored by the function `storeCheckpointTime()`. Also the index of the current time step is saved by the function.

After the first sub-iteration, the time in `OpenFOAM` is reset by the function `reloadCheckpointTime()`, which resets both the time and the time index.

4.3.2. Field checkpointing

The fluid solver must start a new sub-iteration with exactly the same initial conditions, therefore all the fields defined in `OpenFOAM` must be reverted to their previous value. In appendix B, an example is shown of how the mesh updating is performed. Since `OpenFOAM` solves the fluid equations using a finite volume, the various physical properties are discretised to a field. Different fields exist, depending on the type of variable and the location where they reside.

The type of the variable is dependent on its tensor rank. Properties such as pressure and temperature are rank 0 tensors, and are therefore scalars. Rank 1 properties, such as velocity are vectors and rank 2 tensors are referred to as tensors. The location of the properties can either be on the cell centres, the cell faces centres or on the mesh points. In `OpenFOAM` syntax these are respectively volume (vol-), surface (surface-) and point (point-) properties.

Next to the field at the current time step (t^n), `OpenFOAM` holds references to the values of several fields at t^{n-1}. Dependent on the time integration scheme also the fields at t^{n-2} are stored. These fields can be accessed by the pointers `<field>.oldTime()` and `<field>.oldTime().oldTime()`. The old fields are used for time integration.

The type of field of a certain property is then the combination of the rank and/or type and the location of the property by the following naming configuration: `<location><Type><Field>`. Hence, the velocity and velocity flux are respectively a `volVectorField` and `surfaceScalarField` (because the orientation of the flux is determined by the cell face normal vector). Dependent on the flow configuration, different types of fields exist. The most common fields are the `volScalarField` and `volVectorField`, while the different types of tensorfields are hardly used.

For checkpointing the different `OpenFOAM` fields, the function `setupCheckpointing()` is used. This function lists all objects which are defined on the `OpenFOAM` mesh, after which the fields are added to the checkpointed properties. Prior to a new time step the function `writeCheckpoint()` iterates over all the mesh elements and stores a copy of the field per field type.

When the field should be reverted during sub-iterating, the function `readCheckpoint()` is called. This function assigns the pointer to the stored copy. Furthermore, the old fields have to be reassigned since they are not updated when only the pointer to the current time is updated. Figure 4.3 gives an overview on how the reading of a checkpoint is handled.

4.3.3. Mesh checkpointing

In the previous section the checkpointing of the fields is described. The mesh has to be checkpointed in a similar manner, however this is significantly more complicated because of the way `OpenFOAM` handles the mesh and the mesh deformation.

For the fluid-structure interaction method considered in this thesis a dynamic mesh is used. This type of mesh in `OpenFOAM` inherits the various functions from the general finite volume mesh

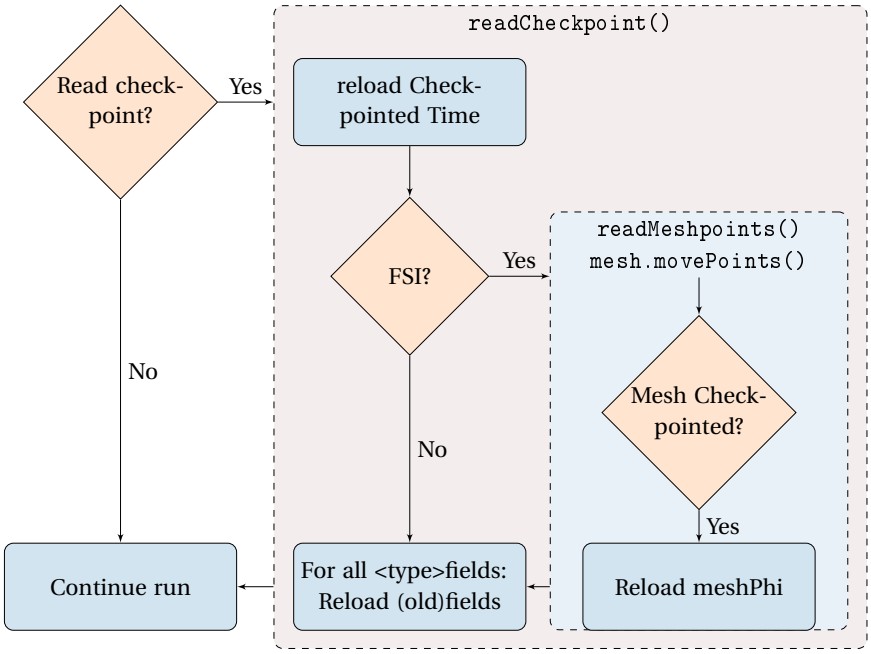

Figure 4.3: Flow of the checkpointing procedure

(`fvMesh`), and adds extra utilities for the dynamic mesh part. During runtime, the dynamic mesh is updated by the solver by calling the function `fvMesh.update()`. In term this function causes the points of the mesh to move and all other fields will be adjusted accordingly.

The mesh hold a number of fields which pertain to the mesh only, and are not recognised by the field checkpointing described in the previous section. The different mesh fields are:

Table 4.1: `OpenFOAM` mesh fields

Field type	Name	description
`pointField`	points	Position of mesh points
`pointField`	oldPoints	Position of old mesh points
`surfaceScalarField`	meshPhi	Mesh flux by mesh movement
`volScalarField::internal`	V	Cell volume
`volScalarField::internal`	V0	Old cell volume
`volScalarField::internal`	V00	Old-old cell volume
`volVectorField`	C	Cell centre
`surfaceVectorField`	Cf	Face centre
`surfaceVectorField`	Sf	Surface vector
`surfaceScalarField`	magSf	Face magnitude

The checkpointing of the mesh requires careful consideration of the procedures in which `OpenFOAM` handles the dynamic mesh. The standard `OpenFOAM` solvers with a dynamic mesh all feature the function call `mesh.update()`, which in terms calls the function `fvMesh::movePoints()`. In the latter function, the most important part of the manipulation is performed.

The first step is to store the old volumes by the function `storeOldVols`. The old volumes of the mesh are utilized in the time integration schemes, see equation 3.2. An internal index keeps track at which time index the old volumes are written to avoid that the function `storeOldVols` is executed multiple times for a time step. Therefore, storing the volumes to the old volumes is performed if and

only if the global index of the time step is larger than the internal index. As soon as the old volumes are updated for a certain time step, the internal index is set to the current time index. This means that during every sub-iteration, the old cell volumes are not changed by any function.

Next, the function `polyMesh::movePoints()` is called which in term calls the function `primitiveMesh::movePoints()`. This actually moves the points of the mesh and creates a temporary field with the swept volume of the mesh faces. This fields leads to the flux of the mesh faces, which is called `meshPhi`. After the mesh flux is computed, the cell centres, face centres, surface vector, surface magnitude and current volume are updated by the function `fvMesh::updateGeomNotOldVol()`. These fields are not dependent on the time derivative of the mesh, but represent merely a mesh state at some time. Therefore, these fields do not possess references to their old times.

Resetting the mesh to the previous time step is performed by calling the function `movePoints()` with the checkpointed points as an argument. The time-independent quantities are then defined according to what would be expected, however the mesh flux is dependent on the mesh movement and the direction of the mesh movement. Therefore, the mesh flux must be saved as any `surfaceScalarField`, and be read when the mesh is reverted to the previous position.

As a minor complication, the mesh flux object is only created when the mesh is moving. This is checked by the Boolean `mesh.moving()`. At the start of many simulations, the mesh is not moving, therefore the mesh flux is only created after the first coupling step, when there is a finite mesh movement. To add the mesh flux to the checkpointed fields, the function `setupMeshCheckpointing` is called the first time the mesh is moving. In figure 4.3 it can be seen that an extra step is required to validate whether the mesh fields exists in the checkpointed fields.

4.4. Synthesis

The fluid structure interaction simulations in this thesis are performed using OpenFOAM and CalculiX for respectively the fluid and structural solver. The coupling is performed by the multi-physics library preCICE. Communication between preCICE and OpenFOAM is performed using the OpenFOAM adapter, which has been developed by Chourdakis (2017a) for conjugate heat transfer. The chapter above treats the extension of the adapter to support FSI simulations.

The OpenFOAM adapter is a dynamic library which is built as a OpenFOAM function object. In this way no changes have to be made to the OpenFOAM source code. The function object is called at various points in the simulation which allows for the OpenFOAM adapter to inject data to and read data from the fluid simulation. The main function used by the OpenFOAM adapter is the `execute()` function in which the coupling procedure is performed.

For the coupled FSI simulation several adaptations were made to the adapter. Firstly, the `Force` class is created which maps the combined pressure and viscous forces to the structure. The structural deformation is mapped back using the `Displacement` class, in which the mesh is deformed. All FSI simulations performed in this work are implicit simulations, which use multiple subiterations per time step. For any time step the OpenFOAM adapter must ensure that the state of the fluid at the start of every subiteration is the same. Therefore, the time and fluid fields and mesh fields are saved in buffers by the function `writeCheckpoint()`. The function `readCheckpoint()` consequently assigns the buffers to the OpenFOAM fields when a new subiteration must be performed.

For the field checkpointing information on previous time steps is used in the time derivative. Therefore the checkpointing includes these fields in the buffers. For the mesh, the location of the points and the mesh flux are checkpointed. The mesh flux field is created when the mesh starts moving, thus this field can not be included in the list of checkpointed properties at the start of the simulation. Therefore an extra check is implemented in the coupling procedure which adds the mesh flux as soon as the field is created.

Chapter 5

Validation of the coupled model

In this chapter the steps are described that are taken during the validation of various cases. The goal is to validate the coupled simulation with a fluid and a structural member, using a typical FSI benchmarking case. Blom (2017) gives an overview of several cases that can be used for the validation of FSI solvers.

The main case which will be used for the validation is the cylinder with a flap. This case by Turek & Hron (2006) is a typical numerical benchmark for FSI solvers. The laminar flow model exhibits stationary or unsteady behaviour, depending on the Reynolds number. The high fluid density and viscosity combined with a low structural stiffness create a strongly coupled system. The cylinder with a flap case will be the basis for further validation cases which are adopted to characterize the FSI method.

The fully coupled FSI simulation entails a large number of parameters, and inaccuracies are often hard to track down. Therefore the simulation is broken down to the basic building blocks, to verify whether these models represent their respective part of the coupled simulation. The efficiency and accuracy of the coupled simulation is dependent on the performance of all separate parts.

First the individual fluid and structural solvers are tested: The fluid simulation is validated in section 5.2 using a similar the "flow around a cylinder" case. Section 5.3 treats the validation of the flap structure used in the FSI simulation. A gravitational load is applied for which the flap response is well documented. For both models a mesh analysis is performed to find a mesh which is computationally feasible and provides sufficient accuracy.

The FSI procedure is dependent on the correct mapping of the displacement and force. To assure that these properties are indeed transferred correctly, two unidirectional coupled cases are evaluated. One with only force coupling and the other with only displacement coupling. Sections 5.4 and 5.5 describe these cases. Furthermore, the mesh deformation influences the fluid behaviour, which could only be treated by creating an extremely weakly coupled case. This is explained in section 5.6

Finally, the coupled simulation described above is treated in section 5.7. The strongly coupled cylinder with flap is well documented and serves as a good comparison for the obtained results. One case with a steady state solution and two cases with unsteady periodic solutions are evaluated.

5.1. Cylinder with a Flap benchmarking case

The domain can be seen in figure 5.1 (Turek & Hron, 2006). The fluid domain has a height and length of respectively 0.41m and 2.5m. On the left side the fluid enters the domain and it leaves on the right side. The cylinder has a radius of r = 0.05m and is located just off the centre of the channel at (0.2, 0.2)m. The small offset is created to assure the domain is slightly asymmetrical. For the unsteady cases this entails that the start of the vortex shedding is more predictable.

Three different inflow speeds are tested which relate to the cylinder-diameter based Reynolds number of 20, 100 and 200. These are called respectively FSI1, FSI2 and FSI3. While the first one

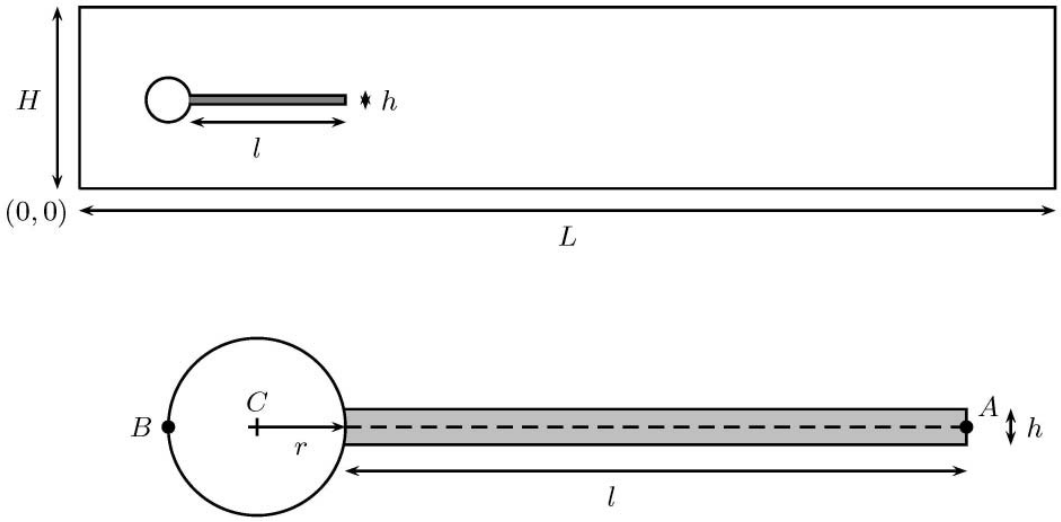

Figure 5.1: Domain for the 2D FSI validation case. The domain has length and height $L = 2.5m, H = 0.41m$. The cylinder centre is located at (0.2, 0.2) and the cylinder has radius $r = 0.05$m. The flexible flap has length and width $l = 0.35m, h = 0.02m$. Adapted from Turek & Hron (2006).

creates a steady wake behind the body, shedding of vortices is found for the higher Reynolds numbers. The flow is completely laminar for the three cases, which facilitates use of the URANS equations without further turbulence modelling. On the benchmarking suite data is available for several quantities such as the force history, flap deflection and the pressure difference over the cylinder (FeatFlow, 2018).

Table 5.1 gives the fluid and structural properties which are used in the different simulations. Two ratios are defined to characterise the relative effect of inertial, fluid dynamical and elastic forces. The density ratio defines the relative importance of the inertial forces over the fluid dynamical forces. The stress ratio is defined as:

$$Ae = \frac{E}{\rho_f \overline{U}^2}, \tag{5.1}$$

which is a measure for the relative importance of elastic and fluid forces. Between the FSI2 and FSI3 it is preserved.

The cylinder with a flap has a prescribed velocity inflow at the inlet. Here, a parabolic inflow profile is specified which is ramped up over a span of two seconds, see equation 5.2. The ramped profile creates a more stable start up of the fluid-structure interaction. The outlet has a zero gradient specified for the velocity. The top, bottom and cylinder with flap are walls with the non-slip condition. The pressure is defined at the outlet, where it is set to zero. Everywhere else, a zero gradient is specified.

$$\begin{aligned} v^f(y) &= \left(1.5\overline{U}\frac{4y(h-y)}{h^2}\right), \\ u(t,0,y) &= \begin{cases} \left(\frac{1-cos\left(\frac{\pi}{w}t\right)}{2}v^f, 0\right) & \text{if } t < 2\text{s} \\ \left(v^f, 0\right) & \text{if } t \geq 2\text{s} \end{cases}. \end{aligned} \tag{5.2}$$

5.2. Fluid dynamical validation

The fluid model is solved using the laminar URANS equations. To validate the accuracy of the solver, the "flow around a cylinder" case is adopted which is very similar to the cylinder with a flap case.

Table 5.1: Fluid and Structure parameters for the three different FSI benchmarking cases.

		FSI1	FSI2	FSI3
Fluid				
Density	ρ_f [kg m^{-3}]	1,000	1,000	1,000
Viscosity	ν_f [m^{2}s^{-1}]	10^{-3}	10^{-3}	10^{-3}
Mean velocity	$\overline{U}$[m s^{-1}]	0.2	1	2
Reynolds number	Re[-]	20	100	200
Structure				
Density	ρ_s [kg m^{-3}]	1,000	10,000	1,000
Young's modulus	E [kg m^{-1}s^{-2}]	$1.4 \cdot 10^6$	$1.4 \cdot 10^6$	$5.6 \cdot 10^6$
Poisson ratio	ν[−]	0.4	0.4	0.4
Ratios				
Density ratio	ρ_s/ρ_f [-]	1	10	1
Stress ratio	Ae [-]	$3.5 \cdot 10^4$	$1.4 \cdot 10^3$	$1.4 \cdot 10^3$

Moreover, better quality reference data is available when compared to the cylinder with flap. The cylinder test case is a standard test problem to assess the accuracy and performance of numerical methods. The benchmarking suite is described by Feng et al. (2005). See figure 5.2 for the geometry of the domain.

5.2.1. Test case

In this suite the inflow condition is defined at the left part of the domain, and different inflow speeds are tested. This corresponds to a cylinder Reynolds number of 20 and 100. Because of the low Reynolds number the URANS equations can be solved in laminar mode, where the Reynolds stress tensor is taken zero. In the first case a stationary flow develops, while a von Kármán street develops behind the cylinder for the case with $Re = 100$. This validation procedure evaluates unsteady cases with vortex shedding.

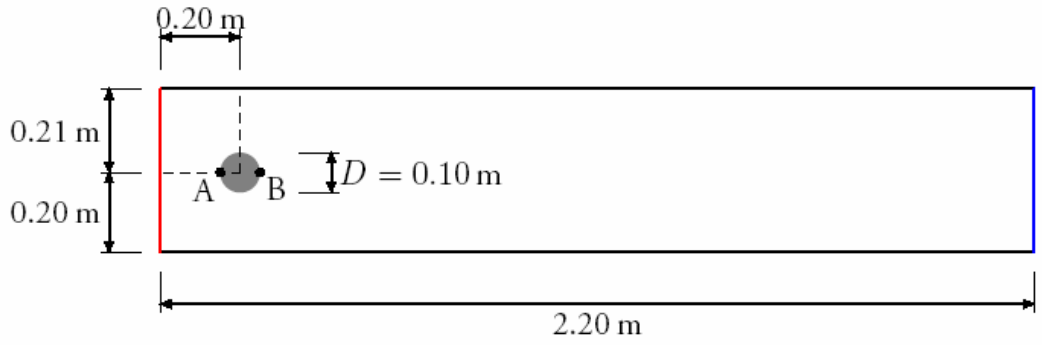

Figure 5.2: The geometry for the 2D benchmark case for the flow solver. From Feng et al. (2005).

The inflow condition is defined by the parabola:

$$u(0, y) = \left(\frac{4\overline{U} y(h-y)}{h^2}, 0 \right) \tag{5.3}$$

where h is the height of the domain and $\overline{U} = 1.5 \mathrm{m s}^{-1}$ to meet the Reynolds number of 100. The cylinder, top and bottom wall have a no-slip condition. Note that the boundary conditions are

identical to the FSI2 case for the coupled simulations, without the ramp up of the velocity.

The validation data is provided by FeatFlow (2018) for a range of refinements. The most refined reference case is displayed in figure 5.3, the mesh is made up of 133,120 elements and has 667,264 DOFs. The lift coefficient oscillates around an average value of just below zero as a consequence of the small asymmetry of the domain. The drag profile displays a oscillation with twice the frequency of lift profile.

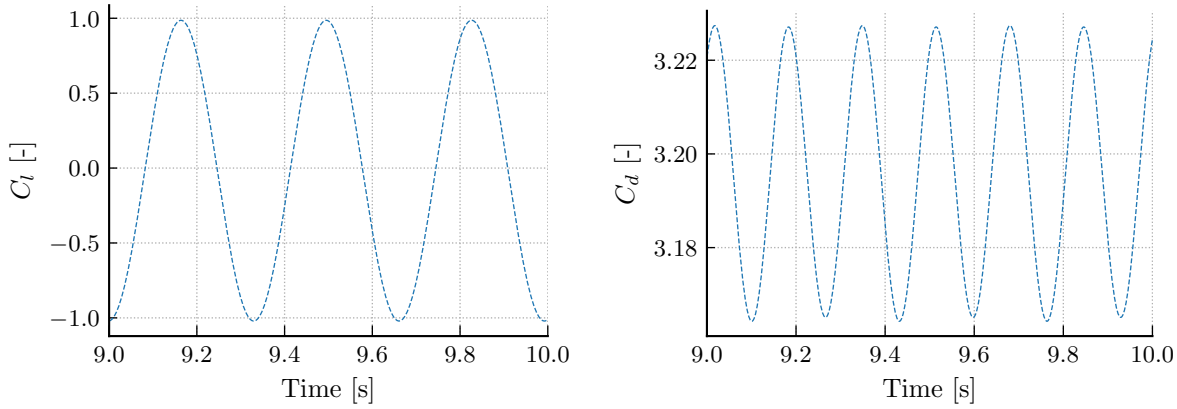

Figure 5.3: The reference (left) lift coefficient and (right) drag coefficient.

After 9s the vortex shedding has developed to periodic behaviour. The frequency of the oscillating flow behind a cylinder can be characterised by the Strouhal number. For Reynolds numbers ranging from 10^2 to 10^5 the Strouhal number is approximately 0.2 (White, 2005).This leads to the following relation with respect to the frequency:

$$f = \frac{StU}{D} = \frac{0.2 \cdot 1.5}{0.1} = 3\text{Hz}, \tag{5.4}$$

which coincides well with the frequency of 3.0189Hz found in the simulation. Note that the maximum velocity from the parabolic inflow profile is taken, since the cylinder is in the centre of the domain.

5.2.2. Discretisation and schemes

By comparing the results listed above to the benchmark values, the accuracy and efficiency of the solver can be distinguished. Next a grid sensitivity study can be performed using this domain. Also the influence of a dynamic mesh and an overset mesh is tested since these are both used for FSI applications.

The solution depends on the type of discretisation and handling of the discretised equations. The second order backwards differencing scheme is used for the time discretisation. This is an implicit scheme which uses information from the two previous timesteps. For a fixed timestep this leads to the following temporal discretisation for a variable ϕ:

$$\frac{\partial \phi}{\partial t} = \frac{\frac{3}{2}\phi^N - 2\phi^{N-1} + \frac{1}{2}\phi^{N-2}}{\Delta t}. \tag{5.5}$$

The spacial discretisation uses other schemes which are related to the type of tensor operation. For the gradient, divergence and laplacian parts of the flow equations different schemes must be provided. Where possible, second order schemes are chosen. The divergence of the velocity vector is computed using the second order linear scheme. Compared to the first order upwind scheme it is more accurate but more prone to instability.

The flow equations are solved using the merged PISO-SIMPLE algorithm, known as the PIMPLE algorithm (Holzmann, 2017). The PIMPLE algorithm combines the unsteady nature of the PISO algorithm with features from the SIMPLE algorithm, such as increased timesteps and better solution control. The actual computation of the new velocity field and pressure is performed by the segregated PISO algorithm. The pressure correction can be applied multiple times in order to allow for larger Courant-Friedrichs-Lewy (CFL)-numbers. For the current simulations two pressure corrections are applied. During every timestep the SIMPLE part of the merged algorithm tries to find the instantaneous field by performing a number of outer correctors. For all runs in table 5.2 maximum 50 outer correctors are applied. A convergence criterion is set for the velocity and pressure field which exits the pimple loop when convergence is reached. The SIMPLE (and therefore PIMPLE) algorithm is based on an inconsistent form of the Navier-Stokes equations because it misses a pressure term. The term is incorporated by selecting the consistent version of the algorithm. By default the solver uses only the PISO method, so the influence of adding PIMPLE controls is treated separately.

Mesh creation for the cylinder case is performed by the OpenFOAM native tools blockMesh for the background mesh and snappyHexMesh for the cylinder. The region around the cylinder is refined by a factor 2 with respect to the background mesh to capture the details of the flow around the cylinder in more detail. Table 5.2 gives an overview of the different mesh refinements that are used.

Table 5.2: The different runs performed to test for a range of parameters.

Testcase	Number of mesh cells	Runtime for 1s on two cores [s]
Coarse	21,170	381
Medium	34,542	766
Normal	53,916	1,269
Fine	74,228	2,974
Very Fine	128,465	43,824
Medium in PISO mode	34,542	299
Medium with dynamic mesh	34,542	1,935
Fine with overset mesh	62,400+ 12,720	47,403

5.2.3. Mesh sensitivity

The influence of the mesh refinement is shown in figure 5.4, where five meshes with increased refinement are compared to the reference solution. For the mesh properties see table 5.2. A slight phase change was corrected to overlap the oscillating signals by overlapping the first maximum in the time window.

The difference in lift (ΔC_l) between the different meshes and the reference solution is shown in the top left figure. The mean value of the lift is insensitive to the reference solution. The amplitude is slightly higher than the reference solution but the average lift is predicted accurately. The relative accuracy is shown in figure 5.5 (top left). For the finest mesh both the amplitude and the mean lift value are within 2% of the reference value.

The drag coefficient increases with refinement. The average drag reaches a value higher than the reference solution for the finest mesh tested. The amplitude increases likewise. The relative accuracy is shown in figure 5.5 (top right). For the finest mesh the mean drag value converges very close to the reference value, until 0.29% of the reference value. The amplitude grows until a value 3.46% larger than the reference solution.

The pressure curve in figure 5.4 shows more difference between the reference solution and the testcases. The reference solution shows that there is a slight asymmetry in the domain, since the peaks in pressure are not the same height. This asymmetry is much clearer in the runcases, indicat-

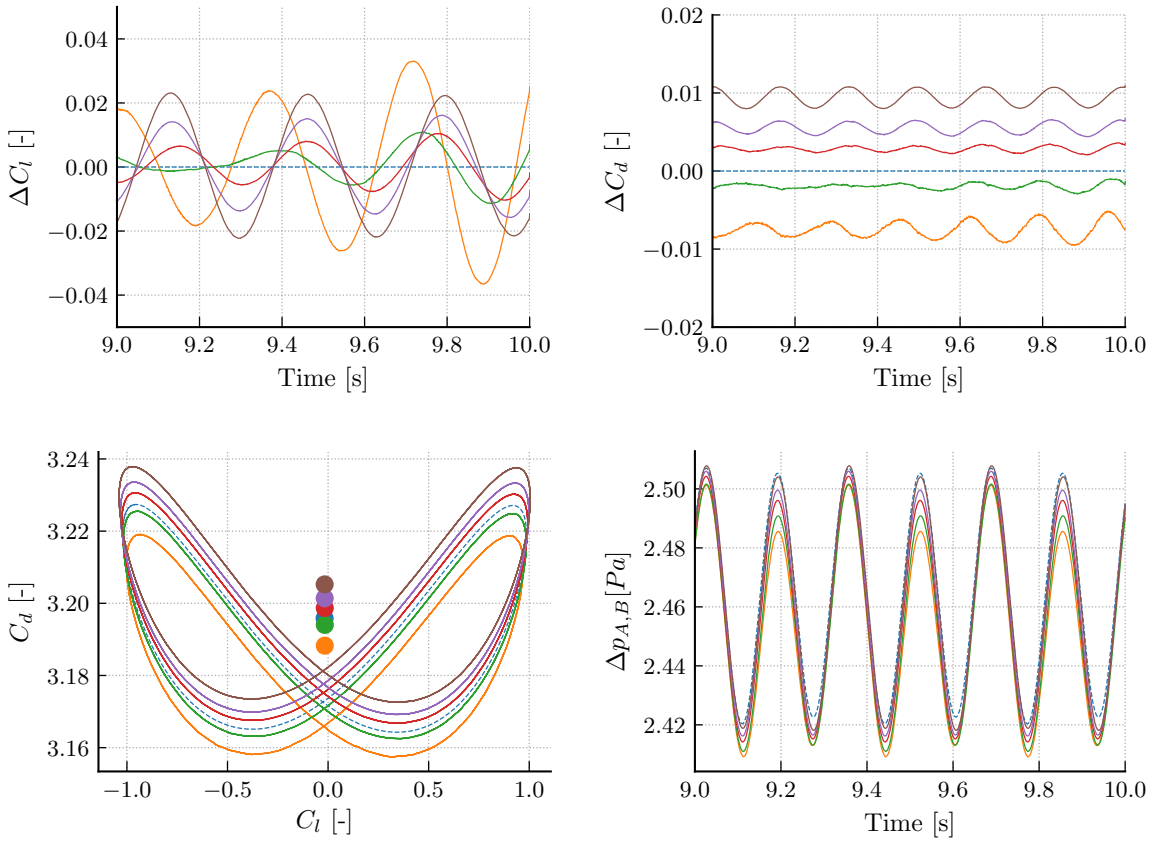

Figure 5.4: Top: The phase corrected difference in lift and drag between the reference case and the different meshes. Bottom-left: the lift-drag curve including the average value. Bottom-right: The pressure difference between point A and B. - - : Reference —Coarse, —Medium, —Normal, —Fine, —Very Fine.

ing that the simulation is not very accurate in representing the dynamic behaviour of the pressure. The pressure prediction is far more accurate for the finest mesh compared to the coarse cases. This is reflected too in figure 5.5 (bottom right). Here the pressure amplitude shows the large discrepancy, but the average value converged very close to the reference solution.

The shedding of the vortices determines the unsteadiness of the flow. The frequency of this shedding is compared to the reference solution in figure 5.5 (bottom left). Apart from one outlier, the frequency of the shedding shows a converging behaviour, and reaches values very close to the reference solution, up to 0.02% difference.

Table 5.3: The lift and drag forces on the cylinder, frequency of vortex shedding and the pressure difference over the cylinder. The percentage offset of all these properties is given with respect to the finest reference case.

Name	Lift coefficient				Drag coefficient				Frequency		Pressure difference			
	Mean [-]	Amp [-]	Mean offset [%]	Amp offset [%]	Mean [-]	Amp [-]	Mean offset [%]	Amp offset [%]	Frequency [s^{-1}]	Offset [%]	Mean [Pa]	Amp [Pa]	Mean offset [%]	Amp offset [%]
Reference	-0.01736	2.00786			3.19583	0.06313			3.0189		2.46369	0.08666		
Coarse	-0.01647	1.97420	-5.10	-1.68	3.18826	0.06166	-0.24	-2.32	3.0253	0.21	2.45521	0.09214	-0.34	6.31
Medium	-0.01632	2.00382	-6.00	-0.20	3.19404	0.06306	-0.06	-0.10	3.0175	-0.05	2.4563	0.09065	-0.30	4.60
Normal	-0.01689	2.03100	-2.73	1.15	3.20335	0.06458	0.24	2.30	3.0196	0.02	2.45923	0.09010	-0.18	3.97
Fine	-0.01691	2.03078	-2.56	1.14	3.20140	0.06445	0.17	2.09	3.0199	0.03	2.46109	0.08981	-0.11	3.63
Very fine	-0.01708	2.04430	-1.59	1.82	3.20524	0.06532	0.29	3.46	3.0181	0.02	2.46298	0.08972	-0.03	3.53
Medium in PISO mode	-0.01633	2.14789	-5.93	6.97	3.21010	0.07262	0.45	15.04	2.9996	-0.64	2.46672	0.10427	0.12	20.31
Medium with dynamic mesh	-0.01629	2.00391	-6.13	-0.20	3.19403	0.06307	-0.06	-0.09	3.0201	0.04	2.45631	0.09065	-0.30	4.60
Fine with overset mesh	-0.01732	1.89424	-0.23	-5.66	3.13814	0.05691	-1.81	-9.86	3.0028	-0.53	2.42175	0.08269	-1.70	-4.59

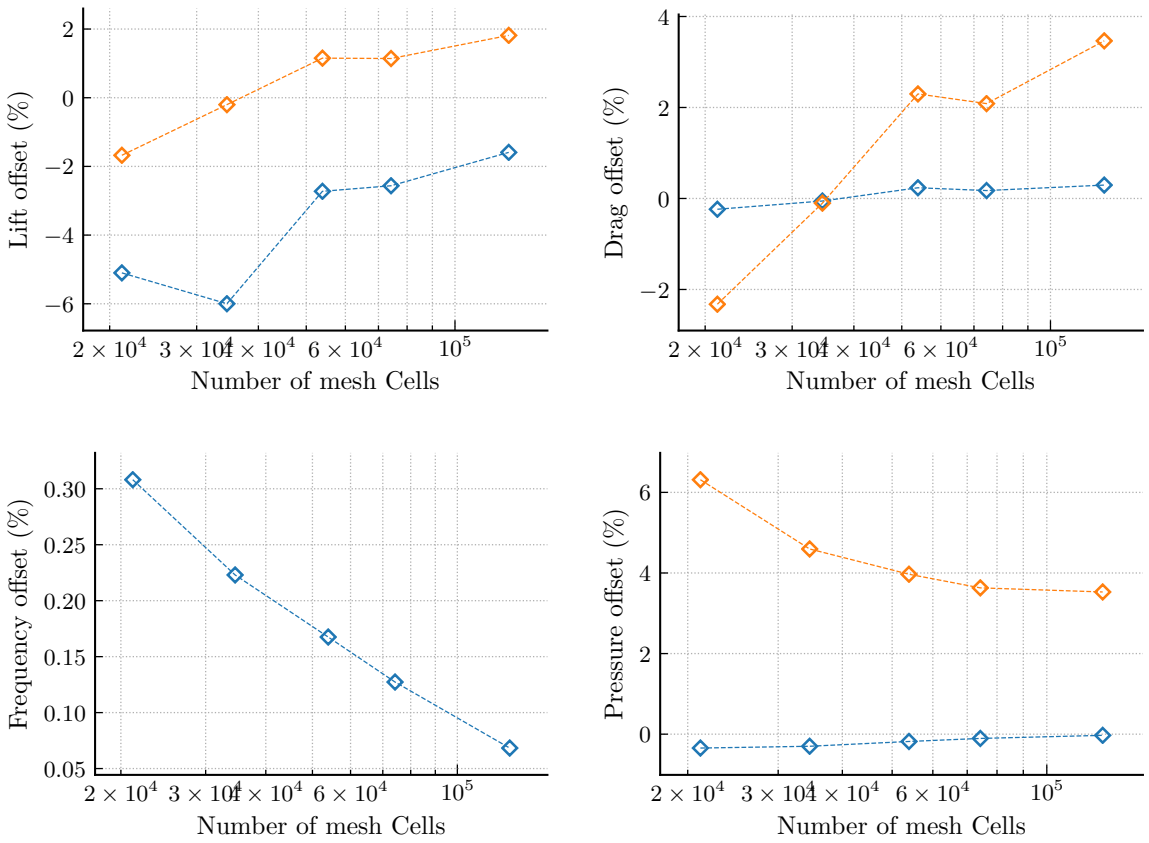

Figure 5.5: Difference between the reference solution and own solution for different mesh resolutions. (top left) ◇ Mean and ◇ average lift. (top right) ◇ Mean and ◇ Average drag. (bottom left) Period of vortex shedding. (bottom right) ◇ Mean and ◇ Average pressure difference.

Model error and convergence

The model error can be categorised by the offset of the most accurate computation with respect to the reference solution. The most refined case is taken for this measure, with 128,465 elements and DOFs. The number of elements is comparable to the 133,120 number of elements of the most refined reference case, but since this is computed by a finite elements method rather than a finite volume method, it has more DOFs.

Table 5.4: The lift and drag forces on the cylinder, Frequency of the vortex shedding and the pressure difference over the cylinder. The percentage offset of all these properties is given with respect to the finest reference case.

	Lift offset [%]		Drag offset [%]		Period offset [%]	Pressure difference offset [%]	
	Mean	Amp	Mean	Amp		Mean	Amp
Model	-1.59	1.82	0.29	3.46	-0.07	-0.03	3.53

Figure 5.6 shows the error of the testcases with respect to the finest run. Therefore, the model error is filtered out. The error and number of elements is shown in logarithmic scale so the slope and order of the method can be deduced.

The lift and drag show that the prediction of the forces on the cylinder do not necessarily have a descending slope for the error. For the overall trend the coefficients converge to the value of the

finest mesh. While the lift and drag are integrated values over the surface of the cylinder, the period and pressure difference are measured directly from the domain. These values display a monotonic decreasing error for mesh refinement.

For each of these plots, the slope of convergence seems to increase for the rightmost point. However, this is most likely introduced because error is taken relatively to the finest mesh, and not the absolute solution. For the error taken with respect to the absolute solution, a linear line would appear with a slope that is dependent on the order of the methods used.

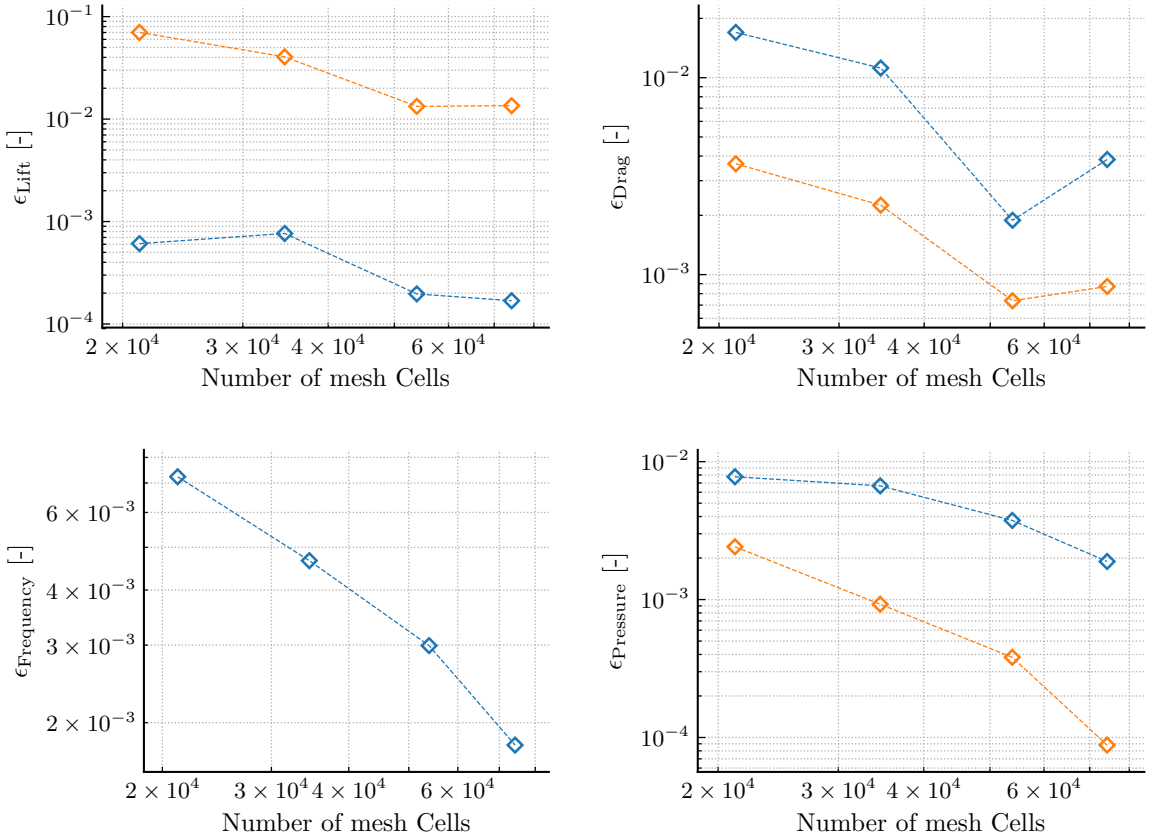

Figure 5.6: The mesh convergence taken with respect to the most refined mesh. (top left) ◇ Mean and ◇ average lift. (top right) ◇ Mean and ◇ Average drag. (bottom left) Period of vortex shedding. (bottom right) ◇ Mean and ◇ Average pressure difference.

For further computations in the FSI analysis a different mesh will be used since the flap is added. A refinement comparable to the medium cased is used. This mesh has large computational advantages over the refined meshes, which is an important detail for the coupled simulations, while it is still reasonable able to predict the flow with sufficient accuracy.

Order of the simulation

The spacial and temporal discretisation are derived using a tailor series which expands the solution to the next point in space or time. This discretisation only takes into account higher order terms, which implies that the error of the solution is dominated by the highest order term which is not included in the computation. For the spacial computation this implies that the error is proportional to:

$$\epsilon = C\Delta x^p. \tag{5.6}$$

Therefore, for a more refined mesh the error should decrease by order p. The cell size Δx is

inversely proportional to the square root of the amount of cells in the 2D domain. Then the order of the simulation can be estimated by evaluating the slope of the logarithmic period graph. The fourth point most likely displays faster convergence because the mesh is close to the solution mesh. Therefore, the first three points which display linear behaviour are evaluated:

$$p \approx \frac{\log\epsilon_1 - log\epsilon_2}{\log\Delta x_1 - log\Delta x_2} = 1.88 \tag{5.7}$$

Theoretically $p = 2$ Since all temporal and spacial schemes used are second order. The approximation of the error is close to that value. Differences between the expected order and the approximation can be caused by influence of the boundaries, first order schemes at start-up and the wall. Also the result depends on the accuracy of the points in the period graph.

5.2.4. The PIMPLE algorithm

The `OpenFOAM` solvers which work with the `PIMPLE` algorithm are ran default in `PISO`-mode. The solver is extended by adding outer corrections with a residual criterion so the timestep is iterated until convergence reached. The velocity and pressure field are iterated until the residual respectively reaches a value below $5 \cdot 10^{-4}$ and $5 \cdot 10^{-3}$. At maximum 50 outer correctors are performed every timestep.

In table 5.3 the difference between the medium case in `PISO` and in `PIMPLE` mode is shown. The former shows a large over-prediction of the force amplitudes. The large amplitude overshoot of the drag is related to the large pressure difference over the cylinder, where the amplitude is 20% larger than the reference case. Applying the `PIMPLE` algorithm reduces this figure to 4.60%. Also the offset in amplitude for the forces is solved more accurately.

The `PIMPLE` algorithm with outer corrections and residual control leads to a better match with the reference values. Therefore these settings are applied in all further runs to improve the accuracy of the solver.

5.2.5. Dynamic mesh algorithm

The dynamic mesh algorithm was tested to find out the effect of the deformation algorithm. All simulations in this research with deforming meshes are solved using the laplacian deformation algorithm. In the FSI computation the mesh will deform and additional fluxes over the boundary must be computed. The dynamic mesh is also an integral part of the overset mesh solver in `OpenFOAM`, therefore it is vital to understand its individual influence.

To feature the dynamic mesh calculation, the solver `pimpleDyMFoam` must be used instead of `pimpleFoam`. This calls the mesh deformation algorithm, even when working with a static mesh. The influence of adopting the laplacian mesh deformation can be seen in table 5.3 by comparing the medium mesh with and without dynamic treatment. The difference between these cases is minute which indicates that the usage of the dynamic mesh algorithm does not influence the solution significantly.

5.2.6. Overset mesh

The overset mesh is a popular spacial discretisation method in FSI applications since it allows virtually free movement for the object of interest. The region between the overset mesh and the background mesh is evaluated by interpolating the fluid fields.

The application of an overset mesh has a large effect on the accuracy of the solution. The amplitude of the force coefficient drops significantly comparing the overset mesh to the equivalent single mesh, as can be seen in table 5.3. This is caused by additional diffusion to the flow variables introduced by the interpolation. Furthermore, the interpolation method is computationally very expensive. Analysis showed that the computational time increased by a factor 15.9 compared to a similar single mesh. Therefore, further analysis in this research does not make use of the overset

mesh.

5.2.7. Synthesis on the Fluid validation

The flow around a cylinder benchmark case is adopted as validation case for the fluid solver, since the domain and flow characteristics are very similar to the cylinder with flap case which is be used to validate the FSI procedure. Various parts of the fluid solver are evaluated to understand the role of these parameters.

The merged PISO-SIMPLE algorithm (`PIMPLE`) algorithm is used to facilitate variable timesteps, where the timestep is determined by the maximum CFL number in the flow. Although higher values could speed up the simulation, the maximum CFL number is limited to unity to make sure no physical transient behaviour is lost. The `PIMPLE` algorithm uses two Pressure Implicit with Split Operator (`PISO`) corrections every time-step, and performs up to 50 `PIMPLE`-loops to converge the URANS equations every timestep by reducing the residual. The value of $5 \cdot 10^{-3}$ is adopted for both the pressure and velocity field.

A mesh study was performed with mesh sizes ranging from 21,170 to 128,465 elements. The most refined mesh provides good accuracy with respect to the reference solution, but was computationally very expensive. A mesh similar to the medium mesh is used for further analysis in the FSI cases, since it provides sufficient accuracy and relatively low computational constraints.

The model error was determined using the most refined case, and the approximate discretisation error could be deduced. The logarithmic plot of the error for the period and pressure showed linear convergence, from which the order of the simulation was deduced, which is approximately 1.88.

The adoption of the dynamic mesh procedure in the `PIMPLE` algorithm was tested. The difference between the solvers `pimpleFoam` and `pimpleDyMFoam` was negligible, and shows that the dynamic mesh algorithm does not influence the solution. The overset mesh has been evaluated but it was found that the interpolation algorithm posed a large penalty on the computational time. Therefore it is not considered for the remainder of this research.

5.3. Structural validation

The structure shown at the bottom part of figure 5.1 is validated separately using the CSD part of the validation suite. Only the flap is considered since the cylinder is a rigid body. The structure of the flap in FSI validation case is modelled by a FEM. The accuracy of the structural solver is tested and the model error can be characterised. Two types of finite element are evaluated in this analysis. Brick elements are commonly used as the basic finite element, while shell elements are common in the modelling of materials which have a structure which is dominant in two directions, such as thin insect wings.

Next, the natural behaviour of the flap is examined by finding the eigenmodes and eigenfrequencies. These can be analytically approximated using beam-theory. The eigenmodes influence the way the flap moves under the periodically applied load.

5.3.1. Test case

The elastic beam is taken here without the surrounding fluid and is subjected to a gravitational force in downward y-direction with magnitude: $g = 2\text{ms}^{-2}$.

Three different test are set up: CSM1 and CSM2 test the stationary deflection for two values of the Young's modulus. CSM3 tests the dynamic response of the beam featured in CSM1 for the dynamic response. Reference data was taken from FeatFlow (2018). The Young's modulus for CSM1, CSM2 and CSM3 is equivalent to the three FSI cases defined in table 5.1. For all three cases the same density of $\rho_s = 1{,}000\text{kg m}^{-3}$ is used.

All cases are ran with a model of one cell in spanwise direction, see for example figure 5.7. The

mesh is defined by the vertices of the elements, or nodes. To enforce strict 2D behaviour all nodes are fixed in z-direction. At the root of the flap at the cylinder the flap is clamped, which means all six DOFs are fixed.

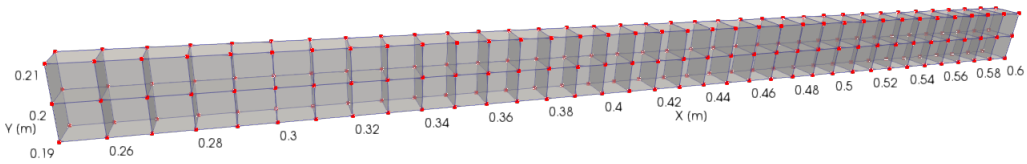

Figure 5.7: Structured mesh with a spacing of 10mm which leads to 280 nodes for 68 elements. The flap is 0.35m long and 0.02m high.

5.3.2. Runs

Several simulations of the structure were performed to analyse the behaviour of the flap. First the number of mesh elements was varied to find the sensitivity of the solution to the mesh refinement. Furthermore, a comparison of two brick and shell elements was performed. The solver `Calculix` works purely with three dimensional elements. Therefore it extrudes the flat shell to 3D brick elements. Table 5.5 shows the different runs that were performed.

Table 5.5: Runs for the Structural Validation.

Case	Element	Mesh Spacing [m]	Number of Elements
Coarse	he8	$20 \cdot 10^{-3}$	36
Medium	he8	$5 \cdot 10^{-3}$	280
Fine	he8	$1 \cdot 10^{-3}$	7,000
Shell	qu8	$20 \cdot 10^{-3}$	36

Figure 5.8 shows the deflection of the flap under gravitational loading for the CSM1 case. The left side is clamped to the cylinder while the right side of the flap is free to move in the x- and y-direction. The flap is coloured with the Von Mises stresses, indicating that the highest stresses occur near the root of the flap at the top and bottom side. Near the tip the stresses go to zero. The point 'A' is defined at the mid of the tip of the structure and the displacement of the flap is measured in this point.

5.3.3. Results CSM1 and CSM2

The static cases CSM1 and CSM2 are evaluated first using the reference displacement in x- and y-direction. Figure 5.9 shows the deformation of point 'A' for the number of finite elements. The reference solution is shown by the dashed line. It is clear from both figures that the solution is highly dependent on the mesh refinement. A coarse mesh leads to a stiffer structure with lower deflection, and the most flexible structure is reached for the finest mesh. Since the relative difference between the meshes shrinks with increasing mesh refinement, the larger meshes create a solution which is closest to a mesh-independent solution.

The effect of the mesh refinement is featured in figures 5.9. The fine case with 7,000 elements

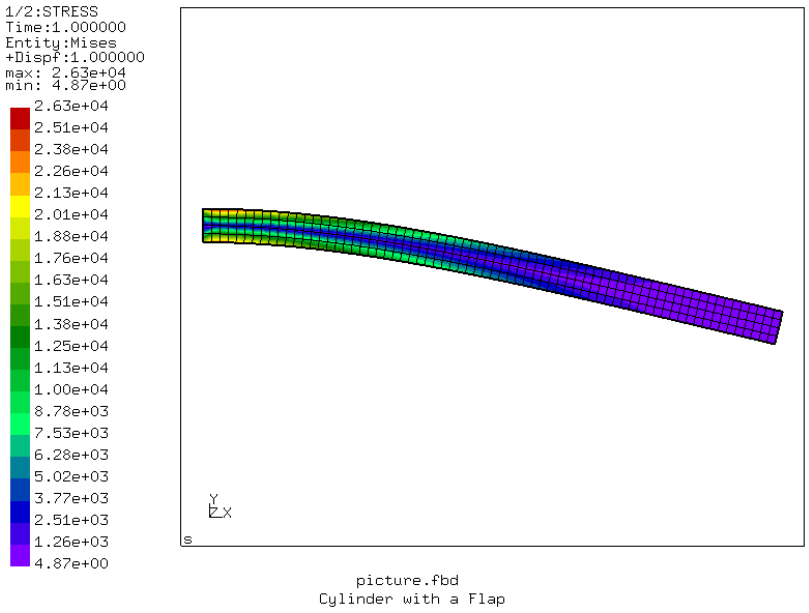

Figure 5.8: Flap under gravitational load

coincides very well the reference values. The difference with the displacement in x- and y-direction is respectively -2.05% and -1.14%

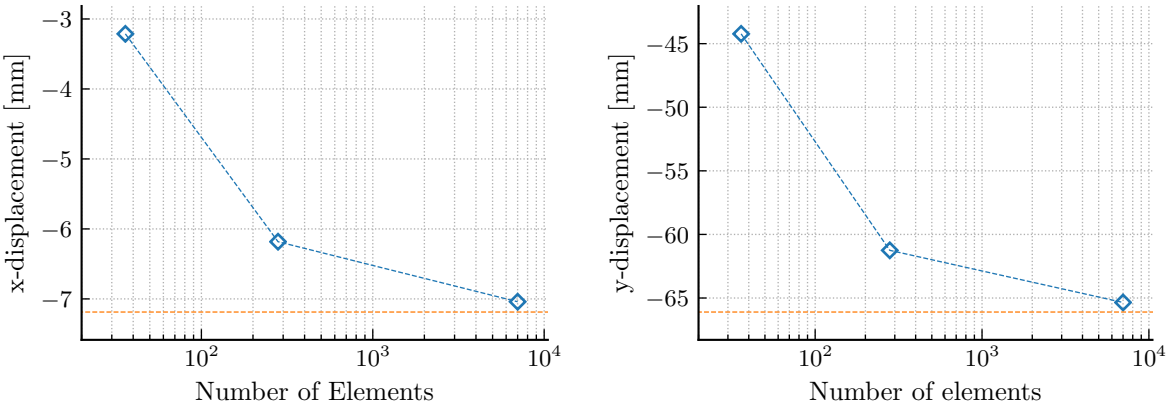

Figure 5.9: The x- and y-displacement of point 'A' for case CSM1. - - Displacement of the reference case, ◇ Displacement for the different mesh refinements.

The shell element case shows similar behaviour to the brick elements as can be seen in table 5.6. This similar behaviour could be expected since the shell elements are extruded to brick elements. However, the shell element flap features only one cell in the y-direction, which is given the thickness of the flap. The brick elements from shell extrusion feature 20 integration points instead of 8. The accuracy of the shell element is close to the most refined brick element. This shows that the shell element is useful for the static computations.

Table 5.6: Displacement of point 'A' in x- and y-direction for CSM1. Percentage offset with respect to the reference value.

	u_x [m]	u_y [m]	Offset x [%]	Offset y [%]
Reference	-7.19E-03	-6.61E-02		
Coarse	-3.21E-03	-4.42E-02	-55.30	-33.09
Medium	-6.18E-03	-6.13E-02	-13.98	-7.34
Fine	-7.04E-03	-6.53E-02	-2.05	-1.14
Shell	-6.96E-03	-6.49E-02	-3.23	-1.87

Case CSM2 features the same model as in CSM1, where the Young's modulus is increased by a factor 4 so it matches the flap Young's modulus in FSI3. Therefore, the structure is stiffer and the displacement of point 'A' is smaller. The reference displacement decreased from -7.19mm and -66.10mm in the respective x- and y-direction to -0.47mm and -16.97mm. Therefore, it can concluded that the model behaves as expected for a variation in the Young's modulus.

5.3.4. Results CSM3

Under the application of the constant gravity force a periodic motion is assumed by the structure. No damping is applied which leads to an identical displacement for every period. The frequency of the oscillating motion is seen in table 5.7. Based on this data it can be derived that a finer mesh leads to a more flexible system since the frequency decreases with refinement.

Figure 5.10 shows the frequency for the amount of brick elements. The reference line gives the frequency which is obtained by the reference case. The best result is obtained for the finest mesh which shows a frequency which is only 0.15% different from the reference solution. The added

Table 5.7: Oscillation Frequency and runtime

Case	Frequency [1/s]	Frequency offset [%]	Runtime [s]
Reference	1.1001		
Coarse	1.3319	21.02	11
Medium	1.1364	3.25	58
Fine	1.1022	0.15	1,076
Shell	1.4444	31.25	139

accuracy is at a penalty as the finest mesh requires approximately a factor 20 more computational time than the medium mesh.

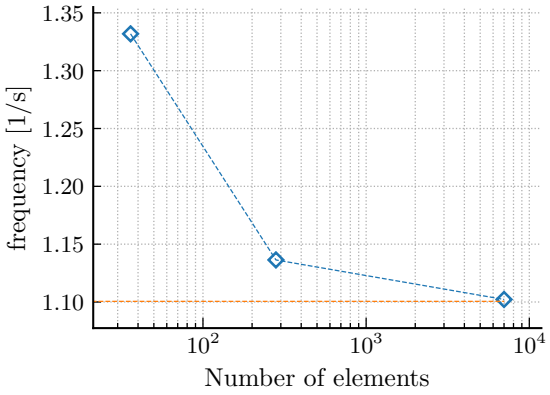

Figure 5.10: Frequency of the oscillation vs the number of brick mesh cells. - - Displacement of the reference case, ◇ Displacement for the different meshes.

The flexibility of the flap as a function of the number of elements is clearly seen in figure 5.11. The frequency decreases and the magnitude of oscillation increases for the number of elements. Therefore, the structure becomes increasingly more flexible with the number of elements, which affects its eigenfrequency.

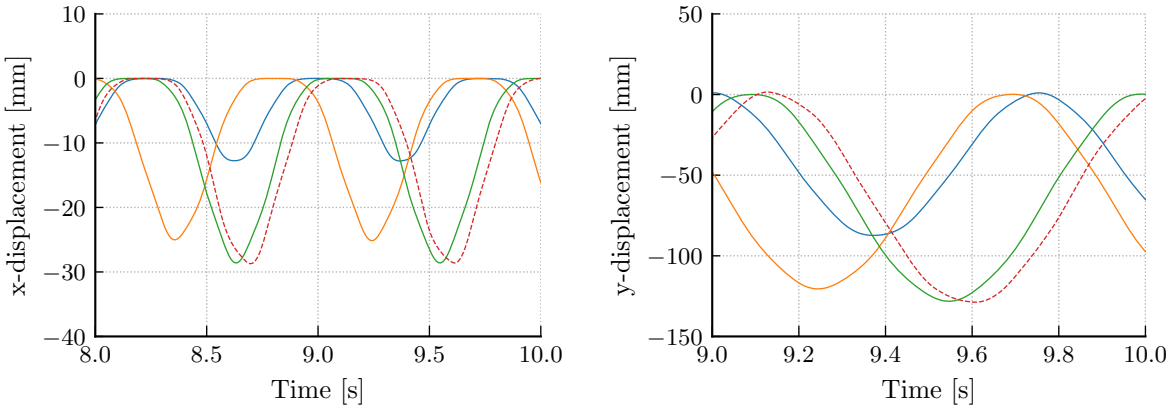

Figure 5.11: The x- and y-displacement of point 'A' for brick element meshes with various number of elements. - - Reference, — Coarse, — Medium, — Fine.

Compared to the brick elements, the shell elements perform poorly for the dynamic case. Smaller displacement is predicted than the reference case, as is shown in figure 5.12: The structure is much stiffer than expected.

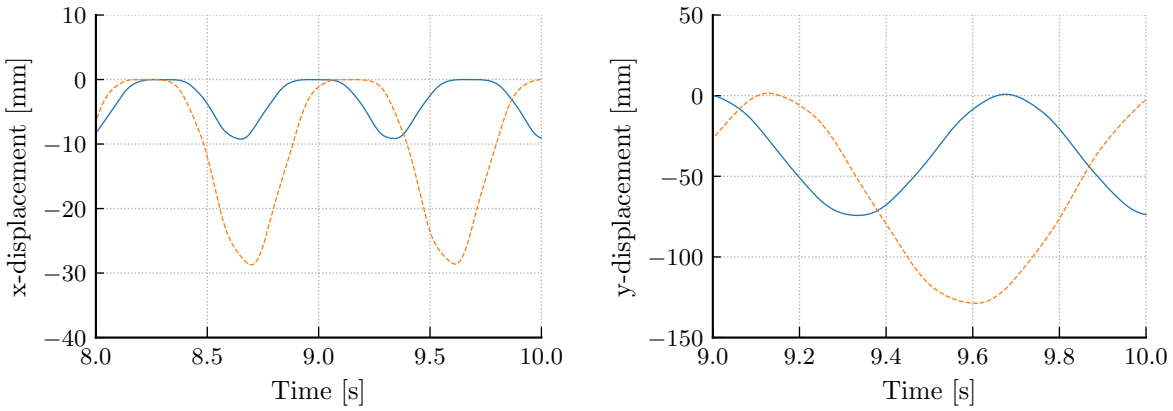

Figure 5.12: Displacement in x- and y-direction for shell elements with additional boundary conditions. - - Reference, — Shell elements.

The structure with brick element is used for the remainder of the work, since it is more accurate in dynamic computations. The medium mesh with 280 elements is chosen since this mesh can be evaluated at a fraction of the computational effort of the fine mesh. Moreover, the mapping procedure in the coupled simulation is less costly for a smaller number of structural elements.

5.3.5. Eigenmodal analysis

In essence the flap behind the cylinder is a cantilever beam. The one end is free to move while the other is fixed in all directions. Natural vibrations can occur in the flap both in bending and in longitudinal direction. No rotational eigenmodes about the x-axis are permitted for the 2D model.

Analytical solutions can be derived for the flap by using a Euler-Bernoulli beam. This approach is taken first to find the eigenfrequency and deformation of the first five eigenfrequencies. Next, this is compared to numerical results from the structural solver.

The shape and frequency of the eigenmodes can derived from the equations E.1, which model the flap as an Euler-Bernoulli beam element. In appendix E the derivation for the longitudinal and bending eigenmodes is given. Figure 5.13 shows the shape of the first four bending eigenmodes and the longitudinal eigenmode. Using the material properties for both the FSI2 and FSI3 case the eigenfrequencies are computed, see table 5.8.

As was already shown in section 5.3.4 the structure is stiffer than the reference data, even for the most refined mesh. This is reflected in the eigenfrequency of the material found by a modal analysis in the structural solver.

Comparing the values from the numerical modal with the analytical solution, it can be seen that the eigenfrequency is higher for the numerical model, especially for the lower eigenmodes. The difference between the eigenmodes is consistent over the different models, which indicates that the influence of flap density and Young's modulus is evaluated correctly by the numerical method.

The difference between the eigenfrequency of the analytical and numerical model can play an important role in the FSI simulation. The motion of flap in these coupled simulations is triggered by the periodical vortex shedding of the cylinder and flap combination. Model errors for the flap eigenfrequency could therefore create a different dynamical situation.

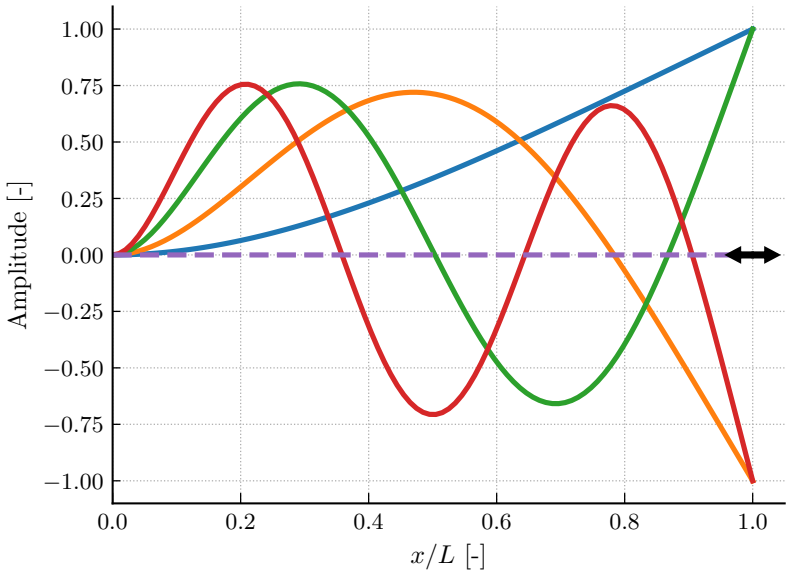

Figure 5.13: The first five eigenmodes of the flap shown with an arbitrary non-dimensional amplitude. Four of these are bending modes, while one is a mode in longitudinal direction. — Bending mode 1, — Bending mode 2, — Bending mode 3, — Bending mode 4, - - Longitudinal mode 1.

Table 5.8: Eigenfrequency for the first five eigenmodes of the flap.

	FSI2			FSI3		
Eigenmode	Analytical [Hz]	Numerical [Hz]	Difference [%]	Analytical [Hz]	Numerical [Hz]	Difference [%]
Bending mode 1	0.312	0.353	13.119	1.974	2.231	13.040
Bending mode 2	1.956	2.172	11.083	12.369	13.739	11.083
Bending mode 3	5.476	5.924	8.185	34.632	37.467	8.185
Longitudinal mode 1	8.452	9.261	9.577	53.452	58.571	9.577
Bending mode 5	10.731	11.204	4.411	67.866	70.859	4.411

5.4. Unidirectional coupling for displacement verification

The verification of the displacement mapping serves two purposes. First of all, the absolute displacement is checked and it is verified whether the displacement mapped from the structural solver is transformed correctly to the fluid mesh. The verification case is the same as the FSI3 case with two additional assumptions: There is no force mapping, and the flap has a gravitational load as in CSM3 which causes it to oscillate.

Point 'A' as depicted in figure 5.1 is used to track in both the structure and fluid solver. After the displacement field is created in `CalculiX` it is written to a buffer in `preCICE`. Next, a mapping from the structure to the fluid mesh is performed. At last, the displacement is imposed on the fluid mesh.

Figure 5.14 shows the displacement of point 'A'. The figure top-right depicts the relation between the y-and x-displacement of the flap. The displacement in y-direction is a factor 20 higher than the displacement in x-direction and is therefore used for comparison. The top-left figure shows the vertical displacement of the point 'A' for both the fluid and the structure. The absolute offset between the two figures is shown beneath. From the bottom-right figure it is clear that the maximum absolute error between the solvers is around 1.1%, with an averate of 0.43%.

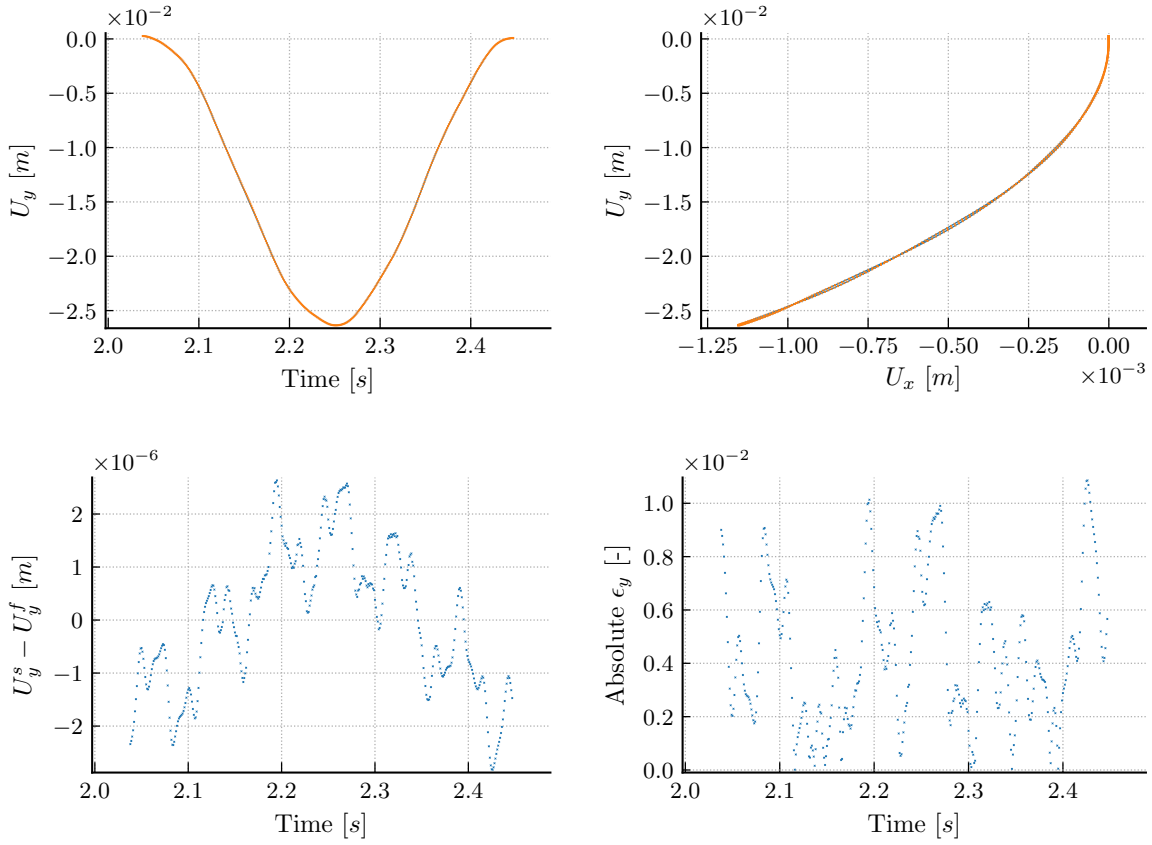

Figure 5.14: top-left: The vertical displacement of the fluid over one period. Top right: The flap movement over one period. —Structure mesh and ×Fluid mesh. Bottom: The offset between the solvers, absolute error over one period

More extensive analysis showed that the displacement offset on point 'A' was close to 10^{-12} for the mapping from the `preCICE` buffers to the fluid mesh. The major part of the offset is therefore caused by the step from the structure mesh to `preCICE`. A possible cause for the difference in displacement is the extraction method used to obtain the data. For the structure solver, fluid solver, and `preCICE` this was all performed individually.

Figure 5.15 shows the velocity and pressure profile for the maximum deformation of the flap. Visually it is evident that fluid mesh is changed to suit the flap deformation.

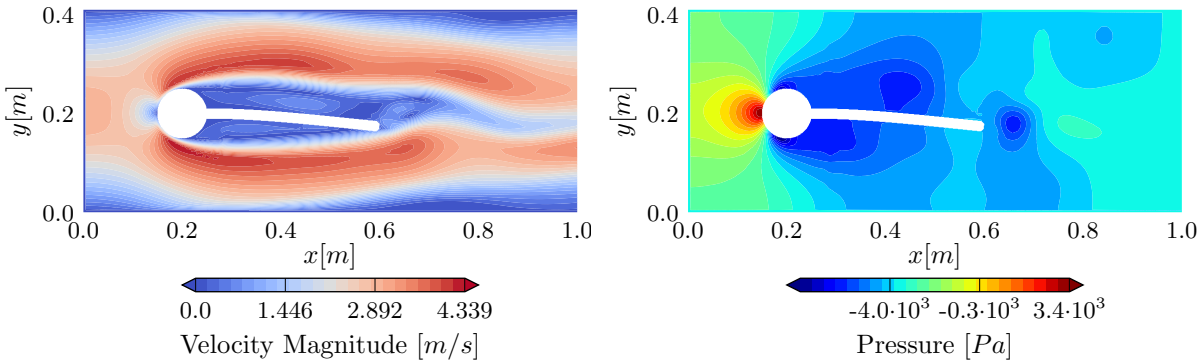

Figure 5.15: Velocity and pressure contours for the unidirectional case at the lowest flap deflection, at 2.25s)

The second purpose of the verification is proving the checkpointing procedure. For an implicit coupled case, a convergence criterion is set to measure the relative or absolute convergence of both the displacement and the forces. In general the criterion is set to a value which assures good accuracy while still providing an acceptable amount of iterations per timestep. For this verification, the convergence criterion is set to a value just above machine precision.

To facilitate only displacement mapping, the force is switched off artificially by altering the source code temporarily. This means that the force is actually passed to the `preCICE` interface, but it is a zero vector. The convergence criterion is therefore only applied to the displacement of the flap.

The hypothesis is that every iteration requires two subiterations for every timestep to reach convergence. The relative convergence criterion is satisfied if both subiterations provide exactly the same result, which is only possible if the checkpointing for the structural solver is implemented correctly. It proved that the first timestep required three subiterations and the other timesteps were satisfied in two subiterations. It appears that the initialization requires one extra iteration from the fluid side.

In the above analysis a coupled simulation is performed where the force mapping is switched off artificially. The structure is subject to a gravitational load similar to the CSM3 case. The displacement mapping from the structure is tracked on both the structure and fluid side which showed that the displacement is as expected. An implicit coupled simulation is then selected with a very strict convergence criterion. Every timestep requires two subiterations which shows that the checkpointing procedure is valid for the structure method and that the displacement mapping is performed accurately.

5.5. Unidirectional coupling for force mapping verification

The second verification is posed to verify the checkpointing of the fluid fields. As explained in section 4.3.2, various fluid fields exist, of which several store old time information. For a coupled simulation without displacement mapping the fluid field should reach convergence within two subiterations. A strict criterion is set on the relative force convergence. The displacement is artificially put to zero so can not be used as a convergence criterion. All timesteps required two iterations, except for the first timestep. Here the same initialisation argument applies as explained in the previous section.

The velocity in streamwise-direction and pressure field around the cylinder with a flap is shown in figure 5.16. It is clear that the flap is static. The force vector on the flap boundary faces is displaced using black arrows. The magnitude of the force is dependent on the face areas of the boundary, for this relatively coarse mesh the maximum force is 0.24N. Just behind the cylinder, a region of refined cells is present which creates a ramp in the force profile.

The pressure plot shows the clear dependency of the force on the pressure field. The low pressure areas below and above the the flap are located at the core of the shed vortices. These low pressure areas create an oscillating force on the flap which leads to its movement in the coupled situation. A small tangential force is also created by the viscous shear force. From the velocity contour figure it is clear that there is an area of reversed flow behind the cylinder which causes a small forward component of the force.

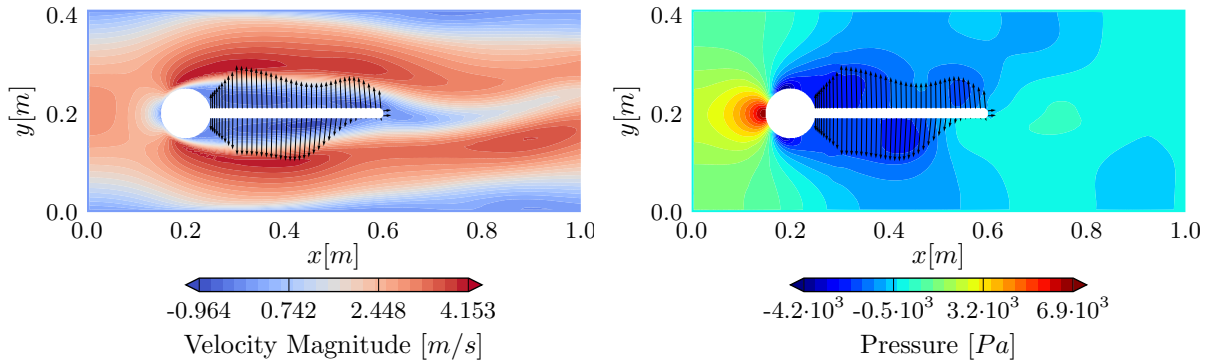

Figure 5.16: Velocity in x-direction and pressure contours for the unidirectional case with the force vectors, at 2.25s)

To verify the mapping of the force a case is created without any displacement by artificially turning off the displacement mapping. The coupled simulation requires two timesteps to converge to a strict convergence criterion. Therefore the mapping is performed accurately and the checkpointing for the fluid fields is implemented correctly.

5.6. Quasi-unidirectional coupling for mesh verification

The verification for the displacement in section 5.4 provides the confidence that the fluid fields are checkpointed correctly. However, the FSI simulation is performed with a moving mesh for which some fields require checkpointing as explained in section 4.3.3. Therefore a third verification procedure was developed to test the mesh checkpointing. Again the criterion is set to a very strict measure so convergence is only reached when all checkpointing performs as intended to.

The flap force must be used as convergence criterion since this is directly influenced by the flow solution. However, also the flap displacement must be introduced in the flow. Since these demands require that both the displacement and force are mapped, a quasi-unidirectional case is developed where the force is extremely low while the structure is very heavy and stiff. A density ratio of 10^{20} and stress ratio of $6.5 \cdot 10^{22}$ result from this. The flap movement is based on gravitational loading as CSM3.

Every coupling timestep is initialized with an initial guess of the displacement. For this simulation, a second order extrapolation is used to create an initial deformation. The actual structure displacement is during the second subiteration of the fluid. Since small differences will exist between the extrapolated and the actual displacement of the flap, every timestep is expected to require three subiterations. This is indeed the case, except for the first timestep which requires one iteration more

Table 5.9: Fluid and Structure parameters for the Quasi-unidirectional case.

		Quasi-unidirectional
Fluid		
Density	ρ_f [kg m^{-3}]	10^{-5}
Viscosity	ν_f [m^{2}s^{-1}]	10^{-3}
Mean velocity	$\bar{U}$[m s^{-1}]	2
Reynolds number	Re[-]	200
Structure		
Density	ρ_s [kg m^{-3}]	10^{15}
Young's modulus	E [kg m^{-1}s^{-2}]	$2.6 \cdot 10^{18}$
Poisson ratio	ν[−]	0.4
Ratios		
Density ratio	ρ_s/ρ_f [-]	10^{20}
Stress ratio	Ae [-]	$6.5 \cdot 10^{22}$

for initialisation.

From sections 5.4 and 5.5 it is known that the mapping of the force and displacement is performed accurately. Also the checkpointing of the structure and the fluid fields are verified. A third verification case is selected to include the effect of mesh deformation on the mapping, which is done by creating a very weakly coupled simulation. Three subiterations are required for every coupling step, which is expected. Therefore the mesh checkpointing is performed correctly.

5.7. Full FSI coupling

In section 5.1 the cylinder with a flap case is described which is used to validate the implemented FSI method. The three different cases are tested and are described below in sections 5.7.2 for the steady and 5.7.3 for the unsteady cases. First the discretisation and simulation set-up are explained in section 5.7.1

5.7.1. Discretisation and coupling set-up

The fluid domain is discretised with a mesh of 25,224 finite volume elements. The mesh is refined around the cylinder and is stretched towards the outlet. The flap width is spanned by four elements. An uncoupled simulation of the same mesh showed that this mesh is sufficiently refined around the cylinder to predict the formation the vortex shedding. The structural domain is discretised using 280 brick elements, with four elements in the flap thickness direction.

The displacement is mapped from the structural mesh to the fluid mesh using radial basis functions with the thin plate spline function. The same interpolation function is used in conservative mode to map the forces from the fluid to the structure. The Interface Quasi-Newton Least-Squares (IQN-ILS) is used to coupled the partitioned solvers. A relative convergence criterion of 10^{-3} is imposed on the displacement and force boundary data. Similar to the fluid validation in section 5.2 the second order backwards differencing time scheme is used for the fluid.

5.7.2. Steady case: FSI1

The steady state case has a Reynolds number of $Re = 20$. The fluid field can be seen in figure 5.17, where the flap has a small deflection upwards. The deflection is underlined by pressure profile which shows that the pressure under the flap is slightly higher than the pressure above it. The lowest

pressure can be found over the accelerated flow over the cylinder, with values near $p = 0$Pa.

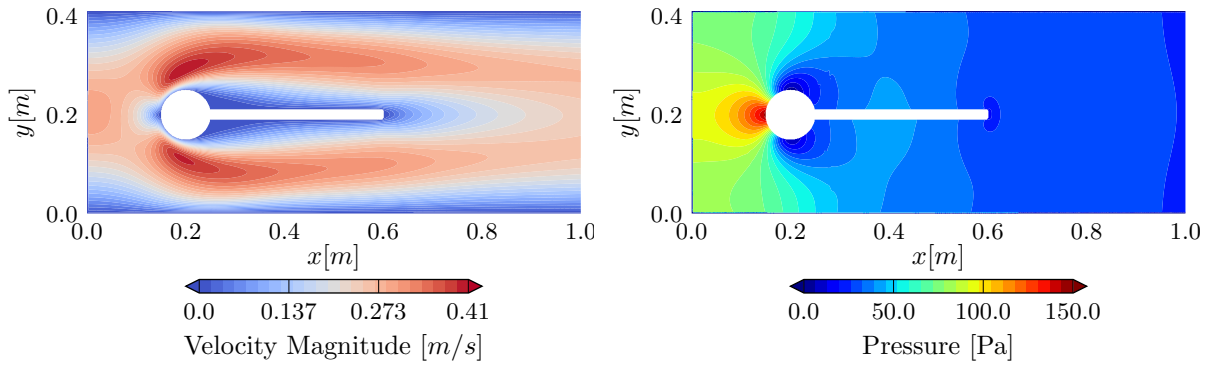

Figure 5.17: Velocity and pressure contours for FSI1 at 20s

Figure 5.18 shows the horizontal and vertical deflection of point 'A' on the flap. The vertical deflection is slightly underestimated, but the horizontal deformation is predicted accurately. The flap is stretched slightly under the friction force. Furthermore, the lift and drag coefficient are shown in the bottom figures. The lift from the simulation shows a high frequency for which no explanation was found. The average value coincides with the reference lift coefficient. Also the drag coefficient is predicted accurately.

5.7.3. Unsteady cases

The two unsteady cases are FSI2 and FSI3. The former has a density ratio of $\rho_s/\rho_f = 10$ which implies that the flap inertia is relatively important. This is reflected in the flapping motion of the wing which follows a near sinusoidal motion, where both the amplitude and the phase are similar to the reference case. A small difference in amplitude is present at the minimum of the motion, where the simulation shows smaller displacements than the validation data.

The force coefficients for the FSI2 case displays that the FSI2 simulation follows the same trend as the reference data. Besides the main oscillation in lift caused by the flapping motion of the flap, a signal with a frequency approximately five times the flapping frequency is seen. In section 5.7.4 this effect is studied. For this case the relative high importance of the flap inertia is evident since the deformation of the wing is hardly affected by the high frequency oscillation.

The drag of the cylinder and flap shows large discrepancies in the shape and amplitude with respect to the reference case. The same high frequency pattern is present as seen for the lift coefficient, although much less pronounced. Furthermore, the peak of the drag shows a phase difference with respect to the reference data. Combining the lift and drag coefficient shows that the motion is influenced largely by the high frequency oscillation. It induces various knots in the curve.

The inertial forces are less relevant in the FSI3 case, while the stress ratio is preserved. This indicates that the flap deflection is more dependent on the fluid forces and lesser so on the flap inertia. The result is seen in figure 5.20, where large differences between the simulated and reference data.

The simulation shows a higher amplitude and lower frequency for the flapping motion. The lift and drag profile are different too. The lift profile shows an high frequency oscillation similar to lift profile seen for the FSI2 case. The different profile in lift could have large implications for the deformation because the fluid forces are relatively important for the FSI3 case.

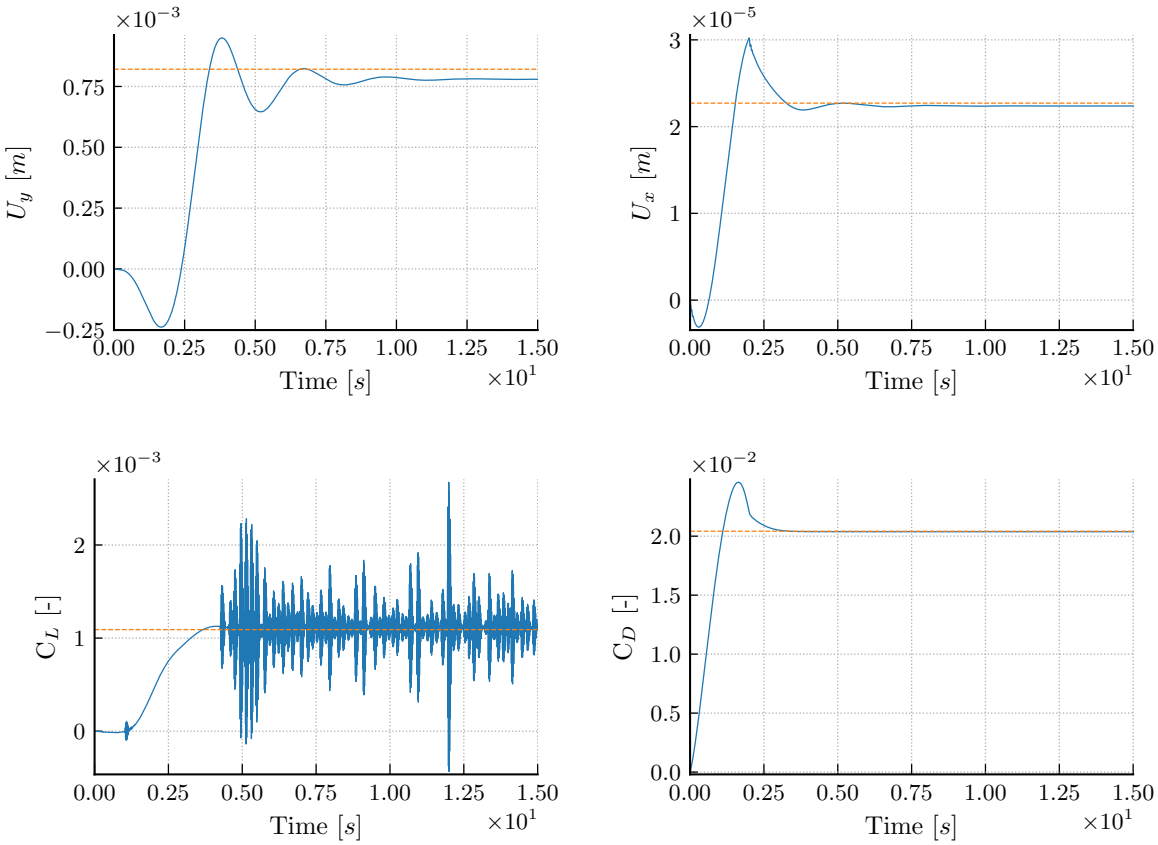

Figure 5.18: top-left: The vertical displacement of the point 'A'. Top-right: The lift coefficient of the flap-cylinder combination. Bottom-left: The drag coefficient. Bottom-right: Lift vs Drag coefficient. —Simulation and - - Reference data.

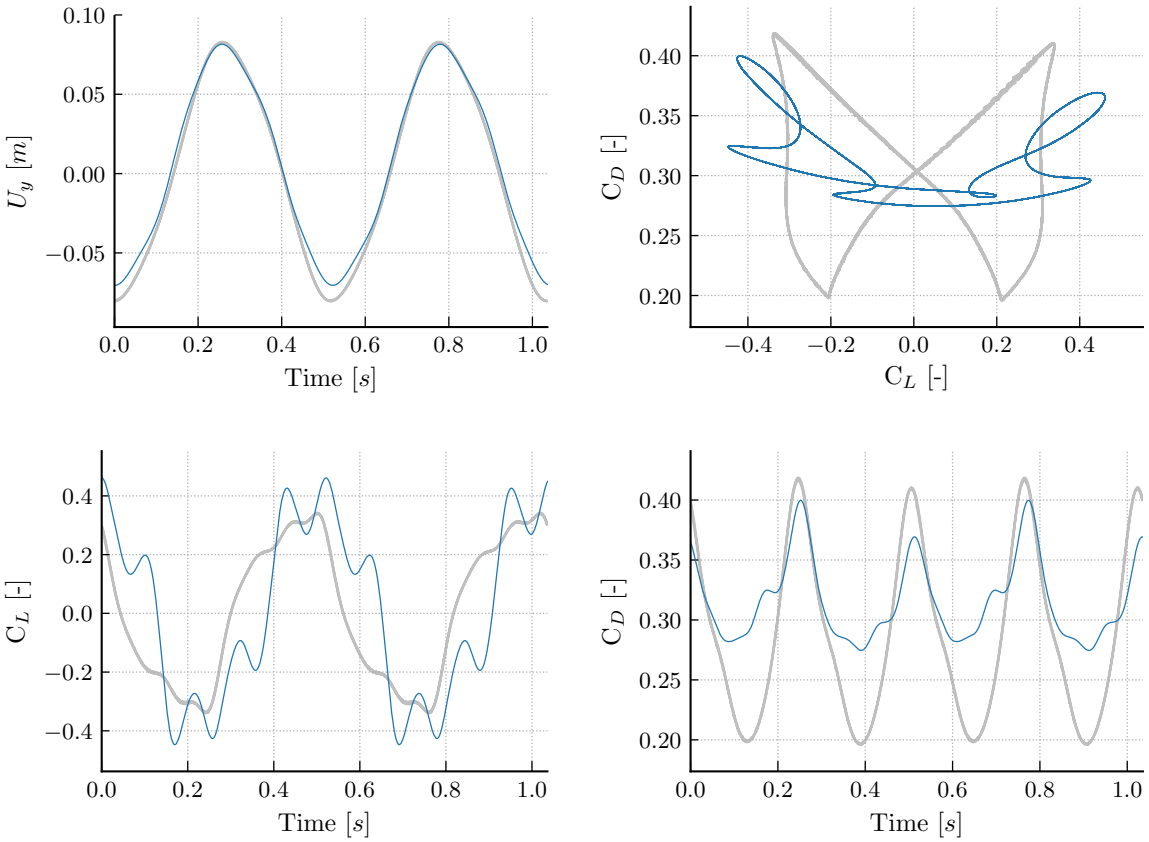

Figure 5.19: Period averaged plots for (top-left) the vertical displacement of the point 'A' for FSI2, (top-right) The lift vs drag coefficient of the flap-cylinder combination, (bottom-left) The drag coefficient, (bottom-right) Lift vs Drag coefficient. — Simulation and — Reference data.

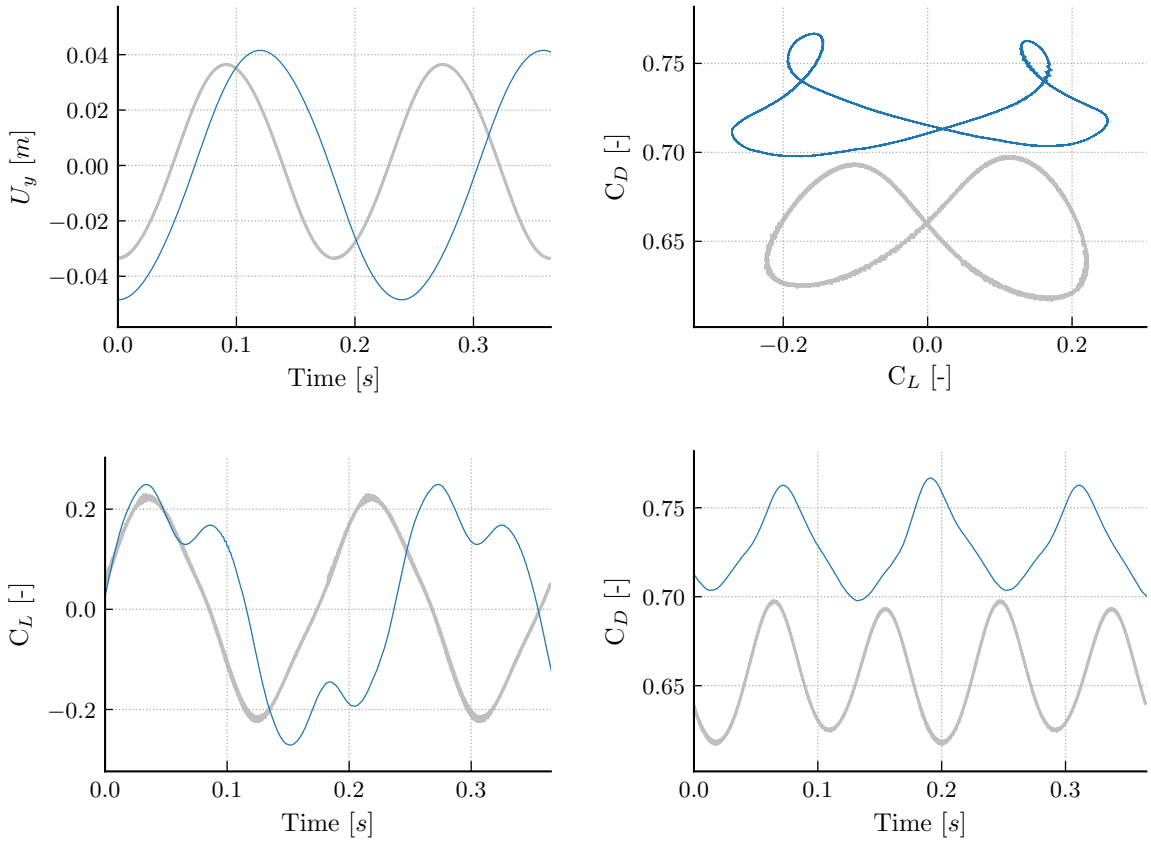

Figure 5.20: Period averaged plots for (top-left) the vertical displacement of the point 'A' for FSI3, (top-right) The lift vs drag coefficient of the flap-cylinder combination, (bottom-left) The drag coefficient, (bottom-right) Lift vs Drag coefficient. — Simulation and — Reference data.

5.7.4. Frequency analysis

Both the FSI2 and FSI3 case displayed oscillations with frequencies that do not occur for the reference data. Furthermore, the FSI3 case shows periodic behaviour with a different frequency then expected. Therefore a frequency analysis was performed for both FSI2 and FSI3.

The left figure shows the frequency spectrum of the vertical displacement for FSI2. The eigenfrequencies of the numerical model of the flap are depicted by the dashed vertical lines. See table 5.8 for the values. For reference the natural shedding frequency of the flow behind the cylinder is computed using the Strouhal number of $St = 0.2$. The addition of the flap has a stabilizing effect on the flow, so a lower shedding frequency is expected in the coupled simulation.

The main amplitude of the FSI2 case has a frequency very close to the second eigenfrequency of the flap and it is located slightly under the predicted shedding frequency. The close proximity of the shedding frequency and the second eigenmode provide a stable state for the flap in which one eigenmode dominates.Furthermore, the peak at the third eigenmode is seen too in both cases.

The longitudinal eigenfrequency with a value 9.261Hz is more pronounced for the simulation data. A signal of the same frequency was seen in the lift profile while this influence was much smaller in the reference case lift profile. The longitudinal expansion and shrinkage of the flap induces pressure oscillations in the domain which in term affect the force coefficients. From FSI2 it is seen that the forces coefficients are very sensitive to the small deflection differences caused by higher eigenmodes.

The frequency spectrum for FSI3 is shows that the reference case has a dominant frequency just below the predicted shedding frequency. The first and second eigenmode have a eigenfrequency which is much smaller or larger, so the flap does not have an obvious flapping frequency. For this case the simulation fails to converge to the same equilibrium as the reference data.

Most likely, the numerical model of the structure is too stiff which causes higher eigenfrequencies. The reference data shows a deformation that is a combination of the first and second eigenmode, but for the simulated data the first eigenmode, and therefore frequency, is more prominent. As a results, the frequency of the motion is lower and amplitude higher (see figure 5.20).

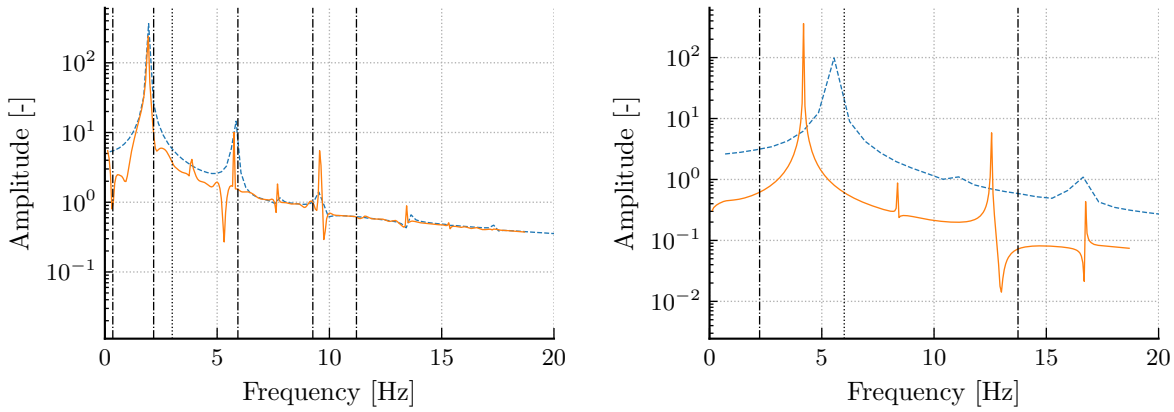

Figure 5.21: Frequency spectrum of the displacement U_y for FSI2 (left) and FSI3 (Right). ····: Strouhal frequency based on the cylinder radius. - - : Eigenfrequencies of the flap. - - : Reference and —: Simulation.

5.7.5. Flowfield

The velocity magnitude of FSI3 is shown in figure 5.22 with the flap in upwards motion. The flap has a larger flapping amplitude compared to the reference data and a region of high velocity flow is the result. The flapping induces a series of chaotic vortices in the flow with associated low pressure.

Downstream of the flap these vortices merge and large gradients are diffused in the flow.

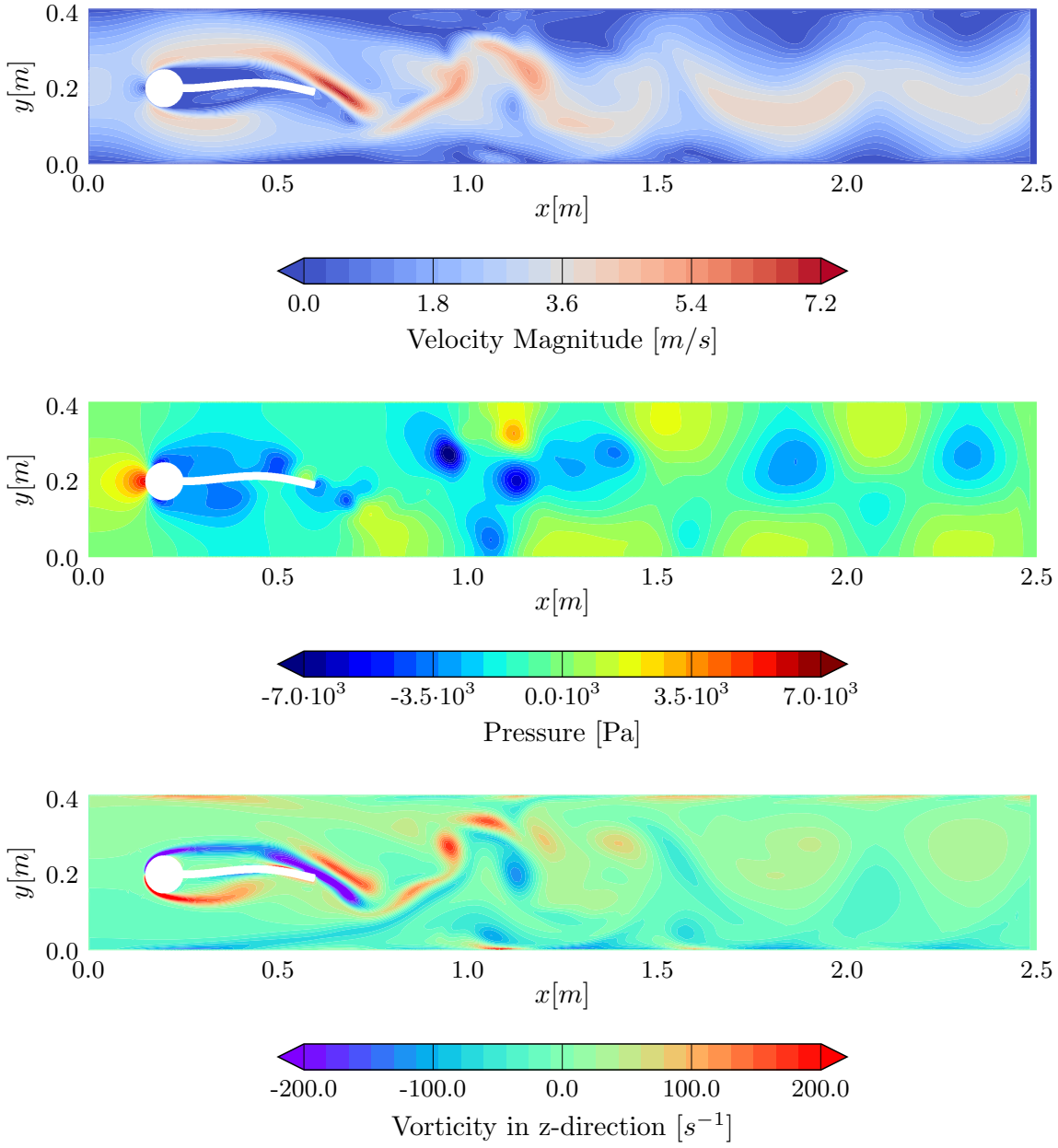

Figure 5.22: (top) Velocity, (middle) pressure and (bottom) in-plane vorticity contours for FSI3 at 10.5s

5.8. Conclusions

This chapter presents the different cases that were used to validate all parts of the coupled system. This is a necessity since many uncertainties arise in the coupled system. Prior to validating the coupled system, first the uncoupled systems were validated and commented on their accuracy and performance.

For the fluid part, the "flow around a cylinder" case is adopted. Here the chosen CFD method is tested for the accuracy of the force prediction, pressure difference in the domain and the frequency of the shed vortices. In this study, the numerical parameters space is explored for settings of the solver which promote both good accuracy and performance. Furthermore, the influence of a dynamic mesh and the overset mesh is tested. The adoption of the dynamic mesh algorithm does not introduce errors in the computation. An overset mesh is not a good alternative for the dynamic mesh because of high computational costs associated with the interpolation algorithm.

The structural part is validated first for the CSM benchmark to assure that the structural model in the coupled simulation behaves physically correct. Since this model is composed of a beam rather than a membrane, a separate validation test-case is adopted to validate the behaviour of a shell element structure. Furthermore, a frequency analysis is performed to find the first natural frequencies of the flap. It is found that the numerical model of the structure is slightly stiffer than expected. This leads to higher eigenfrequencies when compared to the eigenfrequencies which are obtained by an analytical expression.

With both uncoupled solvers validated the coupled simulation can be analysed. By adopting the "cylinder with a flap" benchmarking case, the accuracy of the FSI simulation is derived. First the force mapping and displacement mapping are verified using unidirectional coupling from one participant to the other. A quasi-unidirectional case is created by a very stiff structure under gravitational loading to verify the checkpointing of the moving mesh. From these three cases it is concluded that the mapping and checkpointing perform correctly.

The benchmark by Turek & Hron (2006) treats three cases for FSI: One steady and two unsteady cases. FSI1 shows the solution for the steady state case at a Reynolds number of $Re = 20$. The flap deflection, average lift and drag are predicted accurately. The unsteady case FSI2 shows the largest deflection. Here inertial forces are dominant and the flap shows large deflections at a nearly sinusoidal motion. The natural shedding frequency of the cylinder is close to the second eigenfrequency of the motion so the flap naturally assumes this frequency.

The FSI3 case shows large differences between the FSI3 case. Here the flap displays different dynamic behaviour than the reference case. For FSI2 it was already seen that the excitation of an eigenfrequency can have a large influence on the lift and drag of the flap. The model error in the structural model therefore could have triggered a large difference in dynamical behaviour.

Chapter 6

2D Flapping wing

The coupled FSI solver is validated in the previous chapter. In this chapter the method is applied to a flexible wing structure in a fluid. A simple hovering flapping wing in a 2D domain is considered, at the low Reynolds number of 150, described in Yin & Luo (2010). The mass and stiffness of the wing are varied to change the relative importance of the aerodynamic, elastic and inertial forces which act on the wing. The structure for this case shows large, nonlinear deformations, therefore the case is solved in an implicit FSI simulation.

The 2D wing represents a case in which the influence of the inertial forces can be modelled for a moving wing. Following the results from this chapter it can be concluded whether the FSI method developed in chapter 4 is able to capture well the relative importance of these forces that occur for flapping wings.

6.1. Model description

The flow around the wing is characterised by several nondimensional numbers which can be obtained by combining the structure and fluid parameters. Figure 6.1 shows the flap with the kinematic parameters and with the surrounding mesh. The chord (c) and thickness (h) both influence the fluid and the structure side. The angle of attack is defined with respect to the horizontal direction x.

The wing kinematics are purely defined by the translation x_0 and angle of attack α of the wing at the leading edge. In the current set-up no phase differences between the translation and pitching of the wing are considered. The wing kinematics are determined by the following equations:

$$x_0(t) = \frac{A_0}{2}\cos(2\pi f t), \tag{6.1}$$

$$\alpha(t) = \alpha_0 + \beta\sin(2\pi f t). \tag{6.2}$$

Following from the wing movement the non-dimensional time can be defined:

$$\tau = \frac{t}{T}, \tag{6.3}$$

with T the period of the flapping motion: $T = 1/f$. The relevant non-dimensional numbers are the Reynolds number, non-dimensional stroke amplitude, mass and frequency ratio:

$$Re = \frac{\pi A_0 f c}{\nu_f}, \qquad A^* = \frac{A_0}{c}, \tag{6.4}$$

$$m^* = \frac{\rho_s h}{\rho_f c}, \qquad FR^* = \frac{f}{f_n}.$$

where f_n is the frequency of the first bending eigenmode of the wing. The frequency ratio (FR) is a measure for the flexibility of the flap with respect to the fluid forces and is used to define the relative

importance of elastic and inertial forces. Previous research by Vanella et al. (2008); Luo et al. (2010); Dai et al. (2012) has shown that there is an optimum in the frequency ratio such that the wing has the highest efficiency. For the simple wing considered in this chapter with a mass ratio of 1, the maximum lift was attained at a frequency ratio of 1/3. The maximum lift over drag ratio is found for even higher flexibilities, since the drag for this wing decreased with higher flexibility.

The mass ratio (m^*) defines the ratio between the aerodynamic forces and the inertial force. Luo et al. (2010) showed that for a simple flapping wing with no active pitching the drag increases for higher mass ratios. The forces generated by the airflow typically bend the wing into a shape with a lowered angle of attack, reducing the frontal area and thus the drag. High mass ratio wings lose this benefit because their shape is more determined by the wing inertia.

The parameters used to set up the simulation are given in table 6.1.

Table 6.1: Set-up for the flexible flapping wing

Parameter	Value
c [m]	$1 \cdot 10^{-2}$
h [m]	$5 \cdot 10^{-4}$
ν_f [$m^2 s^{-1}$]	$5 \cdot 10^{-5}$
ρ_f [$kg m^{-3}$]	10
f [s^{-1}]	1.910

The structural properties of the flap can then be determined for the different values of the mass and frequency ratio. In section 5.3 it was found that the structural solver tends to over-predict the stiffness of the structure for any spatial discretisation. Therefore the Young's modulus was estimated using the analytical expression in equation 6.6 after which it was fine-tuned in a frequency analysis by the structural solver. The resulting model has an eigenfrequency which approaches the desired frequency ratio within 0.01%:

$$\rho_s = \frac{m^* \rho_f c}{h}, \tag{6.5}$$

$$E = \frac{12\rho_s}{h^2}\left(\frac{c}{k_n}\right)^4 \left(\frac{2\pi f}{FR}\right)^2. \tag{6.6}$$

where k_n is a constant for a given eigenfrequency.

The flexible definition of parameters easily allows for the choice of different settings. The mass ratio can be increased to increase the relative effect of inertial over aerodynamic forces. Three different mass ratios are tested as shown in table 6.2. In flapping wing analogy, the lowest mass ratio is comparable with a dragonfly wing, the $m^* = 5$ wing is close to a moths wing (Daniel & Combes, 2002). For the highest mass ratio the wing deformation is largely determined by the inertial forces (Luo et al., 2010).

Table 6.2: Structural parameters for the flexible wings

m^* [-]	ρ_f [$kg m^{-3}$]	E [$kg m^{-1} s^{-2}$]		
		$FR = 1/6$	$FR = 1/4$	$FR = 1/3$
1	200	$3.295 \cdot 10^4$	$1.465 \cdot 10^4$	$8.240 \cdot 10^3$
5	1000	$1.647 \cdot 10^5$	$7.320 \cdot 10^4$	$4.117 \cdot 10^4$
25	5000	$8.235 \cdot 10^5$	$3.660 \cdot 10^5$	$2.059 \cdot 10^5$

6.2. Mesh sensitivity study

For the mesh sensitivity study a rigid wing is selected. $A_0 = 2.5c$ and $\beta = \pi/8$ in equation 6.1 define the sweeping and rotation of the wing. A small pitching angle is used to assert some asymmetry in vertical direction to the flowfield, and to generate a finite average lift. An O-grid is shaped around the wing and extruded for 40 chord lengths to form a circular domain. A large domain is required to avoid large recirculation of shed vortices in the domain which create chaotic behaviour. A free inflow/outflow and zero pressure is applied on the outer boundary. The mesh surrounding the wing is shown in figure 6.1 for the coarsest grid.

Under the sweeping and rotational motion the mesh is deformed by solving the laplacian equation for the mesh displacement. To assure the deformation performs well and the mesh quality is preserved two measures were taken. Firstly, the leading and trailing edge were rounded. According to Usherwood & Ellington (2002) the shape of the leading edge is of relative low importance for the overall flowfield, so the round-off is not expected to have a serious impact on the flow simulation. Furthermore, the mesh cells are grown perpendicular with respect to the wing surface. It was found that this reduced the chance of large skewness or even cell collapse.

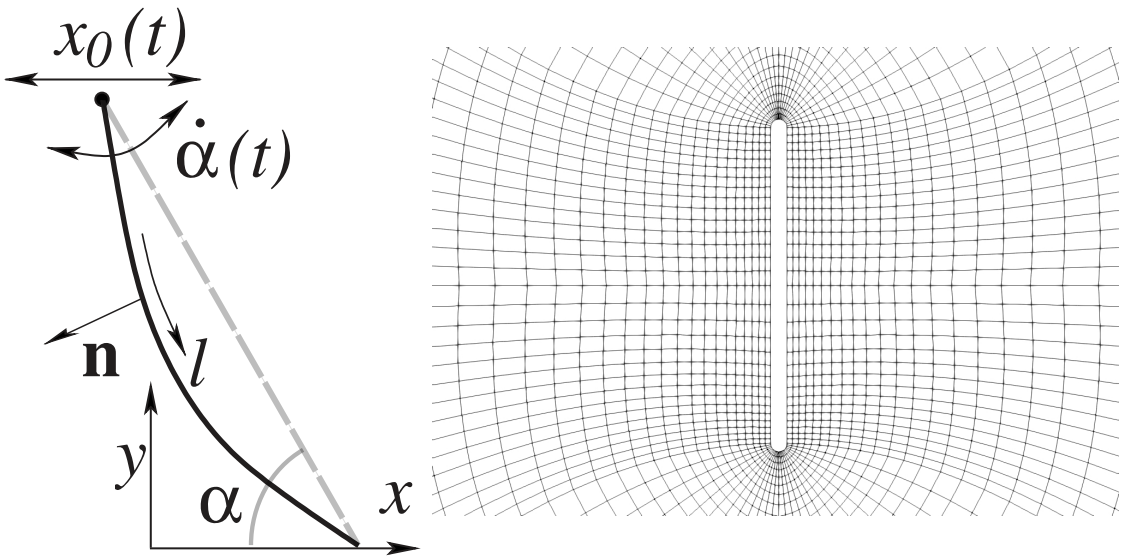

Figure 6.1: The flapping wing (left) definition of the motion, from Luo et al. (2010). (right) The mesh at rest position. An O-grid is shaped around the wing with a strong preference to perpendicular cells near the wall to facilitate a more robust mesh deformation. The wing has a chord of $c = 0.01$m and a 5% thickness. The motion is defined at the leading edge at the top of the wing.

The force coefficients are evaluated for three meshes of increasing refinement. The coarse mesh has 4,968 elements. The normal and fine mesh feature respectively 19,440 and 77,760 elements. The wing surface is refined with respectively 54, 108 and 216 cells, which leads to an average mesh spacing of approximately $0.02c$ for the coarsest mesh. This is comparable to the mesh spacing used for the immersed boundary mesh that Yin & Luo (2010) used around the wing.

Figure 6.2 shows the phase-averaged lift and drag over the wing for 6 flapping periods. The drag is defined as the force opposite to the direction of travel, so the drag vector changes direction during supination and pronation. The range in which the lift and drag occurred over this range of periods is shaded. From $\tau = 0$ to $\tau = 0.5$ the wing is in upstroke. While the wing kinematics imposed to the flap movement are completely symmetric, the lift and drag show very different graphs for the up- and downstroke. This means that the flow is determined to a large extend by the shed vortices of the previous motion.

The average value for the lift and drag (shown in table 6.3) shows good correlation too. The

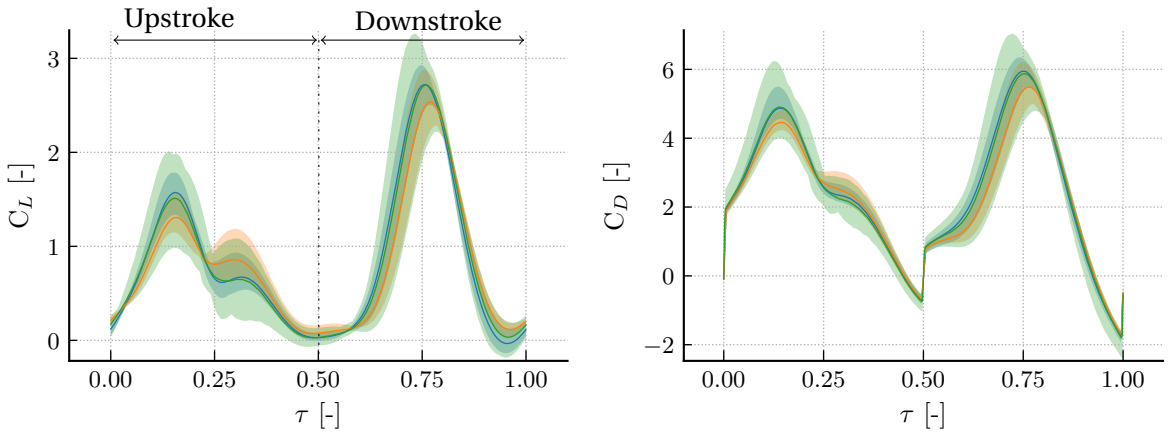

Figure 6.2: (left) Lift and (right) drag coefficients for one flapping period. The line represents the average value over 6 periods, and the shaded area represents the range perceived during these periods. — Coarse, — Normal and — Fine mesh.

average maximum deviation for the lift coefficient is defined by:

$$\Delta C_l = \frac{Avg(C_{l_{max}}) - Avg(C_{l_{min}})}{2}, \tag{6.7}$$

such that range of range of possible lift coefficients can be estimated by:

$$C_{l_{Avg}}(\tau) - \Delta C_l < C_l(\tau) < C_{l_{Avg}}(\tau) + \Delta C_l \tag{6.8}$$

The same can be done for the drag coefficient. Taking the finest mesh as the most accurate solution, both the coarse mesh and the normal mesh fall within the range of the average force value plus or minus the average maximum deviation. Over the range of the motions over 6 periods, it is clear that the average lift and drag of the coarse mesh fall within the possible values for the normal mesh and fine mesh.

The mesh deformation method described earlier performs significantly better with coarser meshes. It is less prone to collapse under large rotation and deformation. Since the behaviour of the coarse mesh shows good correlation with the fine mesh, it is selected to investigate the effect of different mass and frequency ratios.

Table 6.3: Average lift and drag coefficient and the average maximum deviation over 6 periods

Refinement	C_l [-]	ΔC_l [-]	C_d [-]	ΔC_d [-]
Coarse	0.82	0.10	2.46	0.22
Normal	0.79	0.11	2.29	0.23
Fine	0.83	0.26	2.47	0.59

6.3. Results

To investigate the effect of the mass ratio m^* and frequency ratio FR, flexibility is added to the wing according to the parameters given in table 6.2. Furthermore a rigid wing with the same kinematics is tested to obtain the limiting case of $FR = 0$. The wing kinematics are defined by a pure sweeping motion: $A_0 = 2.5c$ and $\beta = 0$. This entails that the wing can only obtain an angle of attack by structural bending.

6.3.1. Average forces and force history

The effect of the mass ratio on the force history is shown in figure 6.3 for four wings: Rigid and $m^* = [1,5,25]$. All flexible wings have a frequency ratio of $FR = 1/3$. The first eigenfrequency is noted for all three wings as the oscillation with a value three times the flapping frequency.

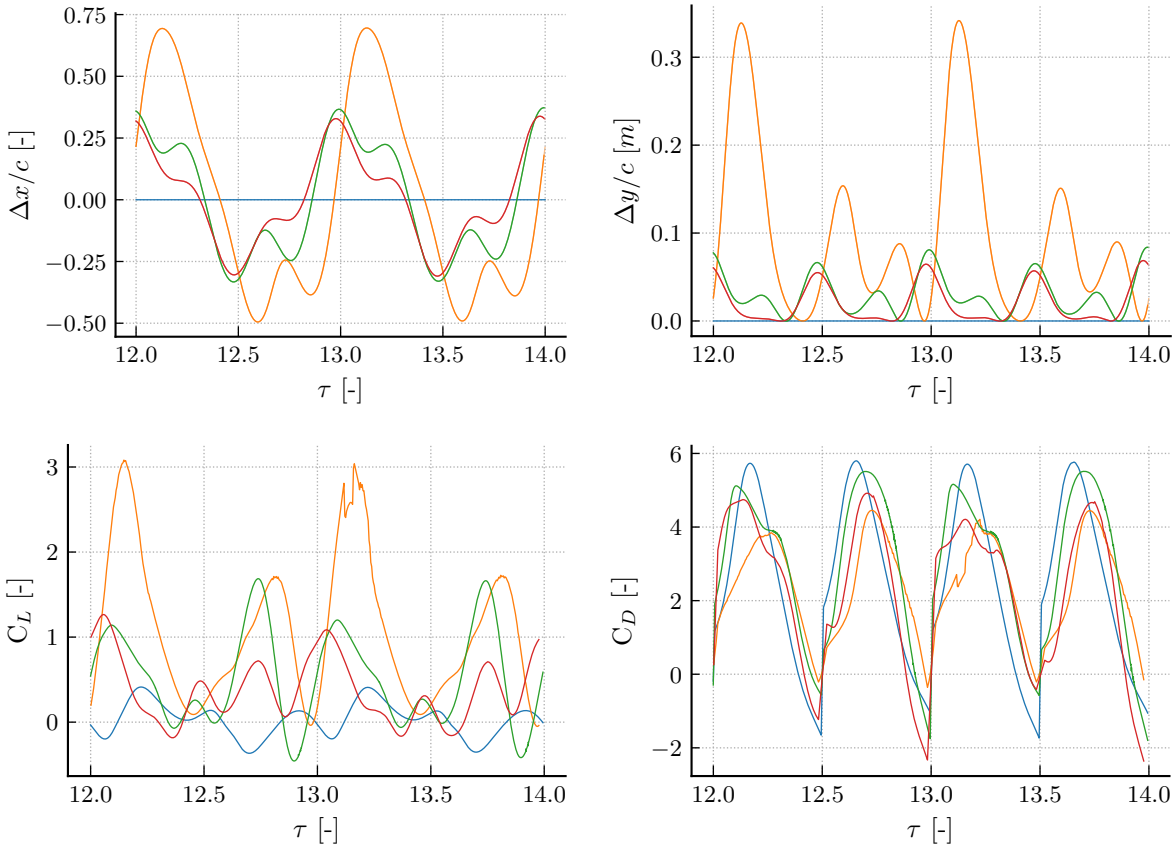

Figure 6.3: Influence of the mass ratio m^* on the (top) tail x- and y displacement and (bottom) lift and drag coefficient over two flapping periods. —Rigid, —$m^* = 1$, —$m^* = 5$, —$m^* = 25$

The tail deflection with respect to the rigid position shows that the wing with the smallest mass ratio has a phase delay with respect to the two heavy wings. Furthermore the deflection of the wing is much larger, with a maximum horizontal deflection of approximately 0.7 chordlength. The delay and larger amplitude of the deflection means that the light wing creates a lower angle of attack during both the up- and downstroke. In both these strokes a large portion of lift is created, whereas the drag is comparable or smaller to the other wings. Large asymmetry is caused because the shedding behaviour between both strokes is different, as will be treated later.

Small differences can be seen between the $m^* = 5$ and $m^* = 25$ wing but these are far less pronounced than the differences with the lightest wing. For both these wings the deflection is nearly symmetrical between up- and downstroke, while the aerodynamic forces are not. This indicates

that the motion is determined by the (symmetrical) wing kinematics. As soon as the wing decelerates during midstroke, the deflection in x-direction changes sign. During both the middle part of the up- and downstroke the $m^* = 5$ wing maintains a higher deflection, which is caused by a LEV which stays closely attached to the wing. The low pressure favours a larger lift and drag creation during this phase of high translational velocity. During the latter part of the stroke a small portion of thrust is created by the wing because of the advanced rotation.

In figure 6.3 the lift and drag profile for the wing with $m^* = 1$ shows irregular behaviour at the point of large displacement. The discontinuous force coefficients are caused by large fluctuations in the pressure field between timesteps. This represents the limits of the current mesh deformation method. Smaller frequency ratios and mass ratios are not feasible to model with the current simulation basis. Figure 6.4 shows failure of the mesh deformation method the case with $m^* = 0.5$ and $FR = 1/3$.

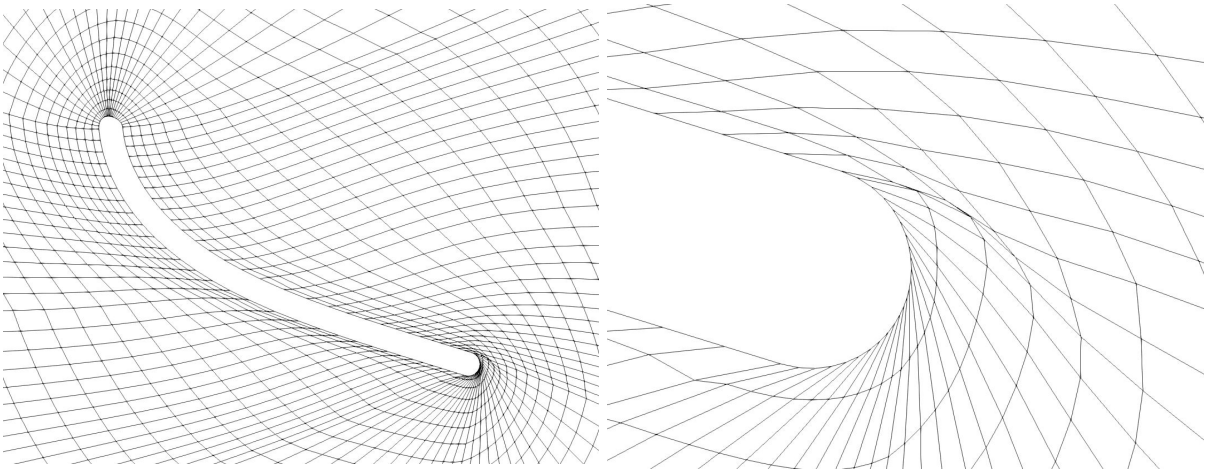

Figure 6.4: Collapse of the fluid mesh for $m^* = 0.5$ and $FR = 1/3$. (left) final timestep of the of the simulation. (right) detail of the trailing edge with mesh failure.

The effect of wing flexibility is determined by the frequency ratio and influences the wing in a different manner. Figure 6.5 shows the tail deflection and force coefficient of four wings: Rigid wing ($FR = 0$) and three flexible wings with $FR = [1/6, 1/4, 1/3]$ for a mass ratio of 1. The flexible wings show deflection with similar behaviour for all three frequency ratios. The flexible wing is close to a scaling of the two stiffer wings.

The effect of a higher stiffness causes the elastic effect to dominate the wing movement in the latter part of the stroke. During the first part of the stroke, the wing is deflected by the wing acceleration (inertial force). The aerodynamic forces can help to maintain this deflection during the latter part of the stoke and prolong a lower angle of attack. See for instance the second peak near the $\tau = 12.8$ for all wings. Nevertheless, a larger wing stiffness advances the wing rotation, which has a large effect on the lift created during the latter part of the stroke.

A larger deflection causes a lower angle of attack and decreases the frontal area. The drag history shows a clear that the drag is reduced for a large portion of the stroke for more flexible wings. However, the advanced rotation by the stiffer wings create a small portion of thrust, as also seen for the rigid wing. This lacks for the most flexible wings.

Figure 6.6 displays the average lift and drag coefficient, and lift over drag ratio for all the tested wings over 15 flapping periods. A wing with an even lower mass ratio of $m^* = 0.5$ is incorporated for two additional mass ratios, which indicates the limit of the method. Furthermore, the data from Luo et al. (2010) is shown on the bottom row for same wing geometry and kinematics. In this work the wing was tested up to frequency ratios of 0.8 for which the flapping frequency almost equals the wings eigenfrequency.

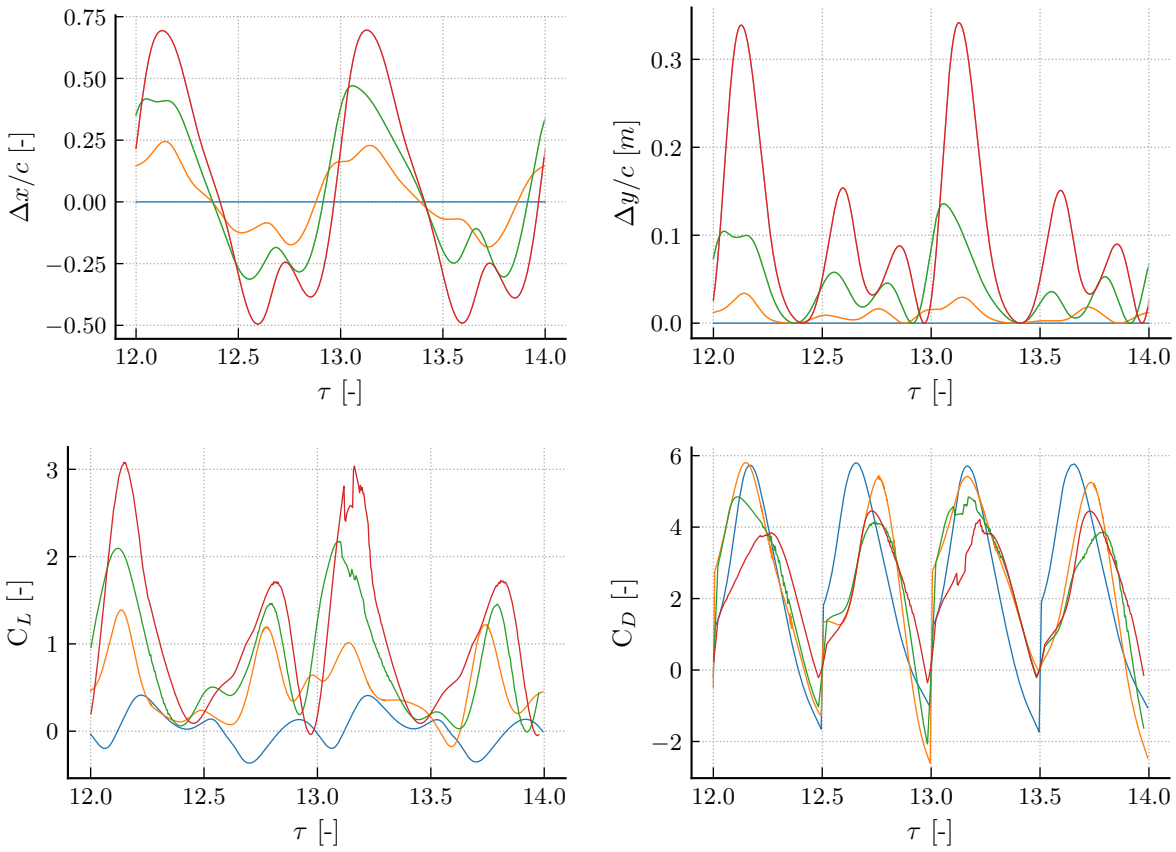

Figure 6.5: Influence of the frequency ratio *FR* on the (top) tail x- and y displacement and (bottom) lift and drag coefficient over two flapping periods. —Rigid, —*FR* = 1/6, —*FR* = 1/4, —*FR* = 1/3

For the tested range of flapping frequencies any flexibility increases the lift over the wing. The wing bending creates a lower angle of attack which points the residual fore more towards the lift direction. Furthermore, a clear relation can be distinguished between the mass ratio and the lift. Lower mass ratios lead to a higher lift for this range of the frequency ratio. This result is also seen for the reference data. The relative higher importance of the aerodynamic forces with respect to the inertial forces helps in maintaining a lower angle of attack throughout the latter part of the stroke. The highest lift coefficient is obtained for the $m^* = 1$ and $FR = 1/3$ wing with a value of 1.076.

The drag shows interesting behaviour for the different mass ratios. It appears that the delayed rotation of the wing for low mass ratios helps in decreasing the drag on the wing by reducing its frontal area. The advanced rotation by the heavier wings initially increases the drag. The peak for the $m^* = 5$ wing at a frequency ratio of $FR = 1/3$ is featured in both the reference data and the simulated data. This point is interesting since it shows a different behaviour for the wings with $m^* = [5, 25]$ and $FR = 1/3$. Up to this point the lift and drag of these two wings were very similar. In the following section the flowfield around this wing is shown to explain the large difference.

For this frequency range a straightforward relation is seen between the lift to drag ratio. A more flexible wing leads to higher ratios. Also the lightest wings create higher lift over drag ratios by means of a high lift creation. This is in good agreement with Luo et al. (2010) who shows the same trend for this range of frequency ratios.

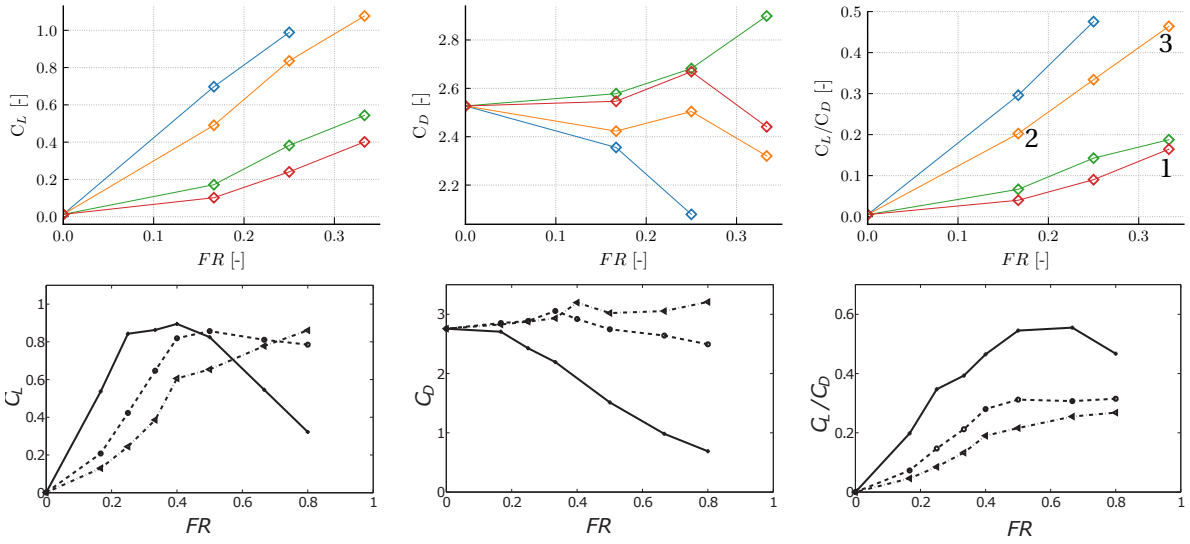

Figure 6.6: Average (left) lift and (middle) drag coeffient, and (right) lift over drag ratio for different mass ratios. (top) FSI simulations with —$m^* = 0.5$, —$m^* = 1$, —$m^* = 5$ and —$m^* = 25$. (bottom) the reference case from Luo et al. (2010) with —$m^* = 1$, - - $m^* = 5$ and -·-$m^* = 25$. Note the scale difference on the x-axis between the top and bottom figures. For both the FSI simulations and the reference data the forces are averaged over 15 periods. The flowfield of points 1, 2 and 3 is shown in section 6.3.2

6.3.2. Flowfield

In figure 6.7 the vorticity flowfield around three wings is shown for one flapping motion. The vorticity is normalised according to:

$$\omega^* = \omega \frac{U}{c} \tag{6.9}$$

The left column indicates the wing in which the inertial force is dominant: $m^* = 25$, $FR = 1/3$, named hereby wing 1. The middle figure shows the wing 2 with dominance of the elastic forces: $m^* = 1$, $FR = 1/6$. The latter column shows the wing 3 for which the three forces are more balanced.

This wing features the highest lift and lift over drag ratio in the tested range.

All three cases shows a similar shedding of the vortices. In the beginning of the period ($\tau = 0.1$), the LEV of the previous stroke remains close to the wing surface and is convected both above and below the wing after stroke reversal. The wake capturing causes rapid build-up of vorticity on the leading edge, but the newly formed LEV can not stay attached closely to the wing ($\tau = 0.3$). At stroke reversal ($\tau = 0.5$), the LEV catches up with the wing and it is shed under the wing and forms counter rotating vortex pair with the previous TEV. The shed vortex pair has a larger downward component for wing 3 compared to the other wings. This indicates that it is more efficient in inducing downward momentum in the flow, while the other wings create a larger horizontal momentum.

Without the wake capturing, the formation of a new LEV takes longer, and around ($\tau = 0.7$) a compact core can be seen around the LE which has grown to a large LEV with significant force contribution near the end of stroke.

The effect of the mass ratio is most evident by the phase of the flapping motion. Neglecting the amplitude of the deflection, the shape of the wing 3 is often similar to that of wing 1 in for $\tau - 0.2$, which indicates a phase delay of $1/5^{th}$ of a period.

Comparing the effect of the wing frequency ratio shows that the vortical structure of the flows are very similar. Also the flap displacement shows smaller effect of the phase delay. Only at $\tau = 0.9$ wing 2 is clearly already near 90° angle of attack, while wing 3 still has a much lower value. The main difference in flowfield is caused by the lower angles of attack of the flexible wing. This helps pointing the resulting force in the direction of the lift vector, while reducing the drag at the same time. For wing 1 the upstroke has a larger deflection and is responsible for the major part of lift production. This effect is much less pronounced for wing 2, since its shape is more determined by elastic forces.

The differences for the heavy wings with $m^* = [5,25]$ and $FR = 1/3$ were already noted before in figure 6.6. In figure 6.3 it was already noted that the deflections and forcefield of these two wings were very similar apart from the latter part of the upstroke, around $\tau = 12.8$.

In figure 6.8 the pressure field is shown on the wing. Here the low pressure field is caused by the attached LEV. For the heavy wing the LEV is too insignificant to counter the inertial forces, however this is different for the wing with $m^* = 5$. As a result of the lowered angle of attack, the LEV stays attached more closely with a large effect on the forces on the wing.

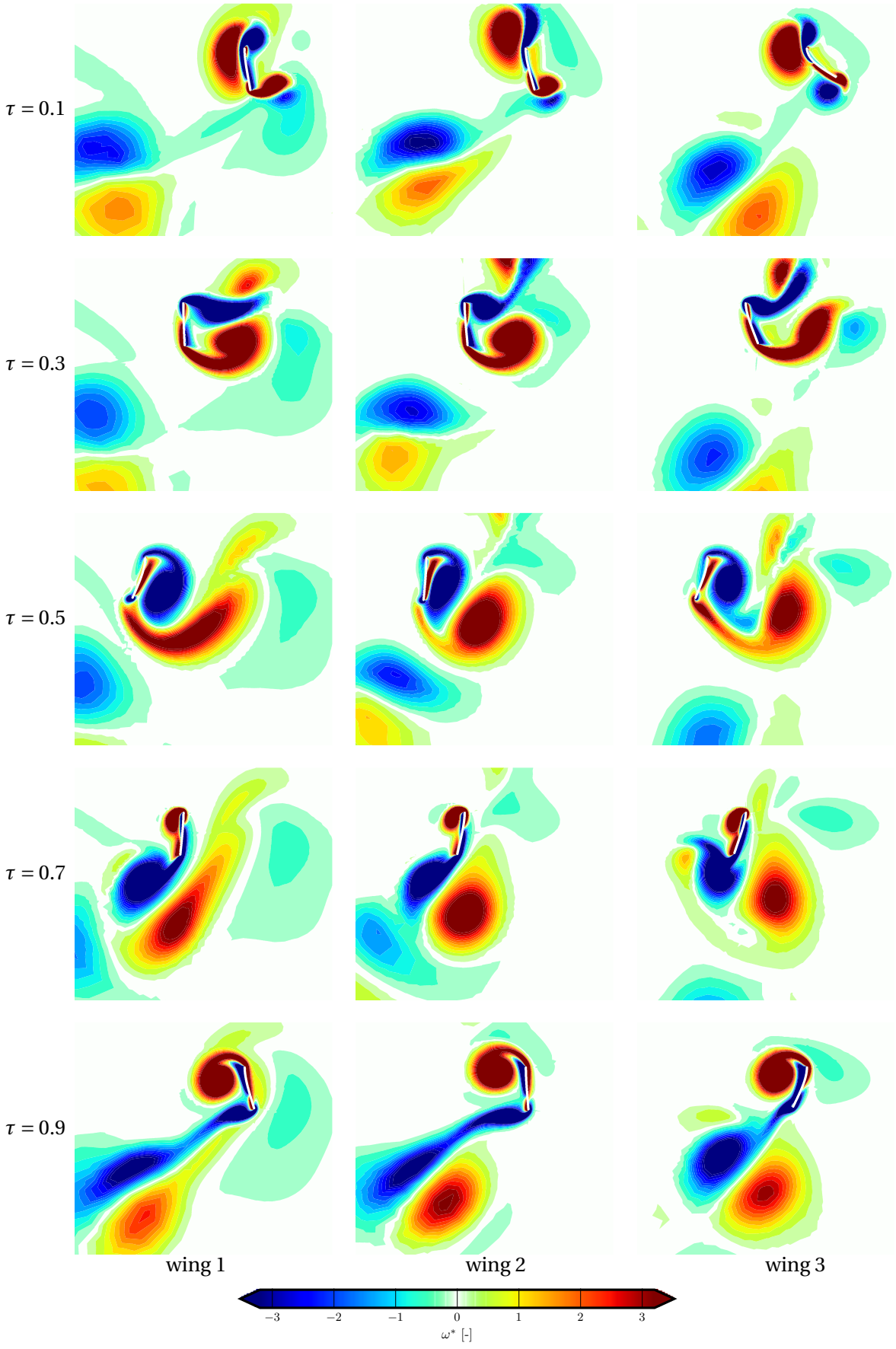

Figure 6.7: Non-dimensional In-plane vorticity (left) Inertia dominated wing with $m^* = 25$ and $FR = 1/3$. (middle) Stiffness dominated wing with $m^* = 1$ and $FR = 1/6$. (right) inertial, aerodynamic and elastic forces in equilibrium with $m^* = 1$ and $FR = 1/3$. A representative period is taken and the time instance is scaled to the time.

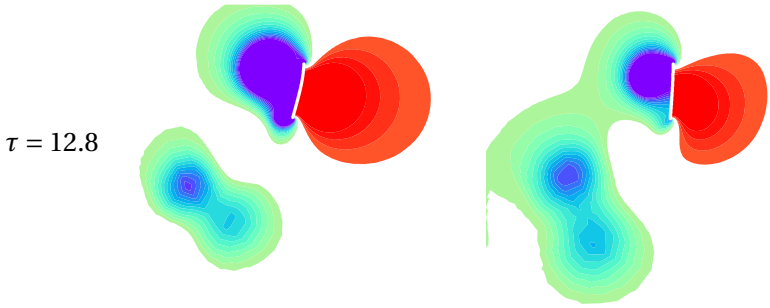

Figure 6.8: Pressure distribution for the wings with frequency ratio $FR = 1/3$ and mass ratio (left) $m^* = 5$ and (right) $m^* = 25$. The low pressure field of the LEV is much stronger for the lighter wing.

6.4. Conclusions

The chapter above treats the influence of different degrees of stiffness and mass of a flapping wing 2D wing. In this way it is tested whether the FSI method developed in chapter 4 is able to capture well the relative importance of the various forces that occur on the flapping wing. To do so, a simple translation motion is prescribed without any pitching. The stiffness and mass of the wing determine the relative effect of the inertial and elastic forces and can be related to the aerodynamic forces by defining the frequency ratio (FR) and mass ratio (m^*).

A large mass ratio renders the fluid forces insignificant due to high inertial forces. The wing deformation is determined by the wing kinematics and hardly by the influence of the flowfield. As soon as the wing starts to decelerate during midstroke the wing deflection is reversed shortly after. A light wing shows a deflection which causes lowered angle of attack during almost the entire stroke because the aerodynamic forces help to sustain the angle of attack.

The advanced rotation of the higher mass ratio wings is not beneficial for the production of lift. For the investigated range of flapping frequencies, a lower mass ratio always leads to a higher lift and lift over drag ratio.

The influence of the frequency ratio is more predictable. The deflection is lower for stiffer wings which creates lower lift and higher drag. The more rigid wings show a slight advance in pitching behaviour.

The horizontal flapping motion creates an asymmetric flowfield between the up- and downstroke which was present for every combination of the mass ratio and frequency for the tested cases. The wings with a relative large influence from the aerodynamic forces to be are influenced by the asymmetry in the flowfield and show a difference in deflection between the up- and downstroke. Especially for the wing with $m^* = 1$ and $FR = 1/3$ this difference is pronounced. Wings dominated by either elastic or inertial forces are less affected by the flowfield and show more symmetric deflection of the trailing edge.

The results regarding the influence of the mass and frequency ratio obtained in this chapter are in good agreement with those by Luo et al. (2010). Therefore the FSI module is able to simulate the relative importance of the various forces in flapping wing aerodynamics.

Chapter 7

Flexible Wing Modelling

The FSI method described in the previous section is applied to model moving wing motion. The interaction around a 2D flapping wing is shown in chapter 6 with the formation of the LEV and TEV. However, the aerodynamics on wings of insects and MAVss can be described best by enhancing a 3D model. Adding another dimension to the FSI method brings new challenges which are addressed in the following sections.

In this chapter a 3D flexible wing is modelled in both a translating and a revolving motion. The wing model is based on the experimental campaign from 2016 performed by van de Meerendonk (2016). The set-up of the simulation is treated first in section 7.1. The chord based Reynolds number is 10,000, so the assumption that the flow can be solved laminar may not be valid. The trade off for adding a turbulence model is treated in section 7.2.

The obtained flowfield and structural deformation from the revolving wing are compared to the experimental data. Here the obtained wing forces can be compared as well as the vortical structures.

7.1. Model Description

The wing model considered in the simulation is a simple flat plate with a rigid leading edge. The wing has span of b = 100mm and a chord length of c = 50mm, which leads to an aspect ratio of 2. The root of the wing is located at R_{Root} = 42mm from the axis of rotation. The reference radius for the wing kinematics is taken at 75% of the span, which leads to a radius of R_{ref} = 117mm.

7.1.1. Structural model

In this analysis three different wings were tested for both the translating and the revolving case. First, a rigid wing is considered which was evaluated by only solving the fluid field. Next two wings of varying flexural stiffness were evaluated. The flexibility of the wing is expressed in the flexural stiffness:

$$EI = E\frac{bh^3}{12}. \tag{7.1}$$

where h represents the wing thickness.

In the experimental campaign, one quasi rigid wing with a high stiffness, and two flexible wings with different flexural stiffness were tested. The properties in the simulation for the first flexible wing were selected to represent the most flexible wing tested in the experimental campaign. For the second flexible wing the flexural stiffness was decreased by a factor two, to obtain a very flexible wing. See table 7.1 for the material properties. The wing thickness is kept constant, so only a change of the Young's modulus is required. The ratio between the elastic forces and the aerodynamic forces is represented by the effective stiffness given by equation 2.19. The values presented in the table are computed without the influence of the Poisson's ratio.

In the experiment the leading edge was kept rigid by a carbon fibre rod which had a diameter of 3mm. The wing thickness varied over the different runs, since three models were tested. It is assumed that the influence on the flow caused by a difference in thickness between the rod and

wing is small, therefore the wing is modelled as a simple flat plate with a standard thickness 5% of the wing chord or $h = 2.5$mm. Since in previous analysis it was found that the structural solver in the coupled simulation could behave unstably if the structural density was too low, a density of 1,000kg m^{-3} was assumed for all models to preserve the density of the wing. The mass ratio can be derived using equation 6.4 which was used in the previous chapter for the 2D wing. Different mass ratios are seen for the experiment and the simulation because of the larger thickness that was used in the numerical model, however the small mass ratios indicate the deformation is influenced more by the aerodynamic forces.

The Poisson ratio was assumed to be $\nu = 0.3$. The effect of the wing weight was assumed to have a minor influence on the deflection of the flap, and gravitational effects are not incorporated too. At last, acceleration and rotational forces are not modelled in the structural model, so the inertial forces of wing acceleration are not evaluated. The wing is discretised with respectively 26 and 50 elements in chordwise and spanwise direction. The flap is one element thick, which leads to a total amount of 1,300 finite elements.

Table 7.1: Structural properties of the wing model.

Model	E [kg m^{-1}s^{-2}]	h [m]	I [m^4]	EI[kg m^{3}s^{-2}]	Π_1 [-]	m^* [-]
			Experimental			
Rigid	$3.30{\cdot}10^9$	$1.00{\cdot}10^{-3}$	$8.33{\cdot}10^{-12}$	$2.75{\cdot}10^{-2}$	55	1/50
Exp1	$4.50{\cdot}10^9$	$1.75{\cdot}10^{-4}$	$4.47{\cdot}10^{-14}$	$2.01{\cdot}10^{-4}$	0.389	1/286
Exp2	$4.50{\cdot}10^9$	$1.25{\cdot}10^{-4}$	$1.63{\cdot}10^{-14}$	$7.32{\cdot}10^{-5}$	0.147	1/400
			Numerical			
Rigid		$2.50{\cdot}10^{-3}$	∞			
Medium	$5.63{\cdot}10^5$	$2.50{\cdot}10^{-3}$	$1.30{\cdot}10^{-10}$	$7.32{\cdot}10^{-5}$	0.147	1/20
Flexible	$2.81{\cdot}10^5$	$2.50{\cdot}10^{-3}$	$1.30{\cdot}10^{-10}$	$3.66{\cdot}10^{-5}$	0.073	1/20

7.1.2. Fluid model and discretisation

The fluid domain for the revolving case is shown in figure 7.1, where the axis of rotation is added for visualisation purposes only. The domain has a radius of 0.6m and is 0.6m high. A fluid region with a radius of 0.2m is specified to rotate with the wing while the outer ring is stationary. In this approach, only the deformation of the wing has to be displaced on the mesh and not the entire movement. The wing is submerged in water under room temperature. The dynamic viscosity is $1.0 \cdot 10^{-6}$ m^2 s^{-1} and the density is 1,000kg m^{-3}.

The wing is modelled using round leading and trailing edges. As was found in chapter 6, this enhances the stability of the mesh deformation method, while not largely affecting the flow field, as found by Usherwood & Ellington (2002).

A similar approach is taken for the translating case. The same wing is modelled in a channel with height, width and length of 0.8m. Since the geometry of the fluid domain is symmetrical around the midplane, only half of the domain is modelled with a asymmetry condition. This is allowed when it is assumed that the asymmetry in the flow is small. For both the revolving and translating cases the wing spans in the z-direction, and the location of the leading edge is fixed on the xy-plane at (0, 0)m. Here the wing movement is modelled by accelerating the flow through the channel.

For both motions refinement is applied to capture the regions around the wing in more detail than the surrounding flow. The wing is discretised with 90 mesh elements in chord-wise direction for the translating wing and approximately 100 elements for the revolving wing. In span-wise direction 120 cells are used for the half wing of the translational case and approximately 270 cells for the full span of the revolving wing. Note that the circular domain has more mesh refinement in the

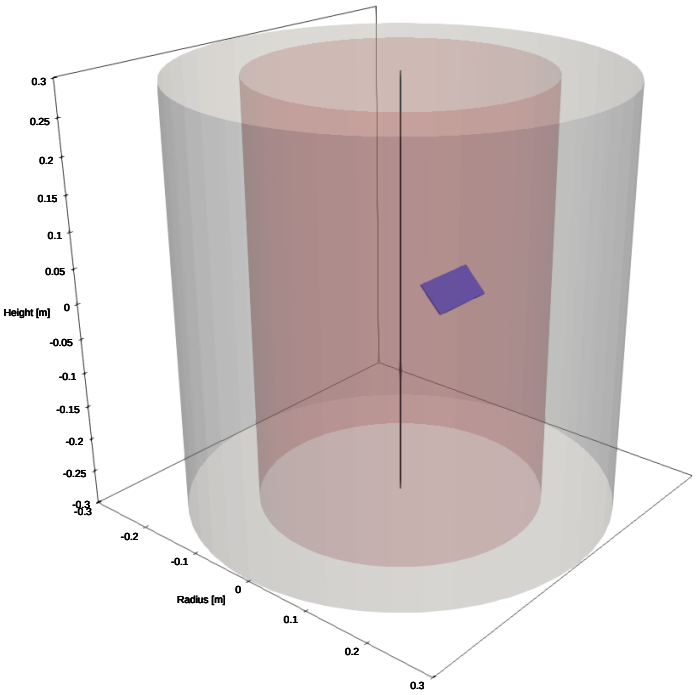

Figure 7.1: Domain of the revolving wing.

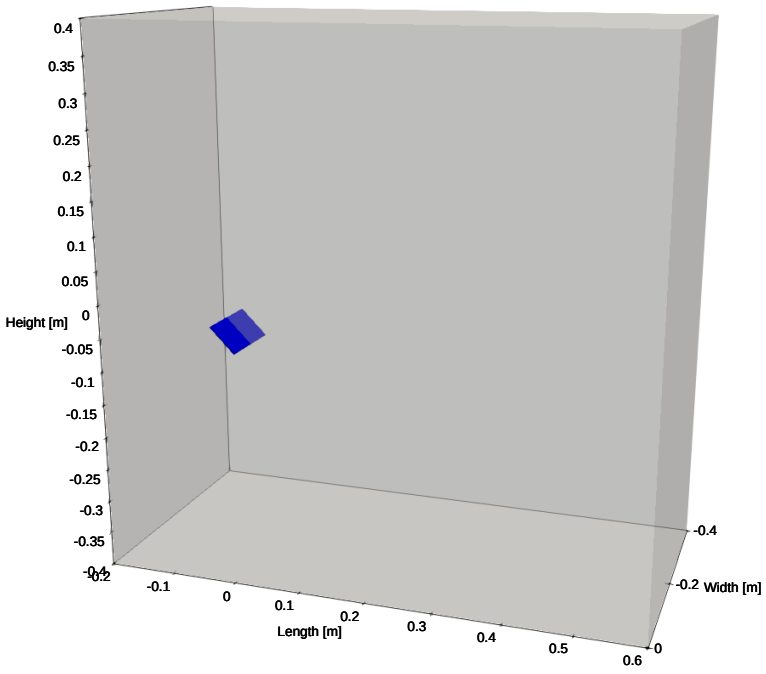

Figure 7.2: Domain of the translating wing.

inner region. In total the mesh of the translational and revolving case contain respectively 1,802,617 and 5,356,085 cells.

All runs for both the translating and the revolving flapping wing were performed using a fixed timestep and no subcycling of either solver. All translational cases and the two revolving cases were solved using a timestep of $\Delta t^* = 2 \cdot 10^{-3}$. The most flexible revolving wing required a smaller timestep for a stable simulation, therefore the value of $\Delta t^* = 8 \cdot 10^{-4}$ was used.

Because the flap can expand and shrink under load application, the total volume of the domain can change by a small amount. For the incompressible solver this means that at least one of the boundaries must allow in- and outflow, otherwise numerical instability will occur. For the revolving case the top boundary was chosen to allow in- and outflow from the domain. The other boundaries are modelled as walls. For the translational case an inflow and outflow are specified.

The force computation relies on both pressure and viscous stresses to compute the force vector, the latter requires a refined mesh spacing near the wing surface to capture the details of the boundary layer. For a simple turbulent boundary layer, three regions can be distinguished: the inner, overlap and outer layer. In the inner layer, the viscous sub layer is the very thin region near the wall, where the velocity profile is linear as seen in equation 7.2 (White, 2005, p. 414). The nondimensional wall distance and velocity are determined based on the wall friction τ_w, wall friction velocity v^*, wall distance y and free stream velocity $\bar{u}$.

$$u^+ = y^+, \qquad \text{for } y^+ \leq 5, \tag{7.2}$$

where,

$$u^+ = \frac{\bar{u}}{v^*}, \qquad y^+ = \frac{y v^*}{\nu}, \qquad v^* = \sqrt{\frac{\tau_w}{\rho}}.$$

Figure 7.3 shows the distribution of the y^+ on the wing surface. The mesh spacing is chosen to make sure the y^+ is smaller than 5 for the majority of the plate, such that the linear region is captured well. In term, the viscous stress can be computed accurately. Some regions exist where the velocity is high, and therefore the y^+ is increased. This is pronounced at the location of the LEV on the top boundary, and the flow around the tip. However, the relative small amount of cells where the y^+ is too large for the assumption of a linear velocity profile is not expected to influence the viscous force on the wing to a large extend.

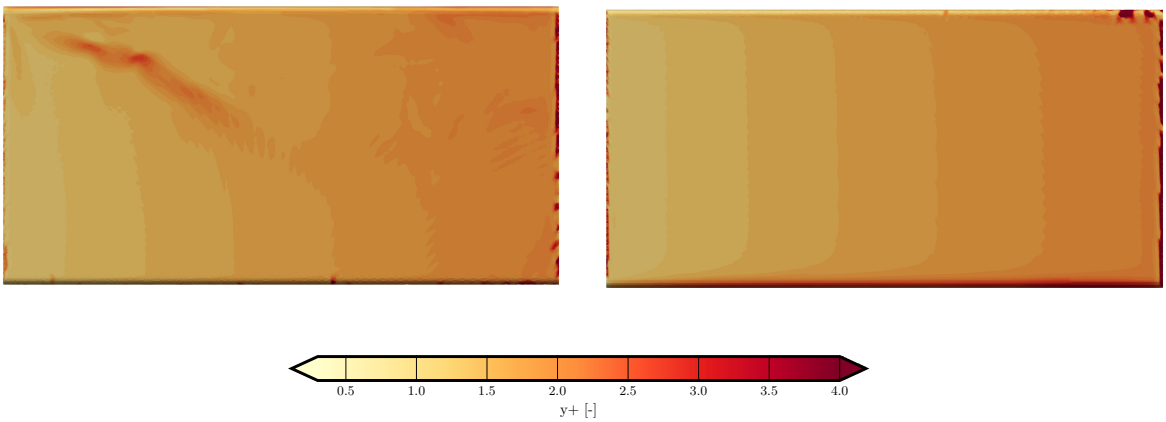

Figure 7.3: Surface of th y+ on the (left) top and (right) bottom side of the revolving wing at $\delta^* = 1$. The root is located on the left part of the figures.

7.1.3. Kinematics and Initial conditions

The revolving wing is accelerated until the terminal velocity is obtained of 0.2m/s at the reference radius. A Reynolds number of 10,000 is reached at the reference radius. The kinematics are expressed in the convection time of the fluid (t^*) and the chords travelled (δ^*):

$$Re = \frac{V_t c}{\nu} = 10,000, \tag{7.3}$$

$$t^* = t\frac{V_t}{c},$$

$$\delta^* = \frac{\delta}{c} = \frac{R_{\text{ref}}\theta(t^*)}{c}, \tag{7.4}$$

where θ denotes the angle travelled by the wing. For the revolving wing $\delta^* = 1$ is equal to an angle of $\theta = 24.49°$.

Spanwise characteristics are defined using the ratio between the local span and total span: r/R. This ratio is defined zero at the root and one at the tip, which is in contrast with the definition of the root and tip radius. ($R_{\text{root}} = 42$mm and $R_{\text{tip}} = 142$mm). The simple range from 0 to 1 is chosen for convenience in explanation of the spanwise flow phenomena on the wing.

The wing Rossby number is computed using the radius of gyration which is based on the area moment of inertia about the axis of rotation I, as given in equation 2.14. The Radius of gyration is $R_G = 96$mm Furthermore, the local Rossby numbers can be found based on the span. These provide a measure for the relative importance of the rotational forces along the span:

$$Ro = \begin{cases} R_{\text{root}}/c = 0.84 & \text{Minimum at the root,} \\ R_G/c = 1.93 & \text{At the radius of gyration,} \\ R_{\text{tip}}/c = 2.84 & \text{Maximum at the tip.} \end{cases} \tag{7.5}$$

The wing is accelerated up to $t^* < 2$, after which the terminal velocity is reached. For the experimental campaign the wing underwent a constant acceleration phase after which the acceleration changed instantly to zero. For the numerical simulation, discontinuity in the the acceleration induces large pressure peaks which cause unwanted behaviour in the FSI simulation. Therefore the wing kinematics had to be adapted slightly in order to provide a stable simulation. The velocity profile is given a smooth ramp up to assure the derivative is continuous:

$$\Omega(t^*) = \begin{cases} \frac{1-cos\left(\frac{\pi}{2}t^*\right)}{2}\frac{V_t t^*}{2R_{\text{ref}}} & \text{if } t^* < 2 \\ \frac{V_t}{R_{\text{ref}}} & \text{if } t^* \geq 2 \end{cases} \tag{7.6}$$

Figure 7.4 shows the chords travelled, angular velocity and acceleration. After $t^* = 5$ the wing has travelled exactly four chord lengths at the reference radius. The kinematics for the translational case are similar to those of the revolving wing but instead of the angular velocity the rectilinear velocity is taken. Therefore, the chord based Reynolds number is 10,000 for the entire span.

7.1.4. Flow parameters

The wing creates a finite circulation over time by shedding the TEV. The relation between the lift force on the wing and the circulation can be expressed by the Kutta-Joukowski theorem. This theorem states that the sectional lift (L') on the wing is directly proportional to the circulation (Γ) around the wing for an incompressible flow (Anderson, 2011, p.280). The formulation of the theorem is given by:

$$\Gamma = \oint \boldsymbol{V} \cdot \boldsymbol{ds} = -\frac{L'}{\rho_\infty U_\infty}, \tag{7.7}$$

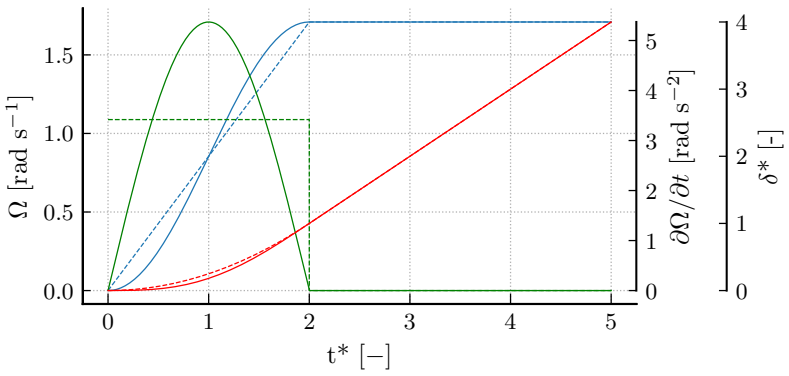

Figure 7.4: Motion of the rotation. Solid lines: In numerical model. Dashed lines: approximation of the motion in the experimental model. —: δ^*, —: Ω, —: $\partial\Omega/\partial t$

where U_∞ is the freestream velocity for the particular wing section. Selecting the spanwise velocity as the reference value the generated circulation can be derived for the wing span. The circulation on the wing can be made non-dimensional by dividing it by the velocity and chord:

$$\Gamma^* = \frac{\Gamma}{V_t c} = \frac{L'(r)}{\rho_\infty r \Omega c V t}. \tag{7.8}$$

The velocity on the wing is normalised by the velocity at the reference location of 75% span-width. The helical density introduced in equation 2.26 is used to represent the spanwise transport of momentum. For this purpose, only the spanwise component of the dot produce between the velocity and the vorticity is considered. The helical density is normalised by the chord and reference velocity.

The same reference velocity is chosen for the translating and revolving case. For the former this inflow velocity is present on the entire span, while the revolving wing experiences a lower velocity for 75% of the span and a higher velocity on the remaining 25%. The consequences of this are shown in section 7.4.

$$U^* = \frac{U}{V_t}, \qquad h^* = \frac{u_z \omega_z}{c V_t^2}. \tag{7.9}$$

7.1.5. Coupling

The FSI on the wing is modelled by mapping the displacement from the structure to the fluid domain. For this mapping thin plate spline (TPS) with a compact support radius of 5mm was adopted. The compact support radius reduces the computational effort that was required for the mapping, since it was noted that the global method required a large amount of time for initialization for the large meshes.

The forces are transferred to the structural boundary using nearest neighbour mapping. Contrary to the cases in the chapters 5 and 6, the domain is three dimensional, which allows the use of nearest neighbour mapping. The choice for this mapping method is driven by computational efficiency.

7.2. Transitional turbulence modelling

The translating and revolving wing introduced in section 7.1 have a chord-based Reynolds number of 10,000. At this Reynolds number, both laminar and turbulent flow can occur, so the effect of flow transition must be evaluated for solution of the simulation. The flow around a wing at high angle attack shows highly unsteady flow structures, a large separated zone and large vortical structures. A validation case which features these flow features is best suitable to test the application of turbulence modelling. The canonical test case by Garmann & Visbal (2011) is used since it features each of the before-mentioned flow properties. The case is described in section 7.2.2.

The geometry and kinematics of the simple wing described in the validation case are recreated and tested for two different methods of turbulence modelling. Firstly, the URANS equations are solved without additional turbulence modelling, leading to a laminar flow where the effects of turbulence are neglected. Secondly the $\gamma - Re_\theta$ model by Langtry & Menter (2009) is tested. This model incorporates transition into the RANS equations and is explained in section 7.2.1.

The force on the simple wing and the flowfield are compared in section 7.2.3. For the flow field PIV data from experiments is used to provide a measure of the error introduced by simulation of this complicated flow field.

The classic RANS models do not allow for laminar zones and thus are very poor in predicting the transitional behaviour around these transitional Reynolds numbers. However, the $\gamma - Re_\theta$ model by Langtry & Menter (2009) performs a basis to predict the transitional behaviour using the RANS equations.

7.2.1. Transitional turbulence model with the RANS equations

The unsteady RANS equations were introduced in equation 3.14. The equations are obtained by separating the flow variables in an average and fluctuating part, and then averaging the equations, which results in an expression for the Reynolds stress tensor. By nature, the averaging has eliminated the growth of linear disturbance which is vital for predicting the onset of transition (Garmann & Visbal, 2011).

However, various ways are available for predicting the onset of transition, such as the e^n method by van Ingen (1956). However, these methods require knowledge of the geometry and mesh. Also, non-local operations are required such following a streamline to track the disturbance growth. Both these properties are difficult to implement in CFD solvers, therefore a method based on local variables is adopted.

The $\gamma - Re_\theta$ model is based on local variables, which makes it suitable for implementation in CFD codes. The central idea is that a relation can be build between the local boundary layer quantities and the transition onset Reynolds number using the strain rate vorticity Reynolds number Re_v and empirical relations. In this way, the transition can be triggered locally and a coupled eddy viscosity model is used to compute for the turbulent fluid properties. The current implementation of the $\gamma - Re_\theta$ is coupled with the SST k-ω model which features two more transport equations (Wilcox, 2008).

The location of transition is predicted using two transport equations. The first is for the intermittency γ. The intermittency is used to trigger the transition locally by scaling the production term of the turbulent kinetic energy. A second transport equation is solved for the transition onset momentum thickness Reynolds number $\overline{Re_{\theta_t}}$. This feature captures the local influence of the turbulence intensity and the turbulence decay. Also effects of the freestream velocity are incorporated in this relation so transition instabilities from outside the boundary layer are taken into account. The $\overline{Re_{\theta_t}}$ brings the empirical relations to the intermittency which is used as a criterion for the onset of transition. The model is not limited to predicting the transition based on local boundary layer properties; also transition induced by flow separation can be predicted by a modification to the relation for the intermittency Langtry & Menter (2009).

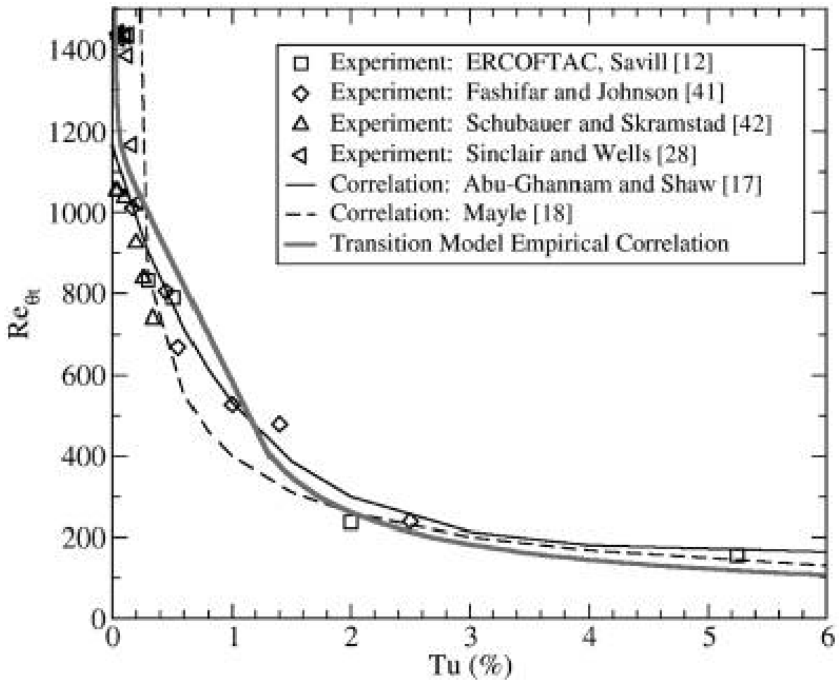

Figure 7.5: Empirical relation between the transition onset momentum thickness Reynolds number (Re_{θ_t}) and the turbulence intensity

The turbulence intensity is given by:

$$Tu = 100\frac{\sqrt{2k/3}}{U}. \tag{7.10}$$

The free flow is assumed to be laminar, so the lower limit as given by the empirical guidelines leads to $TU = 0.027$. The transition momentum thickness Reynolds number is 1,458, deduced from the empirical relations shown in figure 7.5.

7.2.2. Test cases and model construction

The wing tested is derived from a the report of Garmann & Visbal (2011), where the transitional flow over a rapidly pitching airfoil is studied. Reynolds numbers of 5,000, 10,000 and 40,000 are studied with a high-order implicit LES method. The case of the Reynolds number of 10,000 is selected with appropriate motion to closely represent the transitional effect appearing over the 3D wing.

The domain consists of a simple flat wing with rounded edges. The wing has a thickness of 2.5% of the chord. A free stream velocity is applied. The wing pitches according to a specified motion about the quarter chord point. The angle of attack is specified using the non-dimensional pitch rate Ω_0, convective time τ and shape parameter a. The τ_i determine when the wing motion starts, reaches a plateau where the wing is kept for $\Delta\tau_h$ and eventually the return to zero angle of attack. Table 7.2 specifies specific parameters used to create the pitching motion. The resulting angle of attack is shown in figure 7.6 (bottom-left):

$$\alpha(\tau) = \frac{\Omega_0}{2a} ln\left[\frac{\cosh a(\tau-\tau_1)\cosh a(\tau-\tau_4))}{cosh(a(\tau-\tau_2))cosh(a(\tau-\tau_3))}\right]. \tag{7.11}$$

Garmann & Visbal (2011) performed a mesh refinement study and found that a mesh with 254,800 points in the spanwise plane provided a converged solution. The wing is then discretised with 650 elements, with more refinement towards the leading and trailing edge. A similar mesh is

Table 7.2: Parameters to determine the wing pitching motion

parameter	Value	Convective time [-]	Value
a [-]	100	τ_1 [-]	0.25
α_0 [°]	40	τ_2 [-]	$\tau_1 + \alpha_0/\Omega_0$
Ω_0 [-]	0.4	τ_3 [-]	$\tau_2 + \Delta\tau_h$
x_0/c [-]	0.25	τ_4 [-]	$\tau_3 + \alpha_0/\Omega_0$

created for the evaluation of the turbulence models. A mesh and wing were discretised with respectively 254,016 and 648 cells with similar refinement around the wing extrema. The layers around the wing are sized to create a y^* which is always close to one or lower. The $\gamma - Re_\theta$ requires a y^+ of approximately one at the first layer around the wall to capture the boundary layer correctly. The time is discretised using a maximum CFL number of 2.

The pitching motion is simulated by creating a circular domain around the pitching point. The wing grid is extruded to form an *O*-grid with a radius of 100 chord lengths to assure the outer boundary experiences free stream conditions. The entire domain is rotated using the angle of attack defined by equation 7.11. The DGCL is satisfied by taking into account the mesh flux which is created by movement of the mesh.

7.2.3. Results on transitional turbulence modelling

For the translating wing the turbulence is a 3D aspect, which can not be fully captured by the LES in a 2D domain. Therefore the domain is discretised with several elements in spanwise direction. The Reynolds stress tensor in the RANS equation is 3D in nature and does not require additional cells in spanwise direction.

Another effect that influences the simulation is that the spanwise flow can have a large effect on the vortex breakdown and transition. This is not taken into account for the RANS cases because of computational efficiency. The effect of modelling more of the spanwise domain is shown in the left part of figure 7.6. Span over chord ratios of 0.2 to 0.8 are tested and large differences can be seen between the smallest and largest span for the lift coefficient. The upstroke is very similar for all three cases, which indicates that no spanwise effect influence the flow. On the downstroke large differences can be seen which are attributed to spanwise instabilities causing transition.

At τ_i the wing experiences a high rotational acceleration which cause large pressure peaks in the domain. The effect of these peaks is clearly visible in the lift and drag profile. For a zero angle of attack, the pressure distribution only affect the lift coefficient. The peaks in the force coefficient profiles are higher for the laminar and the $\gamma - Re_\theta$, which can be explained by the type of flow solver. The incompressible RANS equations is more sensitive to sudden accelerations than the ILES case with a compressible flow.

Figure 7.7 shows the normalised vorticity, as given in 7.12. Snapshots of the motion at different angles of attack are shown for the laminar, $\gamma - Re_\theta$, ILES, and experimental case. During the upstroke the wing continuously builds up circulation which is shed discretely in a number of TEVs. The location and magnitude of the shed vortices of the RANS cases coincides very well with the TEVs of the experiment. The formation of discrete TEVs instead of a streak of constant vorticity indicates that the diffusion is predicted correctly in this part of the domain. Diffusion can either be caused by viscosity, turbulent viscosity in the case of the RANS and artificial viscosity caused by the spacial discretisation.

At $\alpha = 20° \uparrow$ (upward pitching motion) the leading edge vortex and vorticity in the boundary layer show good coherence with the ILES and experimental case, which indicates that the flow is still completely laminar. At the maximum pitch the ILES an experimental data shows diffusion of

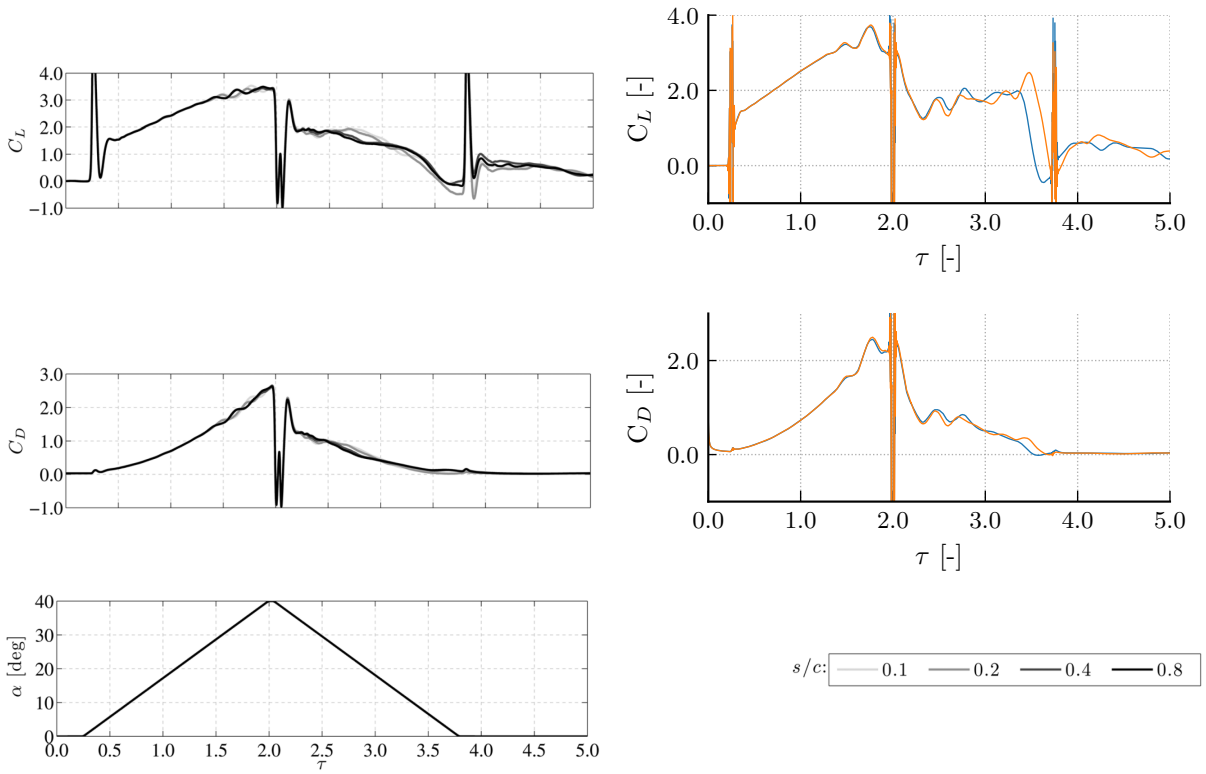

Figure 7.6: The force coefficient on the wing obtained by the ILES (left) and RANS:— and laminar flow:— (right). (bottom-left) the angle of attack of the wing. (bottom-right) Legend of the ILES reference data for different spans, adapted from Garmann & Visbal (2011)

the LEV which reduces the strength of the secondary, counter rotating vortex. The large diffusion is caused by turbulence indicating that transition has occurred. The diffusive behaviour is much smaller for the laminar and $\gamma - Re_\theta$ case, where the counter rotating vortex is ejected from the wing surface. The differences are seen too in the forces on the wing, as the RANS cases shows an oscillation in lift and drag around this time.

When the wing pitches back to zero degrees large scale separation, transition and spanwise flow make the flow hard to predict. The spanwise effect on transition is pronounced as stated in Garmann & Visbal (2011) which leads to higher turbulence energy in the ILES and experimental case. By turbulence mixing the experimental case shows very diffusive behaviour above the wing which is seen in some lesser extend in the ILES case. Figure 7.8 shows the normalised turbulent kinetic energy, which clearly shows that transition has occurred in the region above the airfoil, and that the region of maximum turbulence intensity aligns well with the centre of the shed LEV. However, the influence of the turbulence is limited, as the vorticity profile of the $\gamma - Re_\theta$ predicts low mixing and is similar to the laminar case.

At zero degrees the influence of the turbulence model is clearly distinguishable. The laminar flow allows counter rotating vortices in close proximity near the trailing edge, while these largely eliminate each other for the $\gamma - Re_\theta$ case. Furthermore, the two ejected LEVs and TEV mix more compared to the laminar case.

The higher turbulent mixing reduce the velocity and vortices of the flow which causes a linear reduction in the lift profile between $\tau = 2.5$ to 3.5 for the ILES case. This reduction in lift is not seen for the RANS cases since the vortices are hardly affected by the turbulent diffusion. Furthermore, an oscillation is seen which is caused by the formation of a pair of LEVs which orbit each other and merge between $\alpha = 40°$ and 20°. The sharp reduction in lift after $\tau = 3.5$ is caused by convection of the LEV behind the TE, effectively removing the low pressure area from above the wing. The low pressure area by the shed LEV is clearly seen in figure 7.8.

$$\omega^* = \omega \frac{c}{U_\infty}, \qquad p^* = \frac{p}{\rho U^2}, \qquad k^* = \frac{k}{U^2}. \tag{7.12}$$

The $\gamma - Re_\theta$ case increases the computational time, since it requires the evaluation of four extra transport equations every timestep. Evaluating only the laminar case led to a simulation which was 37% faster.

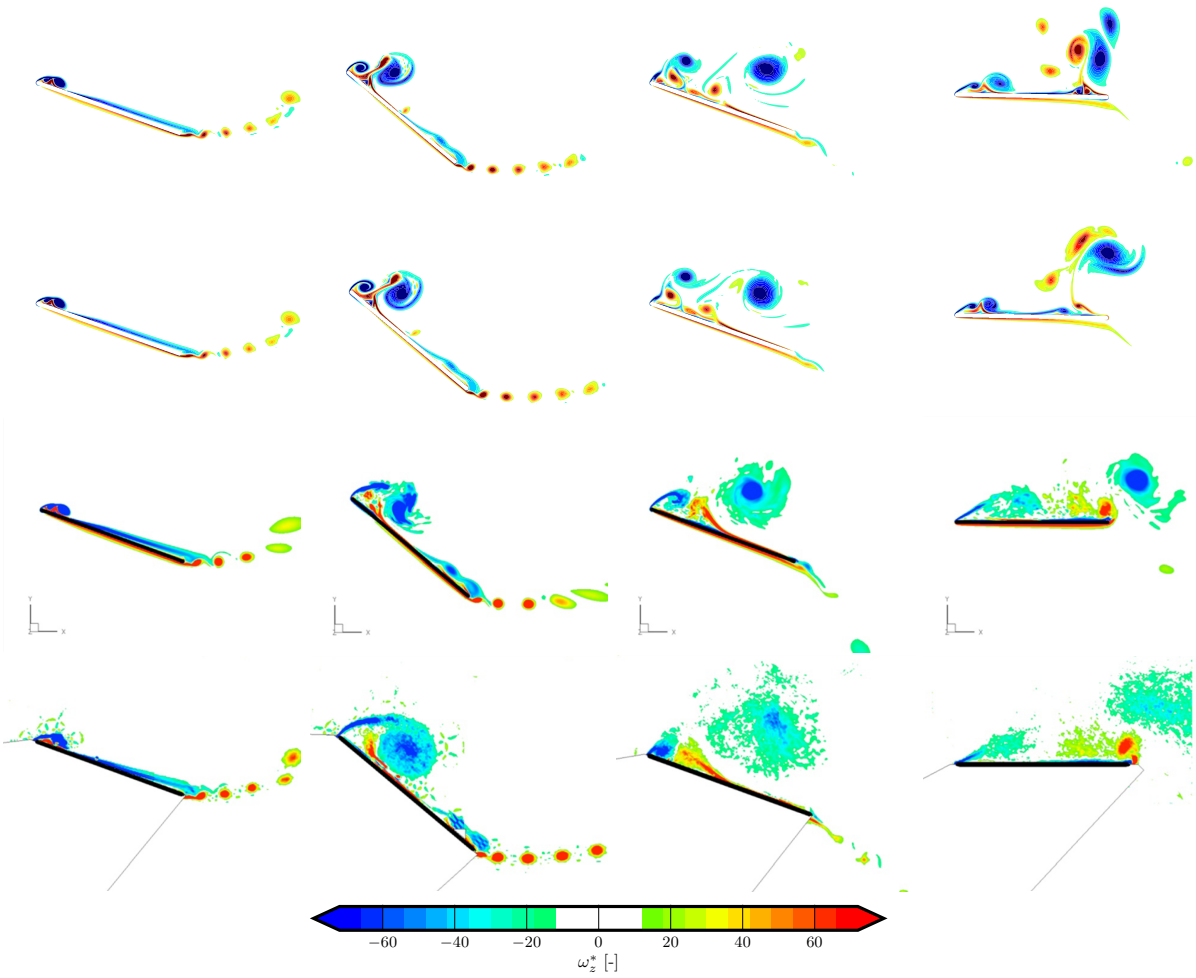

Figure 7.7: Non-dimensional In-plane vorticity. for the laminar (first row), $\gamma - Re_\theta$ (second row), ILES with $s/c = 0.4$ (third row) and experimental case (bottom row). Angle of attack from left to right: 20° ↑, 40°, 20° ↓, 0° The last two rows are adapted from Garmann & Visbal (2011)

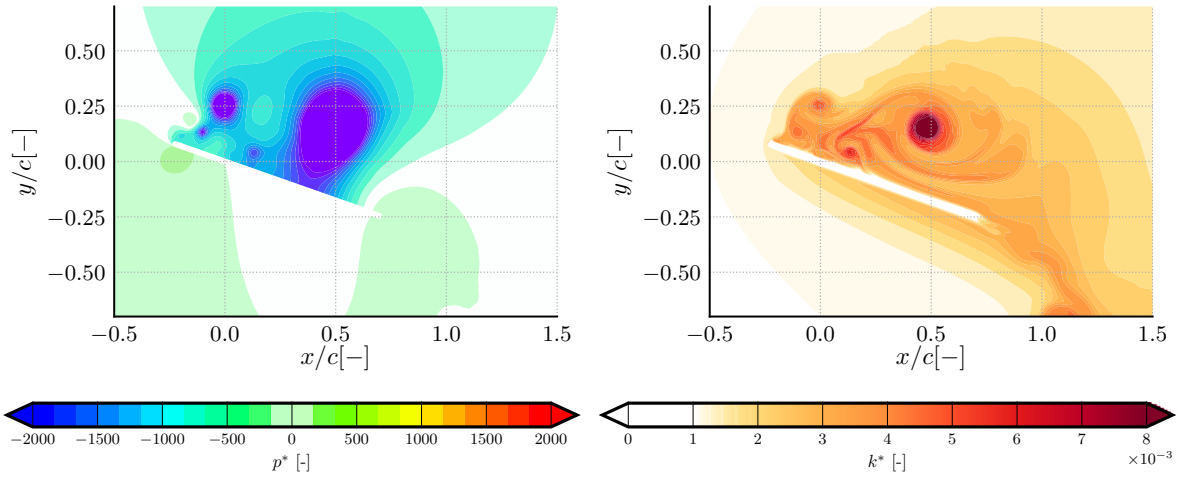

Figure 7.8: (left) Normalised pressure field, (right) normalised turbulent kinetic energy at $\alpha = 20 \downarrow$

7.2.4. Conclusion on turbulence modelling

The difference between the turbulent and laminar flow is small with respect to the error introduced by the RANS assumption. During the upstroke phase, the lift and drag coefficient shows the same trend with respect to the ILES case. However, during downstroke, transition has occurred and turbulent mixing causes the LEV to diffuse. A reduction in lift should follow but this is not seen for the RANS cases. Both the laminar and the $\gamma - Re_\theta$ case shows low turbulent mixing. The individual vortices affect the lift force as seen in the oscillatory behaviour.

In terms of computational efficiency, the laminar case is preferred. Since the inclusion of the $\gamma - Re_\theta$ model does not increase the accuracy of the simulation with respect to the laminar case, it is chosen to solve the 3D wing without additional turbulence modelling.

7.3. Comparison with Experimental data of the revolving wing

The simulation does not model turbulence, which can be noted by the low amount of mixing in the flow. Furthermore, it is subject to a discretisation which can not capture all scales of the transient behaviour. The flowfield and the forces on the wing are compared to experimental data in the following sections.

7.3.1. Flow topology

The vortical structure on the wing after $t^* = 2$ or $\delta^* = 1$ is shown in figure 7.9, where the rigid wing model is shown. Based on this figure it can be seen that the simulation performs well in predicting the size and location of the vortices. The general flow topology consist of four main vortices. The Leading Edge Vortex forms over the leading edge and decreases in size near the tip and the root. The Root Vortex and Tip Vortex form at the extrema of the airfoil and connect with the Trailing Edge Vortex to form a coherent vortex system.

Where the vortices in the experiment break up into smaller vortices, the simulation can sustain the coherent structures for a longer time. The absence of a turbulence model decreases the mixing of the flow and therefore dissipation of gradients found around the wing. This allows for the formation of vortices with a larger strength than would be expected at this Reynolds numbers. Furthermore, the rounded leading and trailing edge might help in increasing stability and therefore promote the formation of larger structures, rather than the shedding of smaller vortices. Since the simulation is able to build up stronger vorticity, the iso-surface of the highest normalized Q-criterion is adapted likewise in the figures.

The location and shape of the TEV matches the corresponding connection to the TV and RV. The angle of the TEV is constant until around $r/R = 0.8$, after which it converges to connect with the TV. This shape is clearly present in both the simulation and the experiment. Besides the main TEV, multiple smaller TEVs are shed om the experiment at the trailing edge which each connect with tip vortices. This effect is more pronounced in figure 7.11, where the medium wing (most flexible wing in the experimental campaign) is shown. The finger-like vortex behaviour is not noted for the vortices of the simulation. In the experiment the circulation over the wing is increased by shedding discrete vortices. A similar increment in circulation is reached in the simulation by continuous shedding of a vorticity sheet. Figure 7.10 shows the vorticity in spanwise direction over the wing at half-span for $\delta^* = 1.5$. In section 7.2.2 vortex discrete TEVs were distinguished for the same Reynolds number with a very fine mesh. The coarser mesh for the 3D case adds more artificial vorticity which inhibits the formation of secondary tip vortices.

The main circulation built up of the wing can be attributed to one clear TEV, which connects to the main TV. Looking at the side view of the rigid and flexible wing, the main difference in flow topology are the finger-like vortex structure from the experiment. These secondary vortices propagate below the wing trailing edge under influence of the rotation of the main TV. The formation of the main TV is the same in both figures, and the TV increases in chordwise direction.

Assessing the formation of the root vortex, severe differences are noted between the experiment and simulation. The RV is much more pronounced for the simulation than for both the rigid and the flexible case. Similar to the tip vortex, a conical shape is seen due to the build up of vorticity. For both the RV and the TV, the circulation is highest near the LE.

Leading edge vortex and breakdown

The LEV shows a typical conical shape for both cases, but in the simulation the structure is more coherent. Where the LEV in the experiment breaks up into smaller vortices, the simulation can sustain the coherent structures for a longer time. The rounded leading and trailing edge might help in increasing stability and therefore promote the formation of larger structures, rather than the shedding of smaller vortices.

The point of maximum chordwise expansion is at the same spanwise location for both LEVs.

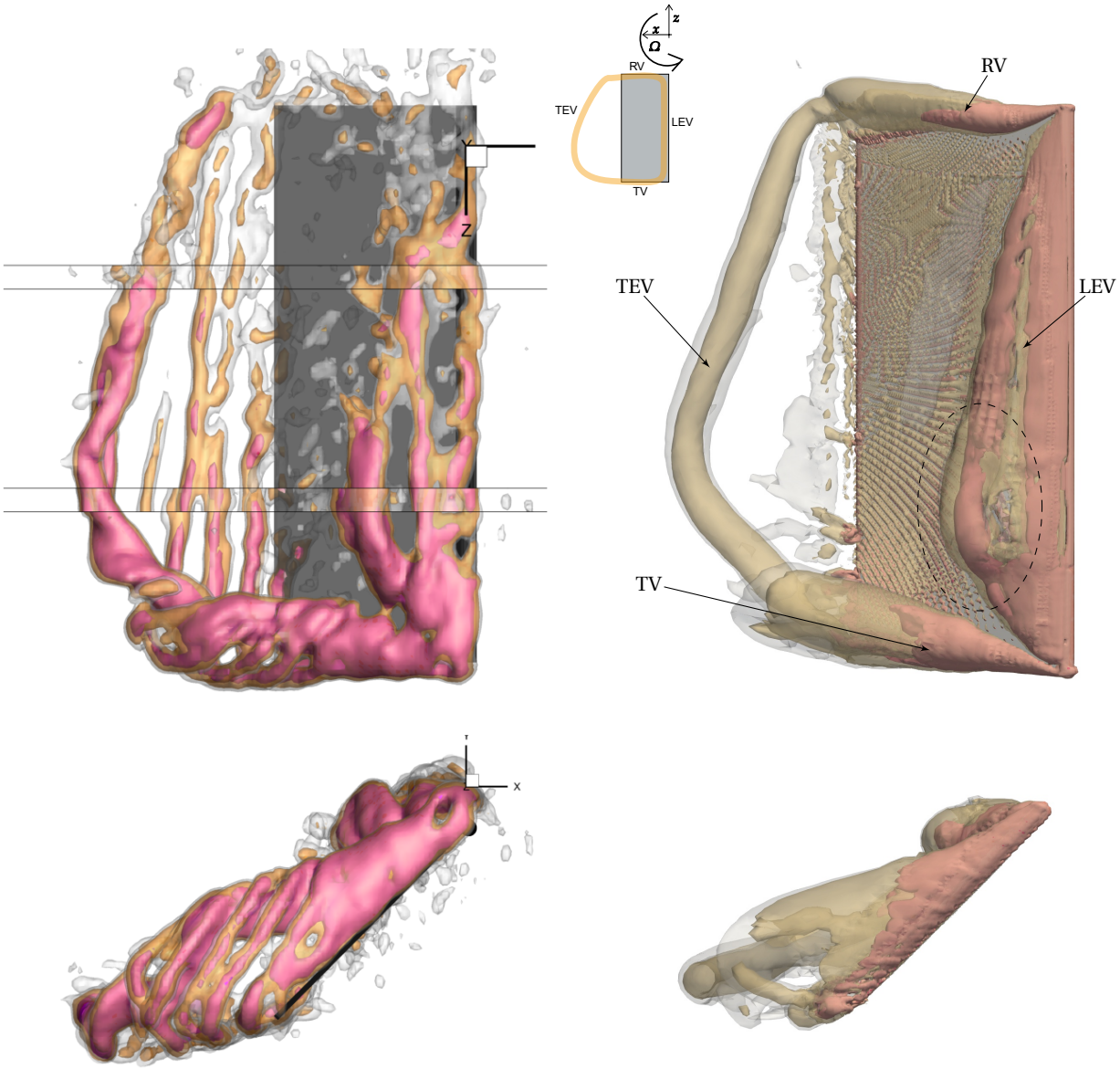

Figure 7.9: Iso-surfaces of the Q-criterion for the rigid wing at $\delta^* = 1$. Left: experimental from van de Meerendonk (2016). Right: equivalent in numerical simulation. Three contour layers are used: $Q(c/V_t)^2$ = [3, 10, 30] and [3, 10, 100] for respectively the experimental and numerical case.

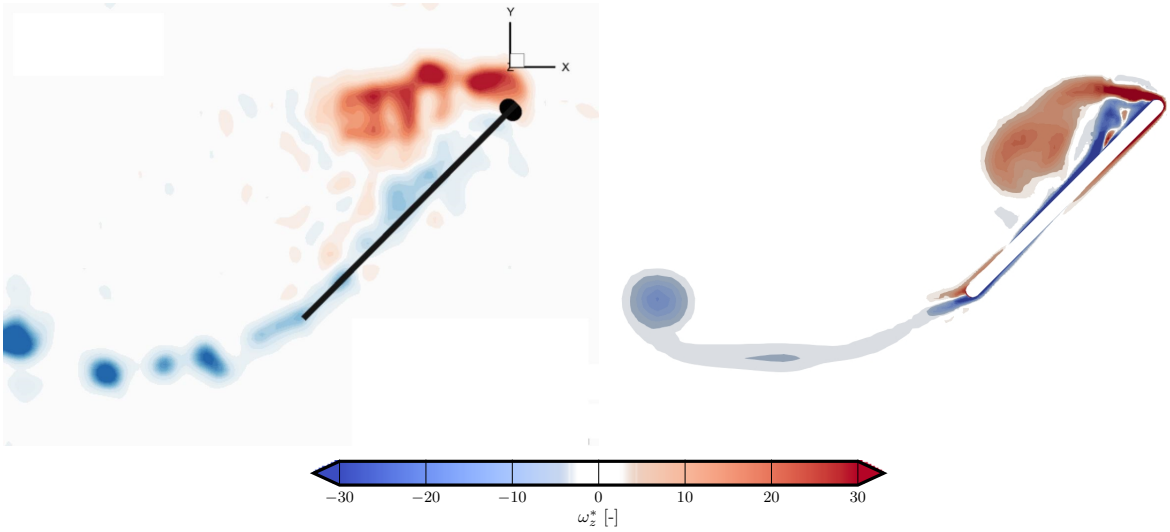

Figure 7.10: Vorticity build up over the wing at $\delta^* = 1.5$ at half span for the rigid wing. (Left) experiment and (right) simulation

Further towards the tip the vortex connects to the TV and is reduced in size. At $\delta^* = 1$ the LEV lifts of the wing surface at a spanwise location of $r/R = 0.6$, which is also seen in the experimental flowfield. This is in accordance with research from Percin & van Oudheusden (2015) and Garmann & Visbal (2013) which feature similar revolving plates.

During the breakdown near midspan the core of the LEV lifts up from the surface and expands in size. The A bubble like structure is formed which is clearly visible in the simulated flowfield. The bubble is paired with the onset of more small scale structures. The onset of the bubble marks the beginning of a chaotic flow behaviour, where the tip vortex and the burst LEV start interacting. A small inboard region of the wing is little affected by the burst, which is in accordance with results obtained by Jardin & David (2015) and Garmann & Visbal (2013). In the spanwise section of $r/R = 0 - 0.4$ the LEV is stabilized by the influence of rotational forces which drain vorticity from the core of the LEV.

The chaotic behaviour reaches a quasi steady state eventually. Here the main flow structures show little variation and the flow on the outboard part of the wing is dominated by small scale structures. Figure 7.12 shows the pressure contours for the quasi-steady pressure on the wing. A low pressure area persists on the suction side whose shape coincides well with the region of chaotic behaviour, as shown by the iso-surface of the Q-criterion. On the bottom of the wing a high pressure area is present at the outboard side. This region has a similar shape and size for the experimental and numerical result.

The shedding of vorticity by the burst LEV can be seen for the pressure, where two streamwise oriented streaks of low pressure near $r/R = 0.7$ are convected from the burst region. This denotes shedding of individual vortices which are paired with a low pressure area.

7.3.2. Wing deformation

The wing deflection can be expressed by the angle of attack. This angle is defined by the angle of the virtual line between the trailing edge and the leading edge:

$$\alpha(z) = \tan^{-1}\left(\frac{y_{LE}(z) - y_{TE}(z)}{x_{LE}(z) - x_{TE}(z)}\right). \tag{7.13}$$

Figure 7.13 shows the angle of attack for the most flexible wing in the experimental campaign and the two flexible wings from the numerical simulation. The majority of wing deflection is formed

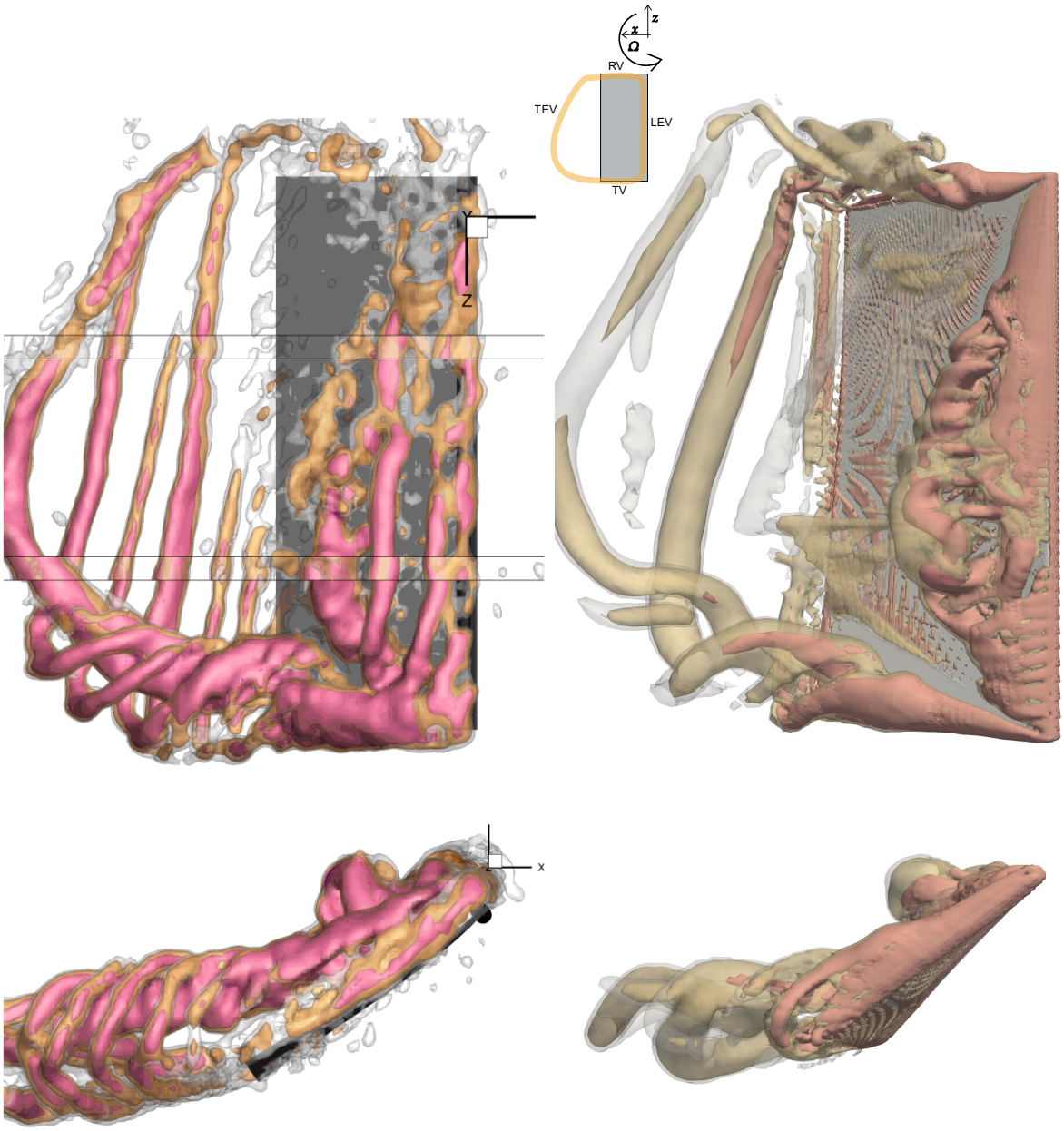

Figure 7.11: Iso-surfaces of the Q-criterion for the medium wing at $\delta^* = 1.5$. Left: experimental from van de Meerendonk (2016). Right: equivalent in numerical simulation. Three contour layers are used: $Q(c/V_t)^2$ = [3, 10, 30] and [3, 10, 100] for respectively the experimental and numerical case.

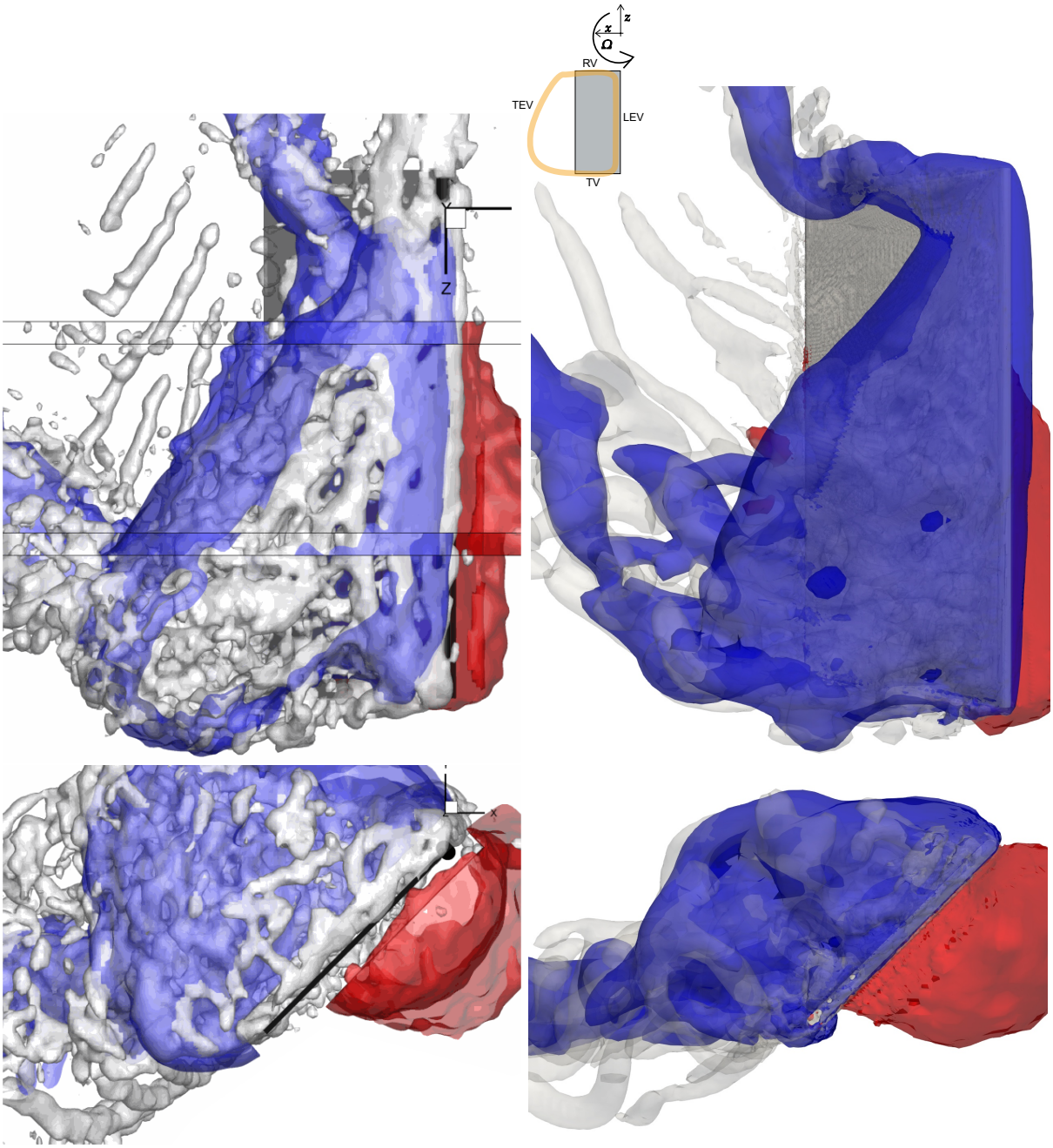

Figure 7.12: White iso-surfaces of the Q-criterion and red, blue for the pressure iso-surface of the rigid wing at $\delta^* = 4$. Left: experimental from van de Meerendonk (2016). Right: equivalent in numerical simulation. $Q(c/V_t)^2 = 3$ and p = 6Pa (red) and −13Pa (blue)

during the acceleration phase. After the initial formation of the angle of attack, the experimental data predicts a relative smooth behaviour of the tip and root angle. The angle on the root and tip decreases likewise until a approximately $\delta^* = 0.4$, after which the root angle recovers and a twist is created in the wing.

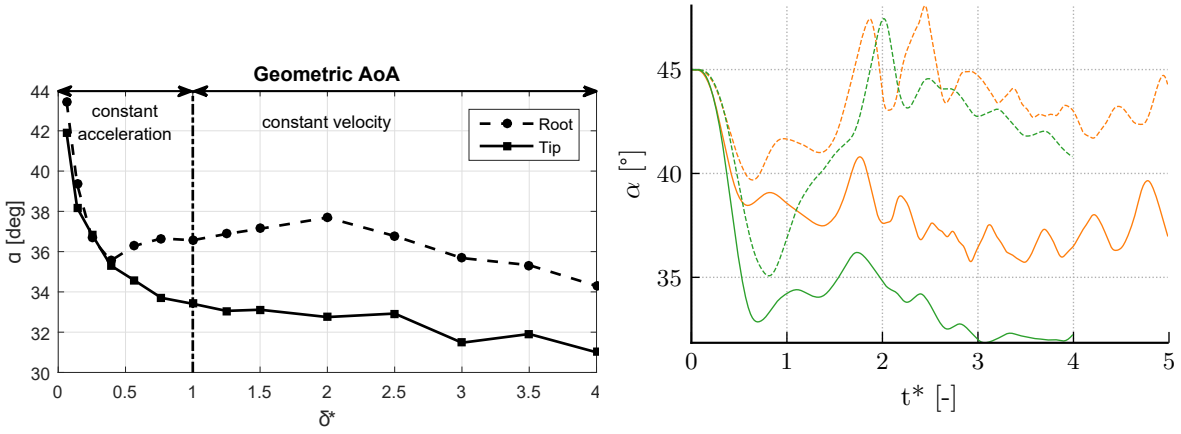

Figure 7.13: Angle of attack on the flexible wing. (left) Experimental data for the angle at the root and the tip for the medium wing. (right) Numerical data for the angle at the root (dashed) tip and tip (solid) for the medium(—) and flexible(—) wing.

The medium and flexible wing from the numerical simulation show similar behaviour for the formation of angle of attack. Near $t^* = 0.7$ the root and tip angles diverge and the root angle of attack recovers to an angle over 45°. The overshoot is most likely caused by the absence of acceleration and rotation forces in the structural model. Furthermore, the numerical model has a higher mass ratio than the structural model so inertial forces can also contribute to the overshoot.

At approximately $t^* = 3$ a quasi steady state is reached where the root and tip angle of attack show oscillating signals for both the medium and the flexible wing. The medium wing has higher stiffness and shows more persistence of the oscillation. The tip reaches an angle of attack close to $\alpha_{\text{tip}} = 37.5°$ is seen for the medium wing, while the experiment indicates an average angle of attack close to 33°. The flexible wing features similar angles of attack. The root angle of attack is lower for the numerical simulation compared to the experimental values. Most likely this is caused by the absence of rotational forces.

7.3.3. Forces on the wing

The pressure on the wing is of great importance because it determines the perpendicular force on the surface. For a Reynolds number of 10,000 and a high angle of attack the force vector is nearly perpendicular to the surface because the pressure forces are dominant over the viscous forces (Birch et al., 2004; van de Meerendonk, 2016).

Force coefficients from the experimental and numerical cases are shown in figure 7.14. For the experimental rigid wing at 45° the lift and drag are nearly the same which as can be expected. As was in figure 7.13 the wing deflects under the aerodynamic load and assumes an angle of attack of approximately 33°. Therefore, force is tilted more in lift direction and the drag is reduced. The total aerodynamic force generated by the wind decreases for more flexible wings.

Similar behaviour is seen for the numerical simulation. The rigid case generates the largest values of lift and drag overall. The lift and drag of the rigid case are very similar which indicates that the force angle is nearly perpendicular to the wing surface. The lift decreases from approximately $C_L = 1$ to $C_L = 0.75$ from the rigid to the flexible case, a drop of 25%. At the same time the drag drops by approximately 50%.

Comparing the most flexible experimental wing with the medium wing from the numerical simulation similar figures are seen for the lift and drag. Both show a quasi steady lift coefficient of $C_L = 0.8$. The drag converges to a value of $C_D = 0.55$ for both the experiment and the simulation.

The added mass effect is seen in both the experiment and the simulation. The constant acceleration of the experimental case causes an instantaneous lift and drag at $t^* = 0$. The value of this instantaneous force is larger for the experimental case because of the higher value of acceleration at zero time.

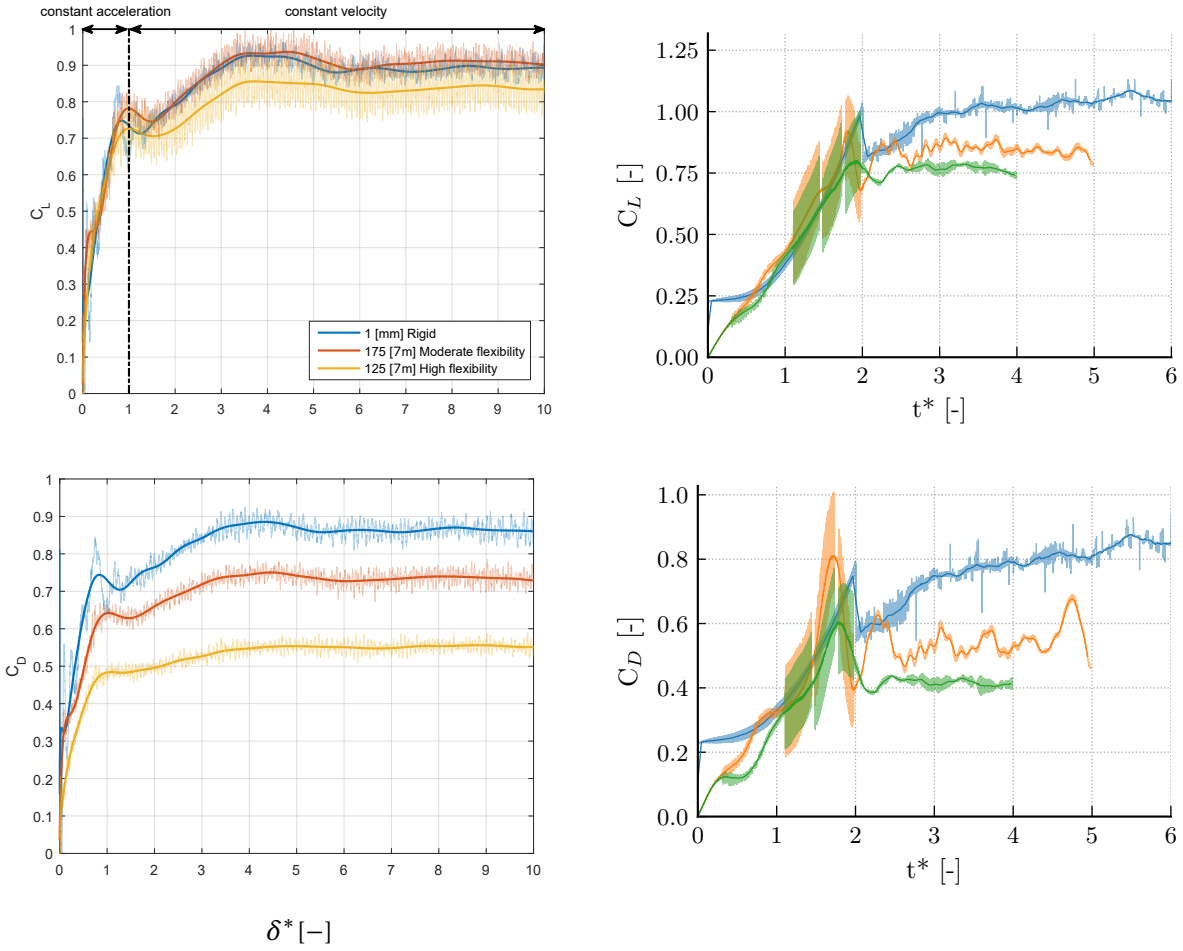

Figure 7.14: Angle of attack on the flexible wing. (left) Experimental data for the angle at the root and the tip for the medium wing. (right) Numerical data for the angle at the tip for the —medium and —flexible wing.

7.4. Flexible Revolving and Translating wings

The following section aims at determining the difference in flow structure between translating and revolving wings. For the latter case, the Coriolis, centrifugal and Euler acceleration play a role in the fluid field around the wing.

As explained in section 7.1 the reference velocity is defined taken at 75% of span for the revolving wing with the reference velocity of $V_t = 0.2\text{m}\,\text{s}^{-1}$. However, comparison of the different motions can be performed best if the reference radius and thus velocity is based on a similarity criterion. In appendix D.2 such a criterion is derived for the aerodynamic force at a constant force coefficient distribution. The reference radius for force similarity (fs) is: $R_{\text{fs}} = 96.4\text{mm}$, or at 54% of the span. The associated velocity is $V_{fs} = 0.165\text{m}\,\text{s}^{-1}$. These reference velocity is higher than this value, which causes the translating wings to experience a higher average dynamic pressure. A factor 1.47 of difference in average dynamic pressure is present between the revolving and translating wings. Therefore, larger deflections and forces are expected on the translating wings.

The simulation for the translating case are performed with the reference velocity of $V_t = 0.2$, while the reference velocity for force similarity should be approximately 18% lower. Therefore, comparison of of the revolving and translating case is always done with this scaling in mind.

The deformation of the revolving and translating case are compared in section 7.4.1. Next the vortex structures in the flow are categorised in section 7.4.2, and their spanwise influence are evaluated in section 7.4.3. The pressure influence is treated in section 7.4.4 and at the aerodynamic forces in section 7.4.5.

7.4.1. Deformation of the wing

The vertical displacement at the trailing edge of the wing tip is shown in figure 7.15 for both the revolving and translating wings. Since the rigid wings do not have any displacement only the flexible wings are considered in the figure.

The vertical displacement on the revolving wing show that the medium and flexible wing reach an average deflection of $U_y = 5\text{mm}$ and $U_y = 9\text{mm}$. Under the acceleration by the pressure forces the wing bends to a large displacement between $t^* = 0 - 0.7$, but it bends back before $t^* = 2$. The translational case shows larger displacements due to the higher loading as was argued before. No reduction in displacement after the initial acceleration happens for this wing. The average displacement for the medium and flexible wing are approximately $U_y = 10\text{mm}$ and $U_y = 16\text{mm}$.

The translational case shows three peaks for both the medium and the flexible wing. These peaks are related to the periodical behaviour of the vortex shedding of the translational wing in the quasi steady equilibrium that is reached. The suction force reaches a maximum just before the vortices are shed and thereby increases the wing deflection. The point of maximum deflection occurs at approximately $t^* = 4.5, 7.5, 12$ for the medium wing. The Strouhal number associated with the shedding is equal to the non-dimensional frequency. This leads to a approximate frequency of $f^*_{\text{shedding}} = St = 0.27$. Similar numbers were found for flat plates by J. M. Chen & Fang (1996). A slightly higher Strouhal number is seen for the flexible wing which is also expected.

The displacement for the revolving and translating wing at $\delta^* = 1$ are shown in figure 7.16. The revolving wings mainly show large displacement at the tip of the wing. As was seen explained in section 7.3 a slight overshoot was seen for the angle of attack of the root section. This is clearly seen in the figure, where the root section has a small downward displacement. This leads to a nearly linear build-up of the angle of attack over the span, as is seen in figure 7.17.

The translating wings show a large displacement which is almost constant along the span. A slight deviation is seen in figure 7.17 which is scaled for the current range of angle of attack. A deviation of under 0.5° in angle of attack is seen between the mid span section and the tip for both translating wings.

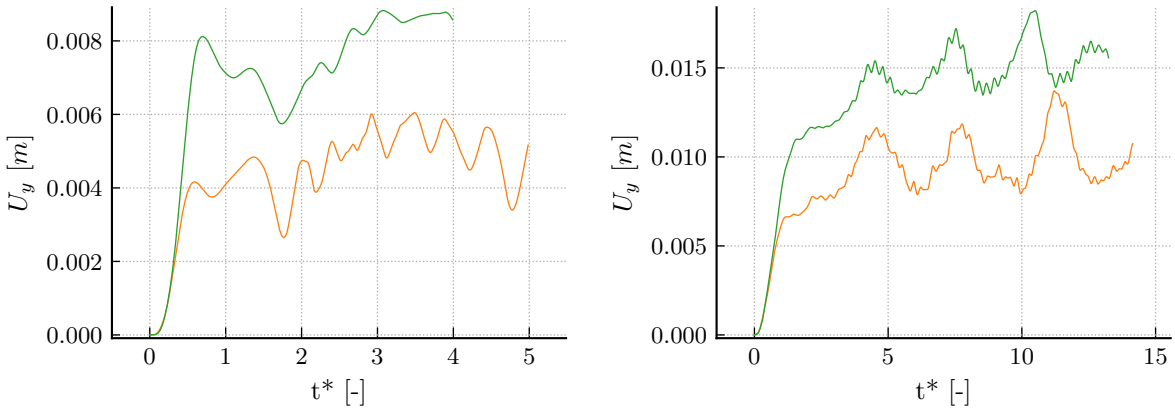

Figure 7.15: Displacement of the trailing edge at the tip for (left) revolving and (right) translating wing. —medium and —flexible wing. Note the scale differences between the figures.

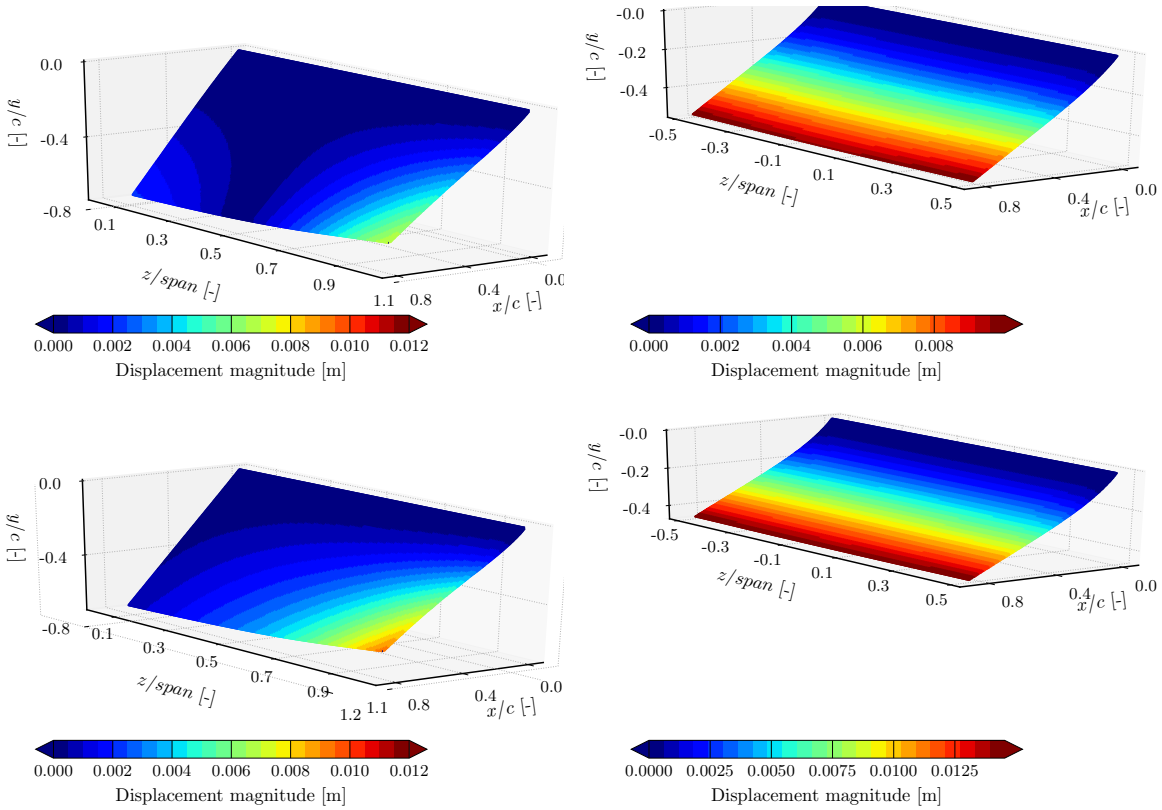

Figure 7.16: Displacement of the (left) revolving and (right) translating flexible wings for $\delta^* = 1$. The top and bottom row represent the medium and flexible wing.

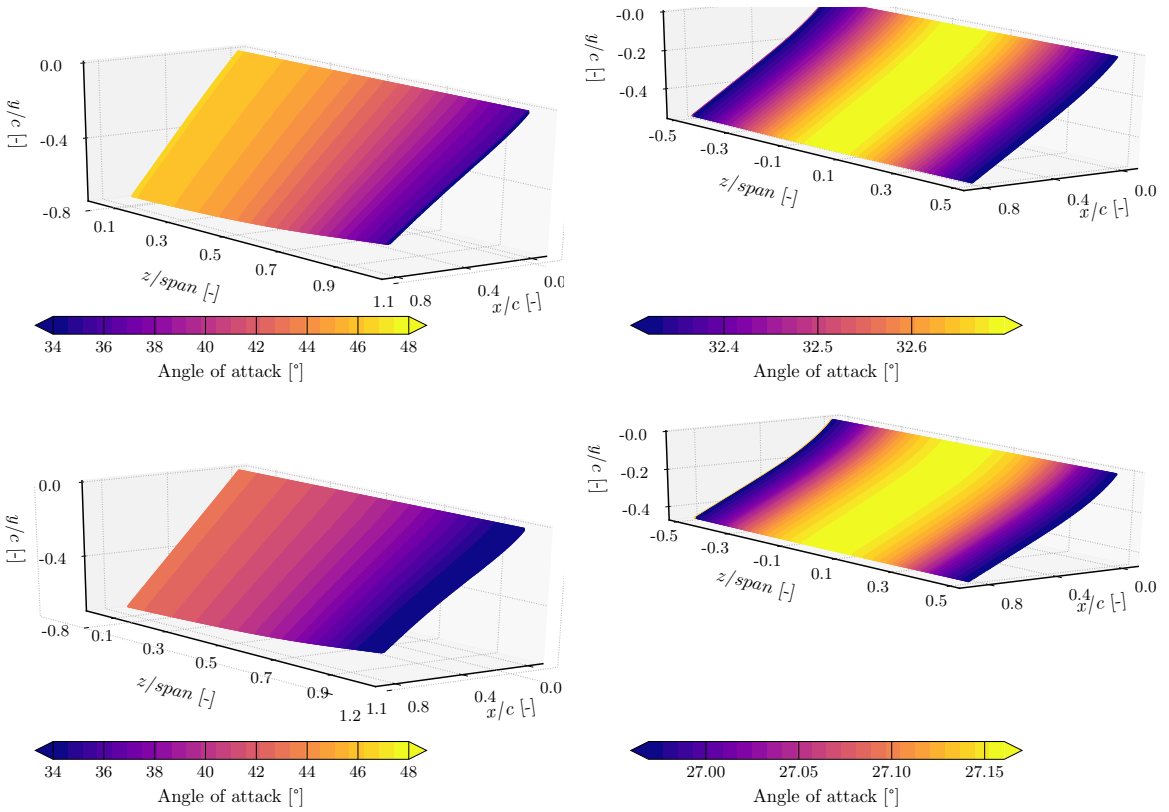

Figure 7.17: Angle of attack of the (left) revolving and (right) translating flexible wings for $\delta^* = 1$. The top and bottom row represent the medium and flexible wing.

7.4.2. Coherent structures

The vortical structure for the three revolving wings is shown in figure 7.18 for $\delta^* = 1.5$. All three wing show a clear vortex ring formed of the LEV, TV, TEV and RV, however the origin of TEV is different for the rigid and flexible cases. The initial TEV for the flexible cases is weak since the wing bends under the applied load. In figure 7.15 it was seen that the wings deflection decreases slightly between $t^* = 0.7 - 2.0$ and in this period the second, stronger TEV is formed. Also two tip and two root vortices are formed which influence each other in a helical structure.

The LEV burst is clearly present for all three wings. The centre of the burst seems to shift slightly inboard for increasing flexibility. The reduced angle of attack on the outboard section could help in stabilizing the flow in this region which shifts the region of instability further inboard.

The region outboard of the breakdown shows a similar conical LEV from the tip to $r/R \approx 0.8$. Here the LEV is anchored to the wing by the TV. The combination for the TV and the outboard part of the LEV is more stable for the flexible wings. The outboard part of the LEV and the TV are larger in size and lose the conical shape that was initially formed. The lower angle of attack for the flexible wings helps attachment of the TV. The outboard part of the LEV is affected by this and is more compact when compared to the rigid wing.

The wing stress is defined as the summation of the pressure pressure and viscous stress contribution. The stress multiplied by the surface area of the wing leads to the force, as shown in equation 4.6. The bottom row of figure 7.18 shows a clear contribution of the LEV for all revolving wings. The stress is highest near the root of the wing and diminishes towards the mid of the span, which indicates the LEV breakdowns near $r/R \approx 0.6$.

On average, the rigid wing creates higher stresses on the wing surface, which denote stronger vortices. Especially compared to the flexible wing the in- and outboard part of the LEV are stronger for the rigid wing. Furthermore, the breakdown of the TV an expansion of the outboard part of the LEV can be seen in the larger area of stress generated by the rigid wing.

The vortical structure for the three translating wings is shown in figure 7.19 for $\delta^* = 1.5$. A clear vortex ring is seen and unlike the revolving case, the TEVs are formed by the same process. After the first TEV, a number of secondary TEVs are shed for all wings which connect in rib-like structures to the tip vortices.

Looking at the side of the wing it is clear that the flexibility plays a large role for the translating wing. Especially the tip vortex is largely affected. For the rigid and medium wing the TV lifts from the wing surface, while it stays attached for the flexible case due to the deflection. Furthermore, the deflection causes the LEV to stay closer ot the wing.

Breakdown of the LEV is seen for all three translating wing and happens by the same process. Just outboard of midspan the LEV lifts off from the surface and forms an arch like structure which is pinned by the tip vortex to the wing surface. These local spots create a high force, but only cover a small portion of the wing area as can be seen in the bottom row of figure 7.19. The largest stresses are found on the rigid wing which builds up the strongest vortices.

7.4.3. Spanwise properties

In figure 7.20 the spanwise velocity is presented for a number of chordwise oriented planes over the span on the revolving wing. The regions of high spanwise flow can be found near the tip and the root, where the RV and TV induce a spanwise flow. The inboard section shows an outboard flow for a large region on the chord, which is countered by spanwise inward flow from the tip vortex around $r/R = 0.6 - 0.7$.

A spanwise flow with a magnitude of above $1.5V_t$ can be seen in the core of the LEV for all three wings but the effect is weakest for the flexible wing. This is similar to previous findings that the LEV on the flexible wing is weaker than the LEV on the stiffer wings. Also the region behind the LEV has an outboard velocity component.

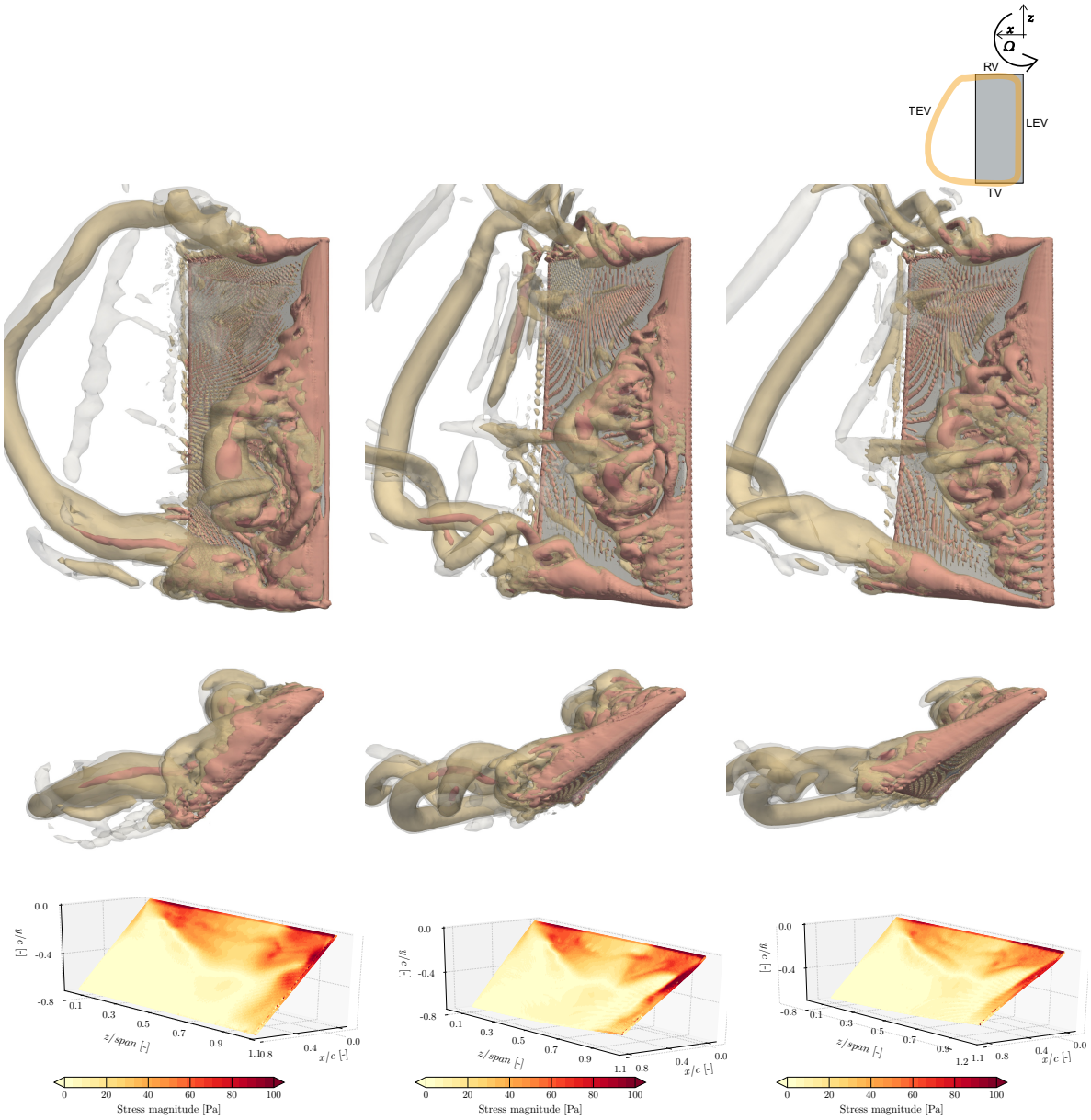

Figure 7.18: Iso-surfaces of the Q-criterion for revolving wings at $\delta^* = 1.5$. From left to right: Rigid, medium and flexible wing, Top view and side view. Three contour layers are used: $Q(c/V_t)^2 = [3, 10, 100]$. The stress magnitude on the top surface is shown on the bottom row.

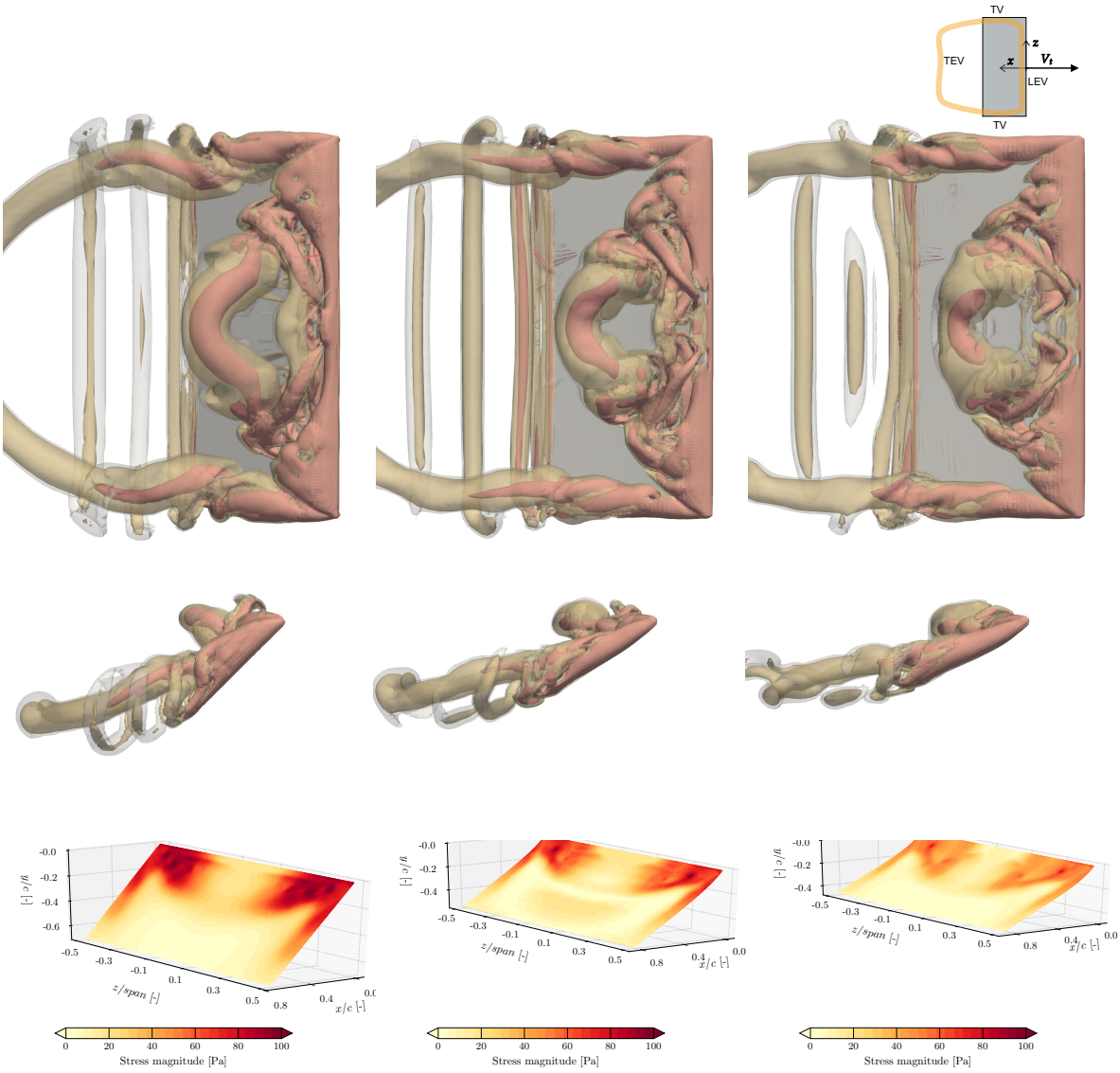

Figure 7.19: Iso-surfaces of the Q-criterion for translating wings at $\delta^* = 1.5$. From left to right: Rigid, medium and flexible wing, Top view and side view. Three contour layers are used: $Q(c/V_t)^2 = [3, 10, 100]$. The stress magnitude on the top surface is shown on the bottom row.

;

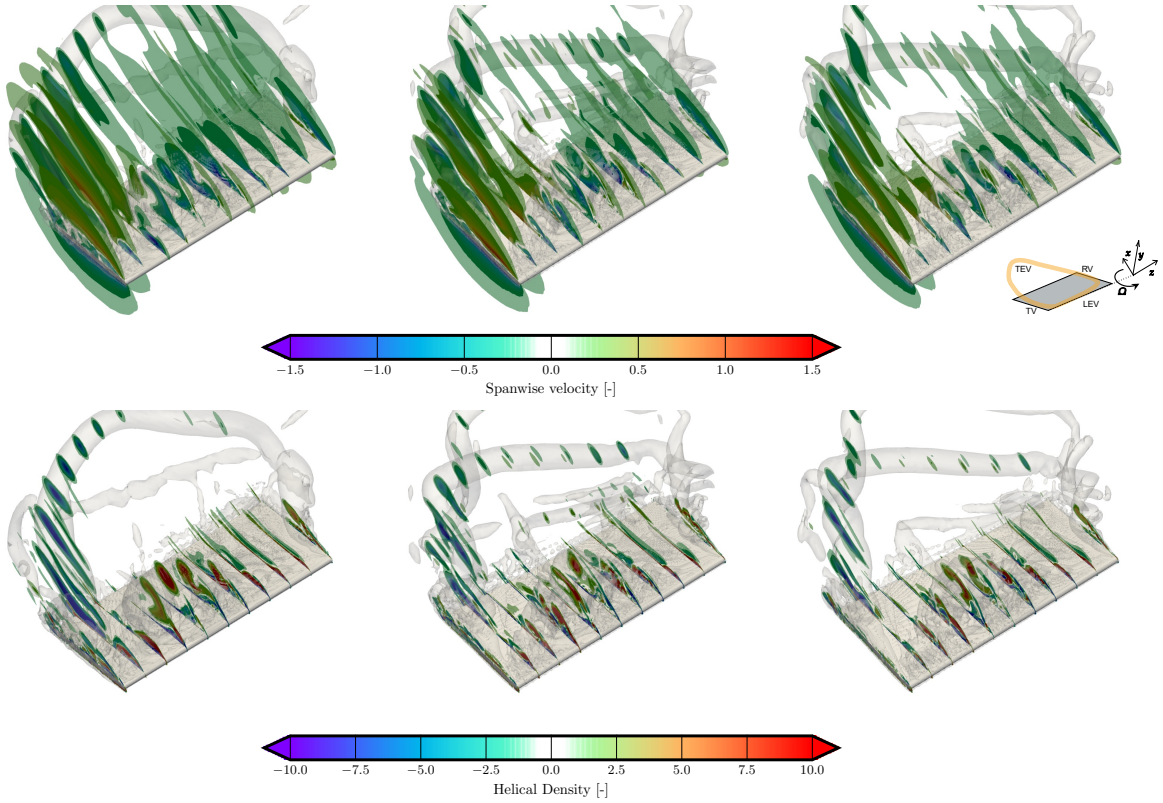

Figure 7.20: Revolving wings with (top) chordwise planes for the spanwise velocity and the iso-surfaces for Q-criterion at $Q(c/V_t)^2 = 3$ at $\delta^* = 1.5$. (bottom) Chordwise planes with the z-component of the helical density. From left to right: Rigid, medium and flexible wing

The z-component of the helical density gives a measure for the transport of the vorticity. In figure 7.20 the LEV the convection of vorticity is positive which means that the vector of the vorticity is aligned with the local flow velocity. The rigid wing shows that the LEV transports vorticity outwards over the entire span at $\delta^* = 1.5$. However, the chordwise sections outboard of $r/R = 0.7$ show considerably less transport of vorticity. The burst of the LEV is caused by local saturation of LEV.

The spanwise velocity of the translational wings shows that the TV creates a flow towards midspan which extends close to the trailing edge at midspan of the wing. This inward flow is the result of a strong tip vortex that is caused by pressure difference of the wing. In the revolving case this inward flow is countered by the region of outboard flow behind the LEV.

The z-component of the helical density is shown also. The LEV created by the translating wing creates a vorticity convection towards the tip of the wing but the vorticity drain is not enough to counter the production of vorticity at the leading edge. Therefore, the LEV near midspan is saturated and detaches from the wing.

A difference between the revolving and translating wings can be found in the TEVs. The translating TEVs are nearly 2D since there is not convection of the vorticity in these vortices. For the revolving wings negative values of helical density are seen which indicate outboard flow.

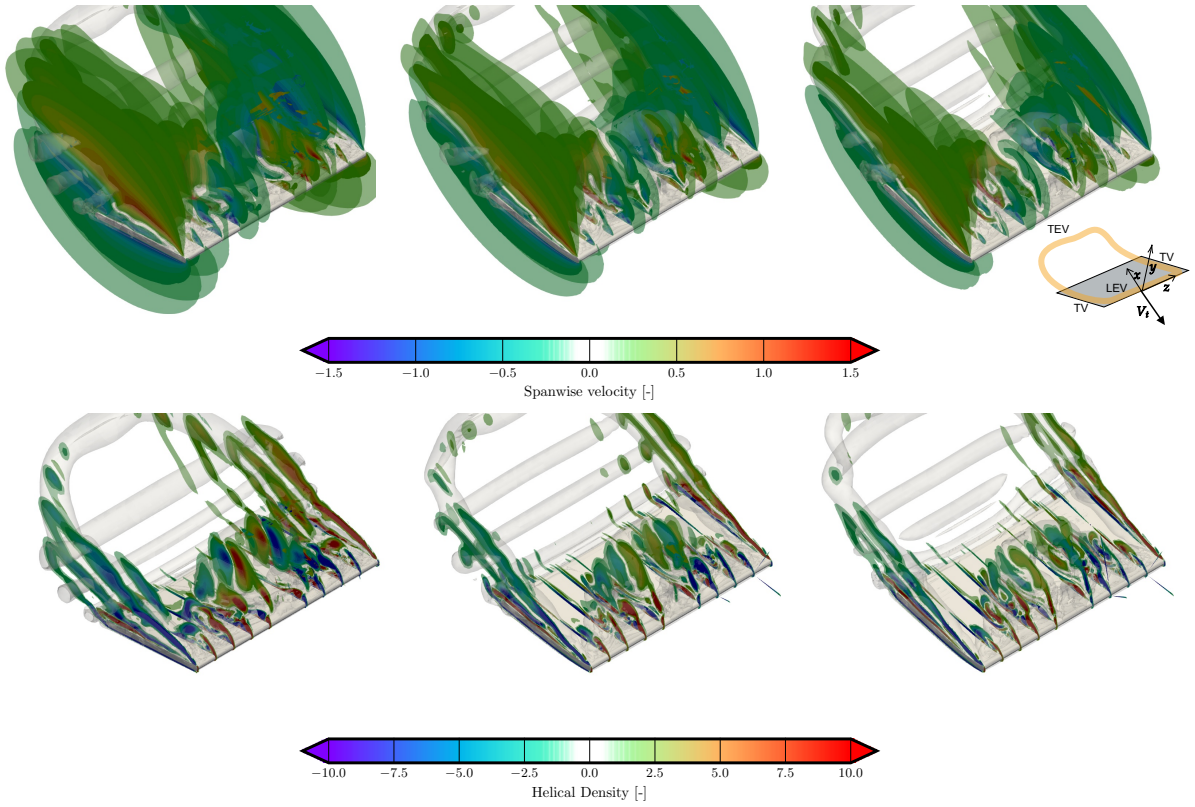

Figure 7.21: Translating wings with (top) chordwise planes for the spanwise velocity and the iso-surfaces for Q-criterion at $Q(c/V_t)^2 = 3$ at $\delta^* = 1.5$. (bottom) Chordwise planes with the z-component of the helical density. From left to right: Rigid, medium and flexible wing

7.4.4. Pressure on the wing

As mentioned in section 7.3 the pressure is dominant over the viscous forces to determine the force on the wing. Figure 7.22 gives the pressure on the revolving wing for two different times: at $\delta^* 2$ the wing has just reached a constant travelling velocity and the forces for both the revolving and translating wings are close to their maximum value. Next the developed flowfield is shown.

The pressure field show good correlation with the iso-surface of the Q-criterion. This underlines that the vortices are indeed responsible for the creation of low pressures. Furthermore, the pressure shows a more smooth field compared to the Q-criterion after vortex breakdown, which eases the characterisation of the vortex structures.

Revolving wing

The revolving wing shows that the LEV build up from $r/R = 0 - 0.5$ is relatively independent of the wing stiffness. The conical shape and strength of the LEV is comparable for the three cases. On the outboard section the flexible wings bend to create a larger angle of attack. This permits a more stable LEV. Moreover less circulation is built up because of the deflected wing so saturation of the LEV is reached later. As was already seen for the rigid wing in section 7.18 the TV and outboard section of the LEV break down and expand in size, which creates the large region of low pressure on the outer part of the span.

At $t^* = 2.5$ ($\delta^* = 2.5$) the LEV pressure field of the translating case is relatively simple and a large portion of the LEV is still connected to the wing, pinned by the TVs. The LEV lifts up at midspan and is eventually shed in the flow for all three cases. The region of low pressure decreases with increasing flexibility, which was seen too for the revolving wing.

The second time displayed is close to $t^* = 8$ ($\delta^* = 7$), at which the quasi steady state is fully developed. Note that revolving medium and flexible wings have a maximum time of respectively $t^* = 4.8$ and $t^* = 3.6$, which is equal to $\delta^* = 3.87$ and $\delta^* = 2.6$. Because of the high computational effort for these cases and the lack of a restart option for the coupled simulation no higher times could be achieved. The latest time is therefore shown instead for the developed flowfield.

For the quasi developed flow the vortical structure is much more chaotic as can be deduced by the Q-criterion iso-surfaces. A large number of smaller scale vortices are interacting are produced after the breakdown of the LEV. Similar behaviour was seen for the experimental flowfield for the Reynolds number of 10,000.

The spanwise location where vorticity is shed is different for the rigid and flexible wings. The rigid wing has a LEV which extends up to a large part of the span and it grows in size until it reaches the trailing edge at $r/R \approx 0.75$. Outboard of this section vorticity is shed in the freestream in a chaotic combination of vortices. For the flexible wings the LEV is not stable for a large portion of the span. It breaks down near mid-span and here a large portion of the vorticity is drained to the freestream. These results are in contradiction with the experimental data obtained in van de Meerendonk (2016), where similar vortical structures were seen for the rigid and flexible wings. However, further analysis is required to find out if the breakdown location is not altered for the later times.

Translating wings

The translating case is depicted for all wings at $t^* = 1.5$ ($\delta^* = 2.5$) and $t^* = 8$ ($\delta^* = 7$) in figure 7.23. At the rigid wing, vorticity is shed from the leading edge and tips, but it convects immediately in the freestream. Therefore suction forces diminish on this wing. for the medium wing the LEV is created in closer proximity of the wing and some build-up of vorticity is allowed before the LEV is shed. This behaviour was already recognised in section 7.4.1 for the displacement of the wing. Similar shedding was seen for the flexible wing but a a slightly larger frequency. Moreover, figure 7.23 shows that shedding occurs only at the mid span. The lowered angle of attack allows a portion of attached flow near the tips.

7.4.5. Forces and vorticity

In figure 7.24 the force coefficients for the revolving wing and translating wing are shown. The incompressible flowfield is very sensitive to small changes and fluctuations are quickly introduced in the pressure. Even the rigid revolving wing without any structural deformation shows some in-

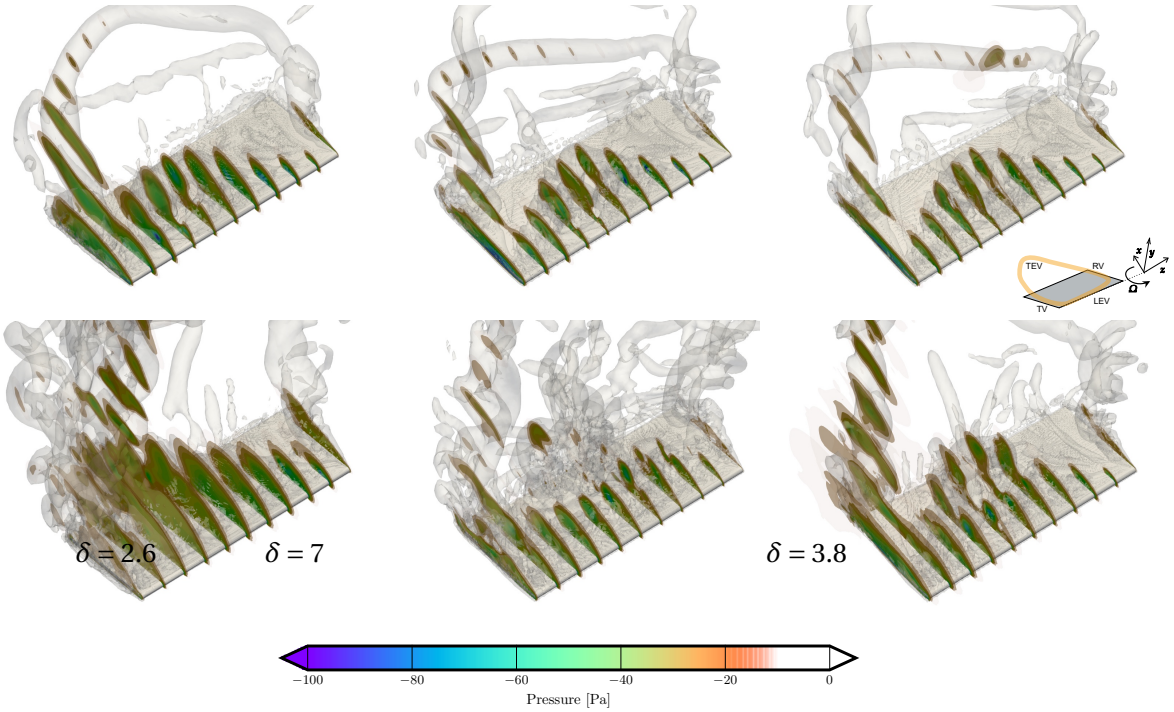

Figure 7.22: Revolving wings with (Top row) chordwise planes for the pressure and the iso-surfaces for Q-criterion at $Q(c/V_t)^2 = 3$ at $\delta^* = 1.5$. (Bottom row) Same wings with the (quasi) developed flowfield. From left to right: Rigid, medium and flexible wing

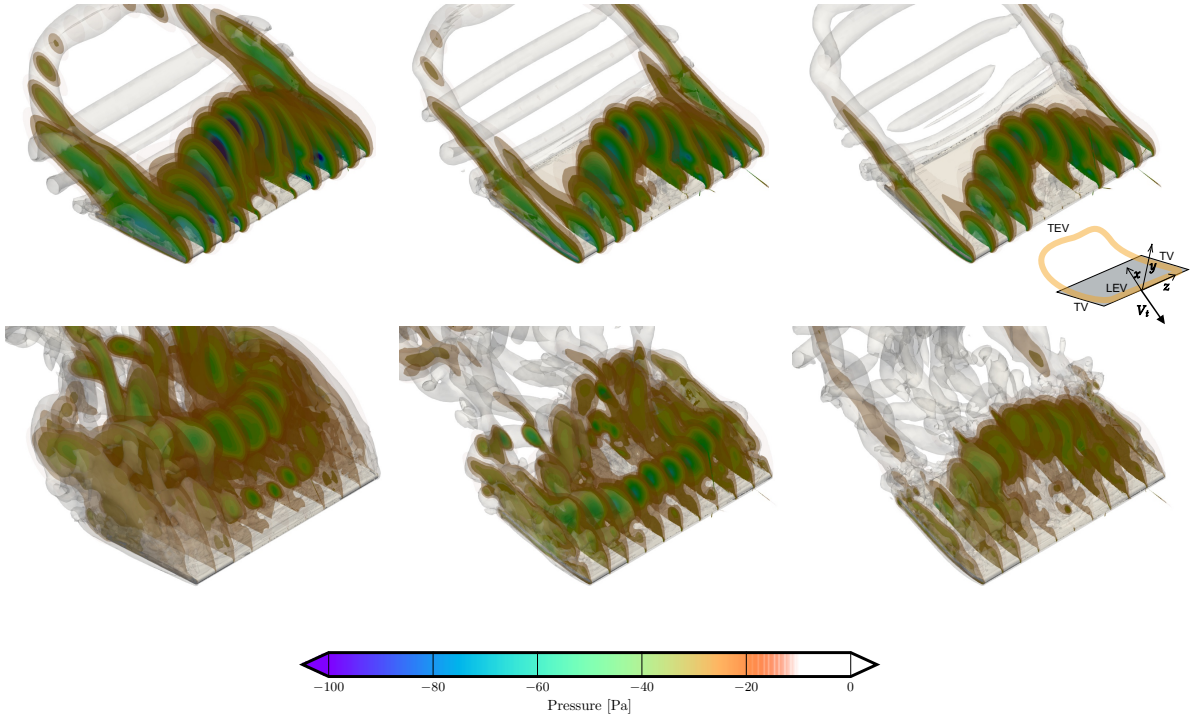

Figure 7.23: Translating wings with (top row) chordwise planes for the pressure and the iso-surfaces for Q-criterion at $Q(c/V_t)^2 = 3$ at $\delta^* = 1.5$. (bottom row) Same wings with the (quasi) developed flowfield at $\delta = 7$. From left to right: Rigid, medium and flexible wing

stability for the forces on the wing. For this reason the averaged value over 10 timesteps is plotted through the raw signal.

During the acceleration period both flexible revolving wings show a large spread of the force coefficient. The most flexible translating wing shows a peak in the lift and drag around $t^* = 2.6$. This indicates that the coupled timestep did not converge. Fortunately, the simulation seems to recover well for all these regions and the effect the forces is limited for later times.

Influence of flexibility on the lift and drag

A sharp reduction in lift and drag at $t^* = 2$ for both the revolving and translating wings denotes the end of the acceleration period and force contribution by the added effect. The accelerating motion contributes more to the drag than the lift on the wing, as the lift over drag ratio increases slightly for the wing at $t^* = 2$. Thus the accelerating motion creates a pressure gradient oriented in the direction of the motion that creates a small additional drag.

The added mass effect is only seen on the rigid wings which create a finite lift and drag at $t^* = 0$. All flexible wings create zero lift and drag at the start of motion. Also no sharp reduction is seen at the end of the accelerating motion that can be attributed to the added mass effect.

The scaling argument explained in appendix D tells that the reference radius (R_{ref}) is located too far outboard. As a result the translating wing would generate more force than the revolving wing with the same constant coefficient distribution. For analysis of the graphs in figure 7.24 the force coefficient of the translating wing are scaled to provide comparison with the revolving wing.

For both the revolving and translating wings the highest lift and drag force are seen for the rigid wing, which matches well with the stronger vortices seen in section 7.4.4. The total force on the wing therefore decreases with additional flexibility.

Figure 7.25 shows the distribution of stress on the suction side. For the revolving wing the LEV with associated low pressure creates a large region of low pressure on the inboard section of the wing. Further outboard the influence of the pinned LEV by the TV shows a large influence. Meanwhile, the translating wing shows larger deflection of the wing surface, but lower suction stresses are seen.

The lift over drag ratio of the rigid translating wing reaches a steady value of 1.0. This is in good coherence with literature which states that at high Reynolds numbers and high angles of attack the force vector is oriented perpendicular to the wing surface. A angle of attack of $\alpha = 45°$ then leads to a lift over drag ratio of 1. The revolving wing displays a value of $C_L/C_D \approx 1.25$ for the developed flow. It was found that the wall boundary condition at the side and bottom permit the formation of a pressure gradient in vertical direction. The wing basically acts a rotor that induces a higher pressure at the bottom of the domain. As a result of this pressure gradient the lift coefficient is increased while the drag coefficient is unaffected.

The lift over drag ratio shows an interesting relation for both the translating and the revolving wings. The lift over drag ratio for the revolving wings increases by approximately 28% and 44% for respectively the medium and the flexible wing. For their translating counterparts an increment of respectively 50% and 90% is seen.

Spanwise circulation generation

The spanwise characteristics of lift generation is shown in figures 7.26 and 7.27, note that only half of the span is shown for the translating wing. Here the non-dimensional local circulation (equation 7.8 that is normalized with the local wing velocity is shown.

The rigid revolving wing for $t^* = 0-2$ shows that circulation is built up over the entire span of the wing, and it rises most quickly near $r/R = 0.6$ which indicates outboard vorticity transport from the inboard section. When saturation is reached, the vortex lift off is clearly distinguishable by the region at $r/R = 0.6$ and $t^* = 2.5$. Similar behaviour was found by Jardin et al. (2012) for formation of the circulation on the wing, see figure 2.18.

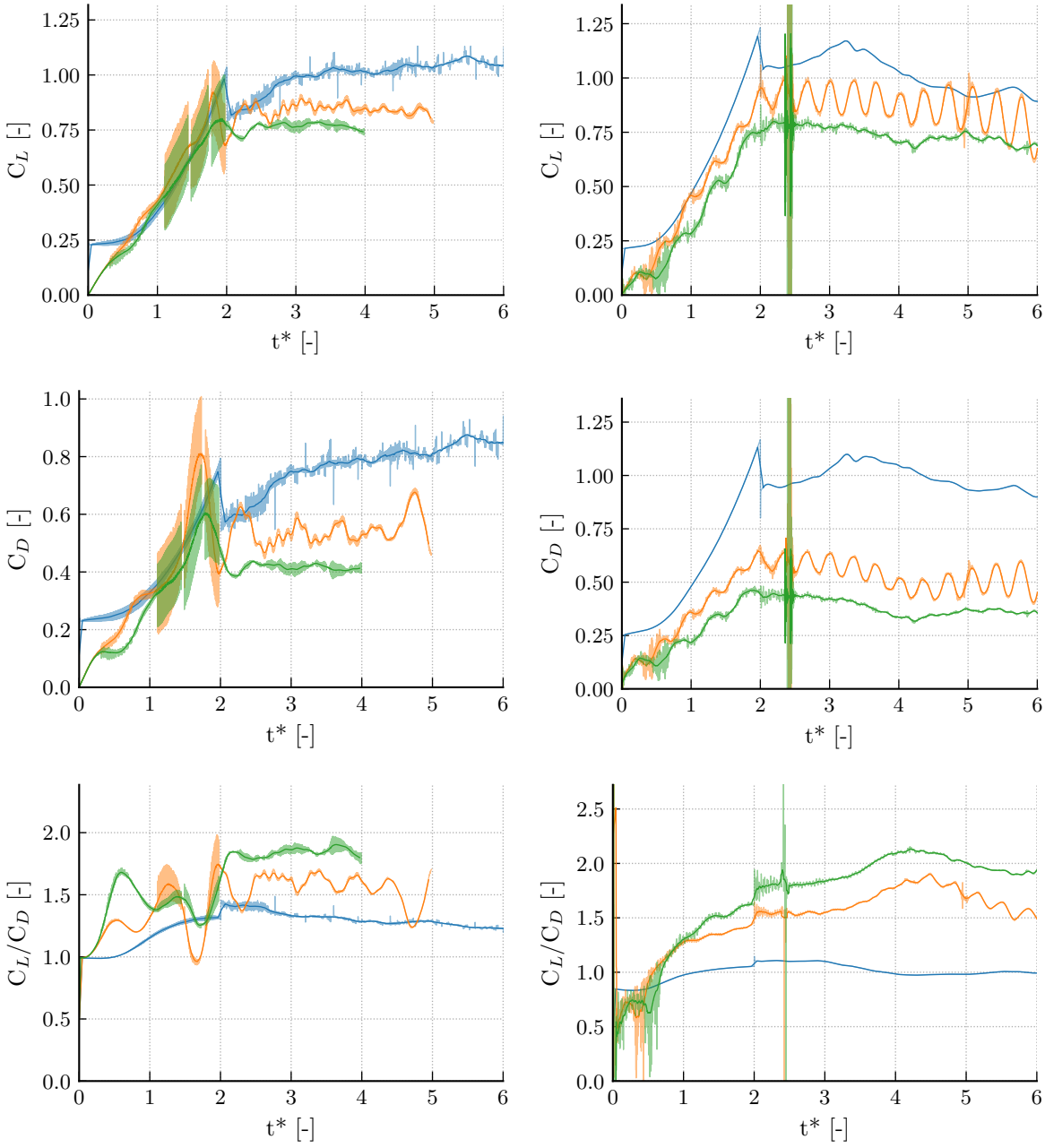

Figure 7.24: The reference lift, drag and displacement graphs of the (left) revolving and (right) translating wing: — Rigid, — Medium flexible and — Flexible. (top) The lift coefficient, (middle) the drag coefficient, (bottom) The lift over drag ratio.

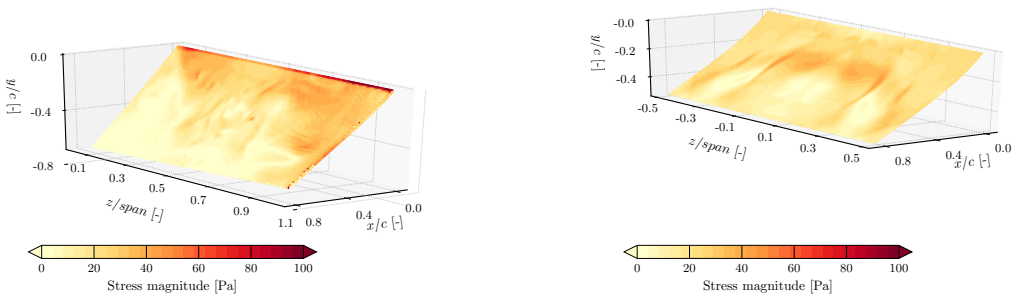

Figure 7.25: The stress on the top wing surface for (left) the revolving wing at $t^* = 4$ and (right) the translating wing at $t^* = 6$. For these values the flow is considered quasi-steady.

Just after the acceleration period a strong contribution of the attached tip vortex is seen on all wings. For the flexible wings the contribution is more stretched in time, which indicates that the tip vortex stays attached for a longer period of time. The steady state solution of the rigid wing shows that largest values of local circulation are generally found near midspan. The vorticity is drained on the outboard section.

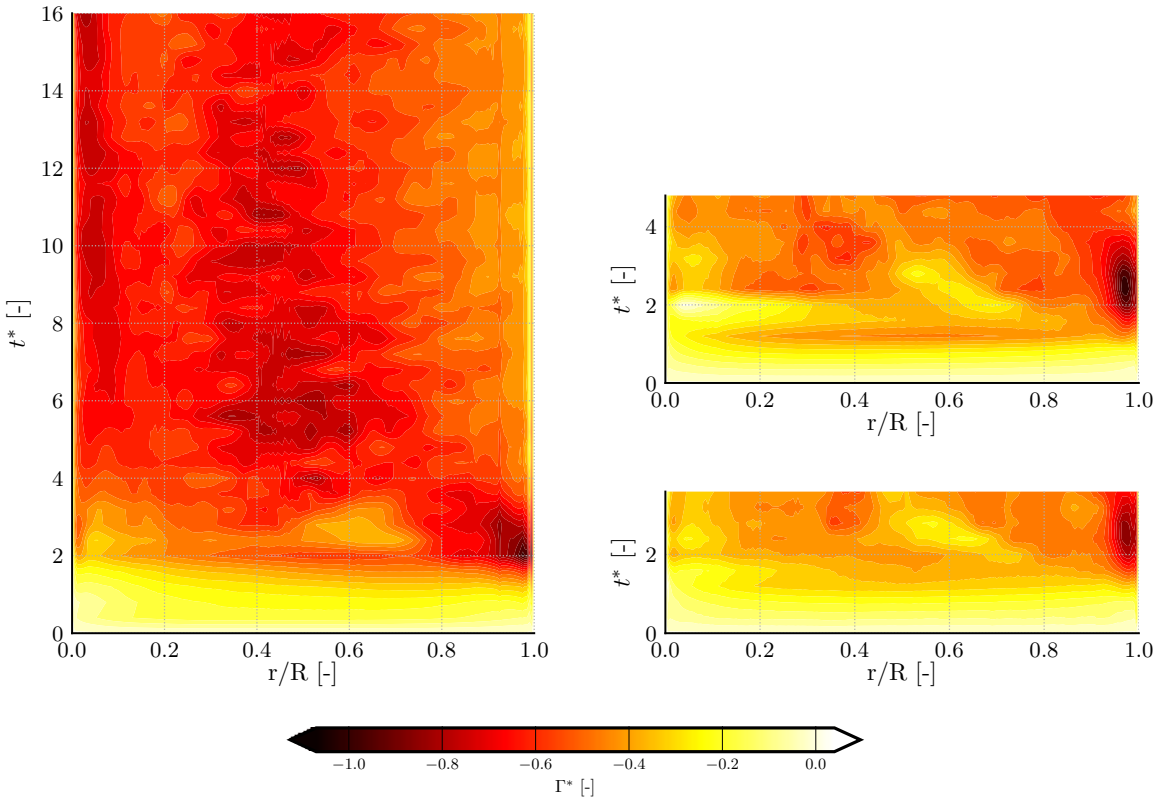

Figure 7.26: Circulation on the revolving wing over time. (left) Rigid, (right top) medium and (right bottom) flexible wing.

The local circulation on the translating wings shows large influence of the stiffness of the wing. For the rigid wing vorticity is built up most rapidly on the centre of the wing where it is quickly shed. Three different spots of high circulation are recognised. In order of temporal appearance these are:

Leading edge vortex combined with the tip vortex which is attached over a large portion of the wing. The anchoring of the LEV which lifts off form the surface, which can be clearly seen in figure 7.19. The arch stays connected to the surface and its connection to the wing surface shift towards the tip until it finally sheds at $t^* = 6$. After this, the local circulation on the surface drops because the vortices and therefore low pressure areas don't stay closely attached to the suction side of the wing any more.

Very similar effects are seen for the two flexible revolving wings during $t^* = 0-3$ although the vortices are weaker. Unlike the rigid wings, the separated arch travels inward and separates from the surface around $t^* = 5$. The medium flexible wing shows two more periods of large circulation build-up and shedding at respectively $t^* = 7.5$ and $t^* = 11$. The strong suction caused a larger deflection on the wing as shown in figure 7.15. The most flexible wing shows that the circulation is determined by smaller structures which shed locally.

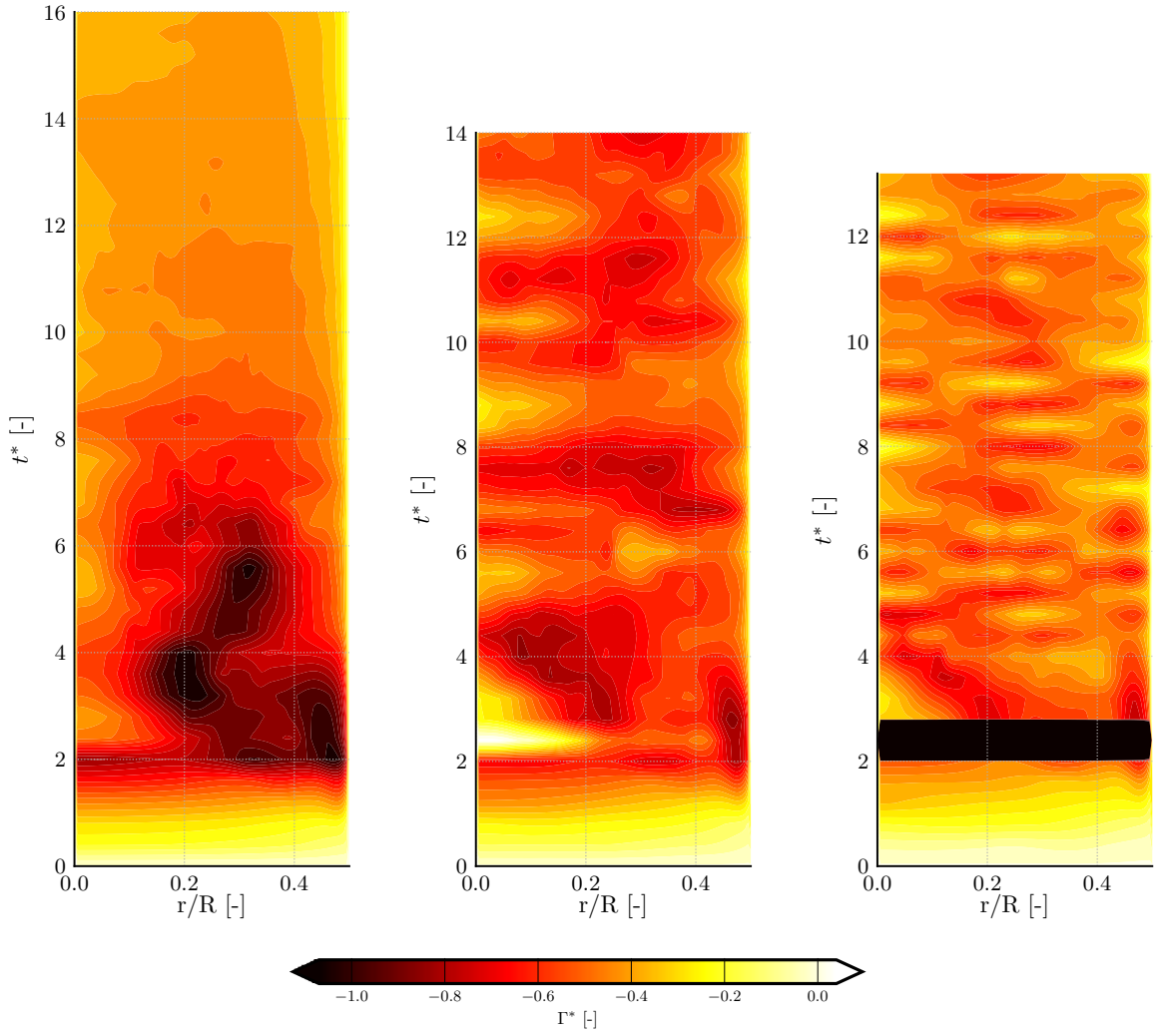

Figure 7.27: Circulation on the translating wing over time. (left) Rigid wing, (middle) medium and (right) flexible wing.

7.5. Conclusions

Six different wings have been tested and the results are presented in this chapter. Three revolving and three translating wings with various degrees of chordwise flexibility. The effective stiffness tested has a value of 0.147 for the medium wing and 0.073 for the flexible wing, which indicates that the aerodynamic forces are relatively more important than the elastic forces. Also the inertial forces are small in comparison with the aerodynamic forces as deducted by the low mass ratio of the wings.

Transitional turbulence modelling

At the Reynolds number of 10,000 transition and turbulent effects occur. To find out the effect of adding a transitional turbulence model to `OpenFOAM`, the $\gamma - Re_\theta$ model was tested for a canonical test case, and compared with experimental and ILES data. The $\gamma - Re_\theta$ model did not add significant accuracy for this type of flow (large separation and lot of spanwise interaction). The error introduced by the adoption of the RANS equations is multiple times larger than the added accuracy of the $\gamma - Re_\theta$ turbulence model.

Validation of the revolving wing

In section 7.3 the rigid revolving wing and the medium revolving wing is compared to experimental data from similar wings. The coherent structure of the LEV, TV, TEV and RV is seen for both the experimental and simulated data. The vortices of the simulation are more coherent and can support higher values of the vorticity. Analysis on the trailing edge at midspan of the rigid flap showed that a the experiment displays a discrete shedding of secondary TEVs. In contrast, the simulation has a more stable flow which displays a vortex streak. The pressure contours over the rigid wing show good coherence between the experimental data and the simulated data. Furthermore, the region of chaotic flow after flow breakdown shows a clear relation with the low pressure region.

The deflection of the wing at the trailing edge is compared for the root and tip sections. The geometric angle of attack on the root and the tip is deduced. This angle is smaller for the experimental data as compared to the simulated wing. Therefore, the deflection is under-predicted by the simulation. Evaluating the force coefficients on the experimental and simulated revolving wings, the same trends are seen: Both the lift and drag decrease for more flexible wings. However, the drag is affected more, which causes an increase in lift over drag ratio.

Influence of flexibility on revolving and translating wings

The deflection of the revolving wing is dependent on the spanwise direction. The root experiences higher travel velocities and thus higher aerodynamic forces. The deflection is largest at the tip. The deflection of the translating wing is much larger compared then the equivalent revolving wings. The high deflection can be attributed for a large part to the higher dynamic pressure on the translating wing. The deflection of the translating wing is hardly dependent on the spanwise location. Both for the medium and the flexible translating wing an angle of attack is found with a spanwise variation of maximum 0.5%.

For the revolving motion the coherent structure of the LEV, TEV, TV and RV is hardly affected by the flexural stiffness of the wing. The tip vortex is slightly elevated because of the wing deflection. The flexible wings show the shedding of secondary TEVs, while this is absent for the rigid wing. This is caused by flap chordwise oscillations over time. The translating wing shows similar creation of the LEV, TEV and to TVs. After the acceleration period the LEV lifts up from the surface at midspan in an arch-like structure. For some time it is pinned to the wing structure by the tip vortices.

The strength of the LEV decreases with flexibility because the flexible wings generate less circulation than the rigid wings. This is seen for both the translating and revolving wings. For the revolving wing the larger deflection of the tip with lower flexural stiffness causes better attachment of the TV to the wing. As a result, the point of LEV breakdown is shifted inwards. The quasi-developed flow on the revolving wings shows that the medium wing displays vorticity drainage near the mid of the

span behind the position of LEV breakdown. Also drainage is seen at the tip region. The LEV on the rigid wing can grow larger until it has a size of the entire chordlength. The vorticity is drained in the most outboard section.

For increased flexural stiffness, the circulation builds up slower for the revolving wings. The shedding of the LEV at a spanwise position of $r/R = 0.6$ is clearly visible for all revolving wing. After the shedding the tip vortex is anchored for a limited period to the wing surface.

The translating wings shows similar build up of circulation during the wing acceleration. The circulation is built up over the wing and shed at midspan for $t^* = 2$. The LEV helps to anchor the LEV to the wing surface which creates high local suction forces. Eventually, the LEV is shed. The rigid translating wing shows a decline in circulation after $t^* = 6$. The flow is not attached any more and the shed LEVs are located far from the wing surface. In contrast, the LEV on rigid revolving wing stays attached and the amount of circulation is relatively constant after $t^* = 6$.

For the translating case the flexible wings provide some circulation in the quasi-steady state. The wing deflection causes a decrease in angle of attack and the vortices are located closer to the surface, hence a suction force is generated. The most flexible case even shows anchoring of the LEVs at near the tip region.

Both the lift and drag coefficient decrease for the more flexible wings. During the wing acceleration the added mass effect is seen for the rigid wings. The lift over drag ratio for the rigid wing should be close to unity because the wing is at an angle of $\alpha = 45°$ and the pressure force angle is nearly perpendicular to the wing. For the revolving wing a higher lift over drag was noted because the wing acts as a propeller, increasing the pressure at the bottom of the domain. For the revolving wing the application of flexibility increases the lift over drag ratio by respectively 28% and 44% for the medium and flexible wing. The same translating wings see an increase of respectively 50% and 90% lift over drag ratio.

Chapter 8

Conclusion and Recommendations

In this work a new FSI method is proposed and validated. The method is used to perform analysis to different flapping wings to gain insight on the influence of flexibility of flapping wings. Furthermore, the difference between translating and revolving wings is studied to gain an understanding of the influence of the rotational effects.

8.1. Conclusions

A FSI method has been developed and implemented in the OpenFOAM adapter. The method is based on coupling the open-source fluid solver `OpenFOAM` with the coupling library `preCICE`. For the implementation of the FSI in this adapter a force and displacement class is added. The force class is used to map boundary data from the fluid to the structure. The displacement class deforms the mesh to create an flow geometry. Furthermore, checkpointing of the fluid fields is added which includes previous time values. The checkpointing is required when a timestep is not converged and it sets back the fluid solver to the state before the last timestep. Since the mesh is deforming in the coupled simulation, checkpointing implemented for the mesh too. Here, the mesh points and mesh flux are stored.

Validation of the developed procedure is performed in chapter 5. Prior to the coupled simulation validation, the fluid and structure are evaluated. The fluid validation is performed by the "flow around a cylinder" case since this case is relatively similar to the cylinder with a flap case used for the FSI validation. It was found that the incompressible, laminar flow was well able to predict the shedding behaviour for all meshes. Even for the coarsest mesh the shedding frequency of under 0.4%. Larger differences are present for the pressure difference over the cylinder and lift and drag coefficient. For the FSI analysis a mesh close to the medium mesh was selected, which was is favourable in terms of computational efficiency. The influence of a dynamic mesh which is used in the FSI simulations was tested and had no significant influence on the accuracy of the solver.

The structure is evaluated using three representations of the isolated flap from the coupled simulation. Two static cases show that the structural model of the flap is always stiffer than the reference value. Larger structural meshes approach the deflection given by reference data. Shell elements perform well for the static simulations but fail for the dynamic case. Therefore brick element meshes are used in the remainder of the work. The medium mesh of 280 elements is chosen because it provides sufficient accuracy for small computational costs. The structure is stiffer than the flap from the reference data, which is confirmed by an eigenfrequency analysis. Comparing the analytical solution for first bending eigenmode with the numerical solution, a difference of approximately 13% is seen.

To verify the implemented parts of the FSI method, three cases are adopted with (quasi)-unidirectional coupling of the coupling parameters. In this way, both the mapping and the checkpointing can be verified separately for both the structure, the fluid fields, and the mesh fields. All three cases shows that the either two or three subiterations are required to reach a very strict convergence criterion. Therefore, the mapping and checkpointing of the structure and fluid solver is proved.

At last, the FSI1, FSI2 and FSI3 test cases from Turek & Hron (2006) are evaluated. FSI1 is the steady state case and the simulation shows good coherence with the reference values. The horizontal displacement shows the flap is slightly elongated by the fluid shear force. The dynamic FSI2 case at a Reynolds number of $Re = 100$ shows close resemblance with the reference data for the vertical displacement and the excitation period. It was found that the natural frequency of the cylinder and the second eigenfrequency of the flap were closely matched, so the flap naturally assumes this frequency. The FSI2 flap has a density ratio of $\rho_s/\rho_f = 10$ which indicates that inertial forces are relatively important. The excitation of the 4^{th} eigenmode causes an oscillation in the force coefficients, but this does not influence the flap displacement much due to the high density ratio. It is clear that the forces are very sensitive to excitation of eigenfrequencies of the structure.

For the FSI3 case a the density ratio is unity which increases the relative importance of the fluid forces. Moreover, the flap does not assume an eigenmode since the natural shedding frequency is in between the first and second eigenfrequency of the flap. Therefore a flapping frequency is found other than the reference case with subsequent higher amplitude. The lift and drag profile follow the same frequency as the flapping motion and therefore diverge from the reference value. Even though the FSI3 case shows large discrepancies between simulated data and the reference case the method is validated by the three unidirectional cases and FSI1 and FSI2. FSI3 shows that the coupled simulation is incredibly sensitive to the correct evaluation of eigenfrequencies for the structure.

The influence of the inertial, aerodynamic and elastic forces is further investigated in chapter 6. Here a 2D flapping wing at a Reynolds number of $Re = 150$ is tested for different mass ratios (m^*) and frequency ratios (FR). The flapping motion is defined by a pure sweeping motion and $\alpha = 90°$ angle of attack. Only by structural bending the wing can create a lower angle of attack. The fluid field is highly asymmetrical for the up- and downstroke. Regardless of the stiffness and mass ratio, a similar flow is seen: At the beginning of the cycle the wing encounters a strong shed LEV from the previous cycle. The wake capture causes a strong LEV to develop quickly, but it is shed rapidly and convects downwards paired with the counter-rotating TEV. Therefore the shed LEV is not captured during the reversed stroke and the new LEV is grown more gradually.

The wing shows large sensitivity to the mass ratio of the flap. For large mass ratios the fluid forces are insignificant and the wing deformation is governed by the inertia of the wing. An advanced rotation of the wing is the result. Compared to wings of lower mass ratio the heavier wings create smaller lift and more drag. The frequency ratio relates the elasticity of the flap to the fluid forces. In the tested range the lift increases for higher frequency ratios. This is mostly because the wing shows larger deflections which case a component of the aerodynamic force in positive lift direction. The addition of extra elasticity increases the lift over drag ratio for all wings.

In research higher frequency ratios were tested however this was found not feasible for the current mesh deformation method. More elastic structures shows more deformation and the mesh would collapse.

The 3D wings in chapter 7 are selected for two reasons. Firstly the effect of chordwise flexibility on translating and revolving wings is evaluated. Secondly, the effect of a translating versus a revolving motion is tested in this way. In total six simulations are ran: A rigid, medium and flexible wing for each motion. The revolving wings are recreated following the experiment by van de Meerendonk (2016). The experimental results of the flowfield and forces can be compared to the simulated data to find result regarding the accuracy of the coupled simulation.

The flow structure of experiment and simulation are compared which shows good coherence for the large scale structures in the flow. A clear vortex system compromising of the LEV, TV, TEV and RV is observed for both the experiment and the simulation. The latter shows more stable vortices which can sustain larger values of vorticity. The pressure field is compared between the experiment and the simulation. The size and shape of the low and high pressure region below and above the

wing match very well with the experiment. In terms of forces reasonable agreement is seen with the experiment, while the flap deformation is underestimated.

When comparing the translating and the revolving wings it must be realized that the average dynamic pressure on the translating wing is higher than on the revolving wing. Therefore, larger deflections are seen for the translating wing than the revolving wing. The translating wing bends in chordwise direction with very small differences in deflection over the span. The geometric angle of attack falls within 0.5° for both the medium and the flexible translating wing. On the other hand, the deflection on the revolving wing shows a larger deflection on the outboard section, where the wing reaches its maximum velocity.

For the revolving wings the main structure of the LEV, TEV and RV is little affected by flexibility. Oscillations in the flap deflection can cause the shedding of secondary TEVs, which connect to the TV and RV in a helical structure. The strength of the LEV decreases with flexibility because the flexible wings generate less circulation than the rigid wings. The larger deflection of the tip causes better attachment of the TV to the wing and the point of LEV breakdown is shifted inwards. For the developed flow the medium flexible wings show vorticity drainage near the mid of the span after the position of LEV breakdown, and at the TV. The LEV on the rigid wing can grow larger until it has a size of the entire chordlength. The vorticity is drained near the tip.

For the translating wing the build up of vorticity is similar for all wings. The LEV is formed and lifts off from midspan. Near the tips it is anchored to the wing which creates regions of high suction force. The developed flow shows large influence of flexibility. For the rigid wings vorticity shedding occurs, however the vortices are not located close to the surface and therefore hardly a region of large suction. For the flexible wings the wing deflection causes a decrease in angle of attack and the vortices are located closer to the surface. The most flexible case even shows anchoring of the LEVs at near the tip region.

Both the lift and drag coefficient decrease for the more flexible wings. During the wing acceleration the added mass effect is seen for the rigid wings. The flexible wings immediately react to the fluid by deflecting which diminishes the added mass effect. The lift over drag ratio for the rigid wing should be close to unity because the wing is at an angle of $\alpha = 45°$ and the pressure force angle is nearly perpendicular to the wing. For the revolving wing a higher lift over drag was noted because the wing acts as a propeller, increasing the pressure at the bottom of the domain. For the revolving wing the application of flexibility increases the lift over drag ratio by respectively 28% and 44% for the medium and flexible wing. The same translating wings see an increase of respectively 50% and 90% lift over drag ratio.

The development of circulation over the wing in time shows that both the revolving and the translating wings build up circulation which is shed after the acceleration period. This happens near $r/R = 0.6$ for the revolving wing and at midspan for the translating wings. From $t^* = 2-3$ all wings show a relatively high lift component from the attached TV after which it separates from the wing surface. Here large differences are seen between the rigid revolving and translating wings. The revolving wing manages to create a stable LEV on the inboard section while the flow is completely separated from the translating wing.

8.2. Recommendations

Several recommendations can be formulated on the basis of this thesis. For the fluid structure interaction method the following parts can be implemented:

8.2.1. On the FSI method

The coupled simulations performed in this research were bounded by a number of constraints. Further development of the OpenFOAM adapter can extend the capabilities that can be performed with the coupled simulation.

Further validation In chapter 5 a validation procedure is performed using the cylinder with a flap case from Turek & Hron (2006). The coupled simulation is very sensitive to the excitation of eigenfrequencies by the structural solver. For the FSI2 case this caused a discrepancy in the lift and drag coefficient, while the complete dynamical behaviour was altered for the FSI3 case.

Further validation could aim at categorising better the role of the eigenfrequencies on the simulation. Also, a structural model could be used that represents the validation model more closely.

Subcycling The simulations in this thesis are all performed with the same coupling timestep for the different solvers. The fixed timestep is limited by the stability of the fluid solver. The amount of coiling timestep can be reduced for subcycling of the fluid solver. The displacement can then be interpolated using a higher order method to create a displacement with a continuous second derivative for all timesteps. This is necessary to guarantee finite accelerations and a stable situation.

Extension of the code At the moment of this thesis, the FSI module of the OpenFOAM adapter is valid for incompressible, laminar flows. The OpenFOAM adapter should be relatively easy extensible to other flows, for example:

- Compressible flows
- Multi-phase flows
- flows with turbulence modelling

Elaboraration on meshes The deformation of the structure is imposed on the fluid by deforming the mesh. However, in chapter 6 it was found that the deformation method in `OpenFOAM` is prone to collapsing for high rotations. An alternative would be mesh deformation using RBFs, as shown by Bos (2010). This method is used for the mesh deformation in Blom (2017) in `FOAM-FSI`.

Alternatives can also be explored. Large wing deflections could be meshed an overset grid. Also a background grid with the Immersed Boundary Condition would be a valuable addition to the current module.

Parallel capabilities The parallel simulations from this thesis were performed with the strict condition that all the mesh cells adjacent to the FSI boundary had to be located on one core. This creates a large amount of processor boundary faces which is a waste of computational resources. Further analysis and possible implementation of the code should create a method in which the FSI boundary can divided amongst multiple processor boundary fields.

Templating All different fluid fields are checkpointed using a new buffer definition for every type of field. This can be applied in much less lines if C++ style templating is used.

Restart module For the revolving wings the computational time was limited by the time available on the TU Delft cluster. The coupled simulation is not able to restart, due to the limited restart options of `CalculiX`. The addition of a convenient restart option in the `Calculix adapter` would therefore be a valuable addition.

8.2.2. Recommendations for flapping wing research

On the side off FSI in flapping wing research several recommendations can be formulated.

Improving the current simulation Evaluating translating and revolving wing case from chapter 7 several parts could be improved. Firstly, a finer mesh would help in capturing more small scale effects. Also the addition of a turbulence model capable of handling the largely separated flow can increase the accuracy of the computation. Furthermore, the mass ratio was not preserved for the current simulations with respect to the experiments. The oscillations seen in the force figures indicate that the structure vibrates at some frequency. This effect can be reduced by selecting the correct mass ratio which would reduce the effect of the inertial forces and therefore structural vibrations.

On the structural side the rotational and translational acceleration forces were neglected. The inclusion of these forces could help at obtaining a more accurate representation of the structural deformation.

Influence of rotational forces For further development in flapping wing research it can be interesting to evaluate the role of the Coriolis, centrifugal and Euler acceleration. The open structure of `OpenFOAM` is very suitable to derive a force field for these fields. Such a research could help in defining the exact role of the rotational accelerations on the stability of the LEV.

Applications for MAVs At last, the coupled simulation can be used to construct more elaborate models and aid in the design of MAVs. An FSI analysis to the DelFly could for example be used to gain a better understanding of the clap-and-fling effect in the 3D flow and aid the design towards more efficient forms of transport.

References

Anderson, J. D. (2011). *Fundamentals of aerodynamics* (5th ed.). McGraw-Hill Education.

Aono, H., Chimakurthi, S. K., Wu, P., Sällström, E., Stanford, B. K., Cesnik, C. E. S., … Shyy, W. (2010). A computational and experimental study of flexible flapping wing aerodynamics. In *48th aiaa aerospace sciences meeting including the new horizons forum and aerospace exposition*. doi: doi:10.2514/6.2010-554

Birch, J. M., & Dickinson, M. H. (2001, August). Spanwise flow and the attachment of the leading-edge vortex on insect wings. *Nature*, *412*(6848), 729–733. doi: doi:10.1038/35089071

Birch, J. M., Dickson, W. B., & Dickinson, M. H. (2004, February). Force production and flow structure of the leading edge vortex on flapping wings at high and low reynolds numbers. *J. Exp. Biol.*, *207*(7), 1063. doi: doi:10.1242/jeb.00848

Blom, D. S. (2017). *Efficient numerical methods for partitioned fluid-structure interaction simulations* (mathesis, Technical University Delft). doi: doi:10.4233/uuid:4f467feb-7155-4465-9508-650f3f507847

Blom, D. S., van Zuijlen, A. H., & Bijl, H. (2015, November). Multi-level acceleration with manifold mapping of strongly coupled partitioned fluid-structure interaction. *Computer Methods in Applied Mechanics and Engineering*, *296*(Supplement C), 211–231. doi: doi:10.1016/j.cma.2015.08.004

Bos, F. (2010). *Numerical simulations of flapping foil and wing aerodynamics: Mesh deformation using radial basis functions* (phdthesis, Technical University Delft). Retrieved from `https://repository.tudelft.nl/islandora/object/uuid%3Aedecee10-7db2-443e-8cdf-d41aaddaa1b2`

Bungartz, H.-J., Lindner, F., Gatzhammer, B., Mehl, M., Scheufele, K., Shukaev, A., & Uekermann, B. (2016). precice – a fully parallel library for multi-physics surface coupling. *Computers and Fluids*, *141*, 250—-258. doi: doi:10.1016/j.compfluid.2016.04.003

Carr, Z. R., Chen, C., & Ringuette, M. J. (2013, January). Finite-span rotating wings: three-dimensional vortex formation and variations with aspect ratio. *Experiments in Fluids*, *54*(2), 1444. doi: doi:10.1007/s00348-012-1444-8

Chen, J. M., & Fang, Y.-C. (1996, July). Strouhal numbers of inclined flat plates. *Journal of Wind Engineering and Industrial Aerodynamics*, *61*(2), 99–112. doi: doi:10.1016/0167-6105(96)00044-X

Chen, Y., Gravish, N., Desbiens, A. L., Malka, R., & Wood, R. J. (2016). Experimental and computational studies of the aerodynamic performance of a flapping and passively rotating insect wing. *Journal of Fluid Mechanics*, *791*, 1-33. doi: doi:10.1017/jfm.2016.35

Chen, Y. H., Skote, M., Steffen, C., & Nordborg, H. (2017). FSI simulation of flexible tandem insect wings in counter stroke. *WSEAS Transactions on Fluid Mechanics*, *12*, 7–15. Retrieved from http://www.wseas.org/multimedia/journals/fluid/2017/a045813-152.php

Chopra, A. K. (2012). *Dynamics of structures: Theory and applications to earthquake engineering*. Prentice Hall. Retrieved from https://books.google.nl/books?id=3cctkgEACAAJ

Chourdakis, G. (2017a). *A general openfoam adapter for the coupling library precice* (mathesis, Technische Universität München). Retrieved from https://www5.in.tum.de/pub/Chourdakis2017_Thesis.pdf

Chourdakis, G. (2017b). *precice-adapter for the cfd code openfoam*. https://github.com/precice/openfoam-adapter. Retrieved from https://github.com/precice/openfoam-adapter

Combes, S. A., & Daniel, T. L. (2003, September). Flexural stiffness in insect wings I. scaling and the influence of wing venation. *J. Exp. Biol.*, *206*(17), 2979. doi: doi:10.1242/jeb.00523

Dai, H., Luo, H., & Doyle, J. F. (2012). Dynamic pitching of an elastic rectangular wing in hovering motion. *Journal of Fluid Mechanics*, *693*, 473-499. doi: doi:10.1017/jfm.2011.543

Daniel, T. L., & Combes, S. A. (2002). Flexible wings and fins: Bending by inertial or fluid-dynamic forces? *Integrative and Comparative Biology*, *42*(5), 1044-1049. doi: doi:10.1093/icb/42.5.1044

David, L., Jardin, T., Braud, P., & Farcy, A. (2012, April). Time-resolved scanning tomography PIV measurements around a flapping wing. *Experiments in Fluids*, *52*(4), 857–864. doi: doi:10.1007/s00348-011-1148-5

de Boer, A., van Zuijlen, A. H., & Bijl, H. (2008, September). Comparison of conservative and consistent approaches for the coupling of non-matching meshes. *Computer Methods in Applied Mechanics and Engineering*, *197*(49), 4284–4297. doi: doi:10.1016/j.cma.2008.05.001Get rights and content

de Croon, G. C. H. E., Groen, M. A., Wagter, C. D., Remes, B., Ruijsink, R., & van Oudheusden, B. W. (2012). Design, aerodynamics and autonomy of the DelFly. *Bioinspiration & Biomimetics*, *7*(2), 025003. doi: doi:10.1088/1748-3182/7/2/025003

Deng, H. B., Xu, Y. Q., Chen, D. D., Dai, H., Wu, J., & Tian, F. B. (2013, December). On numerical modeling of animal swimming and flight. *Computational Mechanics*, *52*(6), 1221–1242. doi: doi:10.1007/s00466-013-0875-2

Deng, S., Percin, M., van Oudheusden, B. W., Bijl, H., Remes, B., & Xiao, T. (2017, July). Numerical simulation of a flexible X-Wing flapping-wing micro air vehicle. *AIAA Journal*, *55*(7), 2295–2306. doi: doi:10.2514/1.j054816

Dickinson, M., Lehmann, F., & Sane, S. (1999). Wing rotation and the aerodynamic basis of insect right. *Science*, *284*(5422), 1954–1960. doi: doi:10.1126/science.284.5422.1954

Du, G., & Sun, M. (2008, July). Effects of unsteady deformation of flapping wing on its aerodynamic forces. *Applied Mathematics and Mechanics*, *29*(6), 731. doi: doi:10.1007/s10483-008-0605-9

Ellington, C. P. (1984, February). The aerodynamics of hovering insect flight. III. kinematics. *Philosophical Transactions of the Royal Society of London. B, Biological Sciences*, *305*(1122), 41. doi: doi:10.1098/rstb.1984.0051

Ellington, C. P., van den Berg, C., Willmott, A. P., & Thomas, A. L. R. (1996, December). Leading-edge vortices in insect flight. *Nature*, *384*(6610), 626–630. doi: doi:10.1038/384626a0

Ennos, R. (1988, November). The importance of torsion in the design of insect wings. *J. Exp. Biol.*, *140*(1), 137. Retrieved from http://jeb.biologists.org/content/140/1/137.abstract

Farhat, C. (2004). Cfd-based nonlinear computational aeroelasticity. In *Encyclopedia of computational mechanics*. John Wiley & Sons, Ltd. doi: doi:10.1002/0470091355.ecm063

Farhat, C., & Lesoinne, M. (2000, February). Two efficient staggered algorithms for the serial and parallel solution of three-dimensional nonlinear transient aeroelastic problems. *Computer Methods in Applied Mechanics and Engineering*, *182*(3), 499–515. doi: doi:10.1016/S0045-7825(99)00206-6

FeatFlow. (2018, January). *Numerical benchmarking of fluid-structure interaction between an elastic object and laminar incompressible flow.* http://www.featflow.de/en/benchmarks/cfdbenchmarking/fsi_benchmark.html.

Felippa, C. A., Park, K. C., & Farhat, C. (2001, March). Partitioned analysis of coupled mechanical systems. *Computer Methods in Applied Mechanics and Engineering*, *190*(24), 3247–3270. doi: doi:10.1016/S0045-7825(00)00391-1

Feng, X., Köster, M., & Zhang, L. (2005, April). *Cylinder flow benchmark with commercial software package – a comparative study* (Tech. Rep.). Fakultät für Mathematik, TU Dortmund. Retrieved from http://www.mathematik.tu-dortmund.de/lsiii/cms/papers/FengKoesterZhang2005.pdf (Ergebnisberichte des Instituts für Angewandte Mathematik, Nummer 287)

Garmann, D., & Visbal, M. R. (2011, September). Numerical investigation of transitional flow over a rapidly pitching plate. *Physics of Fluids*, *23*(9), 094106. doi: doi:10.1063/1.3626407

Garmann, D., & Visbal, M. R. (2013, June). A numerical study of hovering wings undergoing revolving or translating motions. In *31st aiaa applied aerodynamics conference*. American Institute of Aeronautics and Astronautics. doi: doi:10.2514/6.2013-3052

Garmann, D., & Visbal, M. R. (2014). Dynamics of revolving wings for various aspect ratios. *Journal of Fluid Mechanics*, *748*, 932-956. doi: doi:10.1017/jfm.2014.212

Gillebaart, T. (2011). *Influence of flexibility on the clap and peel movement of the DelFly II* (mathesis, Technical University Delft). Retrieved from https://repository.tudelft.nl/islandora/object/uuid:75dc2165-950b-4a42-b1a1-5e2bc2dfd209?collection=research

Gordnier, R. E., & Attar, P. J. (2014, February). Impact of flexibility on the aerodynamics of an aspect ratio two membrane wing. *Journal of Fluids and Structures*, *45*(Supplement C), 138–152. doi: doi:10.1016/j.jfluidstructs.2016.07.023

Guillard, H., & Farhat, C. (1999, January). On the significance of the gcl for flow computations on moving meshes. In *37th aerospace sciences meeting and exhibit*. American Institute of Aeronautics and Astronautics. doi: doi:10.2514/6.1999-793

Gutierrez, E., Quinn, D. B., Chin, D. D., & Lentink, D. (2017). Lift calculations based on accepted wake models for animal flight are inconsistent and sensitive to vortex dynamics. *Bioinspiration & Biomimetics*, *12*(1), 016004. doi: doi:10.1088/1748-3190/12/1/016004

Holzmann, T. (2017). *Mathematics, numerics, derivations and openfoam(r)* (4th edition ed.; T. Holzmann, Ed.). Holzmann CFD. doi: doi:10.13140/RG.2.2.27193.36960

Hunt, J. C. R., Wray, A. A., & Moin, P. (1988). Eddies, stream, and convergence zones in turbulent flows. *Center For Turbulence Research, Report CTR-S88*.

Inman, D. J. (2001). *Engineering vibration*. Prentice Hall.

Jardin, T. (2017). Coriolis effect and the attachment of the leading edge vortex. *Journal of Fluid Mechanics*, *820*, 312-340. doi: doi:10.1017/jfm.2017.222

Jardin, T., & David, L. (2014, Jul). Spanwise gradients in flow speed help stabilize leading-edge vortices on revolving wings. *Phys. Rev. E*, *90*, 013011. doi: doi:10.1103/PhysRevE.90.013011

Jardin, T., & David, L. (2015, March). Coriolis effects enhance lift on revolving wings. *Phys. Rev. E*, *91*(3), 031001. doi: doi:10.1103/PhysRevE.91.031001

Jardin, T., Farcy, A., & David, L. (2012). Three-dimensional effects in hovering flapping flight. *Journal of Fluid Mechanics*, *702*, 102-125. doi: doi:10.1017/jfm.2012.163

Jasak, H. (1996). *Error analysis and estimation for the finite volume method with applications to fluid flows* (phdthesis, Imperial College of Science, Technology and Medicine). Retrieved from `http://powerlab.fsb.hr/ped/kturbo/OpenFOAM/docs/HrvojeJasakPhD.pdf`

Jeong, J., & Hussain, F. (1995). On the identification of a vortex. *Journal of Fluid Mechanics*, *285*, 69-94. doi: doi:10.1017/s0022112095000462

Jones, A. R., & Babinsky, H. (2010, May). Unsteady lift generation on rotating wings at low reynolds numbers. *Journal of Aircraft*, *47*(3), 1013–1021. doi: doi:10.2514/1.46649

Kang, C. K., Aono, H., Cesnik, C. E. S., & Shyy, W. (2011). Effects of flexibility on the aerodynamic performance of flapping wings. *Journal of Fluid Mechanics*, *689*, 32-74. doi: doi:10.1017/jfm.2011.428

Katz, J., & Plotkin, A. (2001). *Low-speed aerodynamics* (2nd ed. ed.). Cambridge :: Cambridge University Press,. Retrieved from `http://catdir.loc.gov/catdir/description/cam021/00031270.html`

Kramer, V. M. (1932). Die zunahme des maximalauftriebes von tragflugeln bei plotzlicher anstellwinkelvergrosserung (boeneffekt). *Z. Flugtech. Motorluftschiff*, *23*, 185–189.

Lai, J. C. S., & Platzer, M. F. (1999, December). Jet characteristics of a plunging airfoil. *AIAA Journal*, *37*(12), 1529–1537. doi: doi:10.2514/2.641

Langtry, R. B., & Menter, F. R. (2009, December). Correlation-based transition modeling for unstructured parallelized computational fluid dynamics codes. *AIAA Journal*, *47*(12), 2894–2906. doi: doi:10.2514/1.42362

Lentink, D., & Dickinson, M. H. (2009a, August). Biofluiddynamic scaling of flapping, spinning and translating fins and wings. *J. Exp. Biol.*, *212*(16), 2691. doi: doi:10.1242/jeb.022251

Lentink, D., & Dickinson, M. H. (2009b, July). Rotational accelerations stabilize leading edge vortices on revolving fly wings. *J. Exp. Biol.*, *212*(16), 2705. doi: doi:10.1242/jeb.022269

Lindner, F., Mehl, M., Scheufele, K., & Uekermann, B. (2015). *A comparison of various quasi-newton schemes for partitioned fluid-structure interaction* (E. O. B. Schrefler & M. Papadrakakis, Eds.). IACM Special Interest Conference. Retrieved from `https://www5.in.tum.de/pub/Lindner2015_MVQN.pdf`

Liu, H., & Aono, H. (2009). Size effects on insect hovering aerodynamics: an integrated computational study. *Bioinspiration & Biomimetics*, *4*(1), 015002. doi: doi:10.1088/1748-3182/4/1/015002

Liu, H., Kolomenskiy, D., Nakata, T., & Li, G. (2017, August). Unsteady bio-fluid dynamics in flying and swimming. *Acta Mechanica Sinica*, *33*(4), 663–684. doi: doi:10.1007/s10409-017-0677-4

Lu, Y., & Shen, G. X. (2008, March). Three-dimensional flow structures and evolution of the leading-edge vortices on a flapping wing. *J. Exp. Biol.*, *211*(8), 1221. doi: doi:10.1242/jeb.010652

Luo, H., Yin, B., Dai, H., & Doyle, J. (2010, January). A 3D computational study of the flow-structure interaction in flapping flight. In *48th aiaa aerospace sciences meeting including the new horizons forum and aerospace exposition*. American Institute of Aeronautics and Astronautics. doi: doi:10.2514/6.2010-556

Malhan, R., Lakshminarayan, V., Baeder, J., Chopra, I., Masarati, P., Morandini, M., & Quaranta, G. (2012, April). Cfd-csd coupled aeroelastic analysis of flexible flapping wings for mav applications: Methodology validation. In *53rd aiaa/asme/asce/ahs/asc structures*. American Institute of Aeronautics and Astronautics. doi: doi:10.2514/6.2012-1636

Malhan, R. P., Masarati, P., Baeder, J., & Chopra, I. (2013, April). CFD-CSD coupled aeroelastic analysis of flexible flapping wings for MAV applications. In *54th aiaa/asme/asce/ahs/asc structures, structural dynamics, and materials conference*. American Institute of Aeronautics and Astronautics. doi: doi:10.2514/6.2013-1644

Masarati, P., Morandini, M., Quaranta, G., Chandar, D., Roget, B., & Sitaraman, J. (2011, June). Tightly coupled cfd/multibody analysis of flapping-wing micro-aerial vehicles. In *29th aiaa applied aerodynamics conference*. American Institute of Aeronautics and Astronautics. doi: doi:10.2514/6.2011-3022

Mayo, D. B. (2014). *An investigation of a mav-scale flexible flapping wing in forward flight: Flow field and airloads experiments with coupled CFD-CSD* (Doctoral dissertation, University of Maryland, College Park). doi: doi:10.13016/M2C61H

Mehl, M., Uekermann, B., Bijl, H., Blom, D., Gatzhammer, B., & van Zuijlen, A. (2016, February). Parallel coupling numerics for partitioned fluid-structure interaction simulations. *Computers & Mathematics with Applications*, *71*(4), 869–891. doi: doi:10.1016/j.camwa.2015.12.025

Moffatt, H. K. (1969). The degree of knottedness of tangled vortex lines. *Journal of Fluid Mechanics*, *35*(1), 117–129. doi: doi:10.1017/S0022112069000991

Nakata, T., & Liu, H. (2012). A fluid structure interaction model of insect flight with flexible wings. *Journal of Computational Physics*, *231*(4), 1822 - 1847. doi: doi:10.1016/j.jcp.2011.11.005

Nguyen, A. T., & Han, J. H. (2016, April). Effects of fluid-structure interaction on the aerodynamics of an insect wing. *Proceedings of SPIE - The International Society for Optical Engineering*, *9797*, 1-10. doi: doi:10.1117/12.2218781

Nguyen, T. T., Shyam Sundar, D., Yeo, K. S., & Lim, T. T. (2016, April). Modeling and analysis of insect-like flexible wings at low Reynolds number. *Journal of Fluids and Structures*, *62*(Supplement C), 294–317. doi: doi:10.1016/j.jfluidstructs.2016.01.012

Noyon, T. (2014). *The effect of wing deformation on unsteady aerodynamic mechanisms in hovering flapping flight* (mathesis, Technical University Delft). Retrieved from https://d1rkab7tlqy5f1.cloudfront.net/LR/Organisatie/Afdelingen/Aerodynamics__Wind_Energy__Flight_Performance_and_Propulsion/Aerodynamics/MSc_Theses/2014/Noyon__T..pdf

Openfoam and the openfoam foundation. (2018). https://openfoam.org/. Retrieved from https://openfoam.org/

Percin, M., & Oudheusden, B. (2015). *Flow visualization and force measurements on accelerated revolving flat plates at low reynolds numbers* (A. A. Forum, Ed.). American Institute of Aeronautics and Astronautics. doi: doi:10.2514/6.2015-3074

Percin, M., & van Oudheusden, B. W. (2015, February). Three-dimensional flow structures and unsteady forces on pitching and surging revolving flat plates. *Experiments in Fluids*, *56*(2), 47. doi: doi:10.1007/s00348-015-1915-9

Phillips, N., & Knowles, K. (2011, July). Effect of flapping kinematics on the mean lift of an insect-like flapping wing. *Proceedings of the Institution of Mechanical Engineers, Part G: Journal of Aerospace Engineering*, *225*(7), 723–736. doi: doi:10.1177/0954410011401705

Poelma, C., Dickson, W. B., & Dickinson, M. H. (2006, August). Time-resolved reconstruction of the full velocity field around a dynamically-scaled flapping wing. *Experiments in Fluids*, *41*(2), 213–225. doi: doi:10.1007/s00348-006-0172-3

Rusch, A. (2016). *Extending SU2 to fluid-structure interaction via preCICE* (bachesis, Munich School of Engineering). Retrieved from https://www5.in.tum.de/pub/Rusch2016_BA.pdf

Sane, S. P. (2003, October). The aerodynamics of insect flight. *J. Exp. Biol.*, *206*(23), 4191. doi: doi:10.1242/jeb.00663

Shahzad, A., Tian, F. B., Young, J., & Lai, J. (2017). Numerical study of rigid and flexible wing shapes in hover. *Journal of Physics: Conference Series*, *822*(1). (cited By 0) doi: doi:10.1088/1742-6596/822/1/012007

Shyy, W., Aono, H., & Kang, C.-k. (2013). *An introduction to flapping wing aerodynamics.* New York, UNITED STATES: Cambridge University Press. doi: doi:10.1017/CBO9781139583916

Thomas, P. D., & Lombard, C. K. (1979, October). Geometric conservation law and its application to flow computations on moving grids. *AIAA Journal*, *17*(10), 1030–1037. doi: doi:10.2514/3.61273

Triantafyllou, M. S., Triantafyllou, G. S., & Yue, D. K. P. (2000, January). Hydrodynamics of fishlike swimming. *Annu. Rev. Fluid Mech.*, *32*(1), 33–53. doi: doi:10.1146/annurev.fluid.32.1.33

Trizila, P., Kang, C.-K., Aono, H., Shyy, W., & Visbal, M. (2011, April). Low-Reynolds-number aerodynamics of a flapping rigid flat plate. *AIAA Journal*, *49*(4), 806–823. doi: doi:10.2514/1.j050827

Turek, S., & Hron, J. (2006). Proposal for numerical benchmarking of fluid-structure interaction between an elastic object and laminar incompressible flow. In *Fluid-structure interaction: Modelling, simulation, optimisation* (pp. 371–385). Berlin, Heidelberg: Springer Berlin Heidelberg. doi: doi:10.1007/3-540-34596-5_15

Uekermann, B. (2017). *Precice.* https://github.com/precice. Retrieved from https://github.com/precice

Usherwood, J. R., & Ellington, C. P. (2002, June). The aerodynamics of revolving wings i. model hawkmoth wings. *J. Exp. Biol.*, *205*(11), 1547. Retrieved from http://jeb.biologists.org/content/205/11/1547.abstract

van de Meerendonk, R. (2016). *Three-dimensional flow and load characteristics of flexible revolving wings at low Reynolds number* (mathesis, Delft University of Technology). Retrieved from https://repository.tudelft.nl/islandora/object/uuid%3Ad7cfbf36-a5ba-4361-bb66-d53ef7344e5e

Vanella, M., Fitzgerald, T., Preidikman, S., Balaras, E., & Balachandran, B. (2008). Influence of flexibility on the aerodynamic performance of a hovering wing. *Journal of Experimental Biology*, *212*(1), 95–105. doi: doi:10.1242/jeb.016428

van Ingen, J. L. (1956). *A suggested semi-empirical method for the calculation of the boundary layer transition regionl* (techreport No. VTH-74). Technical University of Delft. Retrieved from http://resolver.tudelft.nl/uuid:cff1fb47-883f-4cdc-ad07-07d264f3fd10

Wagner, H. (1925). Über die entstehung des dynamischen auftriebes von tragflügeln. *ZAMM-Journal of Applied Mathematics and Mechanics/Zeitschrift für Angewandte Mathematik und Mechanik*, *5*(1), 17–35. doi: doi:10.1002/zamm.19250050103

Wang, Q., Goosen, J. F. L., & van Keulen, F. (2017, August). An efficient fluid-structure interaction model for optimizing twistable flapping wings. *Journal of Fluids and Structures*, *73*(Supplement C), 82–99. doi: doi:10.1016/j.jfluidstructs.2017.06.006

White, F. (2005). *Viscous fluid flow*. McGraw-Hill Education. Retrieved from h

Wilcox, D. C. (2008, November). Formulation of the k-w turbulence model revisited. *AIAA Journal*, *46*(11), 2823–2838. doi: doi:10.2514/1.36541

Yang, J., Preidikman, S., & Balaras, E. (2008, February). A strongly coupled, embedded-boundary method for fluid-structure interactions of elastically mounted rigid bodies. *Journal of Fluids and Structures*, *24*(2), 167–182. doi: doi:10.1016/j.jfluidstructs.2007.08.002

Yau, L. C. (2016). *Conjugate heat transfer with the multiphysics coupling library precice* (Unpublished master's thesis). Technical University of Munich.

Yin, B., & Luo, H. (2010, November). Effect of wing inertia on hovering performance of flexible flapping wings. *Physics of Fluids*, *22*(11), 111902. doi: doi:10.1063/1.3499739

Zhao, L., Huang, Q., Deng, X., & Sane, S. P. (2010). Aerodynamic effects of flexibility in flapping wings. *Journal of The Royal Society Interface*, *7*(44), 485–497. doi: doi:10.1098/rsif.2009.0200

Appendix A

Numerical researches of flexible flapping wing aerodynamics

Number	Source	year	dimension	Mesh method	Wing geometry	Wing flexibility
	Current work	2018	3	Dynamic Mesh	Yes	
1	S. Deng et al. (2017)	2017	3	Overset-grid method based on RBF	DelFLY	No
2	Wang et al. (2017)	2017	3	-	Plate	Yes
3	Shahzad et al. (2017)	2017	3	IBM	Simple wing	Yes
4	Y. H. Chen et al. (2017)	2017	3	Dynamic remeshing	Dragonfly	Yes
5	T. T. Nguyen et al. (2016)	2016	3	meshless method	Fruit fly	Yes
6	A. T. Nguyen & Han (2016)	2016	3	-	Hawkmoth	Yes
7	Y. Chen et al. (2016)	2016	3	Dynamic mesh	Plate	Yes
8	Noyon (2014)	2014	3	IBM	Plate	No
9	Mayo (2014)	2014	3	Overset grid method	Plate	Yes
10	Gordnier & Attar (2014)	2014	3	Overset grid method	Plate	Yes
11	R. P. Malhan et al. (2013)	2013	3	Overset grid method	Plate	Yes
12	Dai et al. (2012)	2012	3	IBM	Plate	Chordwise
13	Nakata & Liu (2012)	2012	3	Dynamic multigrid	Hawkmoth	Yes
14	Gillebaart (2011)	2011	2	Dynamic with RBF	Clap and Fling	No
15	Bos (2010) (thesis)	2010	2	Dynamic with RBF	2D rigid	No
16	Luo et al. (2010)	2010	3	IBM	Plate and dragonfly	Yes
17	Aono et al. (2010)	2010	3	Dynamic using master-slave	MAV wings	Yes
18	Du & Sun (2008)	2008	3	Dynamic with TFI and Poisson equation	Fruit fly	Yes
19	Vanella et al. (2008)	2008	2	IBM	2D linked plate	Yes

Number	Flow solver	CFD program	Structural deformation	structural solver	Coupling
	Incompressible RANS	OpenFOAM	FEM	Calculix	PreCICE
1	Incompressible RANS	Inhouse	Prescribed	-	-
2	Quasi-steady model	Matlab	Nonlinear plate model	Matlab	Own method
3	Incompressible RANS		non-linear FEM	Inhouse	
4	Incompressible RANS	ANSYS Fluent	FEM	ANSYS Mechanical	ANSYS System Coupling packages
5	Incompressible RANS	Projection method	FEM	VEGA	Loose coupling
6	UVLM	Inhouse	FEM	ANSYS	
7	FEM-DG on incompressible Navier-Stokes				
8	Incompressible RANS		Prescribed	-	-
9	Compressible Navier-Stokes	OVERTURNS	multi-body FEM	MBDyn	Python
10	Incompressible Implicit LES	6th order own solver	Nonlinear p-version plate element		
11	Compressible RANS	OVERTURNS	multi-body FEM	MBDyn	Work preservation with Moving Least Squares fitting
12	Incompressible RANS	Inhouse	FEM for thin structures	NonStaD	MPI
13	Incompressible RANS		FEM for shells	Inhouse	Loose coupling
14	Incompressible laminar Navier-Stokes	OpenFOAM	Prescribed	-	-
15	Incompressible RANS	OpenFOAM	Prescribed	-	-
16	Incompressible RANS	Inhouse	FEM for thin structures	NonStaD	MPI
17	Incompressible RANS	STREAM	multi-body FEM	UM/NLAMS	
18	Incompressible RANS		Prescribed	-	-
19	Incompressible RANS		2-link model	Inhouse	Monolithic

Appendix B

The OpenFOAM adapter `execute()`

The `execute()` algorithm is given in the flow chart below. This flowchart is set up from the side of the OpenFOAM adapter. One cycle is given here. In a coupled situation the given flow is repeated many times.

The block on the left hand side called "precice::adapter" denotes all the work performed between `preCICE` and the structural solver. This includes the mapping of data, but also all other methods `preCICE` hosts to create coupled simulations.

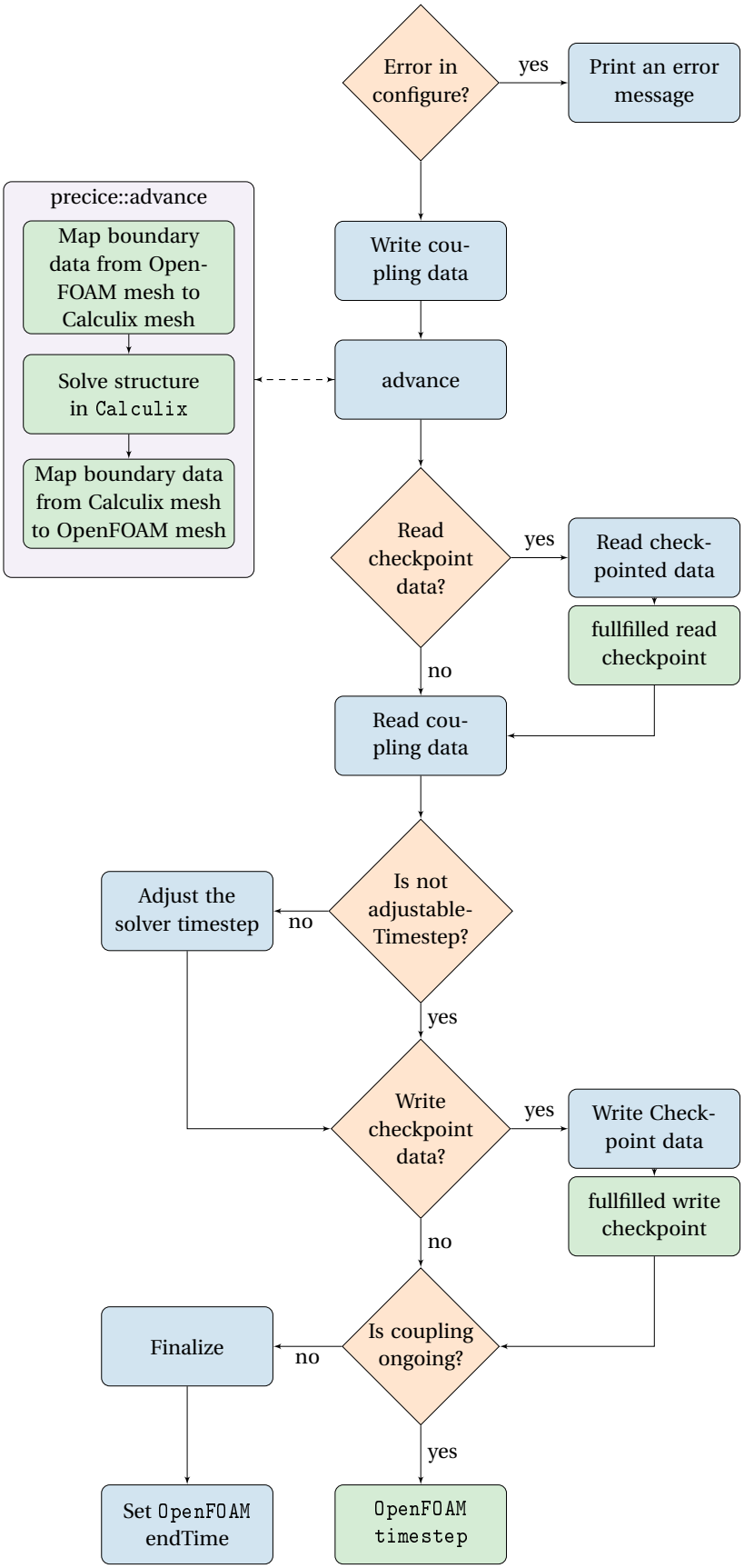
Error in configure?
yes
Print an error message
precice::advance
Map boundary data from OpenFOAM mesh to Calculix mesh
Solve structure in Calculix
Map boundary data from Calculix mesh to OpenFOAM mesh
Write coupling data
advance
Read checkpoint data?
yes
Read checkpointed data
fullfilled read checkpoint
no
Read coupling data
Is not adjustable-Timestep?
Adjust the solver timestep
no
yes
Write checkpoint data?
yes
Write Checkpoint data
fullfilled write checkpoint
no
Is coupling ongoing?
Finalize
no
yes
Set OpenFOAM endTime
OpenFOAM timestep

Appendix C

Selection of Fluid and Structural dynamic codes featured in FSI

C.1. Fluid solvers

In appendix A several CFD programs are listed to solve the fluid field. In the open-source regime `OVERTURE` (incompressible) and `OVERTURNS` (compressible) are used in the research by R. Malhan et al. (2012); R. P. Malhan et al. (2013); Mayo (2014); Masarati et al. (2011) . This range of research with an (in)compressible RANS solver combined with a structured overset mesh.

Stanford University Unstructured (`SU`^{2}) is another open-source alternative, but so far no research with flapping wings was found using this solver. A coupling is available for the open-source coupling software `preCICE`.

Various versions of `OpenFOAM` are available for flow solving. In flapping wing research with FSI, so-far it has only been used in the works of Blom (2017); Gillebaart (2011), who adopted `foam-extend-3.2`. However, `OpenFOAM` is an extremely useful toolbox which provides the user with many functionalities. It is the largest open-source flow solver available and is under constant development.

C.2. Structural solvers

Many structural solvers and FEM methods exist and have been used in past research. Vanella et al. (2008) performed a numerical study towards 2D flexible wings. The structural modelling was performed using a simplified wing model made up of two pseudo elements with a torsional spring. The wing body was then created using an interpolation between two elements, leading to a wing deformation with only one degree of freedom. This could be captured by one equation only.

An other method which resolves the wing structure is the twist model as defined by Wang et al. (2017). The coupled system in this research is specifically designed to be computationally cheap, in contrast to many existing FSI models. This allowed the coupled system to be used in an optimisation routine. The model predicts the wing deflection under lift and inertial load quite accurate, but the assumption lead to discrepancies in the overall displacement of the model and the FEM validation case.

Masarati et al. (2011); R. Malhan et al. (2012); R. P. Malhan et al. (2013); Mayo (2014) use the structural package Multibody Dynamics (`MBDyn`) to solve the nonlinear structural dynamics of shell elements. The structure can be extended with nonlinear beam elements to model the effect of carbon rods. The software `MBDyn` has was already coupled to a Vortex Lattice method for rotorcraft applications. Furthermore, the software primary goal is to solve multi-body systems. A flapping mechanism with multiple bodies can therefore be easily treated with this software.

`NonStaD` is used in the research by Luo et al. (2010); Dai et al. (2012), and is the nonlinear part of a finite element package specifically written to handle thin-walled structures such as frames, membranes, plates or shells.

T. T. Nguyen et al. (2016) presented a model for a flexible *Drosophila*: One with a uniform stiff-

ness and the other with a Leading Edge Reinforced (LER) wing with a realistic stiffness distribution. For the modeling of the domain, `VEGA` is used. This is a C++ library to model nonlinear three-dimensional deformable models which can handle large deformations. The LER wing was modelled by creating a mesh in which the veins of the wings had a higher Young's Modulus and density.

`Calculix` is a 3D FEM code whose syntax is based on the commercial code `Abaqus`. The code handles a multitude of different finite elements for structural computation, and can handle large, nonlinear deformation. Shell and beam elements are represented in the collection of elements. Internally these elements are extruded to 3D elements since the `Calculix` solver can handle 3D elements.

Rusch (2016) developed an interface between the coupling software `preCICE` and `Calculix`. Both CHT problems, and mechanical fluid structure interaction can be handled by the adapter.

Appendix D

Derivation of scaling arguments

D.1. Mass Ratio

The ratio between inertial and aerodynamic forces is called the mass ratio. To derive this scaling argument, first a form for the aerodynamic and inertial forces is derived. Th starting point for this derivations are the kinematics of the 2D flapping wing given in chapter 6.

Equation 6.1 gives the definition for the displacement of the leading edge. The velocity and acceleration of the leading edge are respectively the first and second derivative of the displacement. This leads to the following relations for the velocity and acceleration:

$$U \sim fc, \tag{D.1}$$

$$a \sim f^2 c. \tag{D.2}$$

The aerodynamic forces can be computed for an arbitrary constant with the suitable aerodynamic coefficient:

$$\begin{aligned} F_{\text{aero}} &= \frac{1}{2}\rho_f U^2 C_{\text{aero}} S \\ &\sim \rho_f f^2 c^3 b. \end{aligned} \tag{D.3}$$

In term, the inertial forces can be derived using Newtons' second law:

$$\begin{aligned} F_{\text{inertia}} &= m_{\text{wing}} a \\ &= \rho_s (cbh) f^2 c \\ &\sim \rho_s c^2 f^2 bh. \end{aligned} \tag{D.4}$$

The mass ratio is then found by the ratio between the inertial and aerodynamic forces:

$$m^* = \frac{F_{\text{inertia}}}{F_{\text{inertia}}} \tag{D.5}$$

$$= \frac{\rho_s c^2 f^2 bh}{\rho_f f^2 c^3 b}$$

$$= \frac{\rho_s h}{\rho_f c}. \tag{D.6}$$

D.2. Translating and Revolving wings

The revolving and translating wing studied in chapter 7 represent a different motion for which the parameters can be compared using the same reference velocity V_t. In the current approach, the reference velocity is defined at a certain section of the wing span, however, this may not represent the best reference situation.

In the following scaling argument it is argued that the translational and revolving wings can be compared best if the force generation is the same on both wings for a constant lift coefficient distribution. The lift is computed formulated by the integral form over the span:

$$L = \frac{1}{2}\rho U^2 C_L S = \int_{R_{\text{root}}}^{R_{\text{tip}}} L' \,\mathrm{d}r, \tag{D.7}$$

for which the lift on the translation and the rotating wing is the same.

A relation between the two wings can be set up. The lift coefficient is taken constant and the chord and density are the same for the translating and revolving wings. Then equating $L_{\text{translating}} = L_{\text{revolving}}$ leads to:

$$\int_{R_{\text{root}}}^{R_{\text{tip}}} V_t^2 \,\mathrm{d}r = \int_{R_{\text{root}}}^{R_{\text{tip}}} \Omega^2 r^2 \,\mathrm{d}r. \tag{D.8}$$

To achieve similarity between the two cases, the reference velocity is now introduced on the revolving wing as:

$$V_t = \Omega R_{\text{ref}}, \tag{D.9}$$

where R_{ref} denotes the position the reference span should be taken such that the translating and revolving wing generate the same amount of lift for a constant lift coefficient.

Solving the integral leads to the representation in equation D.10, where b is the span of the wing. This equation is further manipulated to find a form for the reference radius R_{ref}:

$$V_t^2 b = \frac{V_t^2}{R_{\text{ref}}^2} \frac{R_{\text{tip}}^3 - R_{\text{root}}^3}{3}, \tag{D.10}$$

$$R_{\text{ref}} = \sqrt{\frac{R_{\text{tip}}^3 - R_{\text{root}}^3}{3b}}. \tag{D.11}$$

Filling out the values for the wing defined in section 7.1 a reference radius of $R_{\text{ref}} = 96.4\text{mm}$ is found. The reference velocity at this location is $V_t = 0.165\text{m}\,\text{s}^{-1}$. This is different from the values used in chapter 7. Here the reference radius and velocity are respectively: $R_{\text{ref}} = 117\text{mm}$ and $V_t = 0.2\text{m}\,\text{s}^{-1}$. This leads to a situation where the forces on the translational case are enlarged with respect to the revolving one.

Appendix E

Analytical approximation of the flap eigenfrequencies

The shape and frequency of the eigenmodes can derived from the equations E.1 and E.2, which model the flap as an Euler-Bernoulli beam element. The vibrations in longitudinal direction are determined by the equilibrium between the unsteady force F due to flap acceleration in the x-direction and the flap internal force due to strain. Taking the first derivative of the equation allows the force to be replaced by the acceleration of the beam element only dependent on the shape w. E denotes the Young's modulus, A the area of the section and ρ the density of the material. The resultant form is a second order Partial Differential Equation (PDE) (Inman, 2001):

$$F = EA\frac{\partial w}{\partial x}, \qquad M = EI\frac{\partial^2 w}{\partial x^2}, \tag{E.1}$$

$$\rho A\frac{\partial^2 w}{\partial t^2} = EA\frac{\partial^2 w}{\partial x^2}, \qquad \rho A\frac{\partial^2 w}{\partial t^2} = EI\frac{\partial^4 w}{\partial x^4}. \tag{E.2}$$

A similar approach is taken for the equilibrium in moment about the z-axis on the flap. The second derivative is taken in x-direction so the moment can be replaced by an expression dependent on the shape w. This leaves a fourth order partial differential equation shown on the right side of equation E.1. I denotes the moment of inertia about the spanwise axis.

The fixed end of the flap is restricted in movement, so the first and second derivative of w are zero. At the free end no force or moment can be supported. For the longitudinal motion this implies that the first derivative of w with respect to x must be zero. For the bending motion the shear and moment, respectively the second and third spacial derivative are zero, which leads to the following boundary conditions:

$$w(0,t) = 0, \qquad \frac{\partial w(L,t)}{\partial x} = 0, \tag{E.3}$$

$$\frac{\partial w(0,t)}{\partial x} = 0, \qquad \frac{\partial^2 w(L,t)}{\partial x^2} = 0,$$

$$\frac{\partial^3 w(L,t)}{\partial x^3} = 0.$$

The next step is solving the PDEs using separation of variables: $w(x,t) = X(x)T(t)$. Substitution of this form in the equations of E.2 and ordering terms leads to the following definitions:

$$\frac{X''}{X} = \frac{\rho}{E}\frac{T''}{T} = -\sigma^2, \qquad \frac{\rho A}{EI}\frac{X''''}{X} = \frac{T''}{T} = -\omega^2. \tag{E.4}$$

For the spacial part of the longitudinal eigenmodes the solution of the PDE can be written as a combination of a sine and cosine, where σ is the separation constant. The zero displacement boundary condition at the clamped end means that the a_2 coefficient is zero. The boundary condition at the end of the flap implies that a family of solutions exists for specific values of σ.

$$\begin{aligned} X(x) &= a_1 \sin(\sigma x) + a_2 \cos(\sigma x), \\ &= b_1 \sin\left(\frac{2n-1}{2L}\pi x\right) \qquad \text{for } n = 1,2,3,... \end{aligned} \tag{E.5}$$

where L is the length of the beam. A similar derivation is performed for the temporal part of the PDE which leads to:

$$T(t) = \sin\left(\frac{2n-1}{2L}\pi\sqrt{\frac{E}{\rho}}t\right) \qquad \text{for } n = 1,2,3,... \tag{E.6}$$

which has eigenfrequencies:

$$f_n = \frac{2n-1}{4L}\sqrt{\frac{E}{\rho}} \qquad \text{for } n = 1,2,3,... \tag{E.7}$$

The bending modes are derived in a similar manner. However, the solution of the fourth order Ordinary Differential Equation (ODE) for X includes hyperbolic sine and cosine parts:

$$X(x) = a_1 \sin(\beta x) + a_2 \cos(\beta x) + a_3 \sinh(\beta x) + a_4 \cosh(\beta x), \tag{E.8}$$

$$T(x) = b_1 \sin(\omega t) + b_1 \cos(\omega t), \tag{E.9}$$

where:

$$\beta^4 = \frac{\rho A \omega^2}{EI}.$$

The four boundary conditions for the clamped and free side are then applied to equation E.8. This leads to a system of four equations for four unknowns which can be solved. This system of equation can only have non-zero solutions if the determinant of the solution matrix is zero. Therefore solutions exist for specific values of β the following expression which can be found by numerical approximation:

$$\cosh(\beta L) cos(\beta L) + 1 = 0. \tag{E.10}$$

Filling in the found eigenvalues β_n in the equation with updated coefficient a_i leads the following definition for the shape of the eigenvalue.

$$X_n(x) = A_1\left[\left(\cosh(\beta_n x) - \cos(\beta_n x)\right) + \frac{\cos(\beta_n L) + \cosh(\beta_n L)}{\sin(\beta_n L) + \sinh(\beta_n L)}\left(\sin(\beta_n x) - \sinh(\beta_n x)\right)\right]. \tag{E.11}$$

The corresponding eigenfrequencies can be deduced using the definitions for the second moment of inertia and the area for an arbitrary span b:

$$f_n = \frac{\beta_n^2}{2\pi}\sqrt{\frac{EI}{\rho A}} = \frac{\beta_n^2 h}{2\pi}\sqrt{\frac{E}{12\rho}}. \tag{E.12}$$